UNIVERSITY OF SOUTHAMPTON

Mass Modelling Techniques for Gamma Ray Burst Missions

Dave Willis

Submitted for the degree of Doctor of Philosophy

DEPARTMENT OF PHYSICS AND ASTRONOMY
FACULTY OF SCIENCE

April 13, 2003

UNIVERSITY OF SOUTHAMPTON

ABSTRACT

FACULTY OF SCIENCE

DEPARTMENT OF PHYSICS AND ASTRONOMY

Doctor of Philosophy

Mass Modelling Techniques for Gamma Ray Burst Missions

by Dave Willis

The current status of gamma ray astronomy is briefly reviewed with the focus on Gamma Ray Bursts (GRBs), detection methods and the various sources of background that a space telescope will encounter. Every gamma ray instrument encounters a high level of background noise in relation to the signal and understanding the structure and modulation of this background is vital to extracting the best science from an instrument. The ever evolving Mass Modelling technique is reviewed and demonstrated in the context of The INTEGRAL Mass Model (TIMM). Discussion relating to isotropy and homogeneity is also included.

Swift is the next mission expected to make a significant impact on the field of GRBs and it is to be launched in September 2003 by NASA. The Swift Mass Model (SwiMM) is presented. The applications of SwiMM include the optimisation of the graded-Z passive shielding design, the predicted likelihood of false triggers when encountering trapped charged particle fluxes and the effects of GRB self-contamination through flux reprocessing. The effects of GRB flux self-contamination are also explored in the context of BATSE burst data for GRB 920525 and GRB 910503 and it is shown that the current detector response for the Spectroscopy Detectors (SD) is inadequate for off-axis bursts. This further emphasises the importance of correctly accounting for this re-processed flux when observing GRBs with Swift.

Swift's Burst Alert Telescope (BAT) is required to have a wide field-of-view to maximise the number of GRB triggers. This has the added benefit of being able to perform an unprecedented all-sky survey in this revealing energy band. The application of SwiMM to the all-sky survey is discussed with each aspect of the modelling technique verified with independent empirical data.

Contents

List of Figures

List of Tables

Acknowledgements

I would like to thank everyone who has contributed or helped me during my work on this thesis. I would firstly like to thank my supervisor for his endless enthusiasm, Prof. Tony Dean, and all members of the Southampton Gamma Ray Astronomy group for their guidance and advice: Drs. Tony (Ralph) Bird, Colin Ferguson, Matt Westmore, Simon Shaw, Jon Lockley, Nene Diallo and Charlotte Perfect. I would also like to express my appreciation to all members of the astronomy department at Southampton, to Ann Parsons (GSFC), Tad Takahashi (ISAS) and Michael Briggs (MSFC).

The two people that helped me attain my initial enthusiasm for the subject were my secondary school physics teachers, Mr Wiles and Mr Baum, and I would like to think this thesis is a product of their hard work (and I believe I wasn't an easy child to teach!) as much as it is of mine.

Finally I would like to show my gratitude for the un-named that made my life as a PhD student a pleasent and productive one.

Preface

The work presented in this thesis has been carried out by the author, in collaboration with others, at the University of Southampton between October 1999 and October 2001. Chapter 4 initially presents the Mass Modelling techniques in the context of The INTEGRAL Mass Model (TIMM). Previous versons of TIMM were developed by Dr. Colin Ferguson (**v3.4**), Dr. Fan Lei (**v1.0a - v3.3**) and Dr. Andy Green (**v1.0**). The author was solely responsible for adapting TIMM **v3.4** to include the SAX WFC as a replacement for the JEM-X X-ray camera.

The burst contamination analysis for BATSE in chapter 6 employed a verson of the BATSE Mass Model (BAMM). This was developed at Southampton by Dr Rudolfo Gurriaran to provide a method of flat-fielding for the BATSE occultation All-Sky Survey (BASS). The author was responsible for adapting the current BAMM code to perform the investigation into the performance of the detector response.

All Swift Mass Model (SwiMM) code and methodology (chapters 5 and 7) were developed solely by the author.

Chapter 1

The Gamma Ray Sky

1.1 Introduction

The gamma ray domain opens a relatively new window to The Universe. Due to the complexity involved in gamma ray detection and atmospheric opacity the realisation that objects in the sky emitted gamma rays came relatively late when compared to other wavelengths. With the advent of neutrino detectors and gravitational wave detectors, gamma ray astronomy can no longer call itself the latest innovation in astronomy. However, the fundamental science that one can obtain from observing in this energy band is the key factor in the continuing popularity and development in the area.

The discovery of Gamma Ray Bursts (GRBs) has, for the first time, provided a class of object that gamma ray astronomy can call its own. With many successful gamma ray missions in progress and many in the planning stages, gamma ray astronomy continues to be as revealing as ever.

Sub-gamma ray astronomy assumes light to be wave-like in nature enabling optical techniques to be used (up to X-ray energies). Gamma rays are assumed to be particle like in nature and so their detection, focusing, imaging and background suppression are far more complex. The possible sources of astronomical gamma rays, the mechanisms for their production and the missions dedicated to their observation are discussed in this chapter.

1.2 Sources of Gamma Rays

1.2.1 Mechanisms for Gamma Ray Production

Gamma rays can occur as a result of various physical processes. These production mechanisms are described in this section.

Electron Positron Annihilation

An electron and positron will annihilate to form two photons, each consisting of the equivalent rest mass energy of a single electron (0.511 MeV).

$$e^- + e^+ \longrightarrow \gamma + \gamma$$

In close proximity the two will be pulled together by Coulomb attraction. The two photons are produced with the energy of $m_e c^2$ and move in opposite directions to conserve the momentum of the system. This process does not require the presence of a nucleon to conserve the momentum of the system. The gamma ray energy of 511 keV is a useful tool within gamma ray spectra whether it is the spectrum of an astronomical object [52] or the background spectra within an instrument [89].

Another aspect of this annihilation is a positronium continuum. When an electron and positron come into contact under suitable conditions they briefly form a particle called positronium which has a lifetime, in the singlet state, of the order of $10^{-10}s$. It can be assumed that the two leptons rotate around each other before annihilating. However, should the leptons have parallel spin, angular momentum is not conserved in a simple 511 keV annihilation. Three photons are emitted over a continuum giving the annihilation line a FWHM of the order of a few keV and the lifetime is increased to $10^{-7}s$. For the spin to be changed, an external magnetic field can be employed. This delayed continuum emission cannot be seen in instruments as the electron or positron can be stolen from the positonium by an external lepton. However, this emission can be observed in space [52].

Nuclear De-excitation

Gamma rays are emitted during the decay of radioactive isotopes. An excited nuclear state will decay according to a definite half-life emitting a discrete photon. The details of these decays can be found in any table of isotopes [31]. Nuclei can be excited in several ways. The resultant nucleus from a nuclear reaction can be excited and so decay spontaneously, emitting a gamma ray. A nucleus can capture a thermal neutron, for example the capture by a hydrogen atom to form deuterium, emitting a 2.23 MeV photon (the binding energy of the neutron in deuterium). Also a collision between an atom and a highly energetic nucleon can produce excited nuclear fragments. All these excited states will decay. The most prevailing decays in astronomy are the decay chains found in supernovae: $Ni^{56} \rightarrow Co^{56} \rightarrow Fe^{56}$ and $Ti^{44} \rightarrow Sc^{44} \rightarrow Ca^{44}$. Also observed is the decay of $Al^{26} \rightarrow Mg^{26}$ which is seen in the galactic plane at an energy of 1.809 MeV [56].

Inverse Compton Scattering

In the case of Compton scattering the photon loses energy by scattering off a stationary electron. Should the electron be moving at speed it can still cause the photon

to scatter but in doing so can impart some of its energy to the photon, equation 1.1. This will only occur when the energy of the electron far exceeds the energy of the photon.

$$E' = E\left(1 + \frac{v}{c}cos\theta\right) \tag{1.1}$$

This process does not create a photon but can up-scatter a microwave photon to gamma ray energies. This process is required to fully reproduce the cosmic diffuse hard X-ray background.

Bremsstrahlung Emission

Bremsstrahlung emission is the emission of a photon when a charged particle with a significantly larger energy than its rest energy is decelerated over a short distance by an absorbing medium. This process occurs, more efficiently whenever there are fast moving electrons colliding with local material. Bremsstrahlung deals with the creation of photons but not at discrete energies, the higher the energy of the electron the larger the fraction of the energy is imparted to the photon. This process produces a continuum spectrum with a characteristic profile and energy cutoff (defined as $\frac{hc}{eV}$ where V is the voltage through which the electron has decelerated).

This form of emission is important as a secondary source of background from beta emitting isotopes within a gamma ray instrument. In astronomical terms this type of emission is more efficient in hot plasma where there are automatically fluxes of fast electrons and target nuclei. When electrons are accelerated by the a magnetic field, such as near a neutron star, it is called *magneto*-bremsstrahlung or *synchrotron radiation* if the electrons are relativistic.

Synchrotron Radiation

Astronomical synchrotron radiation is the dominant non-thermal mechanism for the emission of gamma ray photons. This form of radiation occurs when a relativistic electron spirals in a magnetic field, see figure 1.1. Should the electron be non-relativistic the term is *cyclotron emission* and characteristically is emitted at discrete energies determined by the rotation frequency. Photons are emitted as the electrons are accelerated. The Crab is a perfect example of an astronomical object emitting synchrotron radiation. A detailed description is given in [62].

Proton-Nucleon Interaction and Meson Decay

When cosmic-rays (primarily protons) collide with an atomic nucleus the resulting fragments will include a selection of mesons. Consider a simple cosmic-ray hydrogen collision:

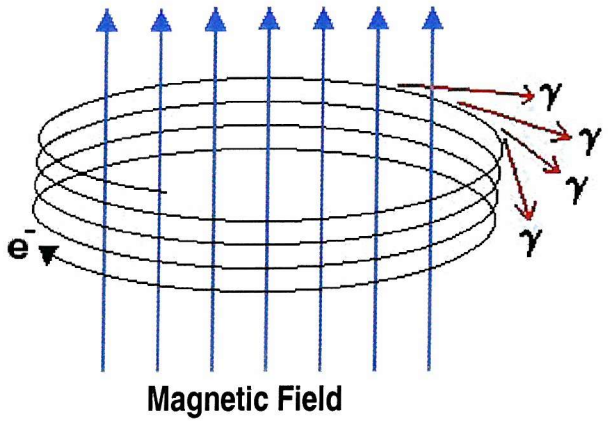

Figure 1.1: **Cyclotron radiation**. *Should the electron be relativistic then synchrotron emission occurs.*

$$p + p \longrightarrow p + p + X\,(\pi^+ + \pi^-) + Y\pi^0$$

Where X and Y are small integers. For both integers to be equal to 1 then the energy of the initial proton must be $\geq$ 290 MeV. These π mesons decay with lifetimes of $2.6.10^{-8}s$ and $8.10^{-17}s$ for $\pi^{+/-}$ and π^0 respectively, producing muons and gamma rays. Muons, in turn decay to an electron, with a lifetime of $2.2.10^{-6}s$. Whatever the route the decay takes, the final product will involve gamma rays whether created directly, emitted as Bremsstrahlung emission or created with anti-matter annihilation. These are some examples of the decay processes:

$$\begin{aligned}
\pi^0 &\longrightarrow \gamma + \gamma \\
\pi^- &\longrightarrow \mu^- + \overline{\nu_\mu} \\
\pi^+ &\longrightarrow \mu^+ + \nu_\mu \\
\mu^- &\longrightarrow e^- + \overline{\nu_e} + \nu_\mu \\
\mu^+ &\longrightarrow e^+ + \nu_e + \overline{\nu_\mu}
\end{aligned}$$

The route taken to decay to stable components and photons may be different and involve kaons or hyperons. Essentially the lifetimes involved are similar, the final product being the important factor in instrumentation.

1.2.2 Astronomical Sources of Gamma Rays

There are a variety or methods for producing gamma rays and combinations of these mechanisms are observed in various astronomical objects.

The Galactic Plane and Interstellar Medium

The Galactic plane is the strongest source of gamma rays in our sky, including diffuse and discrete sources. Due to the large angular size it is often considered to

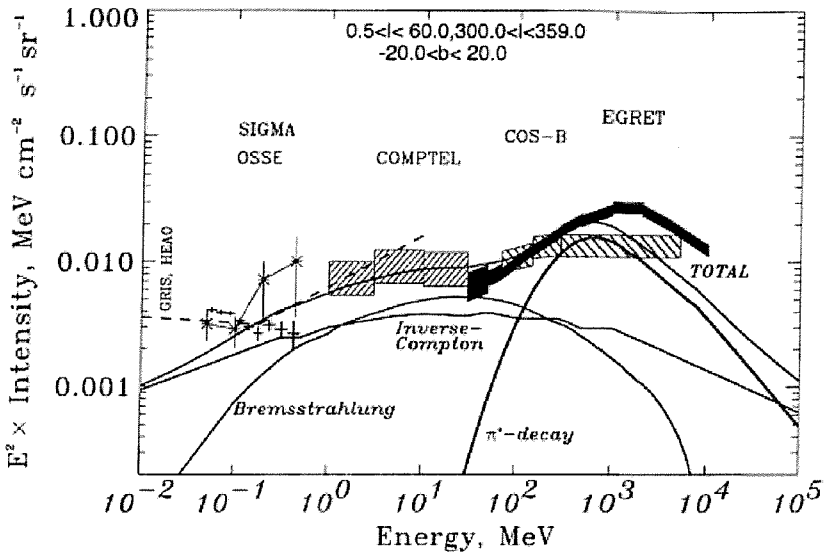

Figure 1.2: **The continuum spectrum for the galactic plane.** *The spectrum is measured by GRIS, HEAO, SIGMA, OSSE, COMPTEL, COS-B and EGRET and has components for various mechanisms fitted to it. The angular extent over which the emission was measured is also displayed. Adapted from Strong et al. (1996).*

be an interfering source of background. Galactic plane emission is in the form of a continuum comprising of several components and discrete line emission, Doppler broadened by the galactic rotation.

Continuum Emission The diffuse continuum emission is confused by unresolved sources in the hard X-ray domain but is better defined at higher energies. The continuum can be described by cosmic ray interactions with the interstellar medium involving 3 mechanisms. Greater than 100 MeV the emission is dominated by pion decay [6] and between 1 MeV and 70 MeV a combination of electron bremsstralung and weak inverse Compton scattering appears to dominate [114]. Figure 1.2 [114] shows the continuum as measured by a number of instruments with the various components fitted to the data. Below 1 MeV discrete sources begin to have an effect, dominating the 40-100 keV energy range [118]. A thermal plasma model of solar abundance (temperature: 2.6 keV) and a three-photon positronium continuum both contribute to the hard X-ray/soft gamma ray region [52].

Line Emission Nucleosynthesis is the major contributor to the galactic line emission. Novae and supernovae produce radioactive isotopes that decay as they are diffusing out into space. The various long lived chains are described in table 1.1 and all the lines emitted are displayed in figure 1.3 [93]. These include the short life-time de-excitation lines from O^{16}, C^{12}, N^{14}, Si^{28}, Ne^{20} and Mg^{24}. A byproduct of these decays can be the 0.511 MeV annihilation line, produced via β^+ decays and by positron annihilation during cosmic ray interactions with the interstellar medium.

Table 1.1: **The main decay chains from astronomical sources expected in the gamma ray domain.**

Decay Chain	Mean lifetime [years]	Emission [MeV]
$Ni^{56} \rightarrow Co^{56} \rightarrow Fe^{56}$	0.31	e^+, 0.846, 1.238, 2.599
$Co^{57} \rightarrow Fe^{57}$	1.1	0.122, 0.014
$Na^{22} \rightarrow Ne^{22}$	3.8	e^+, 1.275
$Ti^{44} \rightarrow Sc^{44} \rightarrow Ca^{44}$	68	e^+, 1.156, 0.078, 0.068
$Fe^{60} \rightarrow Co^{60} \rightarrow Ni^{60}$	$2.2.10^6$	1.332, 1.173, 0.059
$Al^{26} \rightarrow Mg^{26}$	$1.1.10^6$	e^+, 1.809

The 0.511 MeV line is an ideal tool for mapping the various gamma ray active regions of an object such as unresolved supernova within the galactic plane. Due to the close relation of the 0.511 MeV line with individual compact sources, the line can also be highly variable in places on the galactic plane [94]. Figure 1.4 shows the galactic center at 0.511 MeV [92].

Visible nucleosynthesis also occurs in massive stars such as Wolf-Rayet stars. It is estimated that two thirds of all Al^{26} emission (1.809 MeV) is due to hydrostatic nucleosynthesis in Wolf-Rayet stars with the remainder originating from Type II supernova [56]. Figure 1.5 shows the distribution of Al^{26} across the galactic plane.

Compact Objects and Variable Sources

Apart from transient events, by far the strongest discrete source of gamma rays in the sky is the Crab pulsar (PSR0531+21). The Crab nebula is the remnant of a massive star going supernova in 1054 AD. The Crab pulsar is a rapidly rotating highly magnetised neutron star emitting pulses in the radio and X-/gamma ray regions from the centre of the nebula. The high magnetic field and the rapid rotation accelerate charged particles in the vicinity of the neutron star which, by as yet undetermined mechanism, form beams of gamma rays that scan across the sky. The period of this pulsation is complex but can be assumed to be about 0.033 seconds and slows by 0.8 milliseconds per year. This rapid rotation is hard to detect in many gamma ray instruments due to their poor timing resolution. For this reason the Crab pulsar is considered to be a constant source, used to help calibrate satellite missions after their launch. The Crab is also used as a term for other sources' strengths, quoted in milliCrabs ($mCrab$). The spectrum of the Crab pulsar is displayed in figure 1.6 and has a differential energy spectrum of $24.0.E^{-2.3} photons.s^{-1}.cm^{-2}.keV^{-1}$ [134].

Pulsar emission is supported by a synchrotron hypothesis as emission is polarised. 80% of all non-gamma ray emission from the Crab is polarised but does not conform entirely with synchrotron emission from a uniform magnetic field [127], suggesting

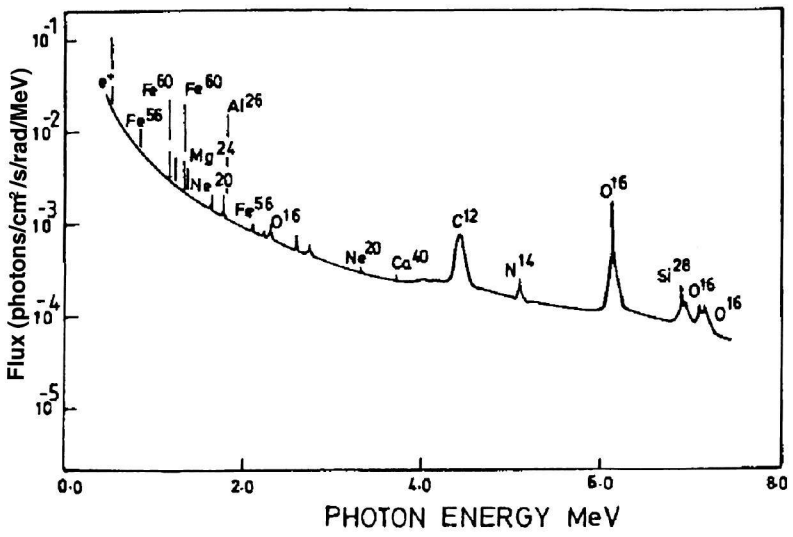

Figure 1.3: **The predicted galactic line emission.** *This figure shows the predicted line emission from the galactic centre assuming various parameters including dust grain radius and the cosmic ray density. The line width is due to thermal broadening and Doppler broadening because of galactic rotation. Adapted from Ramety et al (1992).*

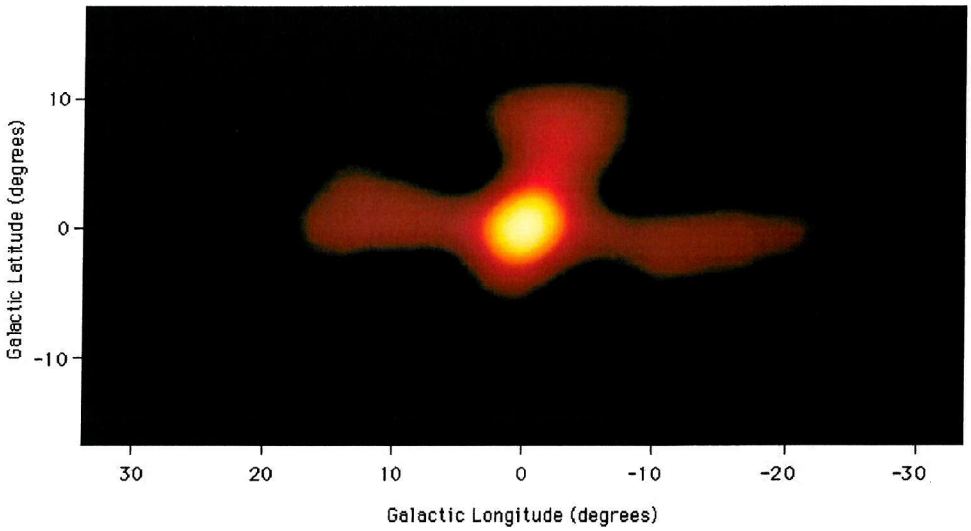

Figure 1.4: **The 511 keV map of the galactic centre.** *OSSE, TGRS and SMM measured this narrow 511 keV line emission for the galactic centre. Models of supernovae within the galactic plane fit the fluxes observed. Adapted from Purcell et al (1999).*

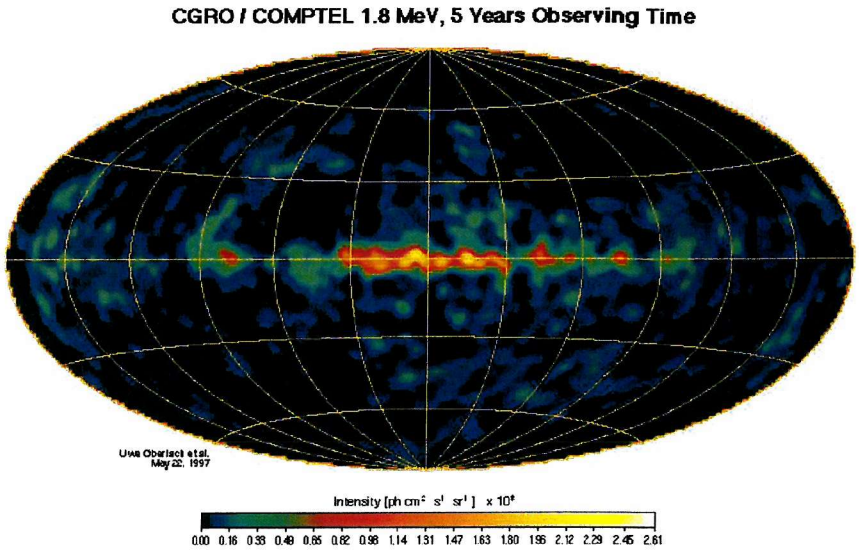

Figure 1.5: **The 1.809 MeV map of the galactic plane.** *A map of this line mostly shows the distribution hydrostatic nucleosynthesis with a third of the flux being due to Type II supernova. Adapted from Knodlseder et al (1999).*

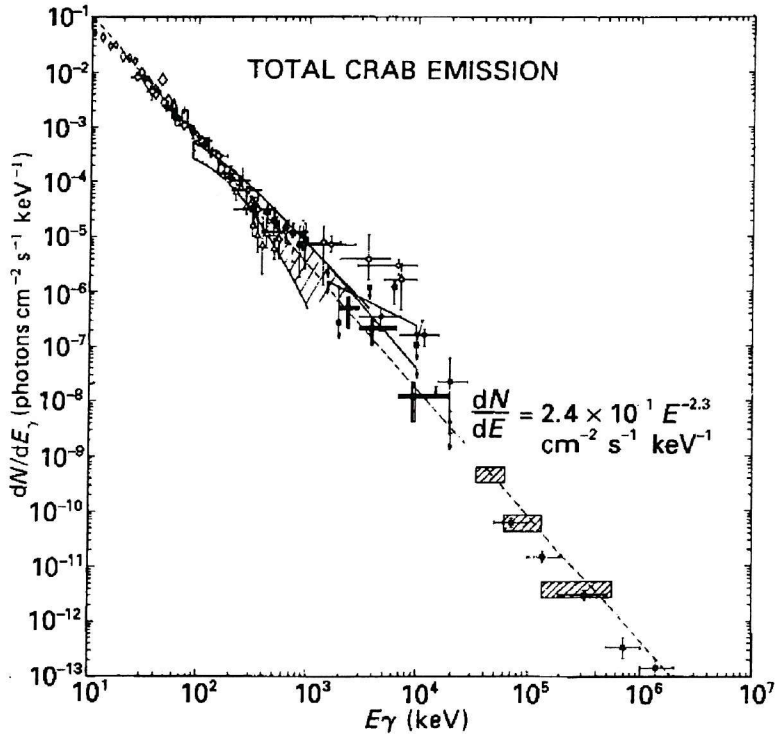

Figure 1.6: **The total Crab pulsar emission.** *Adapted from Zombeck (1990).*

projection effects and inhomogeniety. Evidence of gamma ray polarisation does not yet exist.

Compact objects are observed singularly as described above and in binary systems (in our Galaxy and the Large and Small Magellanic Clouds). These binary systems can be split into four categories: *Black Hole Candidates*, *Neutron Star Systems*, *Soft Gamma Ray Repeaters* and *White Dwarf Systems*. Each is co-orbiting with a main-sequence star that accretes matter onto its compact companion. The behavior of these systems in the gamma ray energy range is defined by the type of compact object. Several sources such as SS433 and Sco X-1 are observed to have jets, these can cause gamma ray emission from relativistic electrons up-scattering photons to gamma ray energies.

Black Hole Candidates Cygnus X-1 is a binary system and one of the first X-ray sources discovered. The variability in the X-ray emission is very short (of the order of milliseconds) suggesting the existence of a black hole [22]. The variability in black hole candidates is due to either instabilities in the mass transfer or in the dynamics of the accretion disk. The CGRO was used to observe Cygnus X-1 and it was seen that emission reached up to 5 MeV (α = -3.2) with no sign of a cutoff in the spectrum. This can be attributed to a hybrid of thermal and non-thermal emission [69]. Microquasars are X-ray binaries with relativistic collimated jets (despite their name they are galactic in origin). The jets are thought to be powered by accretion of matter onto black holes of mass 5-50 $M_{\odot}$ [28].

Neutron Star Systems Neutron star systems can be further split into two categories relating to the companion star: high and low mass. Generally speaking, the observed emission from these sources falls off rapidly near 1 MeV. Low mass pulsar systems have a companion star of less than two solar masses and accretes by a Roche lobe overflow. How the star accretes onto the compact object depends on the magnetic field. X-ray bursters have a low magnetic field ($< 10^{11}$ G). Helium can build up on the surface and eventually cause runaway thermonuclear burning. For a magnetic field of 10^{12} G or more the accretion is channelled onto the neutron star through its poles. In this case the emission is pulsed according to the rotational period of the system. High mass pulsar systems usually involve material accreting onto the neutron star by way of the stellar wind. The emission is proportional to the mass transfer rate. However should the companion star be a Be star (fast rotating, high mass loss rate) the mass transfer is more blurred and forms a disk around the star. When the neutron star passes through this disk on its elliptical orbit a strong burst occurs. 70% or all X-ray binary system are transient sources. The flaring occurs in a range from the very regular eclipsing binary system to irregular flaring systems. The dynamics of these X-ray binary systems are very complex and many classes and sub classes are emerging. A review of these classes of object can be found in Bildsten *et al.* (1997).

Soft Gamma Ray Repeaters These are galactic gamma ray events caused by highly magnetised (10^{15} G) newly formed neutron stars or *magnetars*. They are distinguished from gamma ray bursts by their soft spectrum. They are thought to burst in gamma rays due to a combination of matter accreting onto the surface and fractures in the surface due to the stresses of maintaining the high magnetic field [48]. Few have been positively identified so any generic emission is hard to determine.

White Dwarf Systems It is unusual for a white dwarf system to emit in the gamma ray domain due to the relatively low gravity and magnetic fields of the system. However there is evidence that white dwarfs can be responsible for the neutron capture line at 2.23 MeV [68] due to an unusually high temperature and magnetic field. Flares have also been observed from a rapidly spinning white dwarf system [24] with emission at MeV and TeV energies.

Active Galactic Nucleii

Active Galactic Nucleii (AGN) are very luminous and highly variable, their emission peaks in the X- and gamma ray energy bands. The energy source is thought to be accretion onto a super-massive black hole at the galactic centre. Several classes of AGN are known and the spectra and gamma ray emission mechanisms can be different for each.

BL Lacs and QSOs exhibit evidence of beaming. This produces a hard and featureless gamma ray spectrum of up-scattered photons. The luminosity of these objects in the gamma ray band exceeds the wave bands by as much as 2 orders of magnitude. Relativistic electrons accelerated in the beam inverse Compton scatter photons straying into the beam from the accretion related emission. The jets that electrons are upscattered in contain a highly relativistic plasma that have a high enough Lorentz factor that can explain evidence of superluminal motion.

Seyfert and radio galaxies show a strong scattered component due to the central engine being obscured by a torus of dust. Emission from Seyfert galaxies can be described by thermal and non-thermal mechanisms. There also tends to be a cutoff at about 500 keV [102].

The high variability of AGN suggests that the photon density is large and so photon-photon interactions will be common giving rise to the production of positron-electron pairs. The resultant 511 keV line and continuum are apparent in all but Seyfert galaxies.

Centaurus A is one of the brightest AGN and can be classed as a FR I type radio-loud galaxy viewed from the side and is a promising black hole candidate. The spectra can be defined by a doubly broken power-law as seen in figure 1.7 [112] and will exhibit the emission characteristics of AGN.

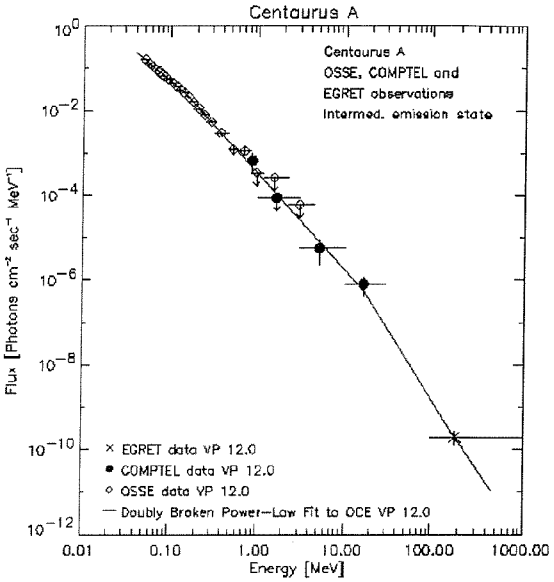

Figure 1.7: **The spectrum of Centaurus A.** *The combined spectrum as measured by OSSE, COMPTEL and EGRET. Adapted from Steinle at al. (1998).*

Galaxy Clusters

Hard X-ray emission has been detected from galaxy clusters such as the Coma cluster [34]. The mechanism behind this is thought to be the inverse Compton scattering of the microwave background by relativistic electrons accelerated by perturbations and turbulence in the inter-cluster medium [35].

Gamma Ray Bursts

In 1963 the US launched a series of satellites to monitor the testing of nuclear devices in space. These satellites named "Vela" were to police a treaty that banned nuclear testing in space or the upper atmosphere. Each pair of satellites orbited on opposite sides of a 4 day orbit and carried X-ray, gamma ray and neutron detectors. A nuclear device let off would be detected by three instruments. If a device was let off while shielded by the moon then the gamma ray detectors would still detect the cloud of radioactive material left behind by the blast. The later Vela pairs (Vela 5a, 5b, 6a and 6b) had good enough timing resolution to triangulate rough positions of any event seen in more than one of the four satellites. Several large gamma ray events were detected and it was seen that the events were not of solar or terrestrial origin [53].

There were 16 bursts detected between July 1969 and July 1972. These were studied with data taken from IMP-6, a solar flare experiment in orbit at the time with a finer spectral resolution. It was seen that the energies peaked at gamma ray energies and so could be discounted as the higher energy component of lower energy events [19].

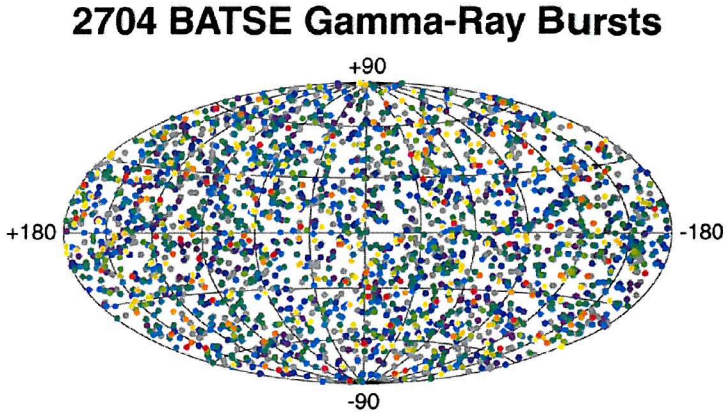

Figure 1.8: **The positions, in galactic co-ordinates, of all the GRBs triggered during the lifetime of the CGRO. Adapted from Fishman and Meegan (1995).**

A GRB is a sudden flash of gamma rays lasting anything from a few milli-seconds to 1000s and by far outshines any other source in the sky with fluxes ranging from 0.01 to 100 $ph.cm^{-2}.s^{-1}$. Perhaps the most important feature of these bursts is derived from the isotropic nature of the bursts [32]. BATSE mapped the positions of the bursts across the sky as seen in figure 1.8 and it was concluded that they were extra-galactic in origin, implying a huge energy budget.

The alternative to the huge implied energy budget was that the GRBs were galactic in origin. This could be possible should the progenitors be distributed in a halo very close by (few kpc) or at a suitable large distance ($\sim$ 200 kpc) so that no dipole could be observed. Neither of these theories can be easily explained due to the frequency of the events (more than 1 per day) and the dipole and quadrupole observational restrictions [80, 65]. Once BATSE had surveyed more than 2000 GRBs with no detectable artifact of the dipole moment a possible galactic origin was abandoned [11].

Two sub-sets emerged [57] and a possible third is now being investigated [76]. The two classes can be separated by their T_{90} time (the time within which 90% of the flux arrived at the detector). The two classes were derived initially from 222 GRBs [57] and is demonstrated in figure 1.9 . Also shown are a plot of 797 GRBs used to predict a third class [76]. The shorter GRBs are generally have a harder spectrum while the longer ones are spectrally softer. The only suggested explanation for this discrimination are different geometries at the emission sites.

A typical profile of a GRB contains many sub-bursts spanning various energies and durations. Figure 1.10 shows some "typical" time profiles for various GRBs. By considering the variability a limit can be placed on the spatial dimensions of the

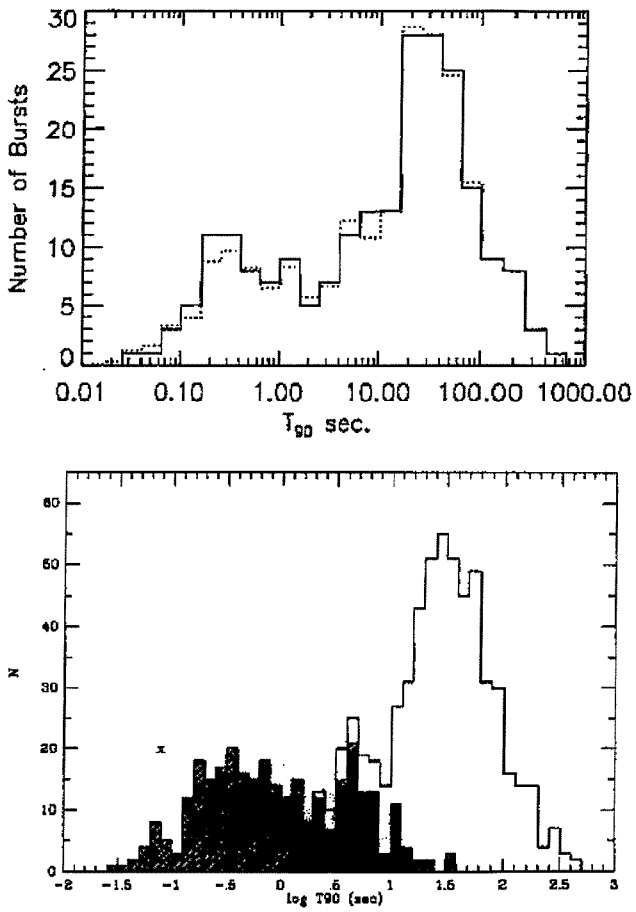

Figure 1.9: **Two plots of the distribution of T_{90} values.** *The top distribution is of 222 GRBs and the two classes can be made out. The lower distribution is of 797 GRBs and a third class between the other two may be apparent. Adapted from Kouveliotou et al. (1993) and Mukherjee et al. (1998).*

event. Variability, $\frac{dt}{t}$, being roughly between the ranges of 1 and 0.05 suggests that the energy is released ($E \simeq M_{\odot}c^2$) from a stellar scale volume. The same amount of energy released from a GRB in a few tens of seconds is the approximately the same energy that our Galaxy emits in 100 years.

In 1997 the Dutch-Italian satellite BeppoSAX provided an accurate X-ray afterglow measurement of GRB 970228 which, after a delay of hours, lead to follow-up observations at other wavelengths [21]. The fading afterglow of GRB 970228 as seen in figure 1.11 provided the first evidence of a link between the gamma ray phenomenology and the location capability of X-ray, optical and radio astronomy. GRB 970228 was observed as a consequence in the optical band [120] and appeared to be associated with a faint galaxy (z = 0.2 - 2.0) providing further evidence of its cosmological origin. GRB 970508 provided the first definite redshift measurements by way of line-of-sight absorption lines in the optical counterpart, restricting the redshift between 0.835 and 2.3 [72]. These first pan-chromatic detections opened up the field of GRBs.

GRBs are manifest at distances equivalent to that of galaxies and quasars and assuming non-beamed emission, an energy budget of $10^{51} - 10^{54} ergs.s^{-1}$ can be estimated. Evidence is growing that GRBs are associated with star-forming regions [17] and so by assuming that the GRB is a consequence of star-formation then the distribution in space may be used as a high-Z probe (z>5). Depending to which progenitor you assume, GRBs are thought to originate up to redshifts of ~20 with the median being above 2. The most distant to date has a redshift of 4.5. By measuring the Log N - Log S of GRBs, a measure of the high redshift star-formation rate can be achieved. Convolved with this is the intrinsic GRB luminosity function and various cosmological effects.

As a GRB has few emission features directly the redshift can only be inferred either by line-of-sight absorption features, redshift measurements of the host galaxy or by assuming something of the luminosity function. The line-of-sight absorption features provide the opportunity to investigate the properties of the Inter Galactic Medium (IGM) and the Inter Stellar Medium (ISM) of the host galaxy. Direct redshift measurement would be preferred as it would reduce possible coincidence error and any assumptions about the luminosity function.

Spectrally a GRB can be generally defined by a split power law with a smooth break, as described by equations 1.2 and 1.3 with the units $ph.cm^{-2}.s^{-1}.keV^{-1}$ [3]. These relations apply over the entire burst though there is some evidence for softening as the burst evolves.

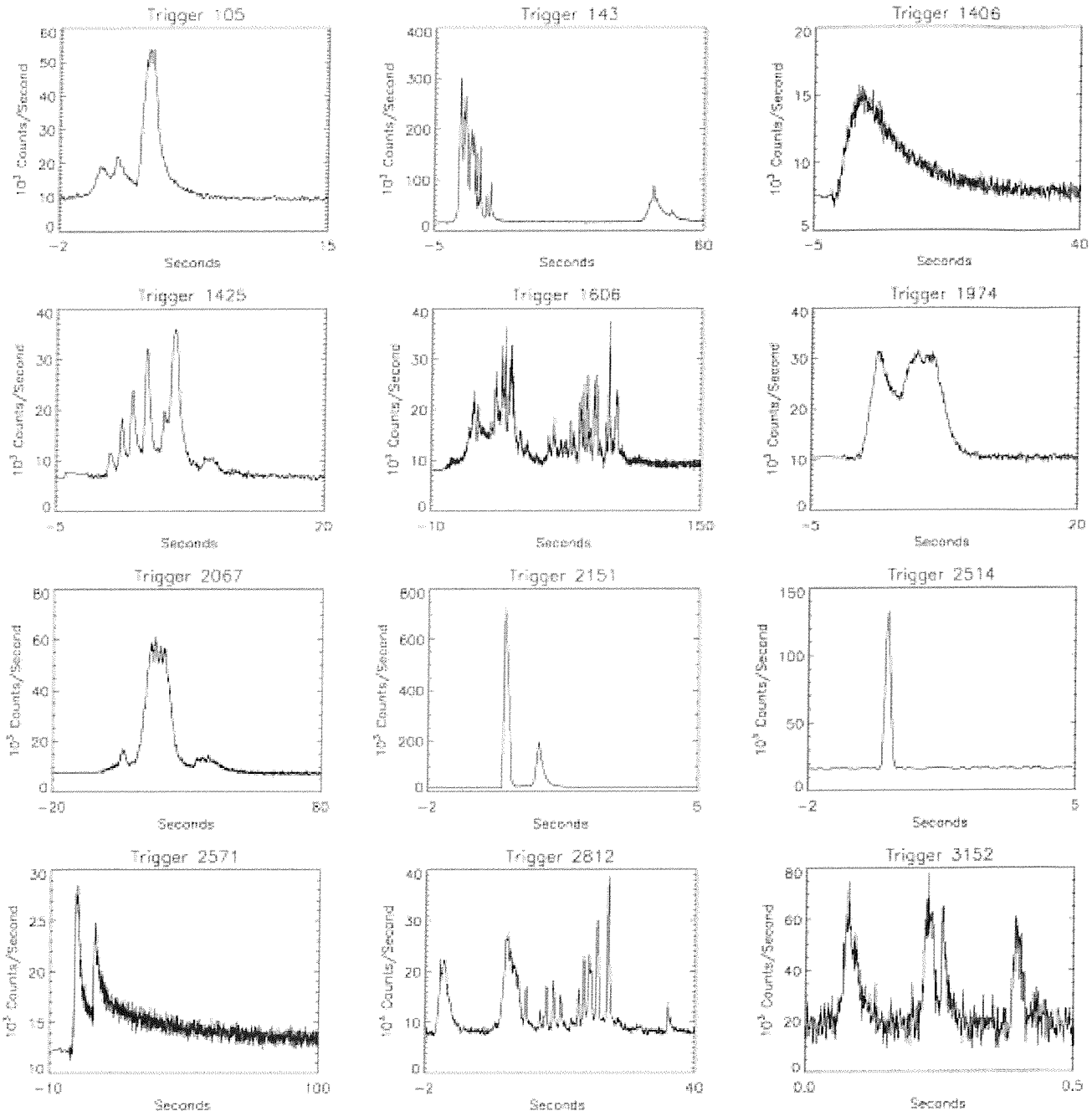

Figure 1.10: **GRB time profiles.** *This series of time profiles shows both the variability in GRB events and the inconsistency from burst to burst. Adapted from Swift documents from HEASARC.*

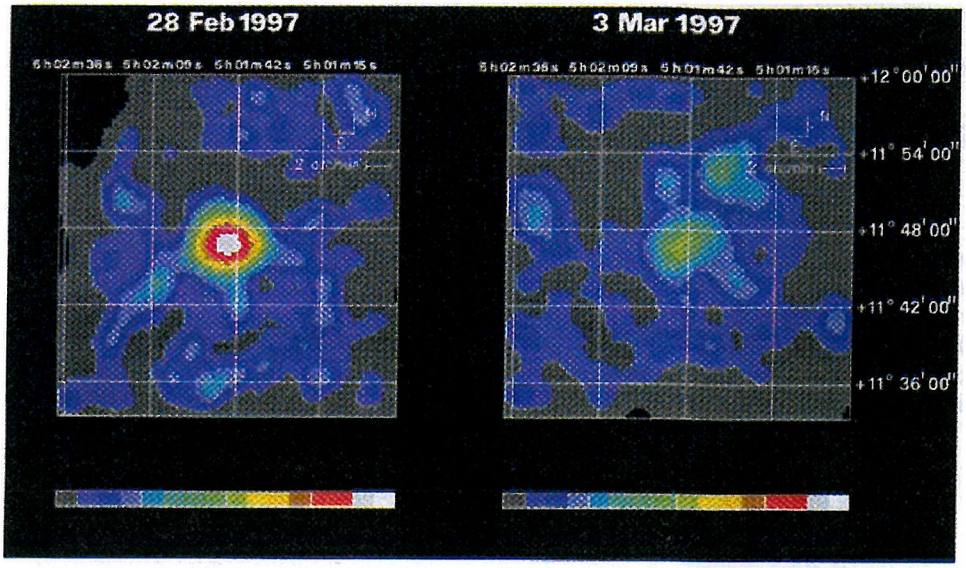

Figure 1.11: **The X-ray afterglow of GRB 970228.** *These sequential images were taken in the 2-10 keV band. White corresponds to 31 counts per second, Green to 6 counts per second and gray to 0-1 counts per second. The probability of the second image being coincidental is 0.001. This image was taken from Costa et al. (1997).*

$$N_E(E) = A.\left(\frac{E}{100keV}\right)^{\alpha}.e^{-\frac{E}{E_0}}, \quad (\alpha-\beta)\,E_o \geq E \tag{1.2}$$

$$N_E(E) = A.\left(\frac{(\alpha-\beta)\,E_o}{100keV}\right)^{\alpha-\beta}.e^{\beta-\alpha}.\left(\frac{E}{100keV}\right)^{\beta}, \quad (\alpha-\beta)\,E_o \leq E \tag{1.3}$$

Two main progenitor theories have emerged as being the most feasible: The hypernova and the compact merger models. The current generic fireball model for the burst propagation has also proved to be very successful in predicting the multi-wavelength afterglows.

One possible explanation is a hypernova [82]. GRBs are a few hundred times more luminous than a supernova and so the term hypernova was adopted. A hypernova is thought to occur when a massive star ($> 10M_{\odot}$) reaches the end of its fuel burning life and collapses into a Kerr black hole. The rapid accretion of matter into the black hole at a rate of up to 0.1 $M_{\odot}.s^{-1}$ can release energies of 10^{51} erg.s^{-1}. These progenitors are thought to live for 10^6 years and so should be close to their birth place. Concurrently the rate of GRBs should also follow the star formations rate.

The other possible origin for such a large release of energy is a merging of two objects involving one or two compact objects [81]. Possible combinations include:

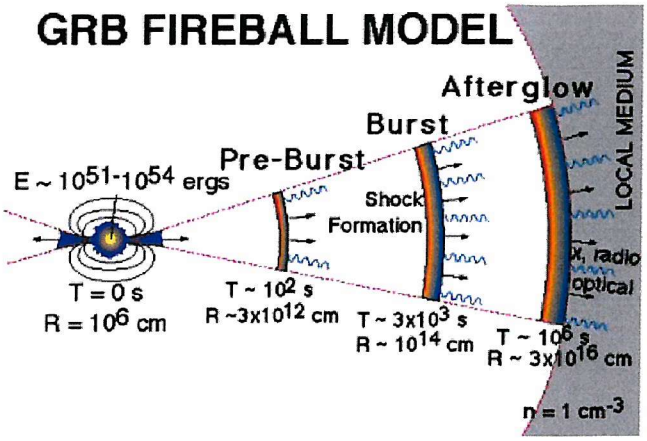

Figure 1.12: **A schematic of the GRB afterglow fireball model. Adapted from Swift documents from HEASARC.**

neutron star - neutron star, black hole - neutron star, white dwarf or He core star - black hole. The binary system radiates its orbital energy in gravitational waves and eventually merges also releasing comparable energy to a GRB but limited to about 10^{52} ergs. These systems will live for much longer periods than the hypernova model (10^9 yrs) and so are likely to be much further from their birth place. The burst rate (about 1 every 10^6 years per galaxy) is also likely to follow the star-formation rate. The only problem is the limit on the energy released.

One factor for reproducing the energy released in a GRB is to consider the emission to be anistropic [33]. This can reduce the energy budget by $\frac{\Omega}{4\pi}$, increasing the availability of possible progenitors. Though the existence of beaming would imply an increase in the burst rate by ~ 100, reducing the availability of possible progenitors. At this stage the degree of anisotropic emission is unclear though evidence of some beaming exists [85].

The problem of the progenitor is not the only question to be answered. How is the energy released converted into, predominantly, gamma rays with the correct non-thermal power law and temporal properties? A fireball model [71] predicts the multi-wavelength behavior of the GRB well [129]. e^+e^- are thought to be accelerated with a Lorentz factor of greater than 100 to produce non-thermal gamma rays. The fireball then decelerates after an internal shock phase as it interacts with the local medium producing the observed afterglow. A break in the spectra moves down through the X-ray band after a few seconds and will reach the optical band up to 1000s later. Figure 1.12 shows the evolution of the fireball model. This process is the only process, other than the Big Bang, that goes from super-relativistic to more normal expansion. The simple model is successful though there are variations that produce a more realistic version [71].

Both models are expected to follow star formation. Figure 1.13 shows several

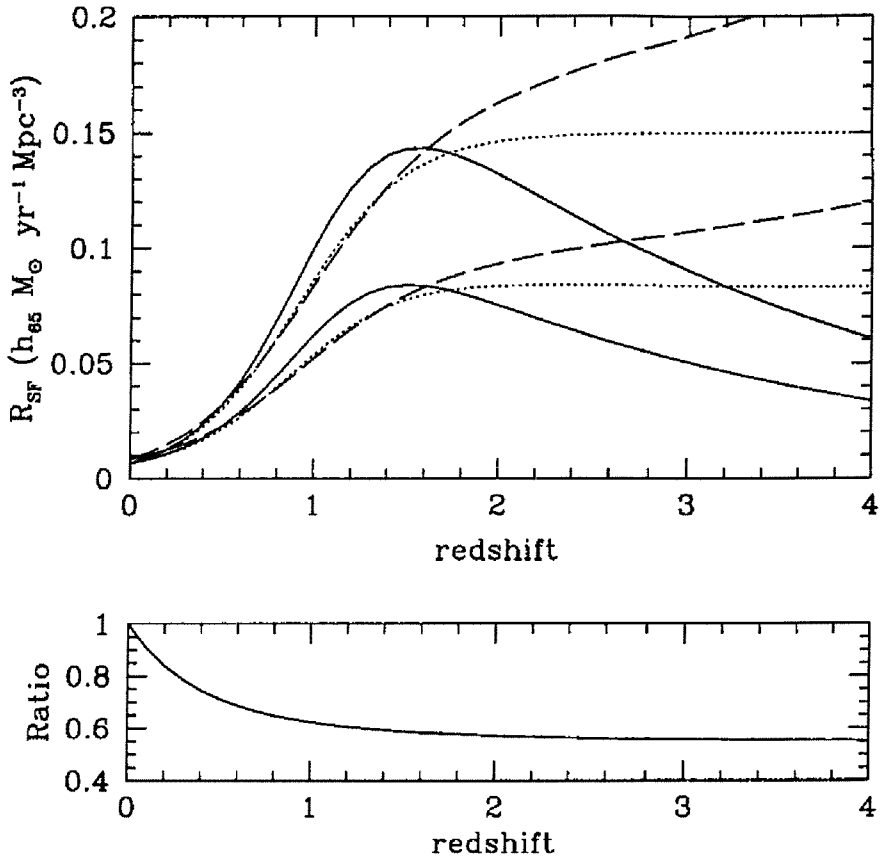

Figure 1.13: **The expected redshift distributions of GRBs.** *Porcianai and Madau and references therein (2000) review these three star formation models in conjunction with two cosmological models.* **The Solid Line** *represents a star-formation rate measured using the UV-continuum with a correction for dust reddening. Due to uncertainties in the data set a second model, displayed as a* **Dotted Line**, *assumes that the star-formation rate above Z=2 is more constant.* **The Dashed line** *reflects a model that suggests that the previous estimations of low Z star-formation is too high while high Z star formation is too low. The upper line of each of the three models is for an Einstein-de Sitter Universe whilst the lower of the lines represents a Λ-dominated Universe. The ratio between the two sets is shown in the panel at the bottom.*

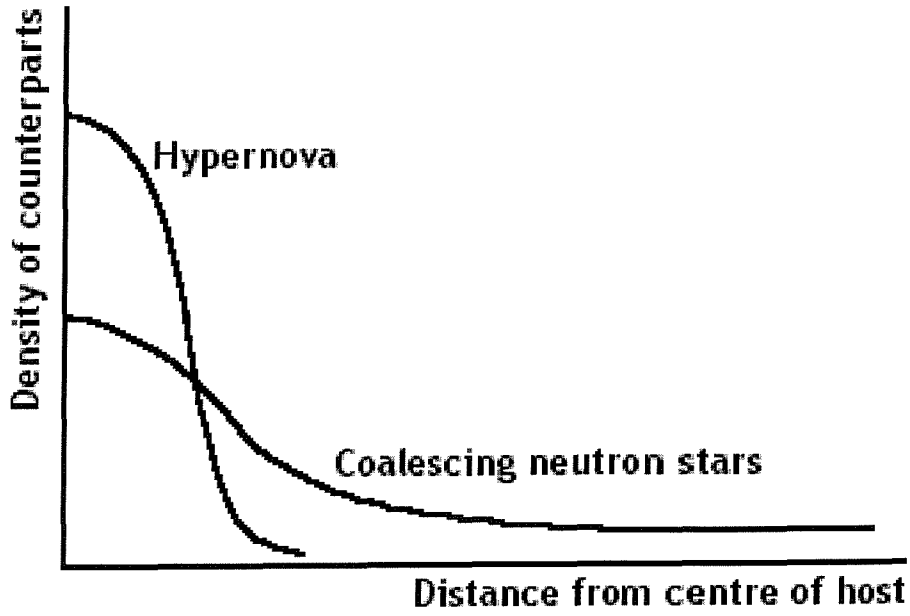

Figure 1.14: **Progenitor models and galactic distribution.** *The two progenitor models predict different distributions of event distances from the centre of their host galaxy. Adapted from Swift documents from HEASARC.*

star-formation models along with two possible cosmological scenarios [88]. Tracing the star-formation out to high redshifts relies on obtaining an accurate $logN - logS$ plot and, considering the large Z involved, the possibility for a burst being lensed in some way is distinct [64]. A burst may be lensed with a separation of up to 20 arcseconds and be delayed by anything up to the order of years. This will distort any $logN - logS$ plot.

For the progenitor to follow the star-formation rate as closely as possible, the model for the hypernova needs to be assumed. Clues to the progentor can be found by considering the most obvious theoretical difference between the two models. Should the progenitor be long-lived (compact merger) then the probability that the system is far from its birth place is large. Whereas a short lived hypernova sysem would still be close to the centre of its host galaxy. By simply plotting the distance that the GRBs are from the centre of their host galaxies, as seen in figure 1.14, the progenitor model will be restricted further. The key to which progenitor is responsible can also be determined by line emission within the spectra. Should the progenitor be related to a supernova then Cobalt and Iron lines will be evident. There is evidence that Fe lines are observed in GRB afterglow spectra [87] and the theoretical possibilities are being explored [2]. However no direct evidence has yet been discovered to determine the true identity of the progenitor.

1.3 Summary

The production of gamma rays can occur by a range of methods and from a variety of astronomical sources. The focus of this thesis is GRBs but by the very nature of monitoring the sky for these mysterious bursts, information would be obtained about all gamma ray emmitting objects within the field of view. Chapter 2 will concern itself with the detection, imaging and shielding in gamma ray instruments.

Chapter 2

Gamma Ray Interaction and Instrumentation

2.1 Mechanisms of Gamma Ray Interaction

Gamma rays are produced by a variety of mechanisms and, as far as gamma ray instrumentation is concerned, interact in three main ways.

- Photoelectric Absorption
- Compton Scattering
- Pair-Production

Each form of interaction is dependent on the energy of the photon and the atomic number of the material it is interacting with. Figure 2.1 shows the dominant process by which photons interact with respect to the photon energy and the atomic number.

The transmission of a photon is dependent on the *linear attenuation co-efficient* of the photons path. All three types of interaction alter the photon in a fundamental way, whether it is full absorption or altering its path through a definite angle. The attenuation co-efficient is the probability of interaction per unit length and can be calculated from the sum of the probabilities of the three processes.

$$\mu = \mu_{photoelectric} + \mu_{Compton\ scattering} + \mu_{pair\ production} \tag{2.1}$$

Therefore the total flux reaching a distance x can be expressed in equation 2.2, x is the distance into the absorbing medium at which the flux is measured. An example of the linear attenuation co-efficient for tin is plotted in figure 2.2.

$$\frac{I}{I_o} = e^{-\mu x} \tag{2.2}$$

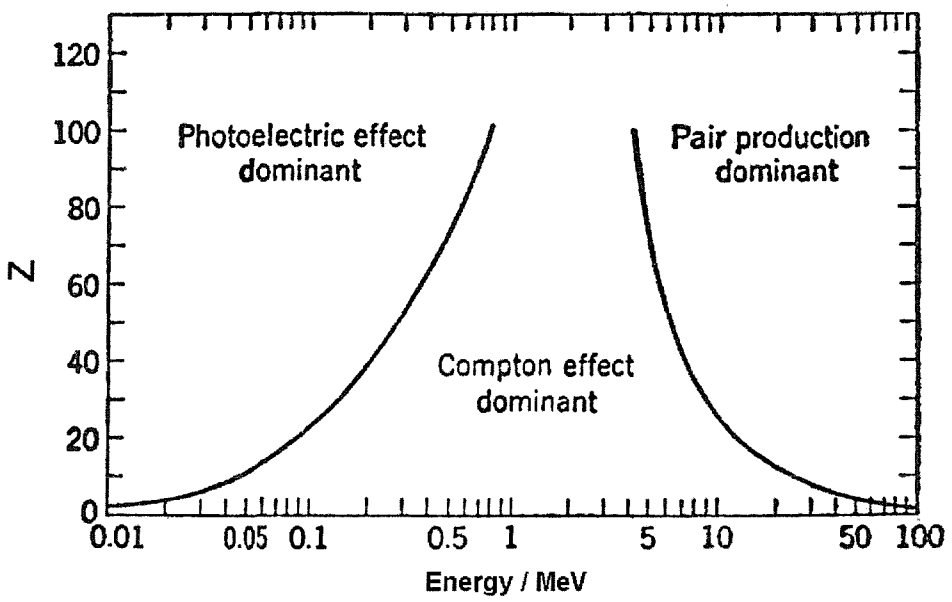

Figure 2.1: **The dominant attenuation mechanism as a function of energy and absorbing medium.**. *Adapted from "Radiation Detection and Measurement" by Knoll.*

2.1.1 Photoelectric Absorption and Fluorescence

Photoelectric absorption occurs when a photon ionises an atom. The incident photon knocks out the electron that is the most tightly bound and is still able to be removed by the energy available. The photon will be absorbed completely leaving the electron with the incident energy minus the binding energy of the electron.

$$E_{e^-} = h\gamma - E_{binding} \tag{2.3}$$

This selection of the tightest bound electron means that when the incident energy reaches a certain value equal to the binding energy of the next shell up, a sharp jump in the attenuation co-efficient occurs. This can be seen in any plot of the energy dependent linear attenuation for a certain material. Figure 2.2 shows the linear attenuation for tin and the K-shell edge can be seen clearly at 30 keV.

Once an electron is removed the ionised atom can quickly recombine with another electron, emitting another photon. This X-ray will be equivalent to the binding energy of the electron removed. This is *fluorescence* and is characteristic of photoelectric absorption. Each element has X-ray fluorescence lines that are specific to that element and at the same energies as the emission lines. This process can be fundamental to any shielding process but the fluorescence of the materials in the instrument must be distinguished from any astronomical emission lines being observed.

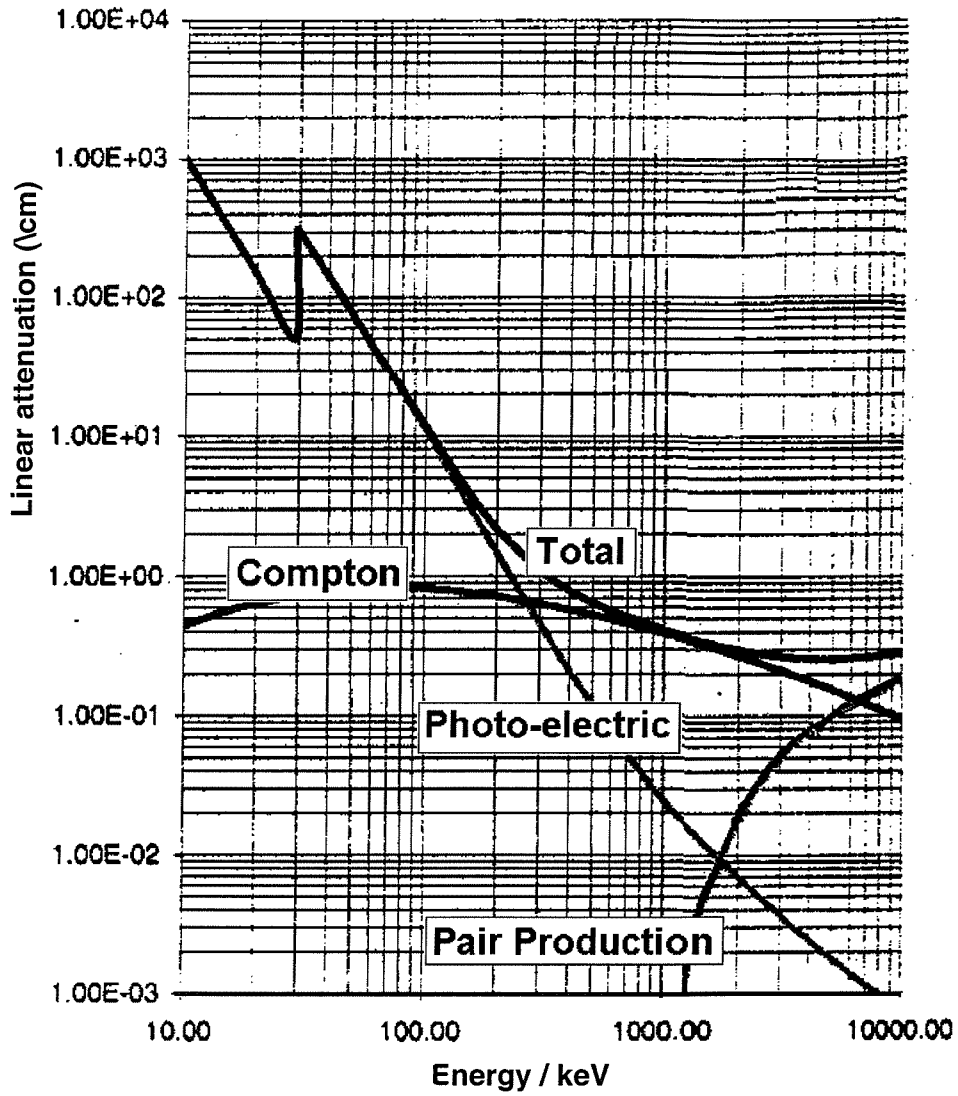

Figure 2.2: **The total linear attenuation of tin.** *It is shown here with the three composite components all marked. Notice that the three processes are dominant at different energies. Adapted from internal documents.*

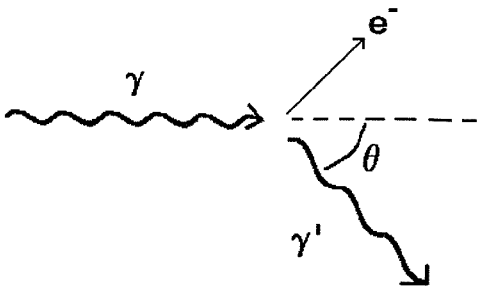

Figure 2.3: **A schematic of Compton scattering.** *The initial photon scatters off an electron through an angle θ and donates energy to the recoil electron.*

2.1.2 Compton Scattering

Compton scattering is the interaction between a photon and an electron within an absorbing material. This process is the most common within astronomical gamma ray instruments due to the dominant energy range. The photon scatters off the electron imparting it with a fraction of its initial energy. The electron recoils with a kinetic energy equivalent to the energy lost by the photon (figure 2.3). From the conservation of momentum we can obtain equation 2.4.

$$h\gamma' = \frac{h\gamma}{1 + \frac{h\gamma}{m_e c^2}(1 - cos\theta)} \tag{2.4}$$

Unlike the photoelectric effect, the photon can never loose all its energy in a single scatter as the binding energy of the electron is trivial in comparison to the initial photon energy. Figure 2.4 shows an example energy deposit spectrum for a monochromatic source. The total absorption peak is at the energy of the initial photons as all the energy is absorbed by the detector by way of multiple Compton scattering or the photo-electric effect. The Compton edge is where the photon has scattered through a maximum 180 degrees and deposited its maximum energy leaving the resultant photons with a reduced energy. The *back-scatter peak* is the peak that occurs at the energy that is equivalent to the difference between the positions of total absorption peak and the Compton edge. This is due to a photon already scattered through 180^o elsewhere depositing the reminder of its energy in the detector. The features seen in this sample spectra are characteristic of any mono-energetic source gamma ray spectrum.

The probability distribution of which angle the photon scatters through is defined by the *Klein-Nishina* formula for the differential scattering cross section per unit solid angle (equation 2.5). Where $\alpha = \frac{h\gamma}{m_e c^2}$ and r_e is the classical electron radius. This predicts the increasing likelihood that the scattering angle is small for higher energy photons.

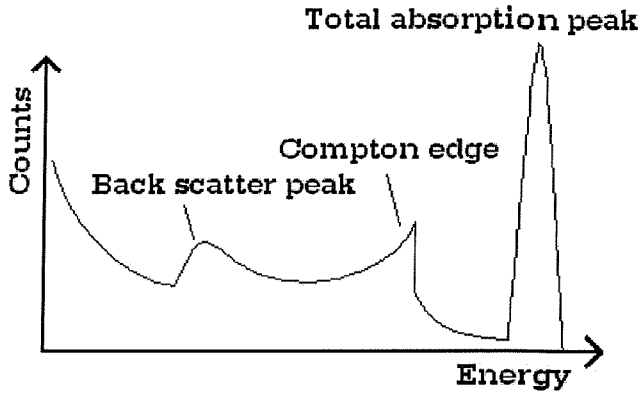

Figure 2.4: **A cartoon generic spectrum of a mono-chromatic source.** *In this case the total absorption peak and the effects of Compton scattering are shown. The non-zero count-rate between the Compton edge and the total absorption peak are due to multiple scattering within the timing resolution of the instrument. The width of the total absorption peak would be due to the energy resolution of the instrument and this would also broaden any feature in the spectra. For the purposes of this generic example the only instrumental broadening is in the total absorption peak.*

$$\frac{d\sigma}{d\Omega} = Zr_e^2 \left(\frac{1}{1+\alpha\left(1-cos\theta\right)} \right)^2 \left(\frac{1+cos^2\theta}{2} \right) \left(1 + \frac{\alpha^2\left(1-cos\theta\right)^2}{\left(1+cos^2\theta\right)\left(1+\alpha\left(1-cos\theta\right)\right)} \right) \tag{2.5}$$

2.1.3 Pair-Production

Pair production is only possible when the energy of the photon exceeds double the rest mass energy of an electron (i.e 2 x 0.511 MeV). Though for pair production to occur readily the energy has to be much higher, as seen in figure 2.1. When a photon with sufficient energy enters the Coulomb field of an atom the photon can disappear to form an electron and a positron moving in opposite directions with the combined kinetic energy of the photon minus the rest mass energy of the two leptons.

$$\gamma \longrightarrow e^- + e^+$$

This process needs to occur near a nucleon so that the momentum is conserved. Once the positron has been created it will come together with an electron over a short time period and annihilate.

2.2 Methods Used in Astronomical Gamma Ray Telescopes

As discussed previously, gamma ray interaction is multifarious and intricate. As a result, the methods for detecting, imaging and shielding in gamma ray telescopes are also multifarious. The concepts involved have to be fitted together coherently to produce a practical instrument design.

2.2.1 Detection

Gamma ray detection can be achieved using one of three basic techniques. These involve the photon inducing an electric pulse directly (ionisation chambers, solid-state detectors) or by inferring the detection from a secondary reaction (scintillation). These three techniques are described and discussed here.

Gas Counters

The chamber contains a gas (or possibly liquid) that can be ionised by the interaction of an incident gamma ray. An external electric field is applied to the gas so that the electron/ion pair created will move apart toward the anode and cathode respectively. The average energy lost by an incident photon, per pair created, is always greater than simply the ionisation energy. This is due to the probability of photon interacting without creating an ion/electron pair. The energy lost per pair created is characteristic of the fluid used in the detector. Typically a 1 MeV photon, stopped fully, would create about 30,000 ion pairs. The ion pairs flow to the electrodes resulting in a measurable current. This is the basic principle behind gas counters. It will also apply to any particle that can produce ion pairs. This system operated without gain is referred to as a ionisation chamber.

The information recorded by the simple gas counter is minimal. Virtually no information is recorded about the direction or initial energy of the photon. Various types of gas counter exist to assist in obtaining these unknowns. An ionisation chamber operated in pulse mode can record the energy deposited in the gas. The electrodes are placed in parallel with a serial resistor-capacitor and, assuming the RC time constant is long compared to the time it takes for the ions to be absorbed by the electrodes (about a millisecond), a pulse is produced. The height of the pulse is proportional to the energy deposited. Should the electric field be increased significantly across the gas counter the electrons released can gain enough kinetic energy to ionise neutral atoms in the gas while they drift to the anode. This process self-multiplies and causes an avalanche of electrons. The pulse is then proportional to the electric field applied. This type of gas counter is called a *proportional counter* and they are commonly used when sensitivity is a priority. A Geiger-Muller (GM) counter is similar to a proportional counter but the electric field is greatly increased. As the field is increased an exponentially growing amount of avalanches are created. However, the collective effects of all the individual avalanches come into play and

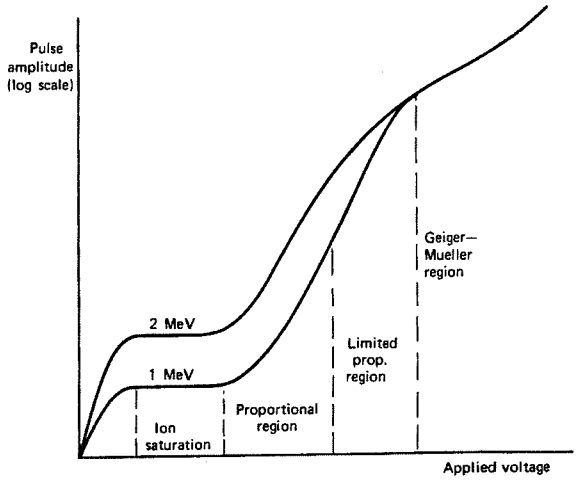

Figure 2.5: **The electric field domains of the various modes of gas counter detection.** *The two lines are for two separate energy deposits. Notice the proportional counter section blending into the Geiger-Muller section of the graph where the pulse height is constant regardless of the number of ion pairs created. Adapted from "Radiation Detection and Measurement" by Knoll.*

terminates the chain reaction. This leads to approximately the same amount of avalanches being created regardless of the initial amount of ion pairs. Therefore the pulse height is constant and the GM counter is just that, a counter. Figure 2.5 demonstrated the various modes of gas counter detection.

A gas counter can be used to determine the energy deposited in the detector. If a grid of wire anodes are placed over the surface of a large area detector spatial details can be also obtained. If several layers or these grids are placed in the gas the path of the input gamma ray or charged particle can be tracked giving some angular resolution within the detector itself.

Scintillation Detectors and Photomultiplier Tubes

Scintillation is the process of converting the kinetic energy of a charged particle to photons. For a scintillation detector, the photons should be easily detectable and have a high scintillation efficiency. The light yield should also be linear with the particle energy and the material be transparent to the produced photons. The scintillation material can also convert gamma radiation to more easily detectable light. No material or method of scintillation can simultaneously fulfill the criteria for every aspect of detection and so the materials used vary for the tasks at hand. Inorganic scintillators such as Sodium Iodide are the most popular and produce the highest light output and linearity but tend to be slower in their response compared to organic materials. The higher Z of inorganic materials favour gamma ray detection whereas the organic materials favour beta and fast neutron detection. The conversion process is the fluorescence of the material after excitation. For organic

scintillators the energy levels of the molecule are used for fluorescence whereas in inorganic materials the energy states determined by the crystal lattice provide the means for fluorescence. This is analogous to the conduction and valence bands in the solid state detectors discussed in the next section.

Once photons of a particular wavelength have been produced via scintillation these photons need to be converted to an electrical signal. The light output from scintillation is very weak to be detected directly (typically a few hundred photons) and so a photomultiplier is used. Photomultiplier tubes (PMTs) carry out this process in two stages. First the photon is converted to an electron by interaction with a photocathode made of a suitable photoemissive material. The quantum efficiency of this initial stage is typically 20-30% at maximum. In the second stage the electron produced will be accelerated and collide with another electrode called a dynode. The dynode is constructed of such a material that the electron is absorbed and causes several electrons to be re-emitted. These electrons are then accelerated, absorbed and multiplied in re-emission by a series of dynodes until a final anode is reached, recording an electronic pulse. The transit time from the arrival of a photon to the production of the electronic pulse ranges from $\sim$20-80 ns. One limitation that a PMT has is the low quantum efficiency. An alternative to the PMT is a solid-state photodiode. The advantages of using a photodiode is the possibility for better energy resolution due to the higher quantum efficiency (typically 60-80%), more compact in size and lower power consumption. All of which are important in space missions. However, conventional photodiodes lack multiplication leading to a small electric signal which in turn leads to noise fluctuations in the small amplitude. Should a large voltage be applied across the photodiode (as with a proportional counter) an avalanche can occur giving the system some internal gain. The area of photodiodes is a relatively new modification and the systematic replacement of PMTs has not happened yet, though the possibility of better spectroscopy is attractive.

Solid-State Detectors

When a material is arranged in a lattice structure, allowed energy bands form within which electrons can exist. Electrons can be bound as part of specific bonds within the lattice and so cannot move, these form the energy band known as the *valence* band. Should the electrons have more energy they are free to travel through the lattice, forming a *conduction* energy band. In an ideal state the valence band will be completely full leaving the conduction band empty, implying no conductivity (metals' highest energy band is not completely full which enables electrons to migrate easily, giving a high conductivity). However, thermal excitation can provide some electrons with the necessary energy to raise to the higher conduction band. The band gap between these two energy bands determines whether the material lattice is a semi-conductor or an insulator. As with the previous methods of gamma ray detection the principle is to create charge carriers that can be detected in an electronic circuit. In this case electrons are excited up to the conduction band forming charge carriers leaving behind electron-holes at the sites where the electrons origi-

nated. Both components to electron/hole pairs can migrate in the lattice to form the electronic signal. To aid in this process the semi-conductor material can be doped with material of either Z+1 or Z-1 compared to the main constituent material. These provide two intermediate *donor* (p-type) or *acceptor* (n-type) levels respectively. These exist between the two energy bands, giving an easier route to excitation. The principle of semi-conductor radiation detection is very similar to the previous two methods but is also relatively new.

Discussion

Three methods of radiation detection have been outlined but the question of which is most suitable is dependent on the mission parameters. Various factors play a part in the choice of detector:

Energy Range, Resolution and Spectroscopy The energy range of a detector is determined by the stopping power. The stopping power of a gas counter would be characteristic of the ionising medium in the case of gas filled chambers the stopping power is poor due to the low density. This can be increased by inserting thin metal plates into the chamber so that any incident high energy gamma ray would pair-produce on collision with the plate. The subsequent annihilation photons could then easily be detected by the surrounding ionisation chamber. The paths and interactions of the gamma ray is traced and the initial energy can be reconstructed. This method can extend the energy range of a gas chamber well into the GeV domain but does nothing below a few tens of MeV. Gas counters still lack the stopping power above 1 MeV, depending on the medium, and are commonly operated in the keV range.

Inorganic scintillators favour gamma ray spectroscopy due to the high Z of the constituents to the lattice and were the traditional choice for spectroscopy in the keV to mid-MeV range before solid-state detectors were developed. The advent of semi-conductor detectors such as the high purity Germanium (HPGe) detector revolutionised the field of gamma ray spectroscopy, enabling the semi-conductor to have the much needed thickness and so stopping power without compromise to the resolution. A comparison of the energy resolution between a Ge(Li) solid-state detector and a NaI scintillation detector can be seen in figure 2.6 [84]. It can be seen that the total count-rate for the NaI is greater by a factor of about 10 but the spectral information obtained by the Ge(Li) is by far superior. Whereas four peaks can be identified in the NaI spectra, the resolution of the Ge(Li) enables 28 peaks to be obtained with a resolution typically between 1.5 and 2.5 keV (FWHM) over the sensitive energy range [79].

Another aspect, obvious in the Ge(Li) spectrum in figure 2.6, is the structure of the spectra. This structure does not only contain the full energy deposits of the photon i.e. lines that indicate the initial energy of the gamma ray. There are also artifacts of Compton scattering. As a detector cannot be infinite in size so that a

photon would deposit all its energy every time, photons will escape only depositing the energy it looses through scattering. Pair production events also lead to lines being detected at 0.551 and 1.022 MeV. These processes result in a structure to the spectra and can be used for self-calibration or removed during a flat-fielding procedure.

Timing Resolution and Pulse Shape As much as the energy resolution of an instrument is astronomically important, the timing resolution can also be vital in the observation of highly variable sources. In the context of these detection methods, the pulse shape is the important factor. The pulse indicates an individual deposit of energy. If these individual pulses are of a finite width in time then there is a point where two separate pulses will merge should the arrival times be close enough. The best performance in terms of timing resolution is also not exclusive to the best performance in terms of energy resolution due to the formation of well defined pulses. For the three methods described above the pulse is formed by different physical mechanisms and the signature pulse shape will be different for each. Ionisation techniques can be tuned for timing resolution by shortening the timing constant (RC) of the circuit. However, this is at the expense of the energy resolution. The process of scintillation involved several stages which reduces the possibility for fast and narrow pulse production. Semiconductors timing resolution is governed by the charge collection time which varies depending on material and operational energy range. They are accepted to have the fastest timing resolution and are now common place where this is a priority. Ionisation chambers are sometimes suitable due to less radiation degradation and simplicity.

Solid state detectors are defined by their charge collection time and concurrently also prone to charge trapping. This defect delays the arrival or some of the collected charge giving the false impression of a lower energy deposit with an exponential tail. This can be compensated for by studying the rise time of the arriving pulse which is dependent on the detected energy deposit.

All timing resolution considerations are on the scale of μs. Most astronomical gamma ray sources are weak in comparison to the background and so obtaining a significant detection makes the timing resolution characteristic redundant. Only on bursting or strong sources is this factor relevant.

Mission Considerations Gamma ray astronomy is different from the kind of radiation detection carried out in the lab and several additional factors need to be considered. The lifetime, power constraints, predicted radiation damage, physical size and intrinsic background noise need to be considered. In terms of energy and timing resolution the semiconductor would be the detector of choice. Unfortunately they can be limited in size, use a lot of power, require cryogenic cooling and are susceptible to degradation through radiation damage, an important factor in a space environment. Also any instrument that requires a gas or liquid to be constantly re-

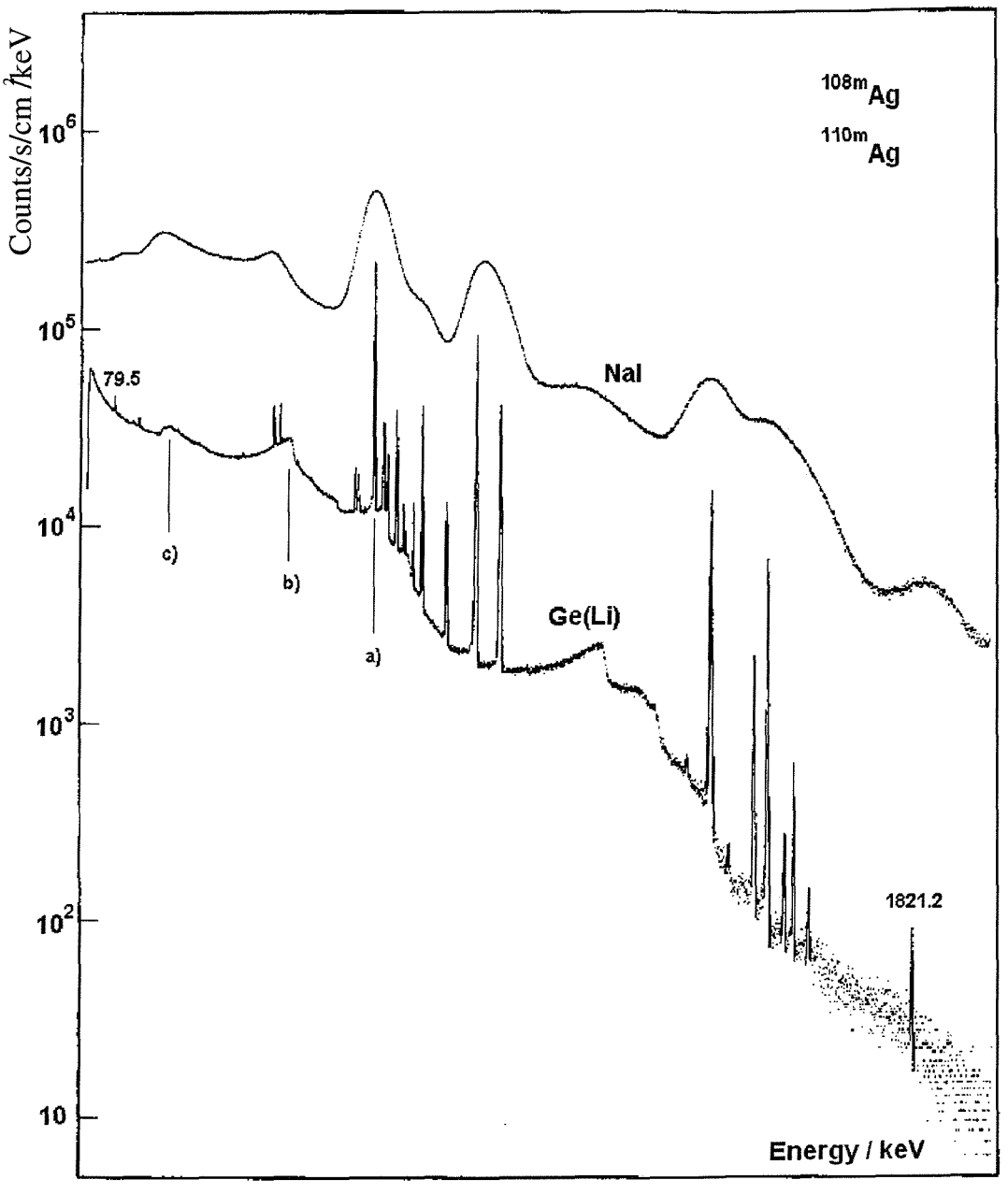

Figure 2.6: **The comparative spectra of the meta-stable isotopes of ^{108}Ag and ^{110}Ag as measured by a NaI scintillator and a Ge(Li) solid state detector.** *Labeled* **a), b)** *and* **c)** *are an example photoelectric peak, Compton edge and back-scatter peak respectively. It is worth noting that the Ge(Li) were mainly used in the 20 years ago but this plot demonstrates the characteristic differences between the solid-state and scintillation methods of gamma-ray spectroscopy. Adapted from "Radiation Detection and Measurement" by Knoll.*

placed (a gas filled ionisation chamber or a semiconductor with cryogenic cooler) will have a restricted lifetime. Where a scintillation device may have comparatively poor energy and timing resolution, it can be advantageous to a gamma ray astronomy mission in terms of reliability, simplicity and longevity.

2.2.2 Imaging

Imaging can be done in a variety of ways. The extent to which these methods deconvolve an image is limited in comparison to other energy domains of astronomy. Standard optical techniques such as Grazing Incidence Optics, used in many X-ray missions, currently can only be used $\leq$15 keV. Imaging can be achieved utilising techniques mostly unique to gamma ray astronomy.

Timing Triangulation

The simplest method, analytically, is to consider the arrival times of peaks in the source flux (e.g. GRBs) at different spacecraft, spread throughout the Solar System. Several modern missions have been launched with a gamma ray burst monitor aboard. The primary objectives for these missions are all different and so can be located far apart leading to large gaps in the arrival times. Using just two instruments will give a possible annulus from which the burst originated. Using three will give a position. This method is used elsewhere but in gamma ray astronomy it lead to the discovery of GRBs and is an integral part of the Gamma Ray Burst Coordinate Network (GCN). The disadvantages are that more than two instruments spaced far apart are required but the advantage is that each instrument need not be very big or sophisticated and so can be bolted onto a variety of other missions as a secondary instrument.

Occultation

Occultation is the measurement of the difference in the flux when pointing at a source and when not. The occultation can occur by pointing next to a source, by the source setting behind the Earth or Moon's limb or by placing an opaque disk in the field of view over the region of interest. The level of sophistication can vary from simply obtaining a source count-rate to mapping the entire sky through Earth occultation as the spacecraft orbits. BATSE, a non-imaging instrument, has been used to analyse the count-rate changes as the Earth's limb progresses across the sky in conjunction with the spacecraft position so that an all-sky map can be produced [39].

The Spark Chamber and Compton Telescope

Tracking a gamma ray within an instrument will give information as to the initial direction of the incident gamma ray. The spark chamber tracks electrons through a gas filled detector. As the photon causes an electron-positron pair to be created at the various metal anode foils within the gas filled ionisation chamber the paths of

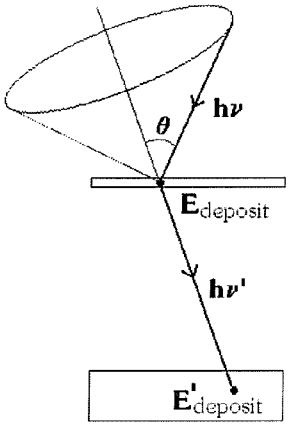

Figure 2.7: **The Compton telescope.** *The projected cone (with angle θ) can be derived from the two energy deposits and positions, assuming that the photon is entirely absorbed in the second detector. This design is basic, the detectors can be arranged in different geometries (e.g. cube) to increase the field of view*

the electrons can be traced and the incident photon's path can be projected back onto the sky. This form of imaging gives an energy dependent angular resolution of the order of a few degrees and is restricted to the higher energy photons that will pair produce.

At lower energies the direction of the incident photons can again be estimated, using a Compton telescope. These typically consist of two parallel plane detectors. The upper one is thin or low Z to detect a small energy deposit as it scatters off the detector material. The second is designed to stop the resulting scattered photon. The Compton scatter is then reconstructed knowing the position of the two interactions and the first energy deposit with respect to the total initial energy. The result from using equation 2.4 is that a cone of possible origins can be projected onto the sky for each event, see figure 2.7. Photons originating from the same source will produce cones that will intersect at their originator. Scintillators are usually used for the two detectors due to the stopping power. Due to the errors in determining the energy deposits, the angular resolution from this technique is similar to that of the spark chamber but is effective at lower energies. Due to the event coordination within the Compton telescope the conventional background can be very low. However, the background from highly penetrating particles is a problem. Neutrons can pass through the telescope leaving a simultaneous deposit in both detectors.

Collimation and Coded Aperture Imaging

The most obvious form of imaging is to place a collimator on top of a detector. This narrows the field of view around the region of interest and reduces the background. Depending on the material and thickness of the collimator, this method is

restricted to sub MeV energies. Also the angular resolution will be very poor. A way to increase this resolution is to have a rotating or scanning collimator. This adds occultation which can provide much finer angular resolution, of the order of arcminutes. In conjunction with a simple, stationary collimator a coded aperture can be used to obtain arcminute resolution. Where a scanning collimator is a form of temporal multiplexing (multi-stage image reconstruction) the coded aperture approach is a form of spatial multiplexing. For equal collecting areas the sensitivity of any focussed instrument will be greater than a multiplexing instrument as all photons across the plane can contribute to the image and so the image experiences noise from photons across the detector. The advantages being angular resolution, wide field imaging and extension to the higher energy range.

A coded aperture acts as a mask projecting its pattern onto the detector plane. The position of this pattern on the position sensitive detector plane denotes the direction from which the source is emitting. The layers of this pattern over the plane from the various sources in the sky can be deconvolved to produce an image. The requirements are that the pixels in the mask are larger than the pixels in the detector plane. The pattern can either be a repeating pattern or a random pattern. The random pattern acts like a large array of pinhole cameras and has an autocorrelation function whose side-lobes are not flat. Ideal patterns have been constructed that give no side-lobes and are based on cyclic difference sets and called Uniformly Redundant Arrays (URAs). These patterns have an autocorrelation function with only 2 solutions. The autocorrelation function defines when a pattern overlaps. With only 2 solutions, one for zero count-rate and one for the specific case when the same pattern can overlap with itself successfully, URAs cannot suggest the existence of an image during the reconstruction that is anywhere else but the at the observed source. Problems occur when the source is only partially coded, the autocorrelation function will give systematic noise as it will not be infallible. This gives false peaks.

From efforts to increase the signal to noise ratio and to optimise the telemetry and CPU rates the open fraction of the mask can be considered. Unfortunately with less than 50% transparency no pattern has been discovered with an ideal uniformly redundant autocorrelation function. Non-Redundant Arrays (NRA) can be constructed with transparencies less than 50% but can included image side-lobes. For an instrument that observes transient sources such as the BeppoSAX WFC the use of a random pattern can be justified.

The important feature of coded aperture imaging is that it produces angular resolution of the scale of arcminutes from about 10keV to 10 MeV. No other method of imaging is so accurate and versatile over the energy range. One of the first astronomical satellite applications of the coded aperture was the Wide Field Cameras (WFCs) aboard BeppoSAX. One of the first space based coded aperture imaging systems, Spacelab 2, was launched in 1985 and was operated from the cargo bay of the space shuttle. A full explanation of the coded aperture imaging can be found in In't Zand (1994).

Table 2.1: **A table of the major gamma ray imaging techniques. Values will vary with the specific design of the instrument.**

Technique	Energy Range [MeV]	Angular Resolution	Imaging Efficiency
Grazing Incidence Optics	< 0.015	5 arcsec	70% (5 keV)
Timing Triangulation	all	$\sim 4^o$	~50%
Earth Occultation	all	1^o	50%
Spark Chambers	10-20000	$\sim 1^o$	25%
Compton Telescope	0.8-30	$\sim 2^o$	0.5-1%
Collimator	< 0.1	n/a	100%
Coded Aperture	0.01-10	1-10 arcmin	<50%

Summary

Several imaging techniques have been described and approximate values are shown in table 2.1. The most important factor in selecting an imaging technique is the energy range over which the imaging is possible. The only real way to image over 10 MeV is to track secondary particles but below this energy the Coded Aperture is the most accurate though may not be suitable for the mission concerned.

2.2.3 Shielding

The need for efficient shielding is paramount. By considering the mechanisms by which gamma rays interact and the methods by which gamma rays are detected it is obvious that even a low level of ambient noise would cause problems for most instrument. The ease of scattering as opposed to total absorption means that any source of gamma rays, whether astronomical or background, will contribute to a diffuse level of noise within a detector. The combined levels of noise in the detector will always be high in comparison to any source flux, reducing the sensitivity. To make an instrument as sensitive as possible the shielding, therefore, has to be as effective as possible.

Two kinds are commonly used: passive and active. Passive shielding is simply high Z material surrounding the detector or collimator to absorb photons and cosmic rays. Passive shielding can be graded in Z so that K-edges in the total linear attenuation compliment to provide a larger total attenuation. The K-edges can also coincide with the fluorescence lines of the outer layer so that fluorescence is mostly shifted down to below the lower energy threshold of the detector. Graded Z shielding is primarily used in the 10-200 keV range to reduce the fluorescence from a single material passive shield. For satellite missions the total mass of the instrument is paramount. For this reason the amount of passive high Z material is limited. Another limitation to how much passive material is used is how much secondary flux is created as a direct result of Cosmic Rays activating the material

around the detector. Assuming that the total mass is restricted to a certain range by the logistics of space flight, there can be a fine balance between adding to the passive material to increase the attenuation and increasing the secondary flux from activated isotopes within the shielding itself. Passive shielding has its limitations but *active* shielding can reduce the background far better with hardly any trade-off for secondary activation and no attenuation-to-mass proportionality. Perhaps the most fundamental difference between the two is that a passive shield is required to completely absorb the incident photon or particle whereas an active shield only requires a detection of the background photon or particle to eliminate it from the recorded data.

Active shielding consists of a separate detector surrounding the instrument. When the scintillating material detects a background charged particle or photon, any coincident detection within the instrument will be ignored. A common use of active shielding is to place a thin plastic scintillator over the fleld of view so that any charged particles will be detected and removed from the data set while the majority of photons will still pass through.

2.3 Recent Advances in Gamma Ray Astronomy

2.3.1 Introduction

Gamma rays are highly attenuated by the Earths atmosphere which makes ground based gamma ray astronomy impossible below TeV energies when air-shower spallation becomes useful. For gamma ray instruments to become a useful tool in astronomy they have to be above a significant percentage of the atmosphere. Some of the first X-ray and gamma ray missions were aboard rockets with wide trajectories. These reached above the atmosphere but were expensive and short-lived. More economical are balloon borne and satellite instruments, being relatively inexpensive or long-lived respectively. The advent of sophisticated space faring cargo vehicles led to larger and more complex satellite instruments being launched. Satellite instruments are currently common place for anything from gamma ray to sub-millimeter wave lengths and even gravitational waves are planned to be studied above the Earth's atmosphere. The benefits of satellite missions are obvious but the drawbacks are in the unavoidable background. Being above the atmosphere and to some extent outside the magnetosphere, the space craft is subject to Cosmic Rays, cosmic diffuse X-rays, atmospheric albedo gamma rays and the inevitable induced radioactivity that comes with such an environment. All gamma ray missions have to cope with a low signal-to-noise ratio and deal with this problem in a variety of different ways. There have been many gamma ray missions since the birth of gamma ray astronomy and some of the important ones are reviewed here.

The emphasis of this review is on Swift and The Compton Gamma Ray Observatory (CGRO). These two missions carry the two instruments that this thesis is

primarily concerned with and they are also the two of the most important missions in the field of GRBs. Instruments aboard the CGRO, BeppoSAX, INTEGRAL and Swift will all be discussed in later chapters with only COS-B and the GCN being included for contextual purposes.

2.3.2 COS-B

COS-B was operational from August 1975 until April 1982 and was the first major gamma ray mission. It carried a single gamma ray instrument, a wire-matrix spark chamber that was triggered by three scintillation counters. The spark chamber was surrounded by a plastic scintillator anti-coincidence shield to eliminate charged particle detection. To cover a broader energy range a small hard X-ray proportional counter was included to extend the lower limit of the energy range [8]. The total range was 2keV-3GeV. The scientific objectives were to observe pulsars and binary systems and produce the first gamma ray map of the Galaxy.

2.3.3 The Compton Gamma Ray Observatory (CGRO)

The CGRO was launched in April 1991 and de-orbited in June 2000. It was the largest gamma ray astronomy mission and consisted of four instruments: The Burst And Transient Source Experiment (BATSE) [0.02-4 MeV], the Orientated Scintillation Spectrometer Experiment (OSSE) [0.05-10 MeV], the Compton telescope (COMPTEL) [0.8-30 MeV] and the Energetic Gamma Ray Experiment Telescope (EGRET) [30-10000 MeV]. Each instrument had its own mission objectives and each detector was tailored to its own needs. The orientations of each experiment are shown in figure 2.8.

OSSE

OSSE consisted of four independently mobile tungsten collimated NaI scintillation detectors operated using its offset pointing capability to determine the explicit count rate of the observed region. Along with the set of four detectors a charged particle detector (plastic scintillator) was included to detect the entry of the observatory into the South Atlantic Anomaly (SAA). During the passage through this highly dense region of charged particles all the instruments were turned off. The four NaI detectors were operated in pairs to simultaneously observe a source and the region adjacent to the source so that the background can be removed [14]. The energy resolution was 8% (0.661 MeV) with a 3.8 degree FWHM field of view. This experiment relied upon source contribution modulation. The scientific objectives were to observe solar flares, supernovae remnants and the electron-positron annihilation line emission in the galactic centre [92] (figure 1.4).

COMPTEL

COMPTEL's aim was to bridge the gap between the comparatively well explored energy domains of <1 MeV and $>$ 30 MeV [101]. The instrument consisted of two

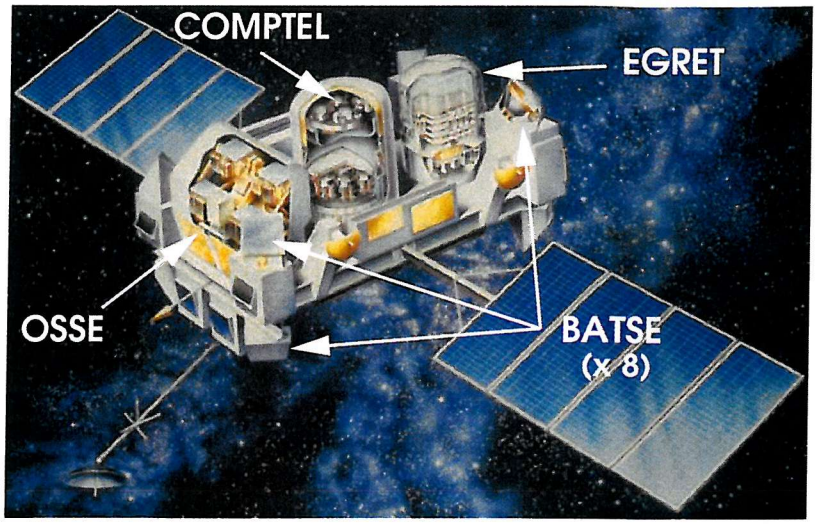

Figure 2.8: **The Compton Gamma Ray Observatory**. *A schematic of the CGRO showing the positions and pointings of the four experiments: BATSE, OSSE, EGRET and COMPTEL. Some of the internal details can be seen, particularly the four scintillators in OSSE, the two detector planes in COMPTEL and the EGRET spark chamber. Adapted from HEASARC webpages.*

detectors placed in a Compton telescope formation. The upper scattering detector consisted of 7 liquid scintillator modules with the lower absorbing detector made of 14 NaI scintillator modules, for its high stopping power. The telescope was surrounded by two plastic scintillator anti-coincidence shields to help eliminate the charged particle background. The scientific objectives included the study of active galaxies, large molecular clouds and supernova remnants.

EGRET

EGRET was designed to cover the higher energy range of the CGROs capabilities. EGRET consists of a spark chamber, similar to COS-B but over 10 times larger and more sensitive. The spark chamber had three sections. The top was a series of closely spaced spark chambers and below was a series of widely spaced spark chambers. The lower section was a time-of-flight coincidence system to determine whether the incident photon was going down the telescope or up. Below the two series of spark chambers, used to determine the direction of the photon, was a NaI(Tl) calorimeter to measure the total energy of the photon. Surrounding all this was a plastic scintillator anti-coincidence shield. The objectives of this experiment were to perform an all-sky survey and to study blazars. The anti-coincidence shield was also used in conjunction with the calorimeter to study GRBs and solar flare events.

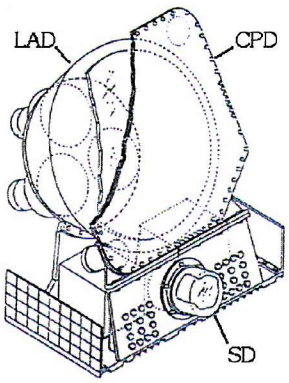

Figure 2.9: **A BATSE module.** *The Large Area Detector (LAD) can be seen in the centre. The disk of NaI is connected to three PMTs while the square Charged Particle Detector (CPD) covering the LAD has two PMTs at opposite corners. The Spectroscopy Detector (SD) is below the LAD. Each of the eight modules are placed at the corners of the CGRO bus. Adapted from BATSE internal technical documents.*

BATSE

Where the other three experiments were single instruments used to study individual sources (diffuse and discrete), the objectives of BATSE were quite different. BATSE consisted of 8 Spectroscopy Detectors (SD) and 8 Large Area Detectors (LAD) placed at the corners of the CGRO (see figures 2.8 and 2.9). The aim was to observe the entire sky simultaneously so that any bursting event would be recorded as it happened. The data revealed the extra-galactic nature of GRBs as seen in figure 1.8. Each LAD consisted of a 2025 cm^2 disk of NaI attached to 3 PMTs and each with a thin plastic scintillator anti-coincidence shield to reduce the effects of cosmic rays. The approximate cosine point spread function meant that the whole sky could be observed simultaneously. No individual imaging capability was possible but the triangulation of the burst could be achieved by considering the burst count-rate in each of the LADs.

The data recorded was split into two data sets: the discriminator (DISCLA) and the continuous (CONT) data sets. The DISCLA data was split into 4 energy channels and sampled at 1.024 s intervals. The CONT data was split into 16 energy channels and sampled at 2.048 s intervals.

Concurrent to the burst monitoring, discrete sources could be monitored using an occultation technique. As sources rose and set behind the horizon of the Earth the size of each step in the count rate was measured and compiled into a data set that was sampled twice every 90 minute orbit for the 9 years. Figure 2.10 shows the measurable steps in count-rate [39]. The modulation of the background is the major source of variability in the data sets but all such variability is on orbital timescales and source induced steps can be extracted [131]. The flux histories for several sources are shown in figure 2.11.

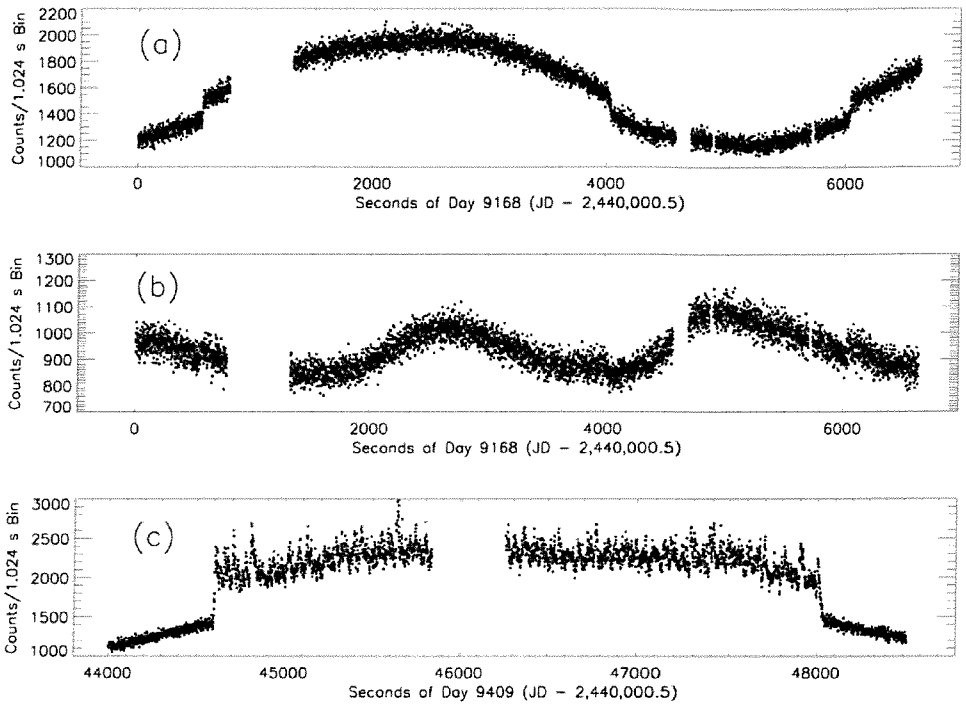

Figure 2.10: **BATSE Occultation steps.** *This extract from the DISCLA data shows the variability due to the background modulation and the setting and rising of The Crab and A0535+26.* **a)** *The Crab in the 20-50 keV energy band. The Crab steps are apparent, the slow variability is due to the cosmic diffuse X-ray component to the background.* **b)** *The Crab in the 100-300 keV energy band. This time the steps in the data are not so immediately apparent as the Cosmic Ray (primary and secondary induced) background dominates the count-rate.* **c)** *A0535+26 in the 20-50 keV energy band. The X-ray binary is bursting and the occultation steps are clear. Any gaps in the data are due to the loss of CGRO telemetry to the instrument being turned off during an SAA passage. Adapted from Harmon et al. (2002).*

The occultation monitoring of sources also lead to the imaging of the sky using the *maximum likelihood imaging* method [16]. This method involves the continuous data being differentiated to identify the sharp variations in the data. The likelihood of a source existing at a certain position in the sky is calculated so as to reproduce the variability in the data set. The significance of each point in the sky is then compiled giving an all-sky map.

2.3.4 BeppoSAX

Launched in April 1996 and operated until May 2002, BeppoSAX performed spectroscopic and variability studies of X-ray sources with angular resolution of ~1 arcmin in the energy range from 0.1 to 300 keV. BeppoSAX carried 6 instruments, a mixture of narrow and wide field instruments [10]. These consisted of a pair of

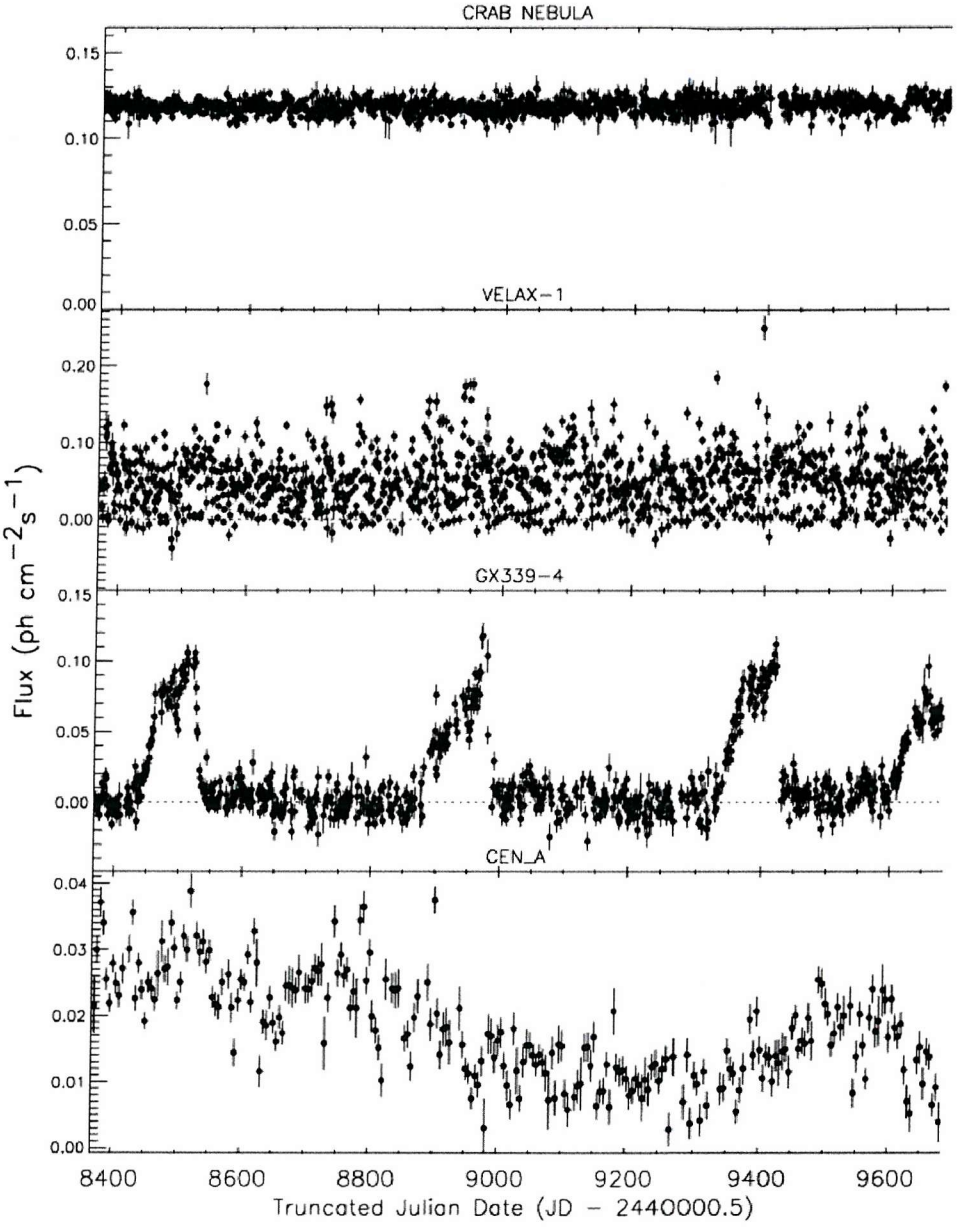

Figure 2.11: **BATSE Occultation flux histories.** *Example flux histories of The Crab Nebula (40-150 keV), high-mass binary pulsar Vela X-1 (20-50 keV), the black hole candidate GX 339-4 (20-100 keV) and the radio galaxy Centaurus A (20-200 keV) from April 1991 to July 1998. Adapted from Harmon et al. (2002).*

X-ray spectrometers (0.1-10 keV and 1-10 keV) a High Pressure Gas Scintillation Proportional Counter (HP-GSPC) (3-120 keV), a Phoswich Detector System (PDS) (15-300 keV) and two Wide Field Cameras (WFC) (2-30 keV). The lateral active shielding surrounding the PDS is used as a burst monitor with an energy range of 60-600 keV. The WFCs utilises a passively shielded multi-wire proportional counter with a randomly coded mask imaging array (40^ox40^o field of view). The WFC are positioned orthoganally to the narrow field instruments and point in opposite directions for monitoring purposes. The scientific objectives included compact sources, active galactic nuclei, galaxy clusters and supernova remnants as well as the study of normal galaxies and stellar coronae. Figure 1.11 shows a excellent example of the WFC's contribution to GRB science [21].

2.3.5 INTErnational Gamma Ray Astrophysics Laboratory (INTEGRAL)

Due to be launched in October 2002, INTEGRAL is the next ESA gamma ray mission. It will cover the energy range of 3 keV - 10 MeV using fine spectroscopy and imaging. The observatory consists of 4 main instruments: the SPectrometer on INTEGRAL (SPI), the Imager on-Board the INTEGRAL Satellite (IBIS), the Joint European X-ray Monitor (JEM-X) and the Optical Monitoring Camera (OMC). A diagram of how these are arranged on INTEGRAL is seen in figure 2.12. To aid these instruments, two star-trackers and the INTEGRAL Radiation Environment Monitor (IREM) have been included. INTEGRAL will reside in a highly elliptical orbit. With the improvement in the spectroscopy and imaging capabilities from previous missions, the main scientific objectives are to closely observe the Galactic Plane and Centre, to observe nucleosynthesis in all its forms and to identify the gamma ray emitting sources with counterparts at other wavelengths.

SPI

The spectrometer SPI consists of an array of 19 high purity Germanium detectors arranged in a hexagonal structure giving an energy resolution of 2.2 keV (FWHM, at 1.33 MeV) and an energy range of 0.02-8 MeV. A tungsten hexagonal coded mask is placed 1.7m above the detector plane giving a fully coded field of view of 16^o (angular resolution: 2^o). To obtain maximum sensitivity the collimator is surrounded with 91 Bismuth Germinate (BGO) scintillation tiles each with 2 PMTs to act as a veto shield. A plastic scintillator active shield has also been included underneath the coded mask to reduce the annihilation line at 0.511 MeV. The detector, mask and veto arrangement can be seen in figure 2.13.
The reason that a burst monitor was not included on the INTEGRAL mission was that most the problems with GRB theory were suspected to be solved by BATSE and the CGRO. This did not happen, however the veto system surrounding SPI can be used as a burst monitor. Though no positional information can be achieved it can be used as a triggering detector in conjunction with other missions with basic burst monitors aboard such as ULYSSES and the Mars Orbiter.

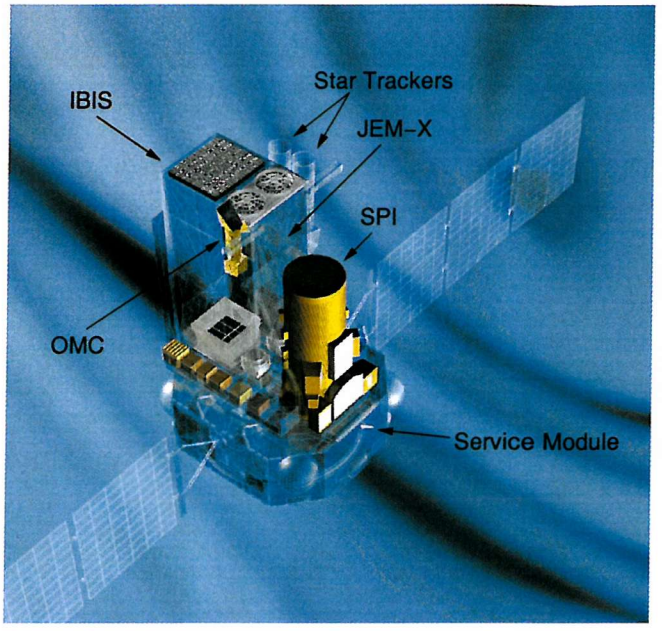

Figure 2.12: **INTEGRAL.** *This is a schematic of the INTEGRAL observatory. The individual instruments can be made out easily. The PICSIT and ISGRI detector modules can be seen below the mask pattern of IBIS. Also the twin mask and detector modules of JEM-X can be seen. Adpated from the INTEGRAL brochure.*

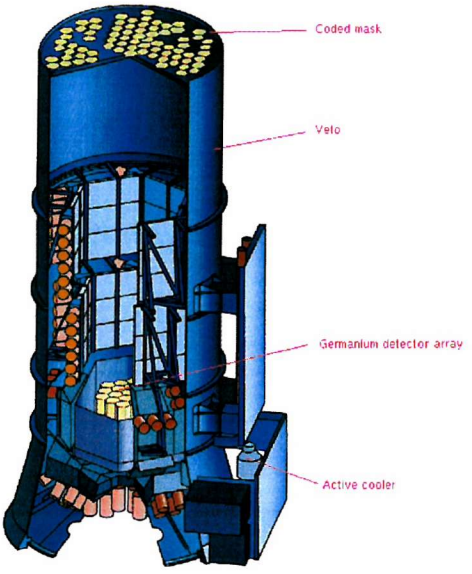

Figure 2.13: **SPI.** *The BGO anti-coincidence shielding tiles can be seen surrounding the inside of the collimator. Adpated from the INTEGRAL brochure.*

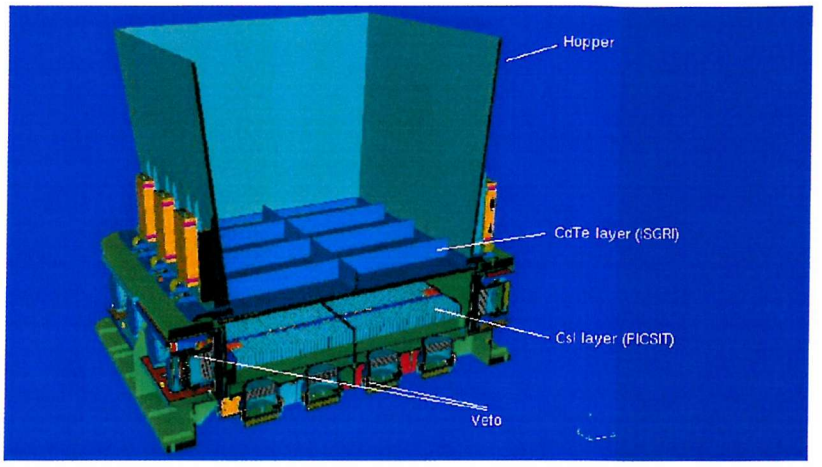

Figure 2.14: **PICsIT and ISGRI.** *The two detector planes are spaced by 9 cm and can be used to trace the paths of photons and can be employed as a Compton telescope. Adpated from the INTEGRAL brochure.*

IBIS

The imager aboard INTEGRAL will give fine angular resolution (12' FWHM) over the energy range of 0.015-10 MeV (E resolution: 60 keV [FWHM at 1 MeV]) and a fully coded field of view of 9^o. The detector array is split into 2 planes. The upper one (ISGRI) is a solid state CdTe array with an area of 2600 cm^2 (16384 pixels, 4x4x2 mm). The lower one (PICsIT) is 9 cm below and consists of an array of scintillating CsI with an area of 3100 cm^2 (4096 pixels, 9x9x30 mm). The reasons for two separate detector planes is to extend the energy range of the detector and also to track the photons in three dimensions for image reconstruction and to veto out non-celestial photons. The pair of detector planes are again surrounded by an active veto system of BGO. Figure 2.14 shows the detector assembly while figure 2.12 shows the positioning of this assembly inside IBIS. The detector plane of ISGRI is 3.2 m below the tungsten coded mask. IBIS is surrounded by a passively shielded lead collimator.

JEM-X

The third major instrument aboard is the X-ray monitor (3-35 keV), JEM-X. As seen in figure 2.12 JEM-X is a double detector set-up using coded aperture imaging. The detector unit is a Xenon filled multi-wire proportional counter and has an energy resolution of 1.5 keV (FWHM at 10 keV). The masks are placed 3.2 m above the detectors achieving an angular resolution of 3' over a fully coded field of view of 4.8^o. Due to the hard X-ray domain that JEM-X operates in, passive shielding suffices to reduce the expected background.

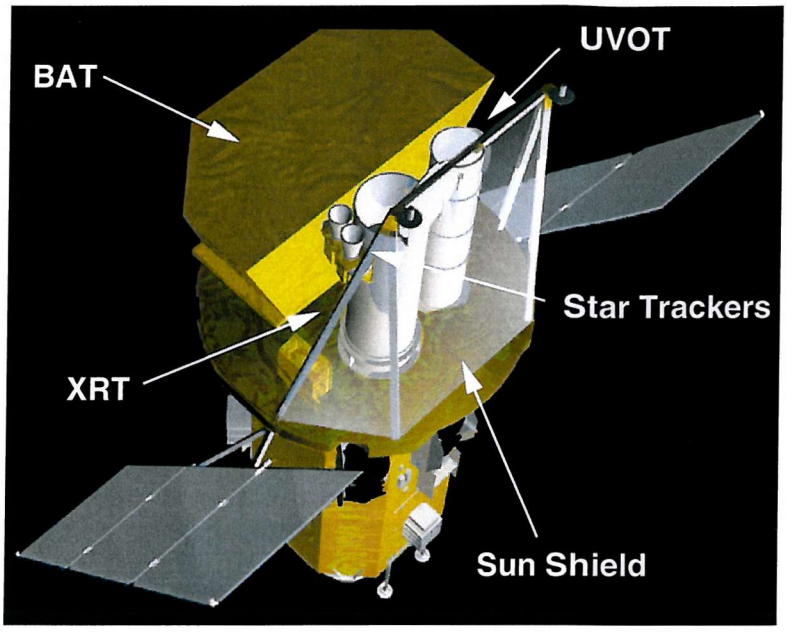

Figure 2.15: **Swift.** *This is a schematic of what the Swift mission will look like. The wide field of view BAT can be seen above the two narrow field instruments. The field of view of the BAT is approximately 2 sr. Adapted from the Swift brochure.*

2.3.6 Swift

With the success of the CGRO in observing GRBs, a whole new field of astronomy was opened up. Swift is a mission dedicated to investigating this powerful phenomena. Swift carries a Burst Alert Telescope (BAT), a wide field of view gamma ray detector, to detect GRBs as they go off. Once the burst has been detected the spacecraft automatically slews to the source at which point it will come into view of the two narrow field instruments. These are the X-Ray Telescope (XRT) and the Ultra Violet and Optical Telescope (UVOT). This autonomous and multi wavelength approach will study GRBs in far more detail than ever before, obtaining data from the afterglow seconds after the initial trigger. Figure 2.15 shows how the instruments are arranged on the spacecraft.

During the 3 year lifetime (launched in 2003) over 1000 GRBs will be studied. The reaction time for each burst is estimated to be between 20 and 70 seconds. The burst detection in the BAT is 5 time more sensitive than BATSE. Burst positions will be obtained within 0.3-2.5 arcseconds. Spectroscopy will be achieved for 0.2-150 keV (BAT and XRT) and six colours will be used by the UVOT (170-650 nm). This will enable the redshift of each burst to be measured with all results made public on the scale of a few minutes from when the burst is triggered.

The BAT

The only way such a wide field of view instrument can obtain the <4 arcminutes positional accuracy is for it to employ a coded mask in conjunction with a detector plane that can achieve high spatial resolution [83]. The detector plane consists of 256 modules of 128 elements of the semi-conductor Cadmium Zinc Telluride (CdZnTe or CZT) [115]. This detector is a adaptation from CdTe and is characterised by a greater energy resolution and charge collection efficiency though the crystal growing procedure for CZT leaves the individual pixels prone to defects which will effect the mobility of the electrons and holes [98]. These 32768 pixels (4 x 4 x 2 mm) are placed 1 m below a trapezium shaped coded mask giving a 2 sr partially coded field of view and a point spread function of 17' (FWHM). The coded aperture technique is a robust method of imaging and is flexible when encountering dead pixels, a distinct possibility with CZT. Due to the large area coded mask (3.2 m^2) and detector plane (5243 cm^2) the surface area of the shielding is large. A passive graded-Z shield (Pb, Ta, Sn, Cu) was selected to reduce the background. The material layers were selected to compliment the sensitive energy range (15-150 keV) with the positions of the K-edges (approximately 75, 58, 25 and 8 keV respectively).

The XRT

The XRT [12] was based on the X-ray telescope that was due to be included in the unsuccessful JET-X mission. Using grazing incidence mirrors (from JET-X) and a CCD set up identical to the one aboard XMM, the energy range is 0.2-10 keV, it has a field of view of 23.6' x 23.6' and an angular resolution of 15". The shielding criteria for X-ray telescopes is different from gamma ray instruments but some principles remain the same. The CCD will be surrounded by several electron defiection magnets and a thermal baffle in front of the mirror prevents temperature gradients distorting the mirror.

The UVOT

The optics for the UVOT [67] were obtained from flight spares from the Optical Monitor aboard XMM. The detector is 2048 x 2048 pixel CCD with a wavelength range of 170-650 nm. The field of view of this arrangement is 17' x 17' and is expected to obtain sub-arcsecond positional accuracy with a sensitivity of 24^{th} magnitude for a 17 minute exposure. Due to the 20-70 second slewing time, about a third of all the GRBs detected by the BAT will be observed by the UVOT.

Scientific Objectives

A key factor in investigating GRBs is the redshift of the burst, the featureless gamma ray spectrum will give no clue as to the redshift. However the UVOT will be able to measure the redshift of the host galaxy, the XRT may be able to measure the Fe line should the burst be associated with a supernova and rapid followup observations will give information on the high Z Lynman-α forest. GRBs provide good

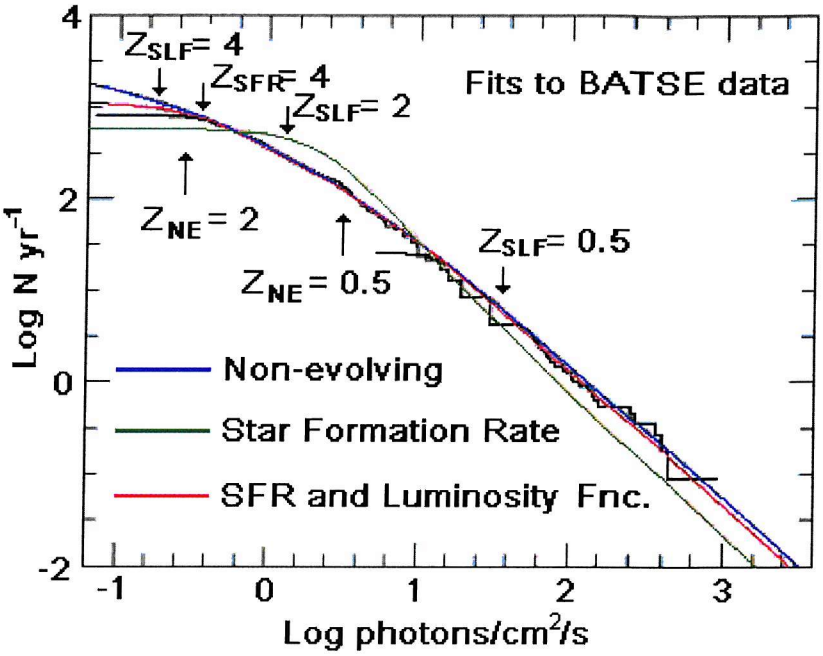

Figure 2.16: **Log N - Log S.** *Three models are fitted to the BATSE data and only two bear a resemblance to the data but with contrasting relations between intensity and redshift. Adapted from Swift webpages.*

backlights to illuminate the Z>4 Ly-α absorption lines enabling an insight into the re-ionisation of the IGM as well as some estimation of the GRB redshift.

The large improvement in the sensitivity of the BAT from previous mission like BATSE will enable much weaker bursts to be detected. Figure 2.16 shows BATSE data compared to three possible log N - log S distributions: a non-evolving model (NE), a model following the star formation rate (SFR) and a model that follows the SFR but also includes some luminosity function (SLF). SFR clearly does not fit and the alternatives give very different results for the redshift-intensity relation. Swift will disentangle the relation between redshift, luminosity and evolutionary effects. The BAT will also be able to detect much weaker bursts and so the redshifts measured by the UVOT and XRT will be extended into a domain where the models diverge. Figure 2.17 shows how the predicted detection of the weaker bursts will help determine the log N - log S model and where previous missions have been inadequate.

In addition to the evolutionary aspects of GRBs, the progenitor is still clouded by controversy. By measuring the position of the GRB within the host galaxy using the UVOT the progenitor may be revealed. As shown in figure 1.14 the distribution of the bursts in relation to their distance from their galactic centre will give an indication of the lifetime and so progenitor. Another indicator of the progenitor would possibly come from examining the evolution of the blast wave and especially

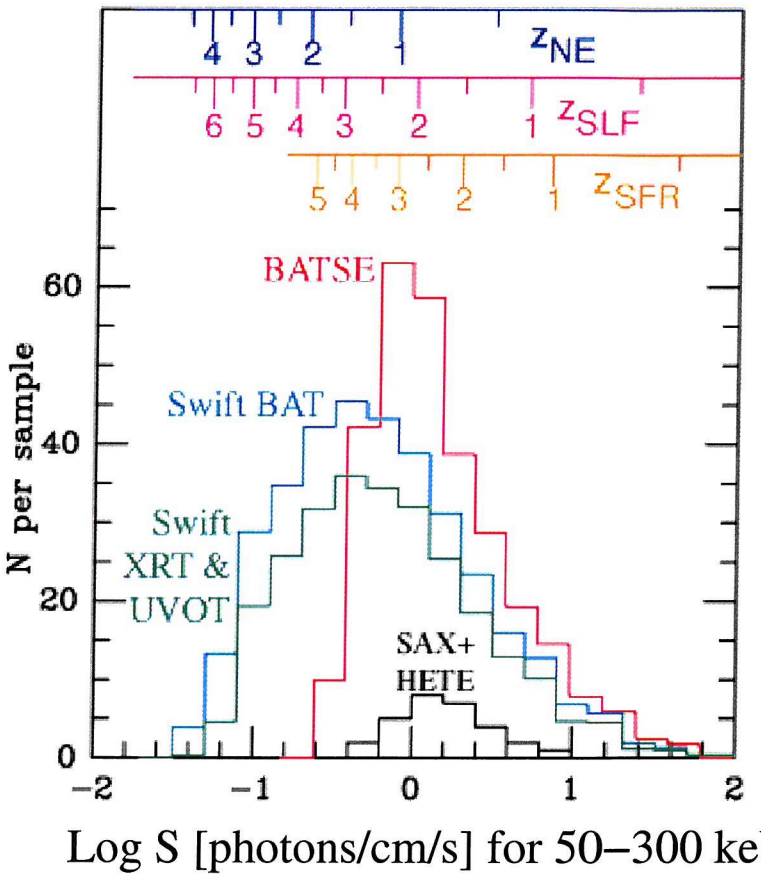

Figure 2.17: **Number of bursts vs peak flux.** *The distributions of the bursts detected by BeppoSAX, HETE-II, BATSE and the predicted detections of Swift. All the BAT detections and XRT and UVOT redshift measurements are included. The redshift scales at the top correspond to the models in figure 2.16. Adapted from Swift webpages.*

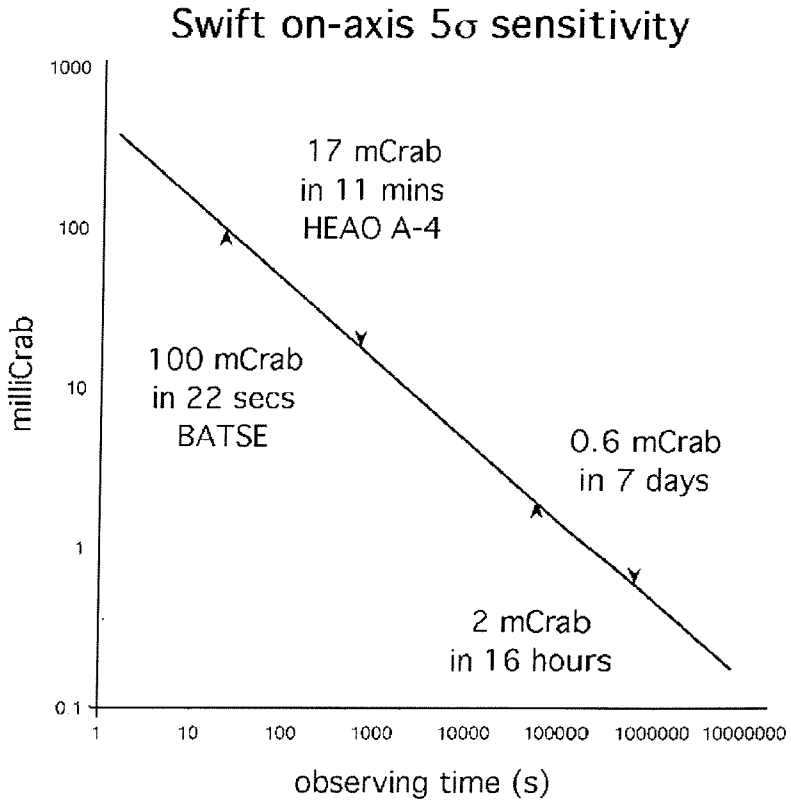

Figure 2.18: **The 5σ sensitivity of the BAT.** *The on-axis sensitivity of the BAT against the exposure time. Comparative performance of previous missions are included. Adapted from Swift webpages.*

the detection of any spectral lines. The XRT is equipped to detect lines and edges with great capability. The details of the afterglow mechanism that can be measured include the density, ionisation element abundance and outflow characteristics. The Swift instruments will be able to observe all these characteristics closely.

The secondary science of the Swift mission is an obvious and serendipitous one. The BAT is a sensitive wide field gamma ray instrument. A burst is expected to occur about once a day, in between the BAT can be used to perform an unprecedented all-sky gamma ray survey. It will be 30 times more sensitive than the previous explicit survey, the HEAO A-4 survey down to 17 mCrab [60]. Figure 2.18 shows a prediction of how the BAT will perform during its surveying.

2.3.7 The GRB Coordinates Network (GCN)

Due to their multi-wavelength, short lived and extra galactic nature, a GRB could occur from any direction and could only last for a few seconds. This sporadic behavior requires a collaboration between instruments of every type from TeV ground based astronomy to radio astronomy arrays. This collaboration is run by the GCN

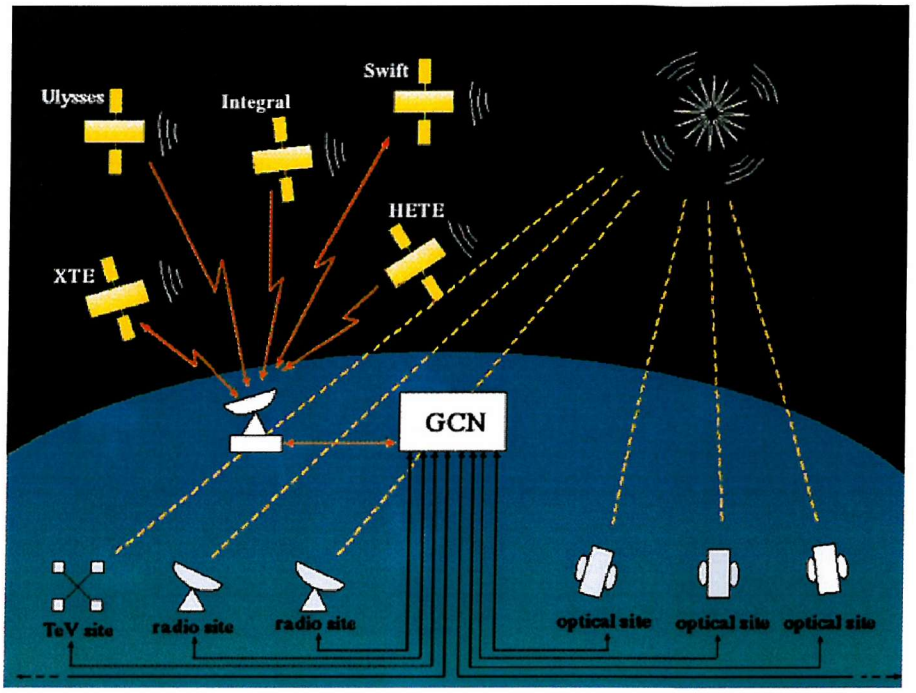

Figure 2.19: **The GCN.** *A schematic of some of the instruments collaborating in the GCN.*

and aims to distribute the positions of bursts within a few seconds of the burst being triggered to all the institutions in the collaborations so that follow up observations can be obtained as the burst is still going. The need for prompt follow up observations is vital to understanding GRBs in the future. Though Swift will undoubtedly be the flagship of the network the first trigger could easily come from several other spacecraft with burst monitors aboard. This would enable Swift to quickly slew and follow up the initial detection. Figure 2.19 is a simple diagram of how the GCN works.

2.4 Summary

The methods by which gamma ray instrumentation can be carried out have been reviewed in this chapter. The importance of understanding gamma ray interaction remains paramount right up to the study of complex gamma ray astronomy missions. The two most significant differences between gamma ray astronomy and the other energy domains are the methods for imaging and the high levels of background. Though the study of GRBs is unique in that the source is stronger than the background noise, the area that requires investigation in future GRB missions is the distributions of the weaker bursts. By understanding the background the sensitivity of a mission can be optimised. This chapter has illustrated the complexity and applications of observing in the gamma ray domain, the following chapter will outline what sources of background contribute to the high levels of noise.

Chapter 3

The Various Sources of Background in Space Based Instruments

The background of any space-borne gamma ray instrument is highly complex and contains many individual components [36]. It will always be high in relation to the true source counts and so its suppression is a necessity, be it on a short life-time balloon mission or a longer life-time instrument attached to a platform launched into deep space. The amount that each component effects the instrument background depends a lot on the nature of the mission. The various sources of the gamma ray background will be described here along with the conditions under which each composite part would become significant.

Modern background prediction primarily relies upon computer modelling and Monte-Carlo simulations. The generation of each background component and the response of the detector are handled by intricate software suites based entirely on non-empirical methods. To obtain a realistic background estimation of the mission it is vital that the incidence and spectral fluxes of the background particles and photons are known accurately, to enable a realistic simulation of the detector performance.

The next most important factor that effects how the overall background can be determined is the position of the Earth with respect to the instrument. The Earth, though not the originator of a gamma ray flux, supplies a flux via Cosmic Ray interactions with its atmosphere providing a Low-Earth Orbit (LEO) mission with a highly time dependent source of background. The Earth can "shadow" the detector from Cosmic Rays while the Earth's magnetic field can both shield the instrument from Cosmic Ray interactions and pool charged particles into radiation belts like the Van Allen belts and the South Atlantic Anomaly. The effect the Earth has is strongly dependent on the inclination and the altitude.

The orbit characteristics may dominate the surrounding background environment

but the design of the instrument will determine how the detector is effected. Only by balancing the effects that this environment will have on the instrument will the best results be achieved. As an example, simply increasing the thickness of the passive shielding will reduce the flux penetrating the shield but it will concurrently increase the photons emitted from activation of the same passive material due to its exposure to Cosmic Rays.

The components to the gamma ray background can be split into two types, the photon induced background and the non-photon induced background. Though Cosmic Rays (including electrons, protons and heavier nuclei) may be responsible for most background radiation it is easier to break it down into the forms of flux as they reach the instrument. For this reason photons reaching the detector after being emitted from a Cosmic Ray proton interacting with the Earth's atmosphere will be considered photonic.

3.1 Hadron Induced Background Components.

The background in gamma ray instruments that directly results from hadrons is primarily due to incident Cosmic Rays, the majority of which are protons [134]. Cosmic Rays physics has long been a topic of astrophysics in its own right. They were discovered early last century and shown to be incident upon the Earth from outer space [41] and that their intensity did not alter significantly between night and day proving that they were not primarily solar in origin. Since then Cosmic Rays have revealed many aspects of our galaxy and indeed particle physics itself owes a lot to the discovery of Cosmic Rays. Cosmic Rays are essentially atoms who have had their electrons stripped from them during their highly energetic trajectories through space. The term "Cosmic Ray" is used to group together any particle reaching the earth from a non-terrestrial source. It can be broken down into Galactic Cosmic Rays, Solar Energetic Particles, Anomalous Cosmic Rays and particles trapped in the magnetosphere of the Earth.

Solar Energetic Particles (SEPs) are particles ejected from the Sun during flares or Coronal Mass Ejections (CME) and are dealt with as a separate source of background due to their highly variable and an-isotropic nature. Magnetospheric particles are also treated as a separate source of background as they are confined to certain regions of the magnetosphere. Like SEPs, they only effect the instrument under specific conditions and so both of these hardonic sources of background will be treated separately in later sections, to be ignored or included accordingly.

Galactic Cosmic Rays consist of protons and some heavier nuclei that originate from supernovae and other highly energetic events [66, 7]. The intensity of this source of Cosmic Rays varies with the solar cycle. The solar wind and interplanetary magnetic field shields the Earth from charged particles in the same way that

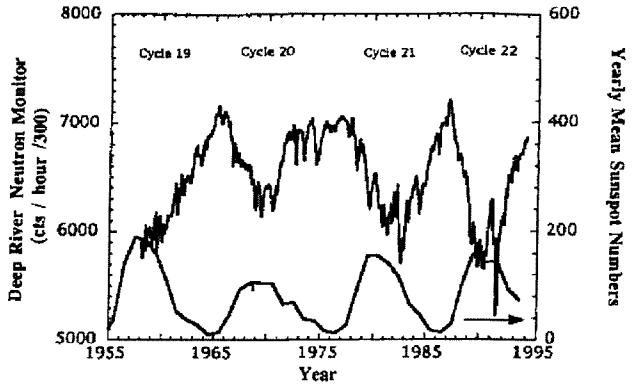

Figure 3.1: **The solar cycle plotted with the neutron flux.** *Notice the anti-correlation of the solar activity with the inferred incident Cosmic Ray flux. Adapted from Klecker (1996).*

the magnetosphere does. The Earth will receive maximum Cosmic Ray flux at the solar minimum (see figure 3.1 [54]).

Anomalous Cosmic Rays were first noticed as a flux that differs significantly in composition from the galactic and solar Cosmic Ray particles. A large proportion of this flux consists of elements with a large first ionisation potential (H, N, O, Ne). The origin of these is most probably interstellar neutral particles that are ionised by solar UV radiation and accelerated by shock-waves in the heliosphere [30].

It is clear that a gamma ray instrument will receive Cosmic Ray flux from various sources and that this source of background needs to be evaluated. Due to the nature of proton bombardment this source of background can be split into two categories: Prompt Cosmic Ray Background and Delayed Cosmic Ray Background.

3.1.1 The Prompt Cosmic Ray Background

This source of background is due to the spallation effects of incident Cosmic Rays on the materials in the spacecraft. It is while considering this source of background that the need for Monte-Carlo simulations becomes most important. A single energetic proton can pass straight through or interact creating hundreds of secondary interactions, see figure 3.2. An incident proton can produce numerous gamma rays.

Whether the prompt cosmic-ray component of the background dominates or is even significant will depend on the orbit of the instrument. Before the methods of estimating the background flux are discussed a brief point has to be made about the effect that the Earth's magnetic field has on the incident Cosmic Rays. The low threshold cut-off energy is determined by the position of the spacecraft within the atmosphere. This minimum cut-off energy can be derived from the Rigidity (R_c), the measure of how easily a particle is deflected by a magnetic field, expressed

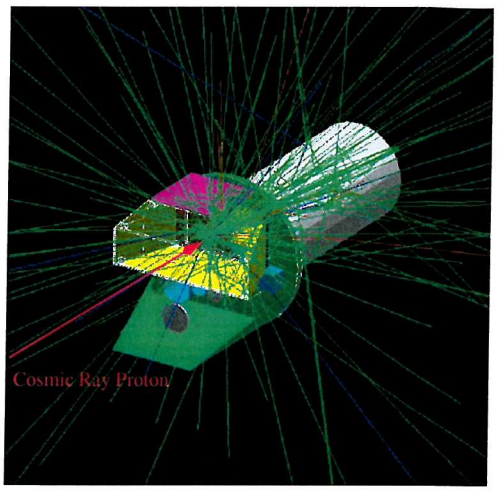

Figure 3.2: **A modelled hadron interaction.** *The red arrow signifies a single 20 GeV proton incident on a model of the Swift satellite. The ray-tracing produces green lines for neutral particles and photons, red is for negative and blue is for positive particles.*

in megavolts (MV) per nucleon (momentum per unit charge). The magnetic field prevents particles below a certain energy reaching a certain depth within the atmosphere. It is defined by obtaining a value for the McIlwain Parameter, **L**, (for instance, from figure 3.3) and obtaining the rigidity (vertical direction) from equation 3.1 [106] (*This equation is a simplification of equation 3.3 and will be discussed explicitly*). This will imply a cut-off energy from equation 3.2 [36].

$$R_c = 14.7L^{-2} \quad (GV) \tag{3.1}$$

$$E_c = 10^3 \left(-0.938 + \left(0.938^2 + R_c^2\right)^{0.5}\right) \quad (MeV) \tag{3.2}$$

The rigidity of the spacecraft's position will play a large part in determining the Cosmic Ray spectrum incident on the spacecraft. The Earth's magnetic field can be modelled by using the International Geomagnetic Reference Field (IGRF). The IGRF is a series of mathematical models describing the Earths main field and its secular variation [15, 18, 58, 70]. Each model comprises of a set of spherical harmonic coefficients. From this, the magnetic field and so the McIlwain parameter, **L**, can be calculated for each position in low Earth orbit.

Unfortunately the geomagnetic cutoff rigidity phenomenon was shown to have "no solution in the closed form" [113]. The inclusion of a full model of the magnetic field could be time-consuming depending on the objectives of the simulation. Some useful approximations were presented by [106]. The first approximation was noticed when the problem was viewed in a geometrical context. There is an axial symmetric cone about a direction to the east within which Cosmic Ray particles

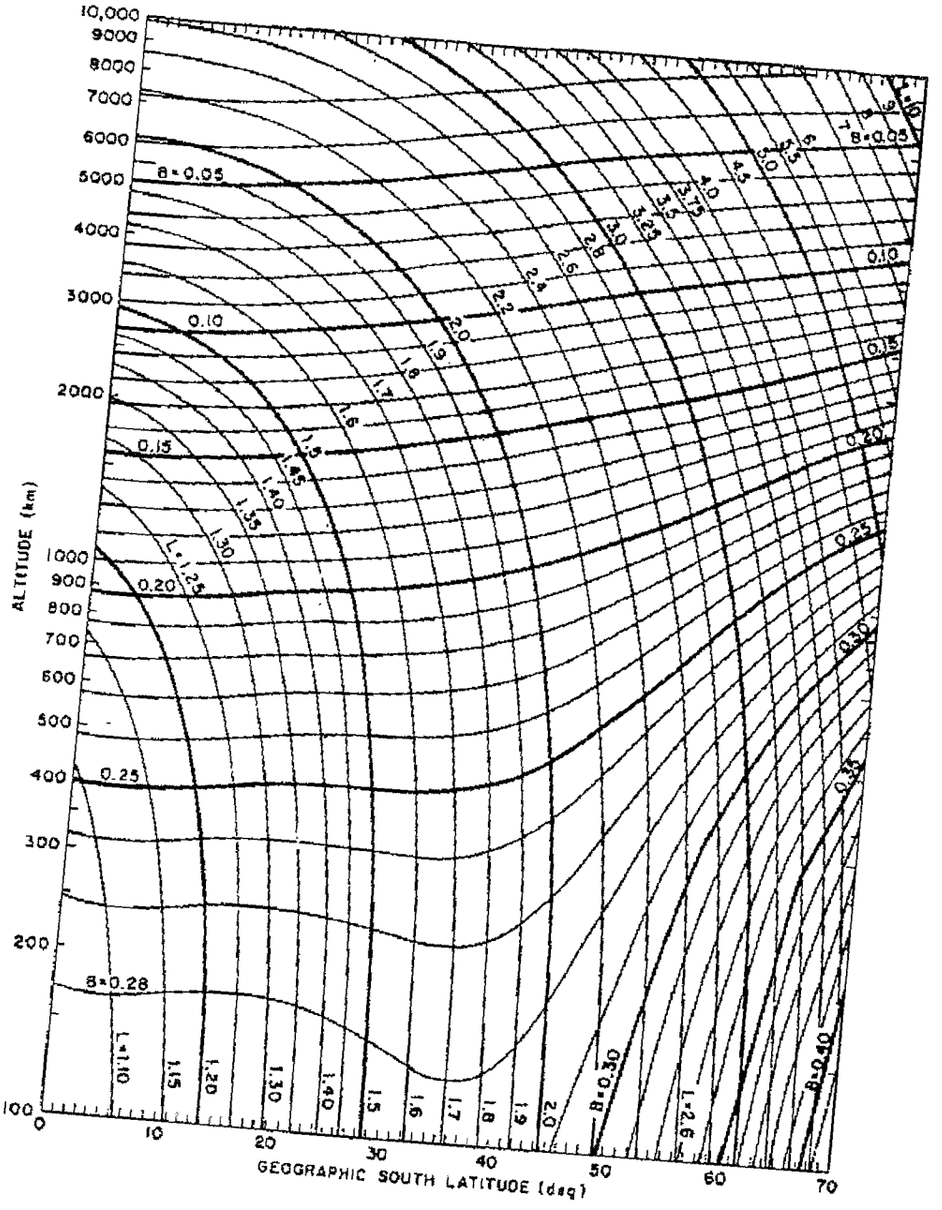

Figure 3.3: **Lines of constant L (in Earth Radii) and B (in Gauss) on a plot of Altitude against Latitude.** *Adapted from Aerospace Corp. Rept No TDR 169 (3510-41), TR-4, Contract AF04(695).*

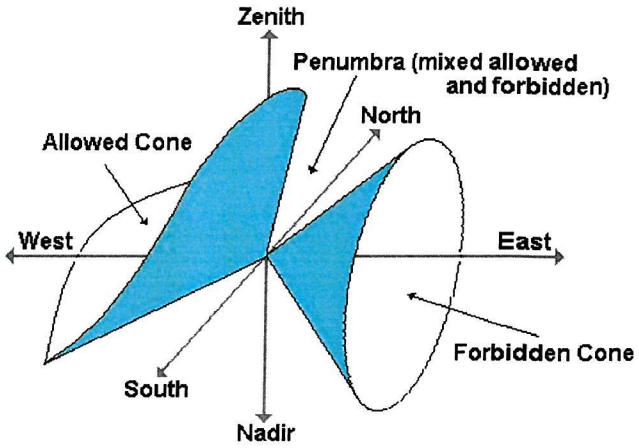

Figure 3.4: **A geometric visualisation of rigidity cutoffs.** *The forbidden cone is an intrinsic property of a dipole field (Stormer, 1955). The allowed cone to the west is not defined by an exact equation but the concept is set-out by (Lemaitre and Vallarta, 1936).*

below a specific energy are forbidden from entering. Figure 3.4 displays this cone along with a cone that describes the allowed transitions. By considering the bipolar field geometry it was also seen that a special case solution exists [113] and is shown in equation 3.3 (M is the magnitude of the dipole moment in $gauss\,cm^3$, λ is the latitude from the **magnetic** equator, θ is the angle from the zenith direction (where the zenith direction is a radial from dipole centre), ϕ is the azimuthal angle measured clockwise from the direction to the north dipole axis and **r** is the distance from the dipole centre in centimeters. M can be assumed to be 8.06 x 10^{25} $gauss\,cm^3$). This can be approximated to equation 3.4 (C_s is the Stormer Constant. The value of which changes with the evolution of the Earth's magnetic field and is derived from IGRF models. It can be assumed to be 58 (measured in 1990). **L** is the McIlwain parameter).

$$R_c = \frac{[M\ cos^4\lambda]}{r^2\left[1+\sqrt{1-sin\,\theta\ sin\,\phi\ cos^3\lambda}\right]^2} \quad (GV) \tag{3.3}$$

$$R_c = \frac{C_s}{L^2\left[1+\sqrt{1-sin\,\theta\ sin\,\phi\ cos^3\lambda}\right]^2} \quad (GV) \tag{3.4}$$

From equation 3.3 and figure 3.4 it is clear that the rigidity is lower from the geomagnetic west direction as a characteristic of the dipole field. Traditionally the vertical down-ward direction rigidity is used as there is the smallest amount of atmospheric absorption and so to calculate the maximum flux that the instrument observes it may be necessary to use the **westerly** geomagnetic cutoff as a worst case scenario. This is defined in equation 3.5 [54, 106].

Table 3.1: **The Cosmic Ray spectrum for solar maximum and minimum.** *Taken from Webber and Lezniak (1974).*

Solar Activity	$\frac{dN(E)}{dE}$ [protons. cm^{-2}. s^{-1}. MeV^{-1}]	Energy Range (MeV)
Solar Minimum:	$7.85 .10^{-7}.E^{+1.00}$	$4.00 .10^{1} - 1.93 .10^{2}$
	$1.29 .10^{-4}.E^{+0.04}$	$1.93 .10^{2} - 5.65 .10^{2}$
	$2.25 .10^{-1}.E^{-1.14}$	$5.65 .10^{2} - 3.44 .10^{3}$
	$3.44 .10^{2}.E^{-2.04}$	$3.44 .10^{3} - 2.55 .10^{4}$
	$2.44 .10^{5}.E^{-2.69}$	$2.55 .10^{4} - 10^{6}$
Solar Maximum:	$2.45 .10^{-6}.E^{0.27}$	$3.56 .10^{1} - 1.02 .10^{2}$
	$9.14 .10^{-8}.E^{0.98}$	$1.02 .10^{2} - 4.91 .10^{2}$
	$4.97 .10^{-5}.E^{-0.04}$	$4.91 .10^{2} - 1.21 .10^{3}$
	$2.54 .10^{-3}.E^{-0.59}$	$1.21 .10^{3} - 3.44 .10^{3}$
	$3.44 .10^{2}.E^{-2.04}$	$3.44 .10^{3} - 2.55 .10^{4}$
	$2.44 .10^{5}.E^{-2.69}$	$2.55 .10^{4} - 10^{6}$

$$R_{c-west} = \frac{(C_s \, cos^4\lambda)}{r^2.\left(1+\sqrt{1+cos^3\lambda}\right)^2} \quad (GV) \tag{3.5}$$

Now the cutoff rigidity has been obtained, it needs to be applied to the Cosmic Ray spectra. Any influence the magnetic field exerts on a Cosmic Ray proton will be at right-angles to the motion of the particle. Whereas a charged particle will loose its kinetic energy when fired into a Coulomb field a Cosmic Ray proton will not loose any kinetic energy to reach a point in the magnetosphere. If it does not have sufficient energy it will be deflected and maintain its kinetic energy. This may seem obvious but it enables a simple cutoff to be used in the Cosmic Ray spectra. There will be an smearing effect due to the an-isotropic variation in the rigidity and this could be included in any model (from equation 3.3) if so desired.

The Cosmic Ray spectrum is defined by table 3.1 [123]. Two spectra are quoted for the Cosmic Ray component. One for the solar maximum and one for the solar minimum. It is apparent that the solar cycle only effects the lower energy spectrum.

For instruments in low Earth orbit the correct cutoff rigidity needs to be applied to the spectrum. This rigidity will vary during the spacecraft's orbit and so the background will modulate accordingly.

The prompt Cosmic Ray background can be partially shielded by using an active veto system, by considering the direct interactions. Any coincident counts by charged particles in the veto and the detector will be ignored. However should a count in the detector be delayed from the veto count because the incident Cosmic Ray left material in an excited state (with a half-life larger than microseconds) then

the resultant gamma ray from this decay cannot be veto-ed out and so is a form of background in its own right.

3.1.2 The Delayed and Secondary Cosmic Ray Background

The delayed component of the Cosmic Ray background cannot usually be fully defined until the instrument is in orbit due to the highly analytical nature of this component. The spacecraft, being at high altitudes, receives a Cosmic Ray flux that interacts and excites the materials in the spacecraft. Therefore the delayed component is both slowly varying, highly specific to the instrument and builds-up asymptotically over a much longer time scale than any prompt Cosmic Ray or gamma ray background [126]. Once the prompt effects are determined the number and composition of the radioactive isotopes can be estimated by Monte-Carlo techniques and so the radioactive environment within the instrument itself can be determined.

A component that is a result of Cosmic Ray interactions is a secondary component that results from Cosmic Rays interacting with material outside the detector, producing photons and leptons. For an estimation of how this secondary component scales with the depth in the atmosphere, equation 3.6 (Where $\frac{dN(E_p)}{dE_p}$ is the incident Cosmic Ray spectrum.) can be used. This determines the scaling parameter, M_R [25] . The origin of this is from observations of how the secondary flux varies with the McIlwain parameter, **L**. An empirical verification can be determined by looking at the intensity of the positron-annihilation line aboard a previous mission (HEAO 3) [63]. Figure 3.5 shows the best fit with a weighting index of 0.7. Other verifications are covered by [36]. So any secondary Cosmic Ray component can be scaled to any orbit, as an approximation. However, this scaling will require an initial analytical model.

$$M_R = \int_{E_{cutoff}}^{\infty} \frac{dN\left(E_p\right)}{dE_p} E_p^{0.7}\, dE \quad \left(MeV^{0.7} cm^{-2} s^{-1}\right) \tag{3.6}$$

3.1.3 Solar Flares

Solar energetic particles can be classed as "impulsive" or "gradual" [55]. The impulsive particles are a result of flares and vary with the solar cycle. 1000 per year at solar maximum and a few per year at solar minimum [95]. Typically the impulsive flux has high electron and proton fluxes, high Helium fluxes, an enhanced heavy element ratio and a low ion intensity. The gradual particles are a result of Coronal Mass Ejections (CMEs). These mass ejections produce a shock-wave in the solar corona and in interplanetary space accelerating charged particles. These ejections are dominated by protons and evolve over timescales of days not hours, like their impulsive relation.

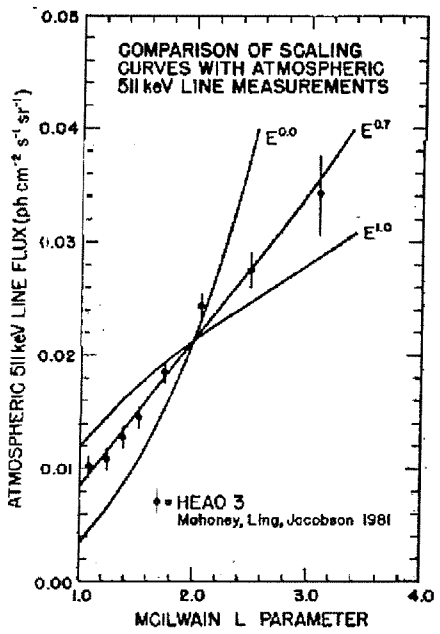

Figure 3.5: **The M_R parameter.** *The HEAO 3 atmospheric 511 keV line measurements provide comparisons for different weighting parameters. $E^{0.7}$ provides the best fit. Adapted from Gehrels (1992).*

If a spacecraft is not in a close Earth orbit the shielding effects of the magnetosphere will mean that solar originating particles will reach the instrument unhindered. So an instrument on a highly eccentric or deep space orbit can directly experience the effects of a solar flares or CMEs. As a source of background each flare is different in spectra and evolution. An example will be presented here as a generic case: The March 1991 Solar Flare Events [97]. This event consisted of an initial flare followed by a CME which was in turn followed by another flare. The propagation of these events are not mutually exclusive and so the background is expected to vary as the event evolves. The measurements were made by COSPIN at 2.5 AU. Figures 3.6 and 3.7 show the aspects to the flare that would be needed for any simulation. Though these will be different for every flare, an idea of the instruments behavior can be achieved.

3.1.4 Magnetospheric Trapped Particles

Magnetospheric particles consist of protons and electrons that are constrained by the local magnetic field in the same way a "magnetic bottle" is used to confine energetic plasma [119]. The two radiation belts are populated by fluxes of energetic particles. The inner belt is compact and extends to about 6400km above the Earth's surface and is filled by dense fluxes of energetic protons. The outer belt is less stable and contains a variety of ions (mostly protons) and electrons of much lower energy. It extends from about 20,000 to 27,000km above the Earth's sur-

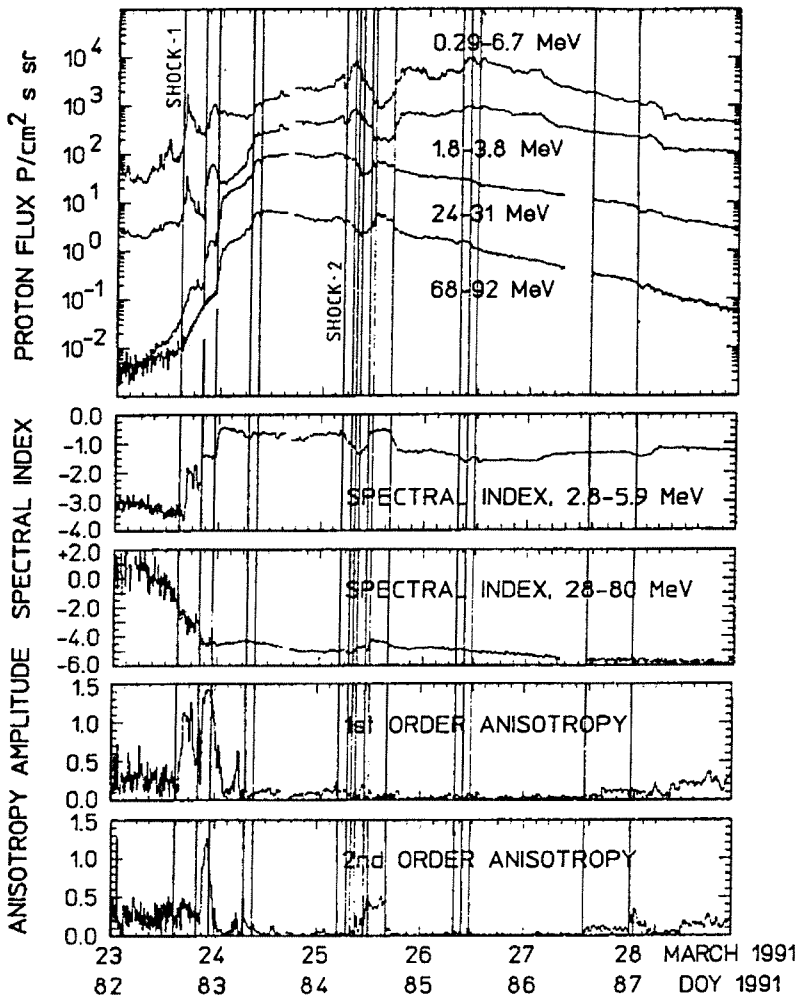

Figure 3.6: **The parametrical evolution of the solar flare events beginning March 23, 1991.** *Taken from Sanderson at al. (1992). the anisotropy modulation in this event is a result of the pointing axis of the ULYSSES spacecraft. ULYSSES has a proton counter perpendicular to the spin axis of the spacecraft. So as the spacecraft rotates the flux received will vary according to how off-axis a flare is with respect to the spin axis. This is important when considering the flux incident on an instrument due to a solar flare.*

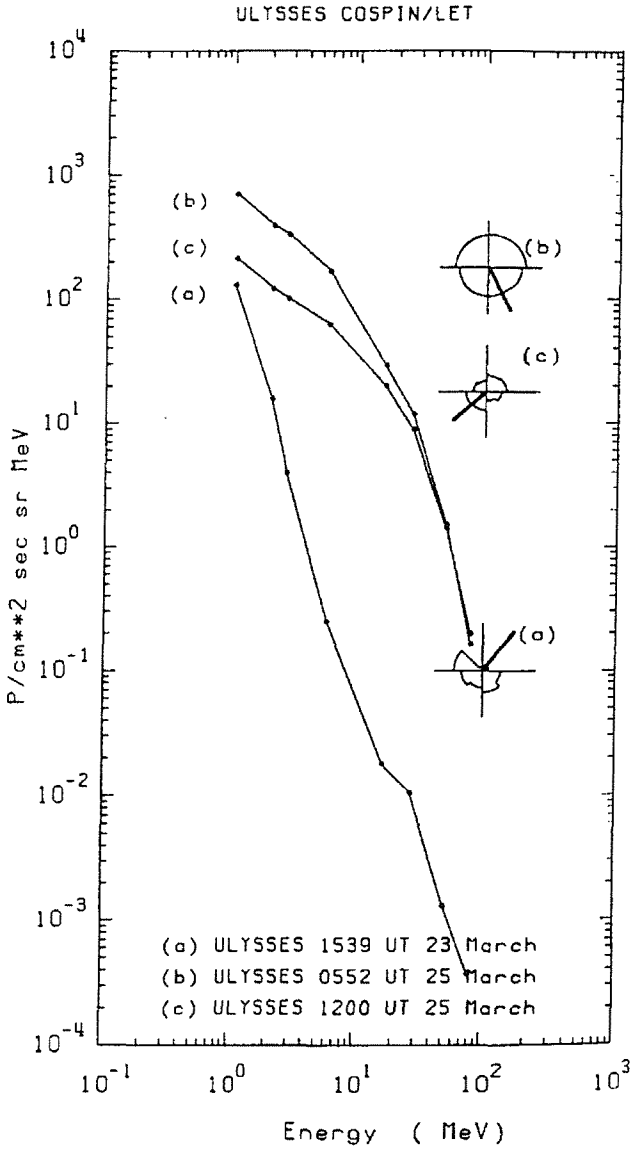

Figure 3.7: **The spectra of the events as they reach the instrument (COSPIN - Ulysses).** **a)** *is for the first shock,* **b)** *is for the second shock and* **c)** *is for the passage through the magnetic cloud. Also shown are anisotropy indications, for the full analysis refer to Sanderson et al, 1992.*

face. The populations of this outer belt fluctuates wildly, interacting with magnetic storms while being populated by the variable tail of the magnetosphere. Unlike the other constituent types of Cosmic Ray these are confined to specific areas around the Earth and so need only to be considered if the instrument is passing through the belts directly. Due to the nature of the magnetic field surrounding the Earth the southern hemisphere has a indentation in the magnetosphere called the South Atlantic Anomaly [37, 86] and can be a major source of background for instruments in low Earth orbit. The regions of trapped particles require different treatment to the standard Cosmic Ray flux and may not have to be considered at all. Figure 3.8 shows the position and flux for protons and electrons in the SAA. For the purpose of instrument background estimation, electrons can be ignored due to the ease of shielding. The electron flux may only be a problem for orbits of high inclination like that of the International Space Station (ISS).

By calculating passages through the SAA a spectrum can be obtained. Figure 3.9 shows an example of the flux calculated for an instrument in low Earth orbit, in this case, the CGRO.

An aspect of the delayed self-radiating background that would need to be taken into account is the passage of a telescope through an area of trapped charged particles such as the South Atlantic Anomaly (SAA). During this passage the instrument will experience a sharp increase in proton flux and the strength of the resultant radioactive decay (mainly gamma and β decays) will modulate with respect to the low Earth orbit passages through these regions [117]. The prediction of this secondary background due to trapped charged particles is highly dependent on the field model used [27]. The delayed component fades as a combination of the power laws of the various decay processes stimulated by the passage through the region of trapped charged particles. Again equation 3.6 can be used to scale this delayed secondary background if a trapped particle fiux term is included [36].

During an SAA passage the spacecraft will also experience a sharp rise in the incident electron flux. These electrons will not cause a radioactive delayed component but will produce a secondary component aswell as a prompt componet due to processes such as Bremsstruhlung.

3.1.5 Neutron Induced Background

Due to the short lifetime and lack of charge, a gamma ray instrument will not experience significant amounts of cosmic neutron flux (except, possibly, in the case of a solar flare). However neutrons will be incident on the spacecraft as a secondary component to Cosmic Ray interactions with the atmosphere and the spacecraft. Neutrons interact with the materials in the telescope in three possible ways: absorption, inelastic and elastic scattering.

Absorption occurs when a nucleus captures a neutron creating an isotope of the

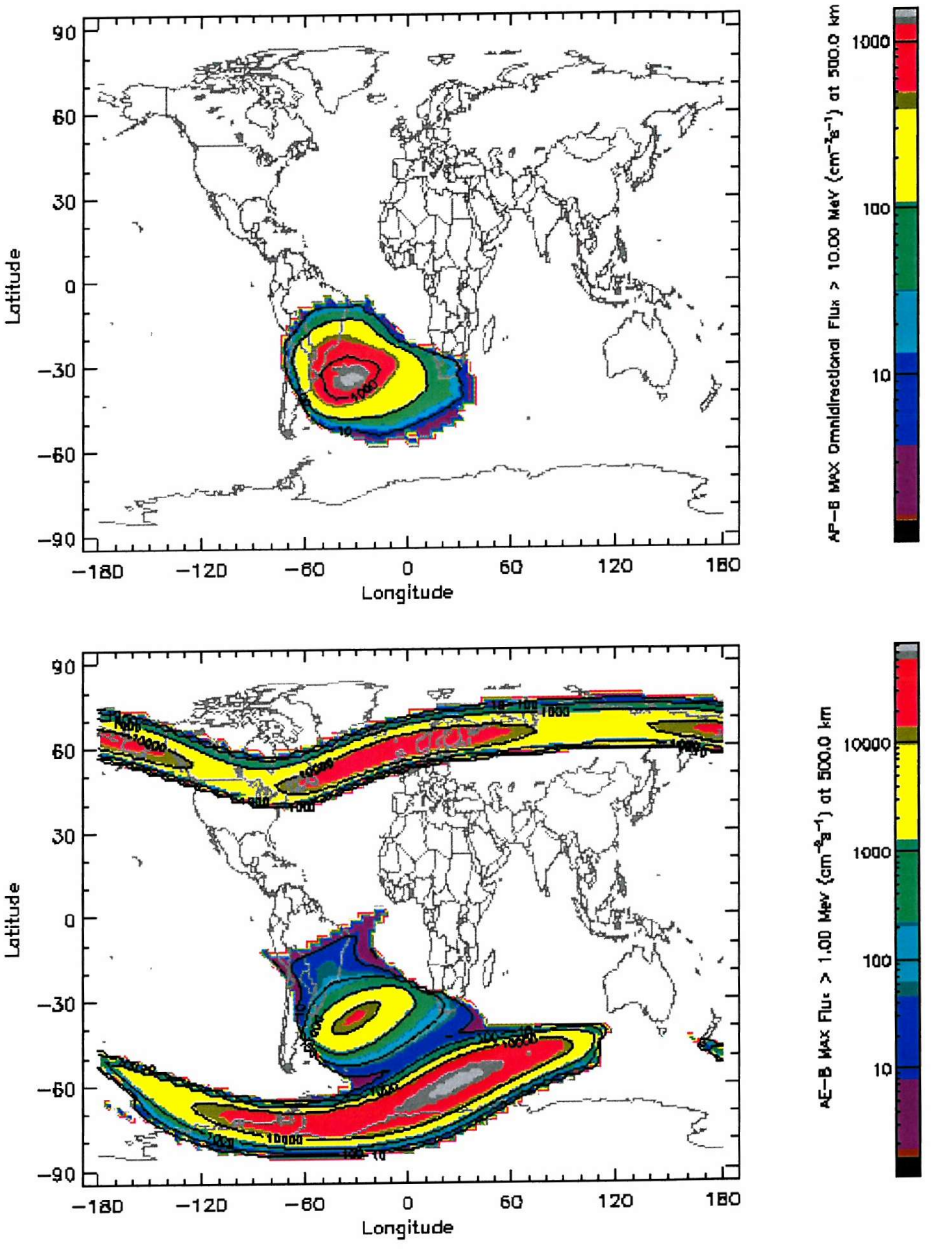

Figure 3.8: **A proton (left) and electron (right) flux contour map of the SAA.** *This map is for an altitude of 500 km.*

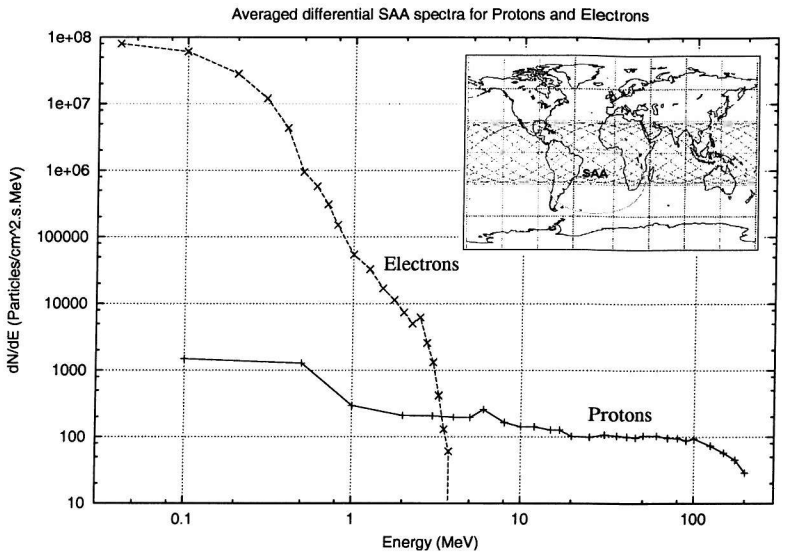

Figure 3.9: **Time-averaged SAA spectrum.** *One days worth of orbits for the CGRO (90 minute period) with relation to the SAA (altitude, 500 km). The spectra is the average differential flux that the CGRO receives during that day due to the passages through the SAA.*

initial nucleus in an excited state. The decay of this excited state by gamma or beta emission introduces many lines into the gamma ray background. The neutron cross-section and half-lives of the excited states of the materials involved are the main factors as to how much this secondary background affects the total gamma ray background.

Neutrons can collide with nuclei without being absorbed. Inelastic collisions cause neutrons to excite nuclei into higher energy states which in turn decay, producing many gamma ray lines superimposed upon the background continuum. The peaks of which are determined by the materials involved. As well as inelastic the interaction can be elastic, transferring the kinetic energy of the fast neutron to the nucleus. This will produce a contribution to the background at lower energies (< 100 keV).

The neutron induced background has been studied with the COMPTEL telescope [124, 73]. Being a Compton telescope it is susceptible to any type of background that can cause a count in both detectors simultaneously. Neutron interactions are unfortunately ideal for this kind of background. For this mission it was seen that the neutron shielding was more important for shielding the atmospheric albedo flux than producing its own secondary neutrons. The atmospheric neutron flux can be described from fits to COMPTEL data and is described by equation 3.7 (Where P_c is the vertical cutoff rigidity, θ is the zenith angle, M is the solar modulation function and R_{nm} is the ground-level neutron monitor rate. α and β are parameters of the fit and have values of $2.55\text{x}10^{-3}$ and 0.152 GV^{-1} respectively) [74]. This equation can be verified and forms of it are presented in equation 3.8 (Measured in

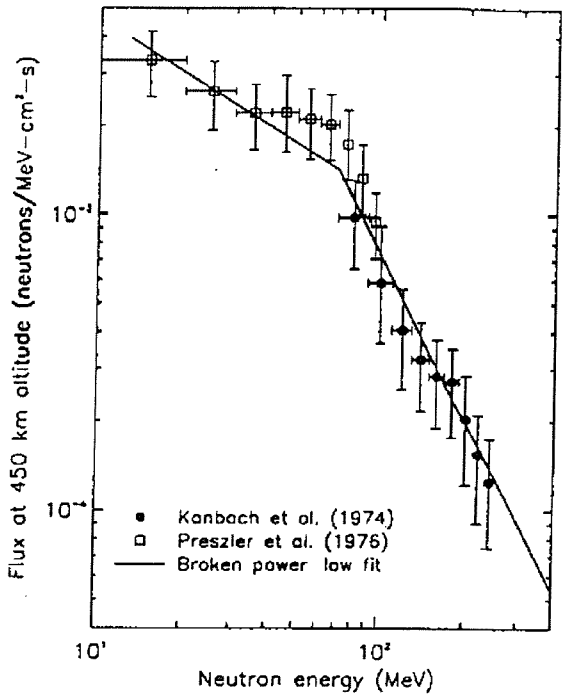

Figure 3.10: **A broken power law fit to orbital neutron flux measurements from two balloon flights.** *Adapted from Morris et al. (1995).*

$n.cm^{-2}.s^{-1}.MeV^{-1}$). Figure 3.10 shows the verification (for a cutoff rigidity of 4.5 GV, a zenith angle of 0^o and $\mathrm{M}(R_{nm}) = 1$).

$$R\left(P_c, \theta, R_{nm}\right) = 16.7\, M\left(R_{nm}\right)\left[1 - b\theta\right] e^{-\alpha P_c} \quad (Hz) \tag{3.7}$$

$$\begin{aligned} \phi_{4\pi}\left(P_c, \theta, R_{nm}, E_n\right) &= 0.036\, M\left(R_{nm}\right)\left[1 - b\theta\right] e^{-\alpha P_c} E^{-0.6} \\ &\qquad [E \leq 70MeV] \\ \phi_{4\pi}\left(P_c, \theta, R_{nm}, E_n\right) &= 8.7\, M\left(R_{nm}\right)\left[1 - b\theta\right] e^{-\alpha P_c} E^{-1.89} \\ &\qquad [E \geq 70MeV] \end{aligned} \tag{3.8}$$

3.2 Photon Induced Background Components.

The photon induced background includes Cosmic Diffuse Gamma Radiation and Earth Albedo Radiation. Both bathe the instrument in photons but the spectra and origin are very different.

3.2.1 Cosmic Diffuse X-rays.

The origin of the Cosmic Diffuse X-rays (CDX) is a topic of current scientific debate [61, 40, 104]. The isotropy of the CDX infers that the origin is either extra-galactic or of a truly diffuse nature (The Galactic Plane, a strong source of gamma rays, is considered as a separate interfering source). The origin is said to be a combination of the total flux from many unresolved extra-galactic sources convolved with a Cosmic Ray electron component. As instrument sensitivity improves then the resolution of these mysterious sources becomes achievable and the true originators revealed. Every known discrete source has been considered as the originator and fitted to the spectra observed. No individual source of gamma rays dominates the spectrum [118, 133]. The current state of understanding points to obscured AGN (primarily Seyfert 2's, [132, 43]) to re-produce the flat spectrum of the CDX, Blazars to re-produce the higher energy spectra [110, 109] with contributions from SNe Ia [44, 96, 121] and galaxy clusters [20] being apparent. The effect of Cosmic Ray electrons Inverse Compton Scattering the Cosmic Microwave Background is also necessary to reproduce the CDX [23, 75]. To determine the true origin would not solely benefit the instrument scientists but also reveal evolutionary aspects of the constituent classes of objects.

The fact that the CDX primarily originates from individual sources means that the isotropy needs to be considered. This background can be considered to be isotropic due to the extra-galactic nature of the sources. Slight granulation does occur over small scales [61, 125] but can be ignored when modelling the background of gamma ray instruments. The CDX can be considered to be entirely isotropic unless the Earth is shadowing the spacecraft.

The CDX has been measured by many instruments since the first balloon flights [29] right up until the latest missions, such as the CGRO [125]. Figure 3.11 shows the CDX spectra as measured by several instruments. The spectrum can be defined as a split power law defined by equation 3.9 measured in $Photons\,cm^{-2}\,s^{-1}\,sr^{-1}\,MeV^{-1}$ [36].

$$\begin{aligned} \frac{dI(E)}{dE} &= 0.54.E^{-1.4} \quad (< 0.02MeV) \\ \frac{dI(E)}{dE} &= 0.0117.E^{-2.38} \quad (0.02 - 0.1MeV) \\ \frac{dI(E)}{dE} &= 0.014.E^{-2.3} \quad (> 0.1MeV) \end{aligned} \tag{3.9}$$

3.2.2 Atmospheric Albedo Gamma Radiation.

The Earth's atmosphere is a strong source of gamma rays. Cosmic Ray particles, primarily protons [134], interact with the atmosphere to produce gamma rays. Above

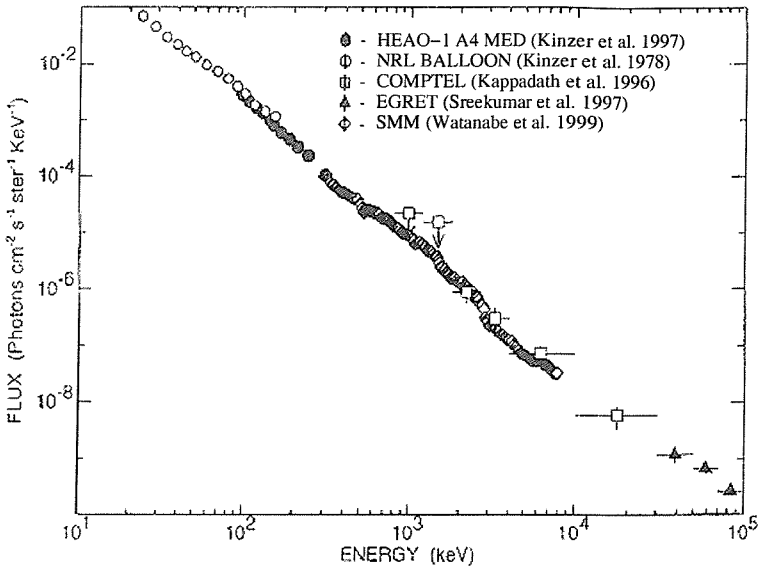

Figure 3.11: **The Cosmic Diffuse X-Ray Spectrum.**

50 MeV the main source is the decay of mesons while below 50 MeV the main source can be attributed to bremsstrahlung radiation from secondary electrons from Cosmic Ray interactions. Figure 3.12 [134] shows the mechanisms by which the albedo gamma rays are produced.

The flux that an instrument observes from the Earth's atmosphere varies with the spacecrafts position and the direction that the instrument is pointing. This is due to the amount of atmosphere that the instrument views and not due to any directional component of the albedo emission. As the emission is secondary to the Cosmic Ray interaction, the flux is isotropic from each unit volume of atmosphere but depth dependent. The intricate nature of the albedo flux requires intensive dynamic simulations for a full evaluation. The methods behind these simulations are described here and some possible generalisations outlined. The two methods considered are:

- Angle averaged method scaled to the correct orbit.
- A discussion of a full, non-empirical model.

Before the methods of estimating the atmospheric albedo flux are discussed a brief point has to be made about the effect that the Earth's magnetic field has on the incident Cosmic Rays. As discussed in the section on the hadron induced background, where the spacecraft is in relation to the Earths magnetic field is paramount to determining the background at that point. The same applies to any position within the magnetosphere, whether it is the flux that the spacecraft receives directly or a position within the atmosphere that is emitting gamma radiation as a result of

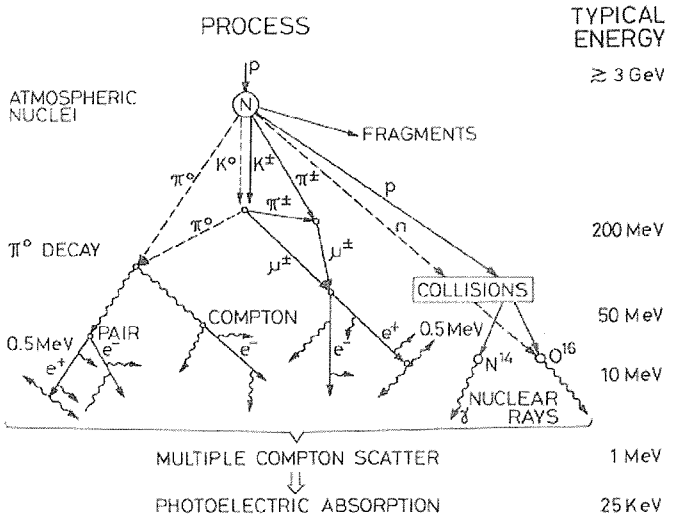

Figure 3.12: **Various gamma ray production mechanisms of Cosmic Ray interactions with the Earth's atmosphere.**

Cosmic Ray interaction.

As can be seen in figure 3.3 the rigidity of a position in the atmosphere is not a simple function of the inclination and altitude. For this reason the calculation of the albedo gamma ray flux presents itself as a complex problem. The context of which will be discussed within each method of background estimation.

The first method considers that the flux is equivalent for all pointing angles and composes of a weighted mean flux. The intensity in this method varies with attitude and altitude [36]. The flux consists of three components: The diffuse gamma ray component described in the previous section, the secondary gamma rays produced by interactions with the spacecraft and the secondary albedo atmospheric gamma rays. The material compositions of the atmosphere and the spacecraft will clearly be different but at gamma ray energies the interactions of Cosmic Rays can be considered to be material independent. The spectra is defined by equation 3.10 measured in $(Photons\,cm^{-2}\,s^{-1}\,sr^{-1}\,MeV^{-1})$ and averaged over all pointing angles for a 28°, 400 km orbit. The origin of these spectra will become clear during the presentation of the fully non-empirical method.

$$\begin{aligned} \frac{dI(E)}{dE} &= 0.36.E^{-1.39} \quad (< 4MeV) \\ \frac{dI(E)}{dE} &= 0.89.E^{-2.05} \quad (> 4MeV) \end{aligned} \tag{3.10}$$

Table 3.2: **Table of scaling factors of secondary particles and gamma rays adapted from (Gehrels, 1992).**

Inclination [deg]	Altitude [km]	M_R $[MeV^{0.7}$ $cm^{-2}s^{-1}]$	$\frac{M_R}{M_{R(28deg,400km)}}$	Effective cutoff [GeV]
Palestine	40	162.0	1.656	3.6
Alice Springs	40	116.0	1.186	6.6
5	300	77.3	0.790	12.2
	400	79.2	0.810	11.8
	500	81.1	0.829	11.4
12	500	83.7	0.855	10.9
18	500	87.8	0.898	10.2
23	400	90.7	0.927	9.7
28	300	95.7	0.979	9.0
	400	97.8	1.000	8.7
	500	99.9	1.021	8.4
44	500	137.0	1.401	4.9
Outside magnetosphere		319.4	3.266	

These spectra can be scaled by considering how the secondary gamma ray flux varies with the low energy threshold for different positions within the atmosphere. This has already been approached in the section on the delayed self-radiating component to the background. Equation 3.6 can be used due to the material independent nature of the interactions. Though here extra generalisations are being included i.e. that the flux emitted from every part of the atmosphere scales by the same amount as that of the position of the spacecraft. This kind of generalisation may or may not be suitable to the background calculation in question.

So by considering the parameter, F_s, the sample spectra for an inclination of 28^o and an altitude of 400 km can be scaled by the factors presented in table 3.2.

This method for estimating the albedo gamma ray flux experienced by the spacecraft does not include pointing angle dependency, uses a reasoned approximation to scale the flux to the required orbit and, in contrast to the other methods described in this chapter, it adds an empirical element to the simulation.

The second method, the integrated emissivity model, was first presented by [25] and involves integrating the emissivity of each element of the atmosphere over the visible atmosphere with respect to the intrinsic atmospheric absorption between the element in question and the spacecraft. The previous method described used this to calculate the angle-averaged spectrum. The method will be briefly reviewed and suggestions made to remove the empirical element to it.

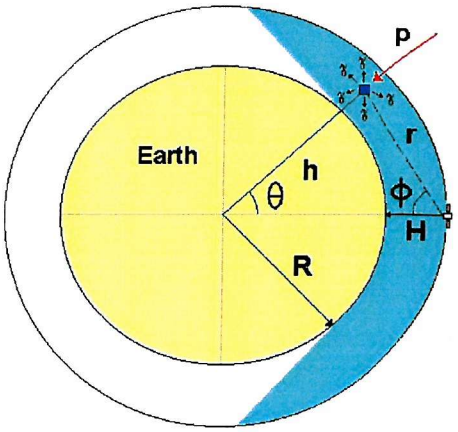

Figure 3.13: **A volume element of the visible atmosphere emits gamma rays induced by a Cosmic Ray interaction.** **R** *is the Earth's radius,* **H** *the altitude of the spacecraft,* **h** *the height of the volume element,* **r** *the distance to the spacecraft from the volume element along the line-of-sight defined by* ϕ.

This method considers the volume of visible atmosphere as shown in figure 3.13. Equation 3.11 calculates the total vertical component of the gamma ray albedo flux incident on the spacecraft.

$$dI_\gamma\left(E_\gamma\right) dE_\gamma = \int_{atmos} \frac{2\pi h\, sin\theta\, \rho\left(h\right)\, \epsilon\left(E_\gamma, h\right)\, h^2\, cos\phi}{4\pi r^2} e^{-\mu(E_\gamma)\int_r \rho(r)dr} d\theta dh \qquad (3.11)$$

The emissivity function used in equation 3.11 was obtained from balloon flight measurements (h, r, θ and ϕ are defined in figure 3.13. ρ(h) and ρ(r) are the air density functions in the directions of h and r. $\mu\left(E_\gamma\right)$ is the air-mass attenuation co-efficient. $\epsilon\left[E_\gamma, h\right]$ is the emissivity function).

[100, 99] expressed the spectral intensity in terms of atmospheric depth, χ_o (measured in $g.cm^{-2}$ from 1-20 MeV above Palestine, Texas, USA at a float altitude of $2.5 g.cm^{-2}$), as shown in equations 3.12. This relation agreed with several other balloon flights [25]. This formed the basis for the emissivity function, equation 3.13.

$$\frac{dI\left(E_\gamma\right)}{dE_\gamma} = 0.535\, \chi_o\, E^{-1.65} \quad \left(ph\, cm^{-2}\, s^{-1}\, keV^{-1}\, sr^{-1}\right) \qquad (3.12)$$

$$\epsilon\left[E_\gamma, \chi\right] = 0.75\, \chi^{0.51}\, E_\gamma^{-\left(1.65+2.56\,.10^{-2}\,\chi^{0.50}\right)} \quad \left(ph\, s^{-1}\, keV^{-1}\, g^{-1}\right) \qquad (3.13)$$

This method of determining the atmospheric component of the gamma ray background can only be considered to be marginally non-empirical due to the origin

of the emissivity function. For a truly non-empirical method (excluding the measurements of the Cosmic Ray spectra) a model for the rigidity as seen in figure 3.3 must be included. The emissivity of a volume element will not follow the relation of equation 3.13 for each latitude due to the non-spherical nature of the Earth's magnetic field, though may be a suitable approximation for some cases. The input Cosmic Ray spectrum will vary for volumes of equal altitude but different latitudes. The effects of rigidity and how to deal with it have been covered and by using a full model of the magnetic field around the Earth a fully non-empirical simulation can be achieved. **L**, can be calculated for each interacting volume of atmosphere. Therefore the emitted spectra from each incremental volume can be determined and convolved to obtain a fully directional dependent and orbital dynamic model of the atmospheric albedo gamma ray background. However, the complexities of this method have been outlined in the section on the primary effects of Cosmic Rays and the difficulties will be amplified for the determination of the albedo gamma ray component due to the inclusion of every element of visible atmosphere. The background estimation, considering the overall aims, could benefit from some of the generalisations also outlined in the previous section.

The other non-empirical aspect to this estimation is the scaling of the flux with the weighting M_R. With the invention of faster computers, the need for this scaling will hold less importance. The background can be re-calculated for various latitudes and altitudes and, using interpolation, the dynamic background variation can be produced without the need for an empirical scaling.

Depending on the accuracy required in the background estimation, several approaches have been discussed. Various aspects to estimating the rigidity at various points within the magnetosphere may turn out to be irrelevant to the albedo gamma ray contribution. However these rigidity considerations will be important in estimating the direct cosmic-ray interactions with the spacecraft and so need to be considered in that context at least. Concurrently aspects discussed with relation to the hadron induced background may be relevant to the atmospheric albedo component.

An interesting factor that could apply is the effect the moon has on the atmosphere. As the seas on Earth are effected tidally by the orbit of the moon the closer and less dense fluid of the Earths atmosphere will also be effected tidally. This effect is seen in the form of pressure variations at the surface and extension of the upper atmosphere. However this effect is small in comparison to the total depth of the atmosphere (about 6%) [111] and so any increase in albedo flux is expected to be small and, as yet, undetermined. Another consideration that may prove significant in future missions is the albedo flux of Cosmic Rays interacting, not with the atmosphere of the Earth but with the Sun's corona. An estimation of this flux is $5.0.10^{-8}\, photons\, cm^{-2}\, s^{-1}$ (E > 100 MeV, at a distance of 1 AU, non-flaring) [103]. This flux should be observable by EGRET but should really be considered as an interfering source rather than a source of background.

3.3 Summary of Background Sources

A gamma ray instrument is susceptible to many sources of background with many different origins. The degree by which each source effects the sensitivity of the instrument varies, primarily, with the orbit or trajectory of the mission. All known causes to the gamma ray background have been covered and only by careful simulation can an evaluation of each componentbe achieved. With the knowledge of how each component of the background behaves, the sensitivity of the instrument can be maximised.

Chapter 4

Mass Modelling

4.1 Introduction

The first mass models were a tool to evaluate the total mass of a space mission. These models calculated the mass of the each of the components of a space mission and by combining the mass of each component calculated the mass of the entire payload. This was done by constructing a geometrical sequence of simple shapes combined with the material properties that represented each component. As the models developed, additional information could be gleaned. The construction of a spacecrafts geometry into a list of simple shapes was then combined with coupled electron and photon shower code developed for Monte Carlo simulations. The first Monte Carlo technique to study shower propagation was employed by Wilson (1952). Each photons *"fate in passing through a given interval was decided by spinning a wheel of chance; the fate being read from one of a family of curves drawn on a cylinder"* [130]. This rather tedious method was computationally developed further in the 1960s. CERN, the originators of the GEANT collaboration developed the standard shower code to include all aspects of photon, lepton and hadron interaction. The GEANT development's aim was to reproduce the interactions of all the particles and photons in their accelerators to envisage the performance of their equipment during the design stage. The subtlety of the physics included increases with every development step. The basic Monte Carlo technique remains but with the ever increasing capabilities of computer processors mean that the intricate tracking of each photon and particle can be maintained to a very detailed level.

Whether the mission is in the design stage, in calibration, in orbit or in post-mission data analysis, a mass model is a vital tool for gamma ray missions. The basic principle of it is to simulate a set of individual volumes that when assembled together match the technical designs of the instrument. Each volume includes information on the material composition and density. The simulated path of a photon or charged particle is tracked through these volumes and the energy deposits in any "sensitive" volumes can be recorded. The paths are simulated for as many photons and charged particles (including secondary particles) that the instrument experi-

ences in orbit, or at least enough to minimise the statistical errors. The summation of the individual energy deposits will give the total counts in the detector within the modelled environment. The shower code developed by CERN was to be run millions of times to reproduce the required flux within a mass model. The level of detail available to the project scientist is almost limitless. Every aspect of every shower can be recorded but with the obvious trade-off with the size of the end product data file. The usual method is to compile a list of events with as much information on the path and products of that event as is practical. It is not worth recording a photon that simply misses the apparatus. This list of "successful" events can then be filtered and compiled into a histogram to produce a spectrum of all energy deposits within a detector.

For activation studies the isotopic production rates can also be calculated for each volume within the geometry. A period of exposure to the cosmic radiation in space activates isotopes into states that will decay. Interactions of the incident Cosmic Rays with nuclei in the model are recorded. This enables the isotope production rates to be calculated. After a specific time of activation the decay rates of each isotope can then be extrapolated. A simulation is then run to reproduce the decay for each of these isotopes. These decay products are simulated as a secondary Monte Carlo simulation. The tracking will be the same to that of any other particle or photon but will originate in the component volume that was initially activated.

This Monte Carlo approach is based on pure physics and can predict the performance of any gamma ray instrument. Only two aspects of this process is based on empirical data. The first is the measurement of the radiation environment that the instrument will encounter. The spectrum of Cosmic Diffuse X-rays (CDX), Cosmic Rays or gamma ray photons produced by our atmosphere, determines the energy distribution of the input flux. For a diffuse flux each particle or photon will be fired into the model from a random point and with a random momentum vector.

The second aspect of mass modelling that is empirical in nature is the nuclear data such as cross-sections and information on isotope decay. This large amount of information is vital to determining the behaviour of the nuclear interactions and decays. If both of these aspects are well defined then the system can be relied upon. However, a missing cross-section could have disastrous consequences should that material be prevalent in the model. Concurrently, should the spectrum of the input flux be inaccurate then the results of the simulation will simply re-process this inaccuracy, possibly magnifying it to a level that would render the mass model redundant. Both of these empirical aspects need to be continually considered as they can provide limitations to the scope of any investigation.

Future development in the field of these Monte Carlo simulations includes producing a suite of software that provides all aspects of photon and particle transport at energies extending down to the optical behaviour of X-rays. The focus of the next generation of GEANT software is to include the performance of the electronic

signal processing as well as the detector physics involved, though every aspect can be selected at will. Modern applications of this photon and particle transport software range from QCD and quark physics to determining the response of focussed X-ray instruments.

The applications in gamma ray astronomy of this mass modelling approach are many. The background in an instrument can be predicted temporally, spectrally and spatially. This leads to the calculation of sensitivity, telemetry rates and efficiency but can also be employed to evaluate consequences of spacecraft design. Shield design, calibration support, burst self-contamination, long term activation, trigger effects, structural shadows and radiation damage estimation are all aspects to evaluating an instruments design with mass modelling. Each model can be tailored to the requirements of the mission concerned. The level of detail within a model will vary depending on the accuracy required and the spatial extent of the instrument.

This chapter will describe the software suite employed by this technique, investigate some isotropy and homogeniety considerations that are vital to any simulation and present a test case to illustrate the use of the GGOD software suite.

4.2 The GGOD Software Suite

The software suite is being continually developed by the gamma ray astronomy group in Southampton. The software is based on the GEANT software developed at CERN to assess the performance of the particle physics experiments there. The suite of software incorporates GEANT, GCALOR, ORIHET and DECAY and has the acronym GGOD. GGOD's Monte Carlo code provides the most comprehensive simulations of particle transport in matter. Through the combination of these four main software packages, GGOD is ideal for the simulation of space environments. The packages incorporated into GGOD are listed in table 4.1. Figure 4.1 shows how the packages link together. The mission specific input parameters are the instruments geometry, the radiation environment and history. The instrument geometry can be obtained from technical drawings with the level of detail being approximated suitably to give the most efficient simulation. The radiation environment can be obtained by considering all the forms of background described in chapter 2, in relation to the spacecrafts orbit. The radiation history is dependent on what the aims of the simulation are but generally includes passages through the SAA and the time the instrument has experienced irradiation.

4.3 Isotropy and Homogeneity

One consideration to the simulation is a mathematical one. Each photon or particle to be simulated has to have a starting point and initial momentum vector. These are chosen at random and are distributed over an imaginary surface that surrounds the geometry for the prompt background simulations. The aim is to achieve truly

Table 4.1: **The component development of GGOD.**

Package	Developed by	Deals with
GEANT	CERN	photon and electron transport (> 10 keV)
GCALOR	ORNL	
- HETC		charged hadron transport (< 10 GeV)
- FLUKA		hadron fragmentation
- MICAP		neutron transport (< 20 MeV)
ORIHET	ORNL, RAL and S'ton	induced radioactivity
DECAY	S'ton	isotope decay

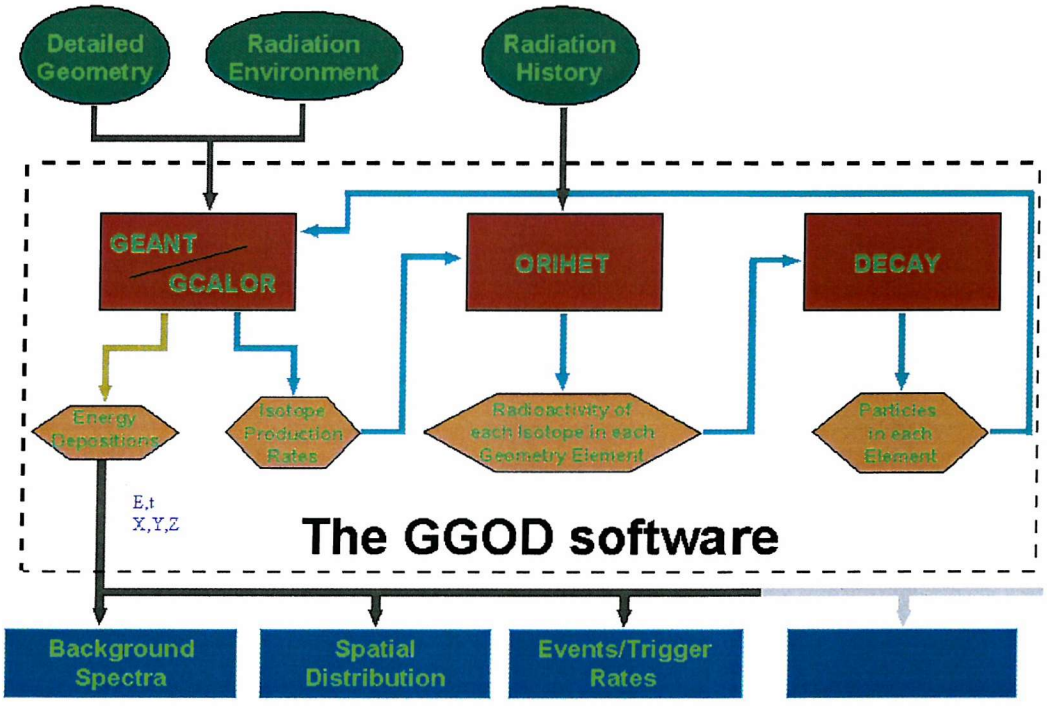

Figure 4.1: **The GGOD data flow.** *The GEANT/GCALOR packages track photons and particles. The energy deposits and isotope production rates are stored. ORIHET calculated the decay rates after a given time and DECAY generates the photons and particles that result from each isotopes' decay process. These particles and photons are fed into GEANT/GCALOR for tracking. The input parameters are the instrument geometry, the environment and the radiation history.*

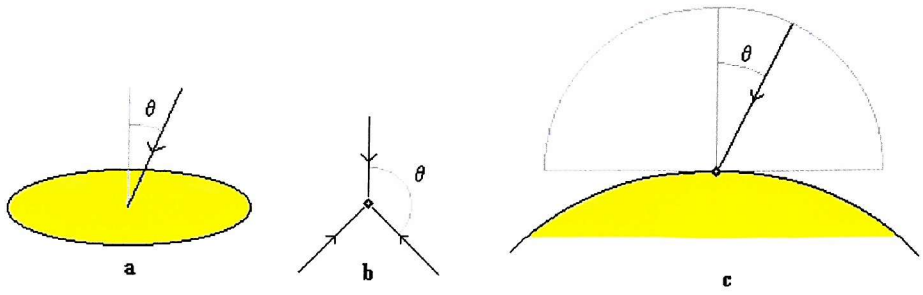

Figure 4.2: **The solid angle projection of various surfaces. a)** *A flat plane, solid angle* π. **b)** *A single point, solid angle* 4π. **c)** *A spherical surface, solid angle* 2π.

homogeneous and isotropic flux from the simulation. The larger the virtual surface, the more photons or particles that require tracking. This was a definite factor in the earlier days of mass modelling but with the advent of increasingly cheaper and more powerful computers, the running time of the simulations need not be such an important factor and the accuracy can be studied closely. The INTEGRAL Mass Model (TIMM) was one of the first missions to be simulated and the computational efficiency was paramount. For these simulations a virtual cylinder was chosen to fire in the particles and photons. The logical choice would be a sphere but a sphere would require a much longer simulation, at the conceptual stage of TIMM. However, now computer power has caught up with the requirements, alternative surfaces to the cylinder can be considered.

The aim of this section is to investigate the properties of the sphere to see if it matches all the requirements for a Mass Model simulation. Now that a sphere is just as practical, in terms of computing power, both surfaces were investigated to see if the requirements are better matched by a sphere than by using a cylinder. This problem will develop into a complex problem and so, for the sake of a thourough explanation of the methodology, will be approached very much in the *spirit of the layman.* Heed must be taken that some of the initial assumptions will not become apparently incorrect until the end of the discussion.

When selecting the starting position and direction of the photon to be simulated the starting position can be easily determined randomly. Alongside the position the momentum vector needs to be considered more carefully so that the surface correctly represents the flux that would pass through it. The differential spectra of the background to be simulated includes a solid angle proportionality (sr^{-1}). The total solid angle observed by a plane, a point and a spherical surface are calculated in equations 4.1, 4.2 and 4.3 and are all different. The solid angle that a surface observes determines the angular distribution of the input flux. Figure 4.2 shows these projections.

$$\Omega = \int_0^{\frac{\pi}{2}} 2\pi \, sin\theta \, cos\theta \, d\theta = \int_0^{2\pi} \pi \, sin2\theta \, d\theta = \pi \tag{4.1}$$

$$\Omega = \int_0^{\pi} 2\pi \, sin\theta \, d\theta = 4\pi \tag{4.2}$$

$$\Omega = \int_0^{\frac{\pi}{2}} 2\pi \, sin\theta \, d\theta = 2\pi \tag{4.3}$$

For a momentum vector to be selected at random these relations need to be adjusted to a linear function in terms of the angle from the normal, θ. This can be done for any function using equation 4.4, $f(x)$ is a function, the probability that $f(x)$ is between x_1 and x_2 is equal to 1.

$$P_{linear}(X) = \frac{\int_{x_1}^{X} f(x)\,dx}{\int_{x_1}^{x_2} f(x)\,dx} \tag{4.4}$$

Via substitution, equations 4.5 and 4.6 show the linear distributions of θ for a cylinder and sphere respectively.

$$P_{\theta_{cyl}} = \frac{\int_0^{\theta_{cyl}} 2\pi \, sin\theta_{cyl} \, cos\theta_{cyl} \, d\theta_{cyl}}{\int_0^{\frac{\pi}{2}} 2\pi \, sin\theta_{cyl} \, cos\theta_{cyl} \, d\theta_{cyl}}$$

$$P_{\theta_{cyl}} = \frac{1}{2}\left(1 - cos2\theta_{cyl}\right)$$

$$Random_{0\to1} = \frac{1}{2}\left(1 - cos\,2\theta_{cyl}\right)$$

$$\theta_{cyl} = Asin\sqrt{Random_{0\to1}} \tag{4.5}$$

$$P_{\theta_{sph}} = \frac{\int_0^{\theta_{sph}} 2\pi \, sin\theta_{sph} \, d\theta_{sph}}{\int_0^{\frac{\pi}{2}} 2\pi \, sin\theta_{sph} \, d\theta_{sph}}$$

$$P_{\theta_{sph}} = \frac{1}{2}\left(1 - cos\theta_{sph}\right)$$

$$Random_{0\to1} = \frac{1}{2}\left(1 - cos\theta_{sph}\right)$$

$$\theta_{sph} = Acos\left(1 - 2\,Random_{0\to1}\right) \tag{4.6}$$

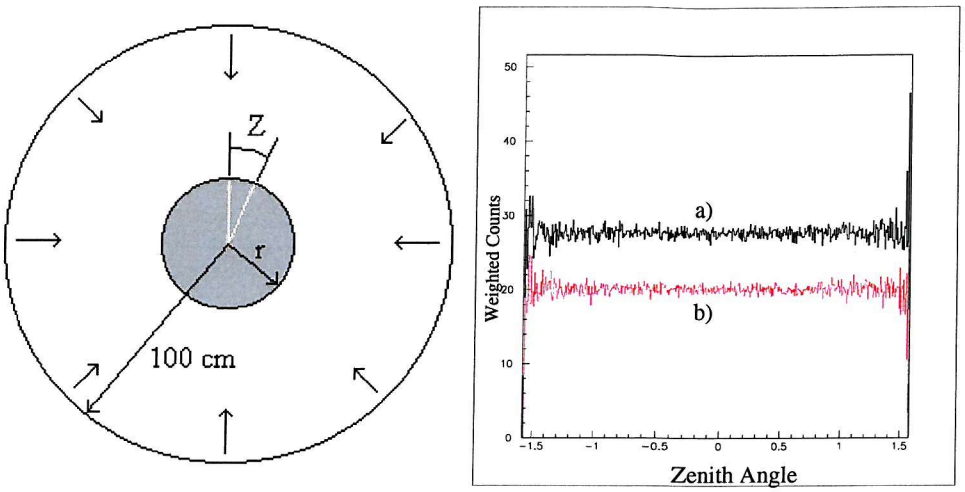

Figure 4.3: **Isotropy evaluation of the sphere**. *This plot shows the weighted counts against the zenith angle. The counts hold the relative weight of* $\frac{1}{cos(z)}$. *It shows the distribution for different sizes of detector sphere;* **a)** $r = 99$ *cm* **b)** $r = 90$ *cm.*

These two distributions of θ are a direct result of the shape of the input surface and so the solid angle that the surface observes. The first test to be performed on these two surfaces was the measurement of the isotropy at the centre of the virtual surface. Through basic Monte Carlo simulations, the flux was shown to be isotropic for both the cylinder and the sphere. Figures 4.3 and 4.4 demonstrate the central isotropy of the sphere and the cylinder respectively.

The sphere and cylinder perform as expected with respect to central isotropy but the isotropy of each surface needs to be considered when an instrument is off-centre. So, the second test that was performed was to measure the off-centre isotropy. The cylinder was tested using a simple collimated detector and was shown to receive constant flux when rotating the instrument from an off-centre position (both off and on the cylindrical axis). Figure 4.5 shows the invariant flux when the detector is rotated off centre and off axis.

The isotropy of the sphere is not as clear in this case as it is with the cylinder. The collimated detector used to evaluate the cylinder's off-centre isotropy. This showed anisotropy but could only be quantified by many simulations. So to minimise the computing time a more analytical method was employed. Instead of using the the simple collimated detector a sphere of lead was simulated with various radii and various off centre positions. This lead sphere was sensitive to all photons simulated and recorded the direction it came from and the initial position on the input sphere. The parameters of this sphere were the radius, **r'**, and the off-centre distance, **r**. The flux was seen to be anisotropic under certain circumstances. Figure 4.6 shows exactly what was recorded during simulations and figure 4.7 shows the anisotropy. Plots **a)** and **b)** show distributions as expected but the real anisotropy is shown

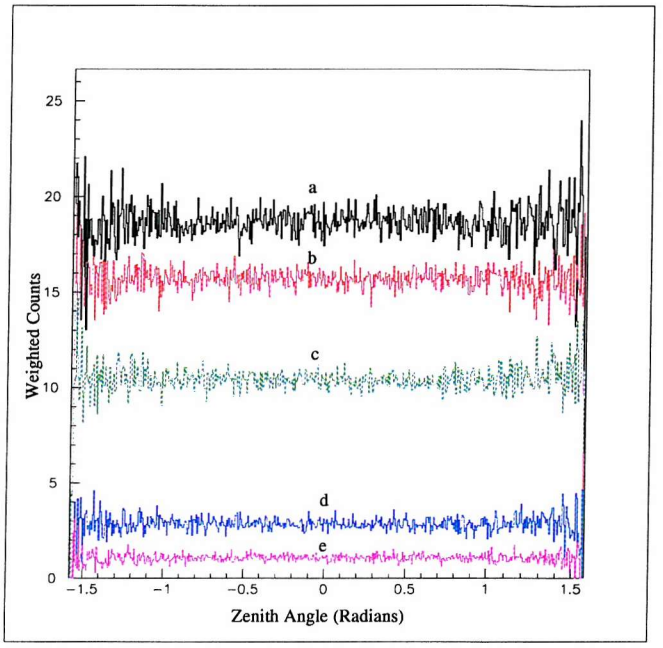

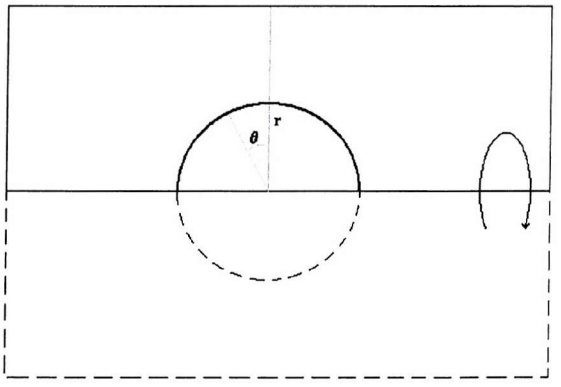

Figure 4.4: **Isotropy evaluation of the cylinder.** *The graph above shows the weighted counts against the zenith angle. The counts are weighted according to the area that a small increment $\delta\ \theta$ will project on the surface of the sphere at a particular zenith angle. Therefore each count will hold a relative weight of $\frac{1}{cos(\theta)}$. The diagram below shows the cylindrical dependence of the graph. All five lines show isotropy.* **a)** *r=74 cm (Cylinder radius = 100, height = 150),* **b)** *r=99 cm (Cylinder radius = 100, height = 300),* **c)** *r=99 cm (Cylinder radius = 100, height = 500),* **d)** *r=50 cm (Cylinder radius = 100, height = 1000),* **e)** *r=50 cm (Cylinder radius = 500, height = 100).*

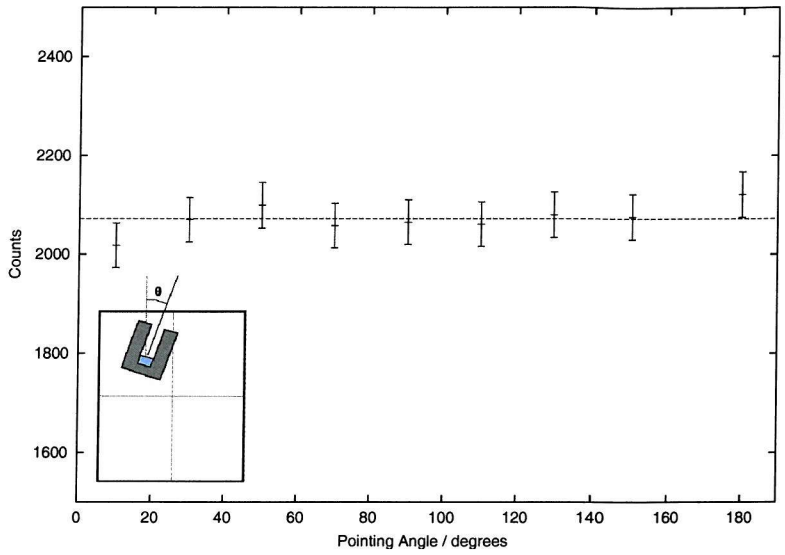

Figure 4.5: **The variation for off-centre scanning through the pointing angle for a cylinder.** *The counts do not vary outside the Poisson statistics. The simple collimated detector was moved 64cm off centre while the cylinder radius remained at 100cm.*

in plot **d)**. The counts received should be evenly distributed across ϕ. This non-uniformity can be measured using the χ^2 statistic. χ^2 rises sharply in relation to the values of **r** and **r'**. The ratio between these two parameters and the radius of the virtual sphere **R** can determine the validity of using a sphere as an input surface. Figure 4.8 shows the parametrical extent to which the sphere can be considered to supply isotropic flux in the context of The INTEGRAL Mass Model (TIMM) [26].

So the second test has shown that a sphere cannot be assumed to be isotropic and only quasi-isotropic when $\frac{r}{R} + \frac{r'}{R} < 0.8$. Indeed as further mathematical proof of a sphere's inadequacy; if the flux was to be integrated to obtain the total counts

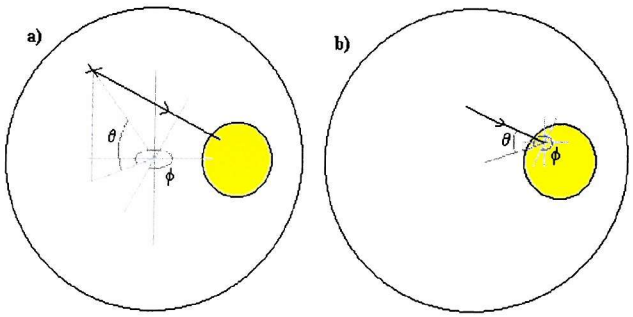

Figure 4.6: **Sphere isotropy evaluation.** *The sphere detects all photons arriving at its surface. The detector itself records* **a)** *the position on the input surface from which the photon is initiated and* **b)** *the direction from which the photon arrives.*

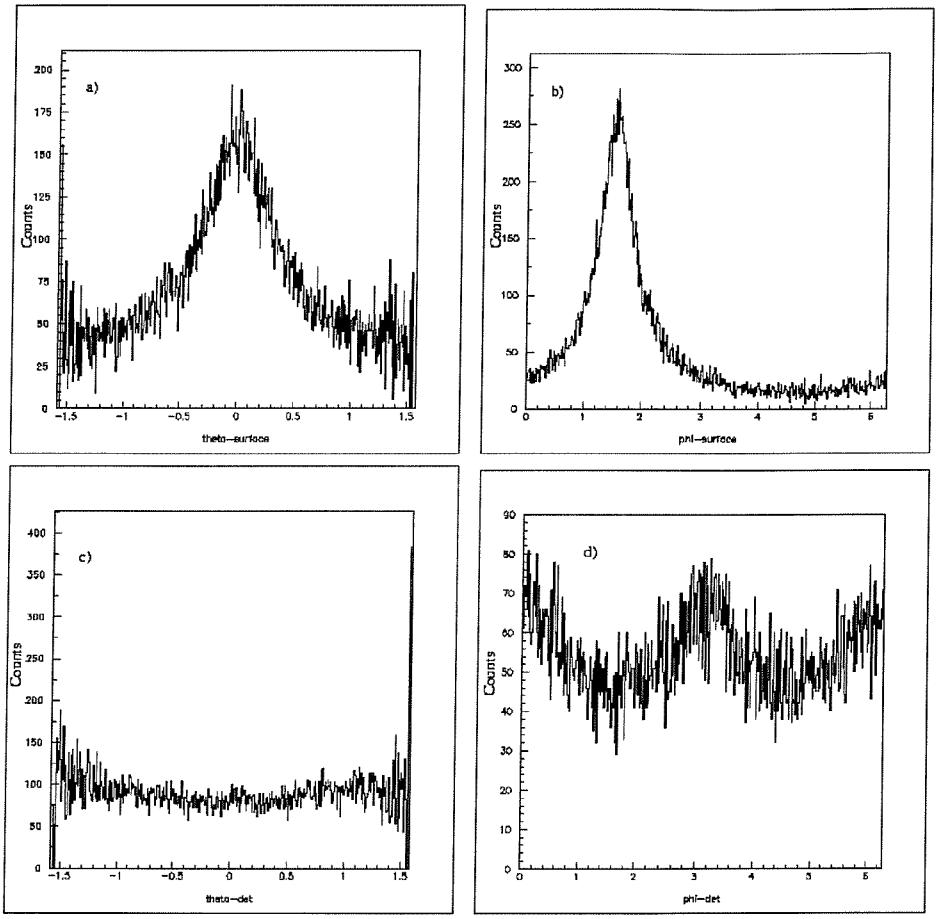

Figure 4.7: **Off-axis simulations of a sphere.** *An example of the anisotropy experiences from using a sphere as an input surface to a mass model simulation. The parameters are:* **R** *= 100cm,* **r** *= 75cm,* **r'** *= 20cm.* **a)** *and* **b)** *show the counts received from points on the input sphere, θ and ϕ.* **c)** *and* **d)** *show the counts received from the directions described by θ and ϕ.*

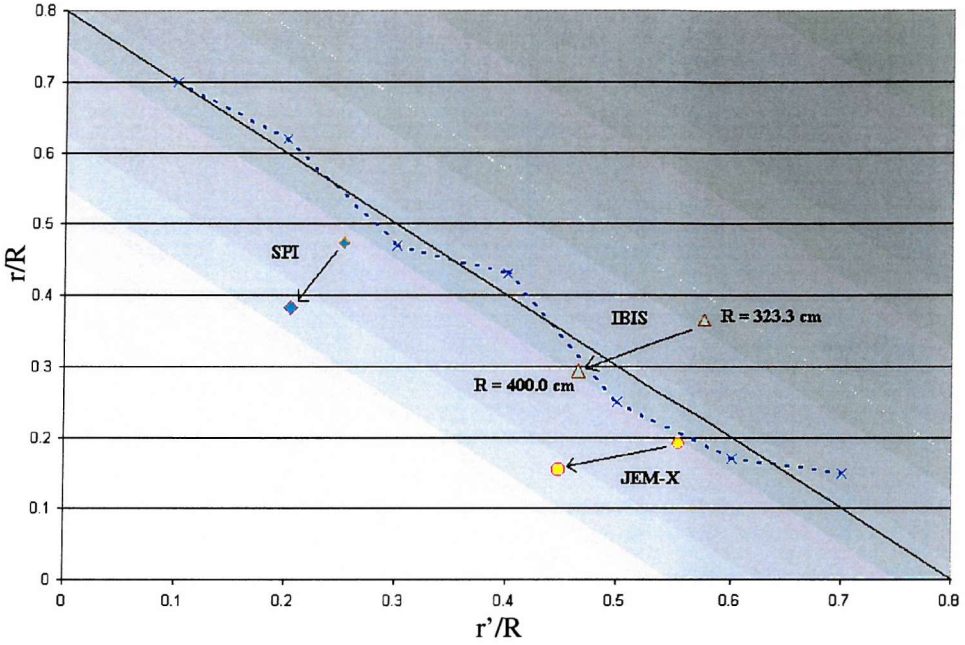

Figure 4.8: χ^2 **deduced limitations.** *This graph shows the extent to which a specific simulation can be considered to be isotropic. The dashed lines connect the data points. Any simulation which employs a geometry below the line will supply an isotropic flux, within the statistical limits.* **R** *is the radius of the input sphere,* **r** *is the off-centre distance of the simulated detector and* **r'** *is the radius of the sphere encompassing the detector to be simulated. Also shown on this plot are the relevant TIMM characteristics. Note that for IBIS, using a sphere just encompassing the model would not supply an isotropic flux to the detector where JEM-X and SPI would be simulated accurately within the limits of the spheres isotropy.*

passing through a small volume at a point **r** from the centre, the expression would still contain the **r** parameter and so cannot be considered to be homogeneous either. Equation 4.7 shows this evidence of inhomogeniety, where *da* is a surface area element.

$$\begin{aligned} F_p &= \int_{All\ sources\ on\ surface} \frac{Luminosity\ of\ source}{4\pi x^2} \\ dF_p &= \frac{L\,da}{4\pi x^2} \\ dF_p &= \frac{L\,R^2\,d\theta\,d\phi}{4\pi x^2} \end{aligned}$$

$$dF_p = \frac{L\,R^2\,d\theta\,d\phi}{4\pi\left(\frac{R^2r+r^3-5r^2R\,Cos\theta+2R^2Cos^2\theta\,r\,Sin\phi-R^3Cos\theta+2r^2R\,Cos\theta\,Sin\phi}{r-R\,Cos\theta}\right)} \tag{4.7}$$

At this stage it is clear that the sphere, as it is, will not perform to the simulations requirements. However, it is possible to apply some mathematical corrections to compensate for this inhomogeniety. The homogeniety of the system was then investigated for the sphere and cylinder. To investigate the effect of homogeneity, 10^6 simulated photons were simulated and were incident on a spherical detector. This spherical detector had a variable radius, **r**. The detector surface count density should scale with r^2 for homogeneous flux for any surface.

Figure 4.9 shows the variation in the flux surface density of the detector sphere as **r** varies. The input sphere clearly does not follow constant flux density whereas an input cylinder or cube does. The input sphere follows the variation defined by the solid angle that the detector sphere presents to each point on the surface of the input sphere. This variation is defined by equation 4.8.

$$Flux = Flux_{input}\,\frac{\Omega}{2\pi} = Flux_{input}\,\left[1 - cos\left(Asin\frac{r}{R}\right)\right] \tag{4.8}$$

The homogeneity and isotropy of an input surface is determined by the distribution of θ_{sph} (eqn. 4.6). If this equation was deduced from the assumption that the surface density of an internal sphere was constant, independent of **r**, then homogeneity could be achieved. This would cause the count-rate from a spherical input surface to follow the theoretical r^2 relationship as displayed in figure 4.9. This calculation is described in equation 4.9 and can be tested accordingly. The calculation considers that every point on a sphere is identical. The parameters of the calculation are shown in figure 4.9.

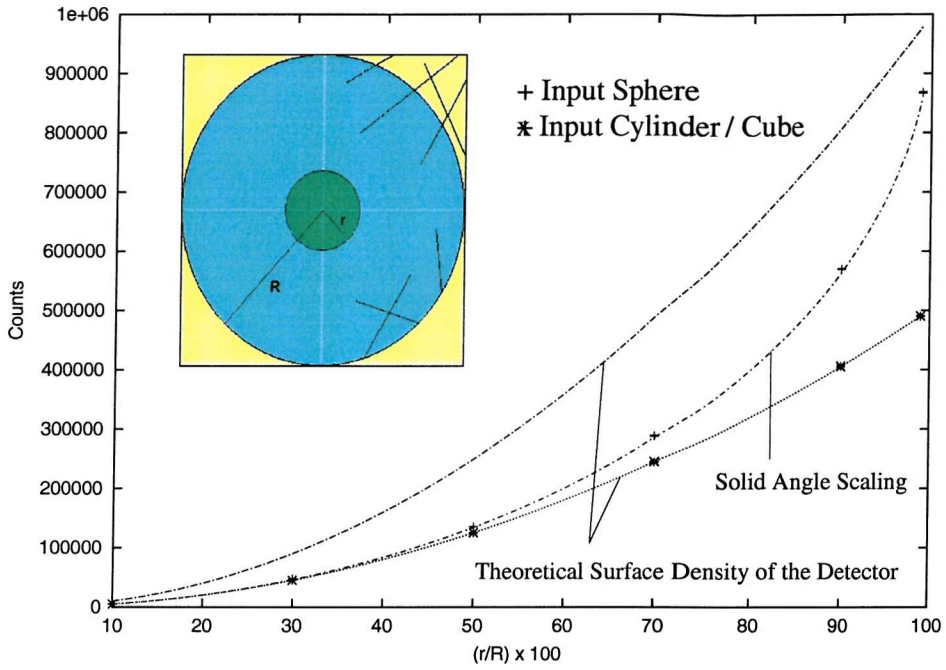

Figure 4.9: **Flux surface density variations of a simple spherical detector.** *This plot demonstrates the homogeneity of the two input spheres. The dotted line and the dot-longdash line shows the flux density that the detector sphere should experience when using the two input surfaces. The dot-dash line is due to the variation in the solid angle that the detector sphere presents. It is clear that an input cylinder (or cube, it was also simulated) gives the correct homogeneous flux whereas a sphere does not follow a constant flux density. The flux density for an input sphere follows the solid angle scaling presented in equation 4.8.*

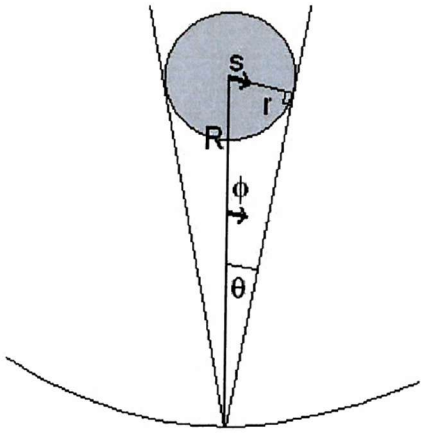

Figure 4.10: **The parameterisation of the homogenity scaling for an input sphere.**

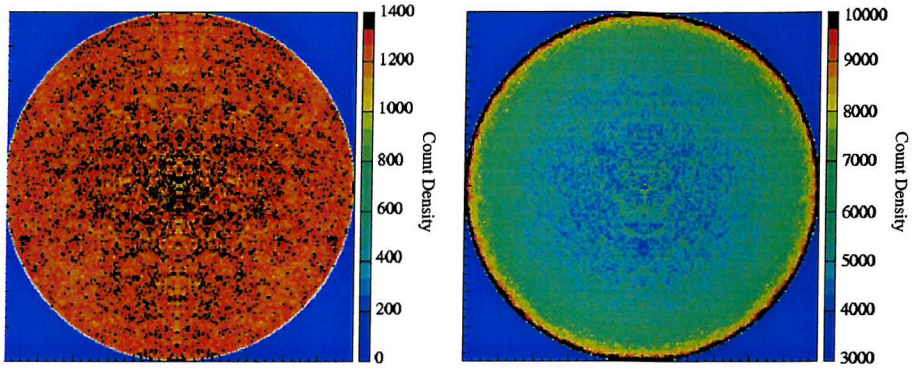

Figure 4.11: **Sphere input surface homogeneity evaluation.** *The count density plot to the left has the input angle distribution in equation 4.9. The count density plot to the right has the input angle distribution as described by the presented solid angle and can be seen in equation 4.6.*

$$P_{photon\ hits\ inner\ sphere} = P(\theta) = \frac{\int_0^\theta p(\phi)\ d\phi}{\int_0^{\frac{\pi}{2}} p(\phi)\ d\phi}$$

$$\int_0^\theta p(\phi)\ d\phi = \int_0^r f(s)\ \frac{ds}{\sqrt{R^2 - s^2}}$$

$$\int_0^r f(s)\ \frac{ds}{\sqrt{R^2 - s^2}} = I\ 4\pi s^2\ 2\pi = A\ s^2 \quad {\scriptstyle (A=I\ 4\pi 2\pi)}$$

$$\int_0^r f'(s)\ ds = As^2$$

$$f'(s) = 2As\ \ ;\ \ f(s) = 2As\sqrt{R^2 - s^2}$$

$$\int_0^\theta p(\phi)\ d\phi = \int_0^r 2As\ ds = \int_0^\theta 2A\ Rsin\phi\ Rcos\phi\ d\phi$$

$$P(\theta) = \frac{\int_0^\theta sin\phi\ cos\phi\ d\phi}{\int_0^{\frac{\pi}{2}} sin\phi\ cos\phi\ d\phi} = 1 - cos^2\theta$$

$$\theta_{sph} = Acos\sqrt{1 - Random_{0\to1}} = Asin\sqrt{Random_{0\to1}} \tag{4.9}$$

Equation 4.9 gives the same relation as equation 4.5, the equation for the distribution of the input angle for the cylinder (or any plane surface). This approach suggestes that an element on the surface of the sphere can be considered to be a flat surface. Figure 4.11 shows a 2D representation of the count density within a sphere. Shown are the spatial flux densities when using the distributions of the input angle that is derived from either homogeniety or from the solid angle projection. The input angle distribution derived from the solid angle projection clearly does not

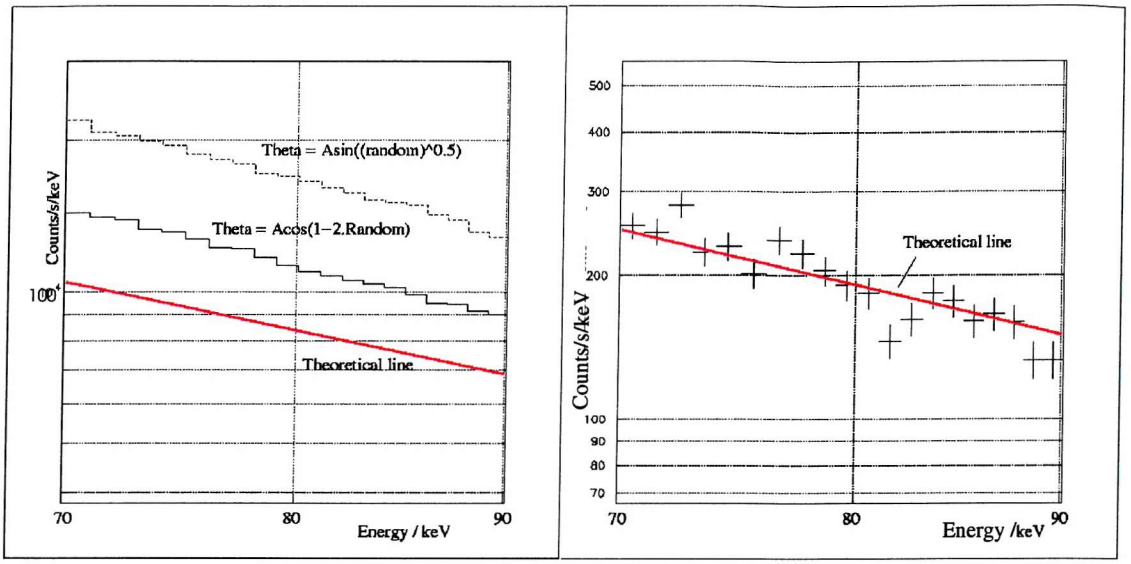

Figure 4.12: **The performance of the true Sphere and Cylinder input surfaces.** *The theoretical number of counts is included on both plots as a red line. The countrates should match this line for an ideal simulation.*

provide homogeniety. The input angle distribution derived from the homogeniety consideration does provide homogenious flux as it stands but, from the initial discussion criteria, suggests that a point on a sphere observes a solid angle as a plane would. This is the point whereby the initial assumtions are shown to be incorrect. The distribution described by equation 4.9 is the correct distibution as an aspect of the integration was not considered in the initial calculations, the function needs to be integrated over an additional azimuthal angle.

The relation seen in equation 4.9 provides homogeneous flux density but this needs to be tested further before any isotropy evaluations can be considered for the input sphere. The context of this investigation is to model gamma ray instruments. For this reason a simple but realistic plane detector was simulated. The count-rate for a plane detector encountering a power law is a simple function of the energy, area, exposure and the solid angle "seen" by the plane (π). Figure 4.12 shows how the two distributions for the sphere performed alongside the cylinder. Also included is the theoretical number of counts that a plane detector would encounter. The plane detector is made of a super-dense material so no photons are transmitted. The number of simulated photons (70-90 keV, power law index = -2.0) was the same for both cases but the surface areas of the input surfaces varied to alter the detected count-rate. Neither input angle distributions for the sphere gave the correct number of counts at the detector plane. The cylinder provides the correct count-rate at the detector plane. The fact that the sphere can supply a homogenious flux distribution but incorrectly predict the count-rate of a simple detector plane suggests that the directions in which the photons are arriving are not isotropic.

4.3.1 Conclusions

Throughout this discussion the virtual cylinder input surface has provided the mass model simulations with all the criteria required of it, isotropy and homogeneity. The sphere has been the surface that as been tested and finally made mathematically consistant in an attempt to provide homogeniety and isotropy. Before this investigation the sphere would be the intuitive choice. The initial decision to select a cylinder was purely a practical one with respect to the geometry and computer power. As is shown here the sphere does not provide the model with its requirements. The tests have included central isotropy, off-axis isotropy, homogeniety and the reproduction of the count-rate in a simple plane detector. The cylinder has passed all these tests.

The possibility in the future of using an input sphere is real but the need to investigate this increasingly complex problem is redundant until the cylinder, or indeed box, fails in the requirements for the model. The cylinder has been used proir to this study with satisfactory results and will continue to be used for the forseeable future.

4.4 Case Study: The SAX WFC and JEM-X

INTEGRAL has two major gamma ray instruments, IBIS and SPI, which are complemented by an X-ray monitor (JEM-X) and a optical camera (OMC). During the development of INTEGRAL the possibility of a replacement for the X-ray monitor, JEM-X, was considered as a contingency plan. The possible replacement was to be an already built, tested and calibrated X-ray camera build as a flight spare for BeppoSAX. The BeppoSAX Wide Field Camera (SAX WFC) operated at similar energies with a wider field of view but with a sensitivity worse than JEM-X. The INTEGRAL Mass Model (TIMM) was employed to assess the performance of the SAX WFC should JEM-X be replaced. A table of the characteristics and considerations in this study can be found in table 4.2.

The plan was to simulate INTEGRAL using The INTEGRAL Mass Model (TIMM) [26] but with the JEM-X geometry replaced with the SAX WFC geometry. All componentes to the background that INTEGRAL is likely to encounter was simulated. These included the Cosmic Diffuse X-ray background, Cosmic Ray interaction and any activation that occurs as a result of irradiation. All effects of due to the Earth's atmospheric albedo gamma radiaiton and any modulation effects of the Earth's magetosphere were ignored due to the highly elliptical orbit of the INTEGRAL satellite. A decision was made, with the aid of these simulations, as to whether JEM-X was to be replaced or not.

4.4.1 JEM-X

JEM-X consists of two identical high pressure imaging micro-strip gas chambers that view the sky through two coded masks located 3.4m above the detectors. The

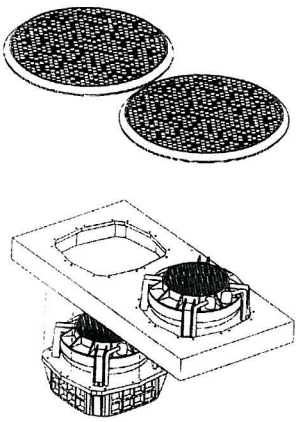

Figure 4.13: **The JEM-X instrument**. *Both detectors are placed next to each other and collimated in parallel. Adapted from internal technical documents.*

angular resolution is determined by the dimensions of the holes in the mask and the separation between the masks and the detector, in this case the angular resolution is 3.35', the best of all the high-energy instruments on INTEGRAL. Figure 4.13 describes the general setup of JEM-X. The detector contains Xenon gas at 5 bar pressure (with CH_4 impurities) which produces an ionisation cloud when a photon is absorbed. The energy and position of this absorption can be determined by the ionisation cloud being amplified and detected at the micro-strip plate. To minimise the detection of cosmic diffuse X-rays through the surrounding collimator an array of 5.7cm high collimators are placed over the detector, though this will unavoidably attenuate the off-axis sources. The fully coded field of view is 4.8° but sources can be observed at angles up to 6.6° off-axis, though the sensitivity will be impaired and the production of ghost-images will become significant. Each of the two detectors have an active area of 491cm^2. The mask is based on a Hexagonal Uniformly Redundant Array (HURA) [42] with a transparency of 25%. The dimension of each cell is 3.3mm (across each face). The mask is made from a 0.5mm thick tungsten plate. The collimator acts to limit the field of view and supports the masks 3.4m above the detectors. The core material of the collimator is molybdenum (180μm) layered with copper (35μm) and aluminium (100μm) respectively, arranged in a graded-Z configuration. This combination of materials acts to limit the K-fluorescence photons produced by the molybdenum and copper. The X-ray window is a 250μm thick beryllium window supported by the collimator structure to resist the internal pressure.

4.4.2 The SAX WFC

The SAX WFC operates on the same principle as the JEM-X detector, using a high pressure gas chamber and a coded mask but is characteristically quite different. The SAX WFC consists of a single detector-mask pairing placed 70cm apart. The mask and detector have sizes of 25.5cm x 25.5cm and 25.6cm x 25.6cm respec-

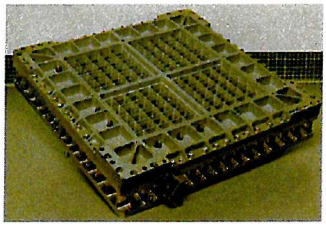

Figure 4.14: **The SAX WFC detector**. *The front view of the WFC detector, clearly visible is the beryllium window support structure.*

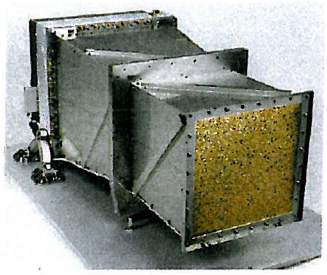

Figure 4.15: **The SAX WFC**. *A photo of the completed "spare" SAX WFC, the other two were launched in 1996 aboard BeppoSAX.*

tively. The detector is a high pressure gas chamber containing 2.2 bar pressure of a xenon/carbon dioxide/helium mix (ratios 0.94/0.05/0.01 respectively). There is no collimator array over the detector as this would limit the field of view, the most important difference between the two X-ray monitors. The sensitive area is 520cm^2 and is divided into a grid of 100 smaller windows. The structure can be seen in figure 4.14. The X-ray window has a 150μm thick beryllium foil covering. The mask contains an array of 256 x 256 elements, 33% of which are transparent to X-rays. The mask pattern is random [42]. The size of each transparent element is 0.9mm (instead of 1.0mm) so as to allow for the grid supporting structure. The collimator structure is divided into two, the structure can be seen in figure 4.15. The field of view of the SAX WFC is only fully coded when sources are viewed on axis. Sensitivity drops off linearly off-axis with a FWHM of 20°. However the random nature of the mask pattern means that ghost images are not a problem when viewing off-axis sources. Ghost images only occur when there is a repeated pattern in the mask but a random mask pattern does not have a perfect autocorrelation function and so produces bumpy sidelobes to an image.

4.4.3 The Mass Model

Most of the parameters for this feasibility study were taken from de Jager (1994) [45]. Any remaining parameters were approximated from photographs and diagrams. The important factors are the size and shape of the collimator and detector and the transparency of the mask. The area of the SAX WFC model that will have the most impact are the finer details of the detector. As much realistic detail as

Table 4.2: **Summary of instrument characteristics for JEM-X and the SAX WFC.** *Adapted from internal INTEGRAL documents and de Jager (1994).*

Instrument	JEM-X	SAX
E range	3-35keV	1.8-28keV
Field of View	4.8° (circ. diam.) Fully Coded	20°x20° (FWHM)
Ang. Resolution	3.35'	5'
Spec. Resolution	19.2% (6keV)	20% (6keV)
Detector gas	Xe (CH_4 impurity)	Xe/CO_2/He (94% Xe)
Mask transparency	25%	33%
Mask cells	Hexagonal 3.3mm diameter	Square 1x1mm
Sensitive area	2 x 491cm^2	520cm^2
Total mass	65.0kg	42.5kg
Mask/detector/FoV shape	Circular	Square
Source location	<20"	<1'
Power required	40.0W	14.1W
Internal pressure	5 bar	2.2 bar
Mask thickness	0.5mm (tungsten)	0.1mm (stainless steel)

possible was included so that the true performance could be estimated well enough for this purpose. Figure 4.16 shows the SAX WFC attached to the top end of IBIS. Compare this to figure 2.12 and the size difference is apparent.

The detectors aboard INTEGRAL were simulated for the equivalent of a 100 second burst of the background, originating from a virtual cylinder just encompassing the geomoetry of INTEGRAL. Four components of the background were considered: The high and low energy cosmic diffuse X-ray; the prompt cosmic ray and the delayed emission resulting from cosmic ray activation. The sum of these can be taken and a sensitivity relation calculated. The highly eccentric orbit meant that no atmospheric albedo radiation needed to be included. The study was carried out assuming that INTEGRAL had been in operation for a year so that any significant activation was also included.

The results of the background simulations can be seen in figure 4.17. The upper region of the sensitive energy range (6-28 keV) is dominated by the cosmic ray background whereas the lower region is dominated by cosmic diffuse X-rays. The simulations were carried out using GEANT 3.2.1 which it must be pointed out is not to be heavily relied upon much below 10 keV. This would have been taken into account if the the SAX WFC had been considered more probable as a replacement for JEM-X. Later versions of GEANT extend well below 10 keV. However as JEM-X and the SAX WFC were simulated as a preliminary comparison to give estimates of sensitivity, this should not be problem.

As the SAX WFC has a much wider field of view than JEM-X the cosmic diffuse

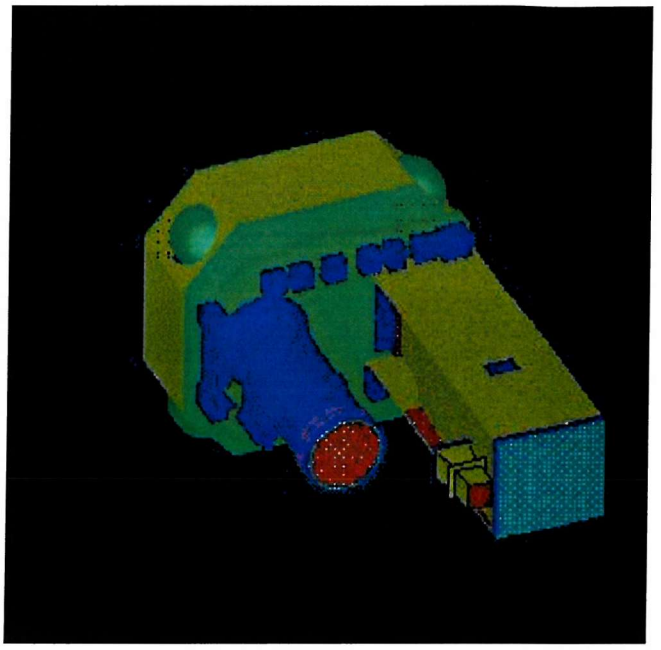

Figure 4.16: **The SAX WFC aboard INTEGRAL.** *The SAX WFC is attached to the top of IBIS and is highlighted by way of a bold outline.*

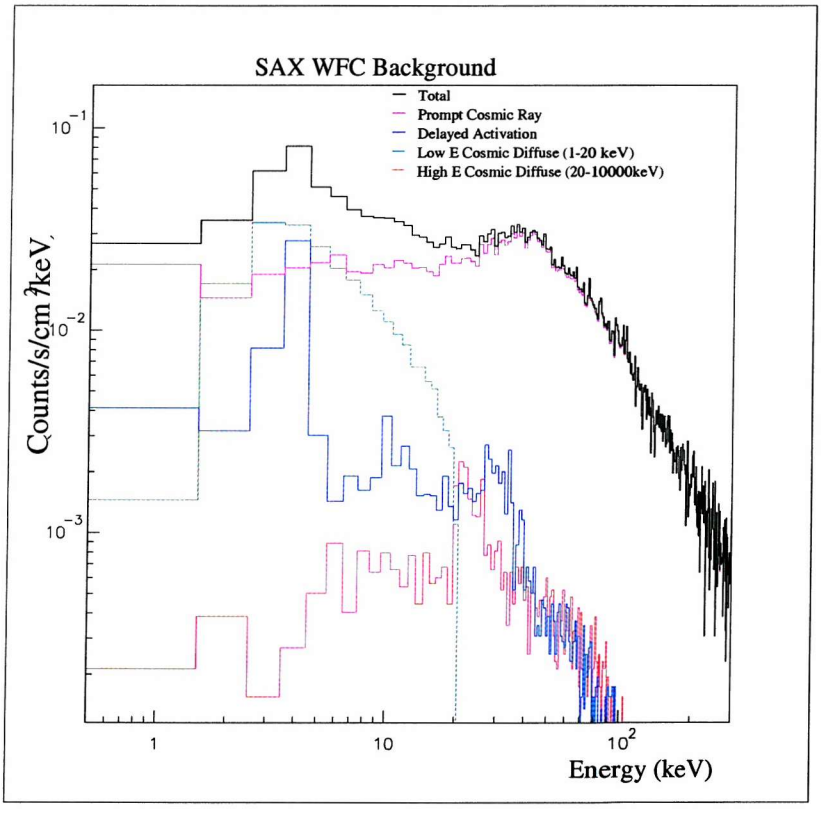

Figure 4.17: **The SAX WFC background aboard INTEGRAL.** *The total and component background count-rates as simulated by TIMM. The low energy region is dominated by cosmic diffuse X-rays.*

X-ray induced counts are expected to dominate the background at low energies, more so than JEM-X. The amount that this component scales up from JEM-X can be estimated using equation 4.10 and is found to correlate with the increase in the simulated background. This estimate of the cosmic diffuse X-ray increase utilises a combination of the ratios of detector efficiency (D), field of view size (S) and mask transparency (M) though the size of the field of view scaling will dominate in this case. The $\frac{\pi}{4}$ factor is introduced to compensate for the difference in field of view shapes.

$$CDX'_{WFC} \sim \frac{CDX_{JEM-X}}{\frac{D'}{D}\frac{S'}{S}\frac{M\,\%'}{M\,\%}\frac{\pi}{4}} \tag{4.10}$$

During INTEGRALs time in space, most of the observing time will be awarded to the scientific community at large (65% during year 1, 70% year 2, 75% (tbc.) year 3+). The remaining time will be reserved for the institutes involved in the development of the project. This programme consists of three main elements: a survey of the galactic plane, deep exposures of the galactic radian and pointed observations yet to be determined. The introduction of the SAX WFC to the weekly scans of the galactic plane (See figure 4.18) will affect the sensitivity of the SAX WFC due to the fact that each section of the galactic plane will be exposed to the SAX WFC up to 7 times (instead of the single exposure from JEM-X during the programme) due to the SAX WFC having a much wider field of view. Though the series of exposures will not all be on axis, and so have a degraded sensitivity, the overall sensitivity of the SAX WFC will improve by a factor of 0.542 during this mode.

Once a simulated background was achieved, a sensitivity curve could be calculated and compared to previous JEM-X simulations (figure 5.10). As would be expected, the JEM-X sensitivity is better than the SAX WFC though the improvement in the SAX WFC sensitivity in the scanning mode is notable.

4.4.4 Conclusions

This simple example of mass modelling showed the power of the technique. Should the need arise, JEM-X could be replaced on the basis of a pre-determined estimate of how the SAX WFC would perform in such an environment. The two cameras that were in operation aboard BeppoSAX were in low inclination low Earth orbit and so experienced a very different kind of variable hard X-ray background. Aboard INTEGRAL the SAX WFC would perform in a very different way. How the SAX WFC camera reacted to this alternative environment was simulated here. Should the SAX WFC be selected on this evidence then further detailed simulations could be performed.

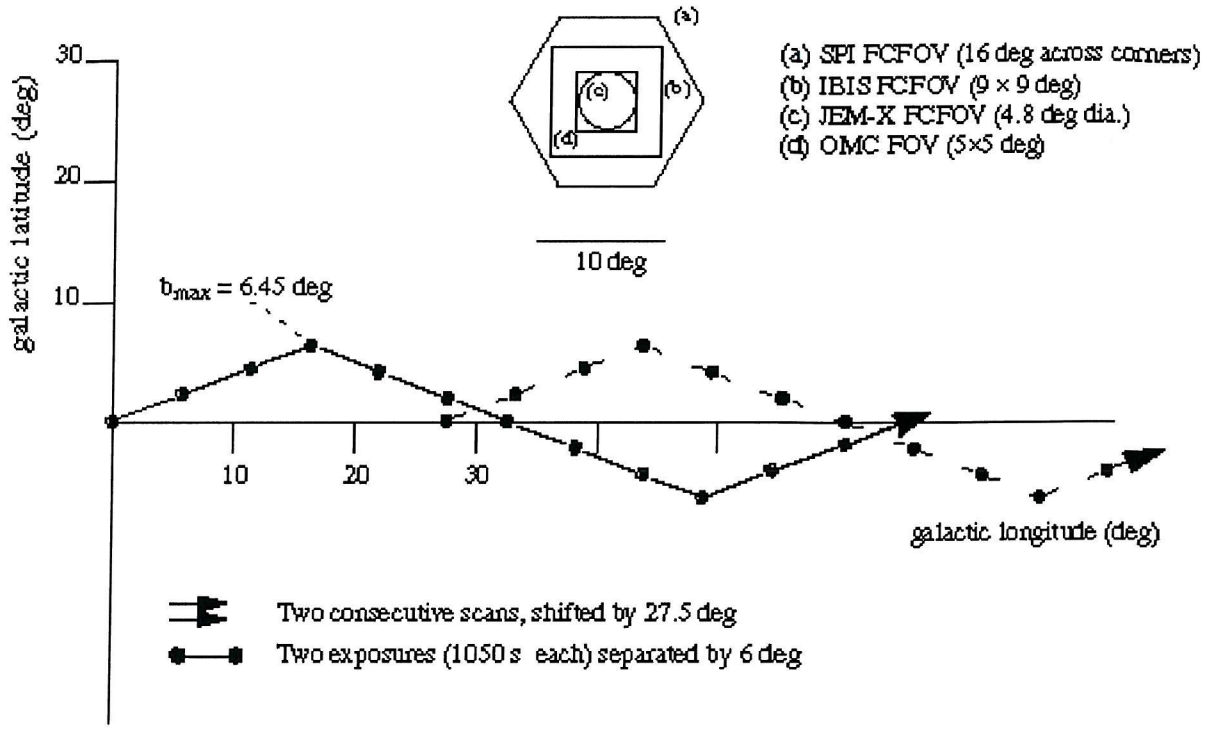

Figure 4.18: **The INTEGRAL galactic plane scanning programme.** *The sensitivity of the SAX WFC will be improved during this saw-tooth scanning procedure (inclined at 21° to the galactic plane) due to the extended field of view. It can be estimated that the sensitivity of the SAX WFC will improve by more than 54% during this scanning programme.*

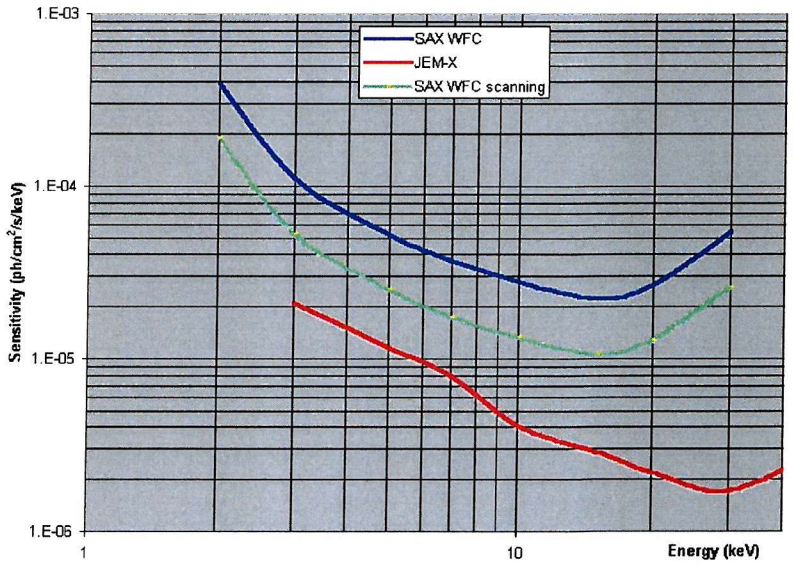

Figure 4.19: **Sensitivity curves for JEM-X and the SAX WFC.** *Also included is the projected sensitivity of the SAX WFC during the scanning of the galactic plane.*

4.5 Summary

This chapter has summarised the method on which the subsequent chapters will be based. The case-study investgation showed how the Mass Modelling approach can estimate the sensitivity of an instrument in a particular space environment. This was an obvious application to the methodology described. The following chapters are all based on the same principles of photon and particle tracking but with applications that vary significantly. The limitations of the Mass Modelling approach are being pushed back and more and more aspects to nuclear interation are included every year. The emphasis on gamma ray astronomy missions has moved from estimations of the background to mission design and data analysis. Due to the complex nature of gamma ray interation and background the importance of this non-empirical approach will continue to grow. Along with the desired increase in sensitivity with each mission comes the need for technological advancement in not just instrument performance but in the area of extracting the small amount of relevant astronomical data. Both areas will be guided by Mass Modelling simulations.

Chapter 5

The Swift Mass Model (SwiMM) - The Design Stage

5.1 Introduction

The gamma ray telescope aboard Swift is the Burst Alert Telescope (BAT) and its primary function is to monitor the sky for Gamma Ray Bursts (GRBs). Once a burst is triggered the location will be quickly calculated and the spacecraft slewed to a position so that the narrow field instruments can observe the event. To maximise the sensitivity of the instrument the background should be reduced as far as possible, and to do this, the design of the shielding is crucial. In the case of the BAT the shielding is a passive graded-Z shield made of lead, tantalum, tin and copper with a mass budget of 32.7 kg, which, considering the surface area of the shielding, is small. To lower the background as much as possible the ratios of the materials in the graded-Z shield will require optimising. The approach used here was to obtain theoretical values for the ratios, simulate them in SwiMM and adjust accordingly. The criteria for the shield optimisation were as follows:

- Mass budget of 32.7 kg
- Pb, Ta, Sn and Cu laminated, in integer layers of 0.00254 cm, into a graded-Z configuration
- Total shield thickness to be variable across the shield
- CZT charge trapping function to be included to reproduce a more realistic background.
- Each shield configuration to be defined by the strength of the weakest possible GRB detected with a signal to noise ratio of 8 (defined as $\frac{S}{\sqrt{S+B}}$).

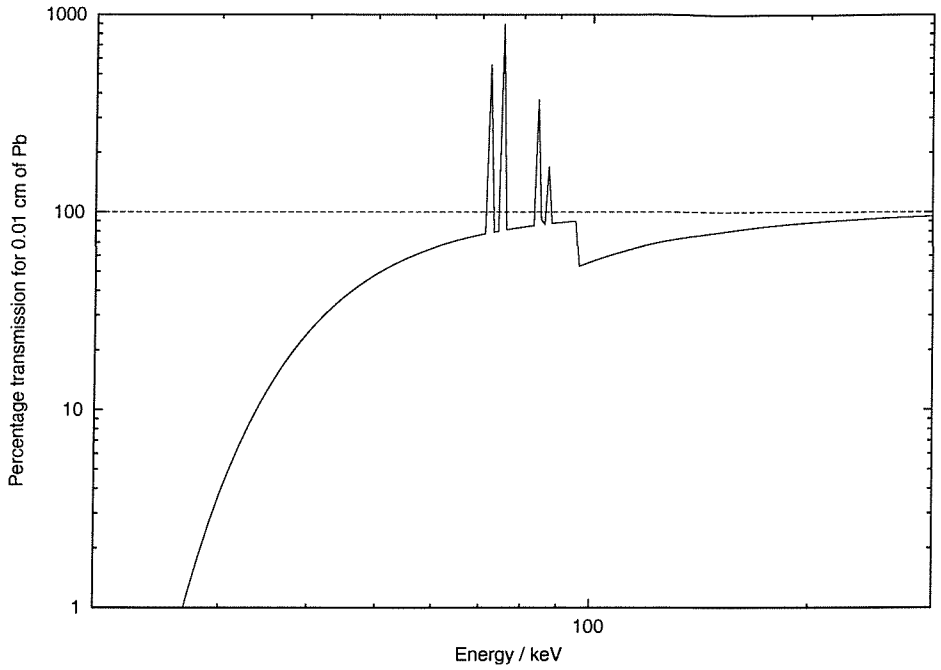

Figure 5.1: **An analytical transmission and fluorescence of a 0.01cm thick lead sheet.** *The main characteristics are defined by the position of the K-edge (95 keV) and the positions of the fluorescence lines.*

5.2 Theoretical Graded-Z Ratios

The first step is to obtain a theoretical minimum transmission with an optimum graded-Z ratio. By considering the total linear attenuation coefficients for the various materials the minimum percentage transmission for the shield can be calculated. Referring to figure ?? it is clear that the coefficient that will form the majority of the attenuation is due to photoelectric absorption. By considering the energy dependence of this and including the most intense fluorescence lines (due to K-shell repopulation), a theoretical ratio can be obtained. Figure 5.1 shows an initial analytical transmission and fluorescence percentage for 0.01cm of lead. By superimposing the energy dependent attenuation relationships for the four materials the K-edges can be balanced with the overlapping fluorescence lines to bring down the total transmission. The energies and intensities are shown in table 5.1 in order of intensity [31].

The criteria of the optimum theoretical ratio was to achieve the lowest ratio across the energy band of 10-150 keV, the sensitive energy range of the BAT at the time of shielding design (The final sensitive energy range was 15-150 keV, a factor that will not effect this theoretical calculation). This criteria included minimising all fluorescence lines.

Table 5.1: **The positions and strengths of the possible fluorescence in the passive shielding.** *Taken from "Table of Isotopes" by Firestone (1996).*

Element	Fluorescence Line Energy [keV]	Intensity [Photons per 100 K-shell vacancies]
Pb	74.97	46.2
	72.81	27.7
	84.94	10.7
	84.45	5.58
	87.30	3.91
Ta	57.53	47.2
	56.28	27.3
	65.22	10.3
	64.94	5.32
	66.98	3.53
Sn	25.27	45.7
	25.04	24.7
	28.49	7.99
	28.44	4.15
	29.11	2.19
Cu	8.05	26.0
	8.03	13.3
	8.91	4.69

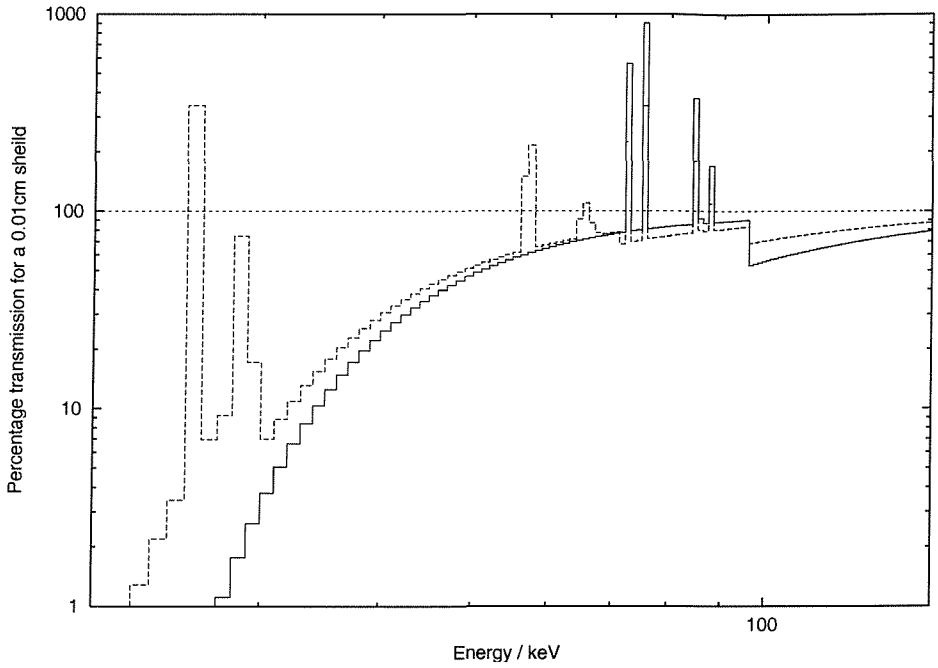

Figure 5.2: **The energy dependent transmission for a graded-Z and pure lead shield.** *The Pb:Ta:Sn:Cu ratio was determined by maintaining the lowest possible transmission across the 10-150 keV energy band. This was found to be* 0.37 : 0.09 : 0.39 : 0.15.

5.2.1 Discussion

The analytical optimum ratio was *0.37:0.09:0.39:0.15* for a *Pb:Ta:Sn:Cu* graded-Z shield, determined by nuclear data [31] and a simple transmission function. This theoretical ratio would suffice only as an estimation. With so little mass available for the passive shielding other factors should be included and can only be accounted for within a Monte Carlo environment. The background experienced by Swift comes from various sources. One source of background that will be unaffected by the shielding is the background that enters through the wide aperture. Any background minimisation should be done in relation to this and so the optimum ratio will be skewed to the higher energies where the Cosmic Diffuse X-ray (CDX) background will be less dominant. The input spectrum therefore determines the ratio that the shielding takes. Of course at higher energies photons interacting in the shield will interact by other processes outlined in chapter 1. This provides the input spectrum with external characteristics, according to the geometry of the instrument. The strengths of any fluorescence lines will also vary according to the scattering within the shielding. It is worth bearing in mind that the amount of material between the photon and the detector will also be dependent on the angle with which it strikes the surface of the shielding.

Along with physical considerations, practical ones need to be considered. The laminated layers can only be constructed from material foils that are available.

Table 5.2: **The mass report from SwiMM.** *Notice that the mass of the graded shielding has not been included as this will vary slightly for different configurations.*

Component	Mass [kg]
Mass of mask supp. stuct.	26.00
Mass of mask	18.22
Mass of detector array	166.00
Mass of BAT peripherals	50.04
Total mass of BAT	292.84
Mass of XRT	245.32
Mass of UVOT	123.68
Mass of Spacecraft	246.62
Mass of Sun Shield	14.46
Mass of Observatory bench	86.21
Total Mass	1009.12

For this reason, each material thickness within the shield will be an integer value multiplied by the smallest available thickness for the material, 0.00254cm. All these factors are included within a mass model and so the optimum ratio achieved here was expected to change with further study.

5.3 SwiMM

The Swift Mass Model (SwiMM) was initially constructed in GEANT 3.2.1 with the specific purpose of optimising the passive shielding around the Burst Alert Telescope (BAT). From technical drawings and mass budgets all aspects of the spacecraft that could influence the flux detected by the CZT detector were included in as high fidelity as necessary. The model includes basic versions of the X-Ray Telescope (XRT), the Ultra-Violet and Optical Telescope (UVOT), the star trackers and the spacecraft itself. More detail went into including the peripheral components: the sun shield, the radiator, the observatory bench and the electronics/ power/ image processing boxes. As for the BAT itself, as much detail was entered as was possible and practical. The mask, though not consisting of the correct number of elements in the designated pattern, was made of 795 lead tiles positioned over the mask area in a chequered pattern, maintaining the 50% transparency. The detector itself was entered into the model as 256 individual elements of CZT (instead of the correct 32768), maintaining the active area and distribution over the detector. Figure 5.3 shows the various components to The BAT and the degree of detail that has been included in the model. Table 5.2 displays the masses calculated by the model in a more traditional application of a Mass Model.

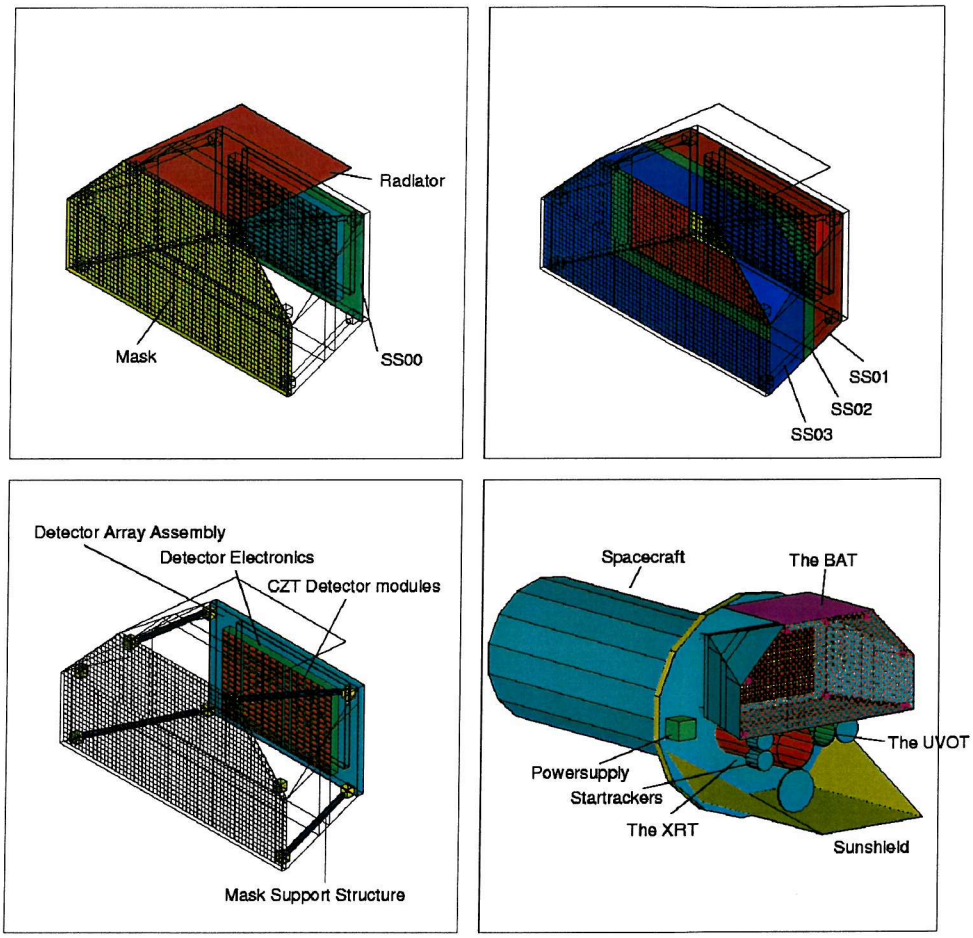

Figure 5.3: **SwiMM Geometry**. *A level of detail can be seen in diagrams of The BAT but microscopic layers in the shield and detector array cannot be seen. The detail in the XRT and UVOT included basic models of the mirrors, detectors and baffles. The two narrow field instruments were modelling with the correct mass distributions and little else for simplicity. The four shield sections (SS) are labeled.*

5.3.1 Optimisation Simulations

The model was set up to simulate the various components to the background and compare the count-rates to the count-rate from a simulated generic GRB. The model was set up to record the following: -

- The direct photon flux through the aperture.
- The scattered flux from the mask.
- The penetrative flux through each section of the shielding.
- The scattered flux from the shielding.
- The count density across the detector plane.
- The prompt cosmic ray spectra.
- The delayed activated component of cosmic ray interaction.
- The height above the CZT that a photon passes through the shield.
- The height above the CZT that a photon interacts with the shield.

(All spectra will be recorded with both the plain spectra and the charge-trapped function convolved with it.)

The Simulated Flux

The input spectra used are described in table 5.3. The generic GRB spectra was formed by the equations outlined by Band *et al.* (1993) [3] and is defined by equations 1.2 and 1.3 with the parameters set to $\alpha = -1.5, \beta = -2.0, E_0 = 250keV$. The cross-over between the two relationship is therefore 125 keV. The simulations intentionally did not represent a completely isotropic flux for the background. To represent the fact that Swift will be in low Earth orbit and generally pointing away from the Earth, the directions from which the fiux were observed were restricted to give a more realistic simulation. The GRB were simulated as a on-axis plane wave. Figure 5.4 shows the directional dependence of the flux that SwiMM simulated.

CZT Performance

When these simulations were run the amount of energy deposited into each volume was recorded, but it is useful to include the performance characteristics of the detector so as to determine how the data would appear when the instrument is in orbit. The charge transport and signal generation process of CZT includes charge trapping within the detector. This modifies the energy recorded according to the lifetimes of the electrons and holes within the semi-conductor and how deep the photon interacts within the detector. This relation is shown in equation 5.1 [*E' is the recorded energy, E is the energy deposited,* λ_e *is the average distance an electron travels before recombination (due to the semiconductor attempting to restore its thermal equilibrium disturbed by the generation of excess charge) and* λ_h *is the equivalent distance for a hole (For SwiMM 2.0E-3 and 2.0E-5 have been used respectively), D is the detector thickness and z is the perpendicular distance from the star-ward surface of the detector*].

Table 5.3: **The SwiMM input spectra.** *Adapted from Gehrels (1992), Webber and Lezniak (1974) and Band et al. (1993) respectively.*

Source of Background	Energy Range /keV	Spectrum $/ph.cm^{-2}.s^{-1}.keV^{-1}.sr^{-1}$
Cosmic Diffuse X-rays	10-20	$8.574\ E^{-1.4}$
Cosmic Diffuse X-rays	20-100	$161.5\ E^{-2.38}$
Cosmic Diffuse X-rays	100-10000	$111.2\ E^{-2.3}$
Albedo + Cosmic X-rays	10-4000	$0.5745\ E^{-1.39}$
Albedo + Cosmic X-rays	4000-10000	$100.0\ E^{-2.05}$

Source of Background	Energy Range /MeV	Spectrum $/ph.cm^{-2}.s^{-1}.MeV^{-1}.sr^{-1}$
Cosmic Ray	3440-25500	$343.78\ E^{-2.042}$
Cosmic Ray	25500-1000000	$244020\ E^{-2.689}$

GRB generic spectra	Energy Range /keV	Spectrum $/ph.cm^{2}.s^{-1}.keV^{-1}$
GRB	10-125	$A.(\frac{E}{100keV})^{-1.5}.e^{-(\frac{E}{250keV})}$
GRB	125-10000	$A.(\frac{125keV}{100keV})^{0.5}.e^{-0.5}.(\frac{E}{100keV})^{-2.0}$

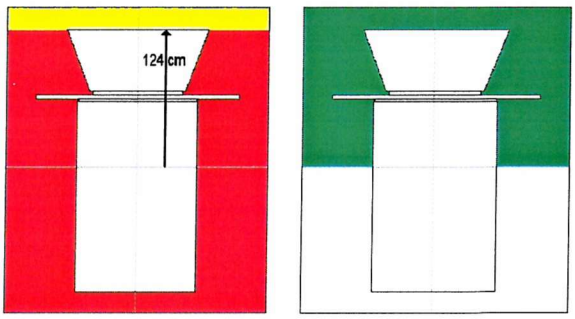

Figure 5.4: **The virtual input surface.** *The above schematic displays from which directions the model received flux. The yellow indicates purely Cosmic Diffuse X-rays, the orange indicates the angle-averaged Albedo and Cosmic Diffuse X-rays while the green shading indicates Cosmic Ray flux. The radius of the cylinder was 140.0 cm and it is 575.0 cm tall.*

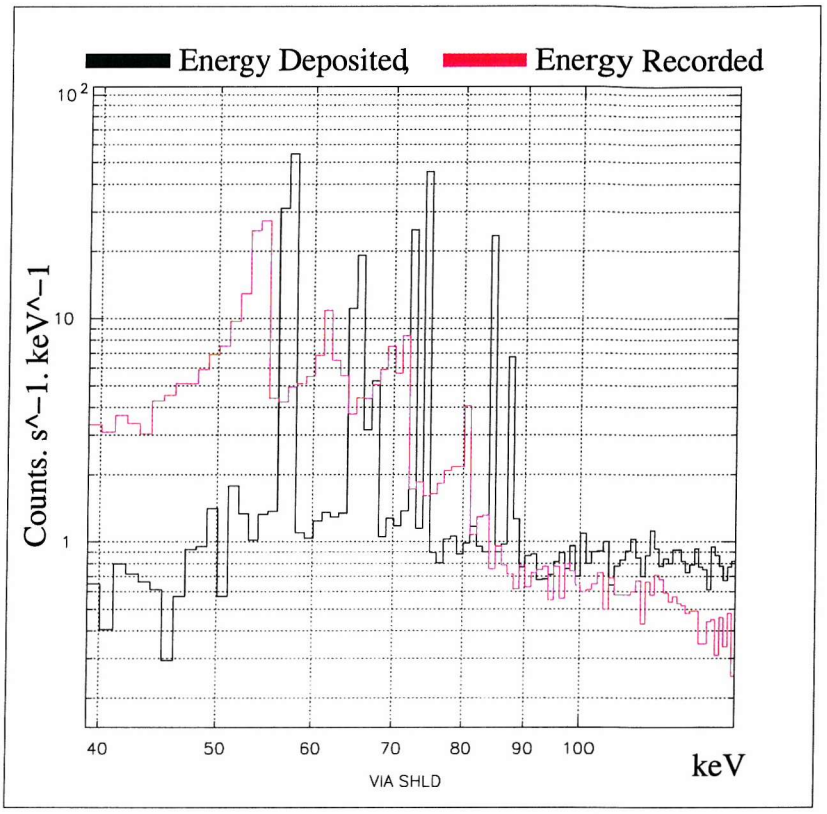

Figure 5.5: **An example of charge trapping**. *This is the scattered component of the spectrum observed by the BAT. The black spectrum is the energy deposited in the CZT and the red spectrum is the energy recorded by the CZT. The Pb and Ta lines are smeared together.*

$$E' = E.\left(\frac{\lambda_e}{D}.\left(1 - e^{-\frac{D-z}{\lambda_e}}\right) + \frac{\lambda_h}{D}.\left(1 - e^{-\frac{z}{\lambda_h}}\right)\right) \tag{5.1}$$

The true energy can never be recorded as a result of this charge trapping characteristics of CZT. It is also worth bearing in mind that higher energy photons will penetrate the detector more and so be affected more by charge trapping. This becomes apparent when studying spectra. Clusters of lines can be shifted so that they appear as one lump, this effect can be seen in figure 5.5. The effect of charge trapping can be countered in the recording of the data by, for instance, taking the rise-time into account. Though this is not used by the BAT, it is used in ISGRI in the IBIS instrument aboard INTEGRAL.

The Mass Budget

The main constraint alongside the materials available was the maximum mass allocated to the passive shielding. Figure 5.6 shows how the allocated mass effected the

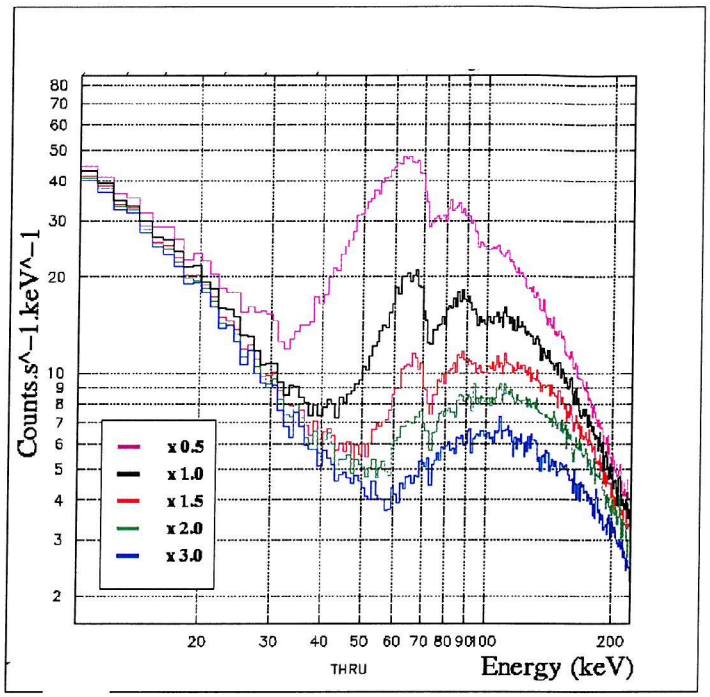

Figure 5.6: **Penetrative flux**. *These spectra show the penetrative flux recorded by the CZT for different multiples of the 32.7 kg, maximum allocated mass.*

penetrative flux while figure 5.7 shows how the total background would have varied with a change in the allocated mass, all material thicknesses scaled accordingly. 32.7 kg was an efficient balance between minimised background and minimal mass budget.

The GRB Trigger

The BAT is designed, primarily, for detecting GRBs and so any optimisation criteria would have to be based on this. With the charge trapping effect included some of the details of the fluorescence within the spectra were lost. The primary concern was to reduce the continuum. The BAT will be triggered to GRBs going off by considering several energy bands, **15-25, 25-50, 50-100, 100-150, 15-50, 50-150, 25-100** and for the sake of this optimisation **15-150 keV**. The equations for a GRB spectra (1.2 and 1.3) contain a factor **A** which is a normalisation factor that determines the strength of the burst. For the purposes of this optimisation process, the exposure was taken to be 1 second. The Signal to Noise Ratio (SNR) could be calculated for each configuration and if the triggering requires a SNR of 8 or more, the weakest possible GRB detected for each configuration was determined. So now there was a real analytical method (eqn. 5.2) of determining the efficiency of each shield configuration. This basis for the optimisation was that the normalisation factor, **A**, was to be minimised.

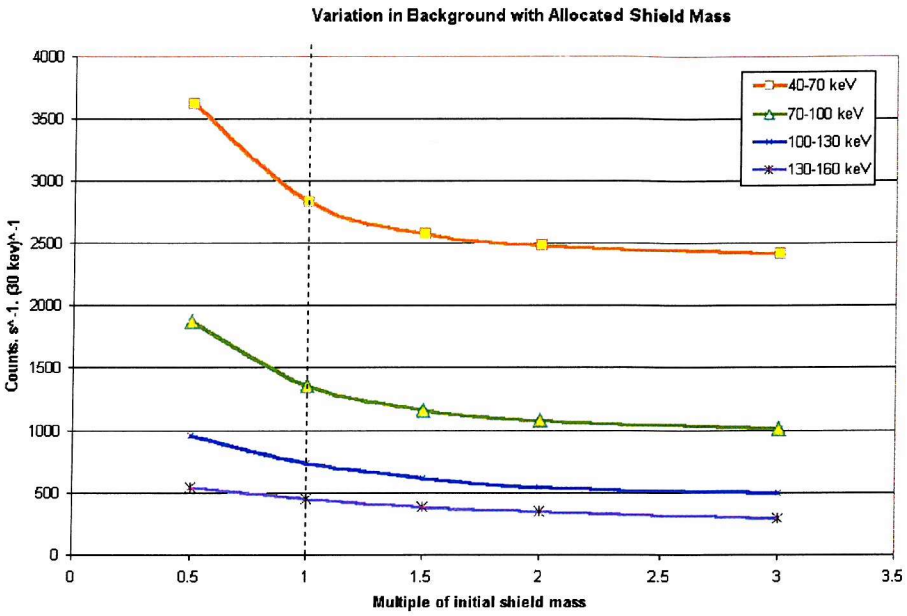

Figure 5.7: **Allocated mass variation.** *This graphs shows the total background counts received by the CZT with different multiples of the allocated mass, 32.7 kg.*

$$\begin{aligned} GRB\ signal &= Spectra.A \\ SNR &= \frac{SA}{\sqrt{SA+B}} \\ SNR &\geq 8 \end{aligned}$$

$$A \geq \frac{32 + 8\sqrt{16+B}}{S} \tag{5.2}$$

The Shield Section Geometry

A major part in the optimisation of the shielding was to distribute the masses around the shield sections. Figure 5.3 shows the geometry of the shield sections. This geometry was determined by analysing where on the shielding photons penetrate the shield and end up in the detector. A simulation was run (**Run 1**) that had each shield section at equal thickness and composition and the penetration distance above the detector recorded. The best way to determine the mass distribution was to split the shield into regions of statistically similar transmission. This can be seen in figure 5.8.

5.3.2 Optimisation Results

Now that a definite method of determining the effectiveness of a shield configuration had been established it was easy to evaluate each configuration. However the

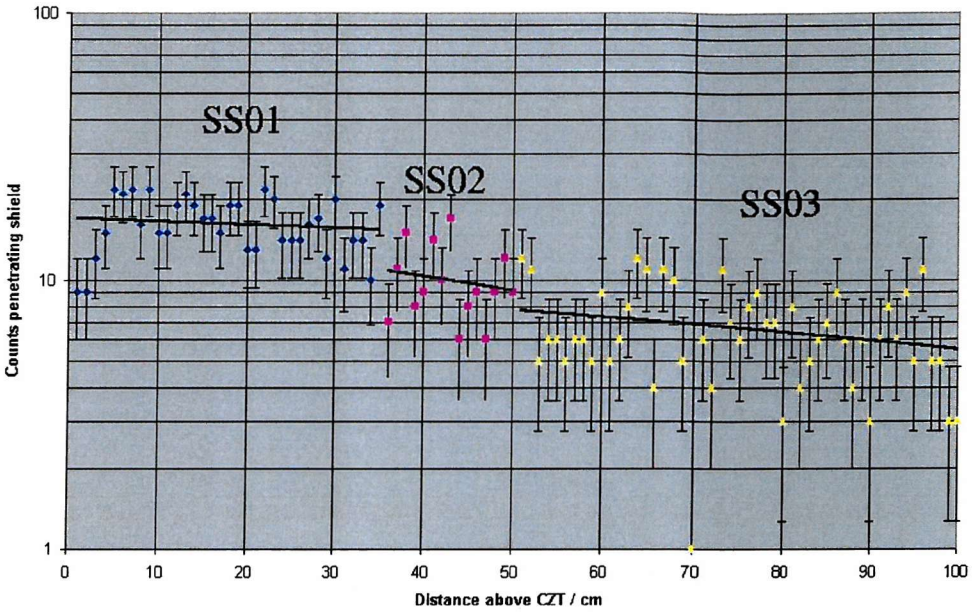

Figure 5.8: **Shield section extent**. *From this plot of the flux penetrating the shield it can be seen that the distribution can be split into three according to the three shield sections. And so by allocating more mass to SS01 and less to SS03 we can even up this distribution. Though it is worth noting that an even height distribution here would not necessarily mean an optimised configuration.*

problem of how to optimise a configuration still remained. Many simulations have been run and 6 of the pivotal ones will be presented here. Table 5.4 summarises the 6 runs presented here. Each run had a matrix to define its configuration and these can be found in Appendix A. An aspect that will not be seen in the spectra is a radioactive component for the simple reason that this effect is essentially independant of the shield consistance on these scales.

Run 1 was an initial run to evaluate the transmission of each shield section. The material ratios were skewed towards the higher Z materials to the ratio of **1:4:5:5** for Cu:Sn:Ta:Pb. This enabled an evaluation of the extent of each shield (See figure 5.8) and how much of the mass should be allocated to each shield section. This run was only intended to be a guide-line.

Run 2 was again used as a useful comparison on which to base the optimisation process. Consisting entirely of lead there was a much lower background and so sensitivity for the 100-150 keV range as expected but the performance throughout the rest of the spectra was not as good, especially in the 50-100 keV range where the Pb fluorescence made its presence felt.

Run 3 was the first realistic attempt at an optimum configuration. The approach for this run was to put a lot of emphasis on the Lead and gradually less on the sub-

Table 5.4: **A summary of the various configurations.** *Runs 1 and 2 represent comparison runs as places to start the optimisation process. Runs 3 and 4 represent the result of two different approaches to the optimisation process. Run 5 is the compromise and the most efficient shielding simulated.*

Run	Configuration Summary
1	SS ratios and thicknesses are equal
2	Pb shield only
3	SS weighted with the theoretical material ratio
4	SS weighted and material skewed to Ta and Sn
5	Optimum run
6	Optimum run - alternative SS00 geometry

sequent lower Z materials. This was to lower the entire continuum with the Lead and smooth out the resulting K-edge with the lower Z materials. The run achieved a smoother continuum with similar fluxes penetrating each shield section but the performance in some of the bands was not as good as **Run 1**. The material ratios were based on the ratios calculated in the previous section.

Run 4 used a different approach: it considered the GRB spectra used to evaluate the shielding. Below 125 keV the GRB spectra is flatter than the background spectra so by minimising the spectra and to some extent ignoring the background flux above 125 keV (which is always going to be much lower) the SNR for this energy range should be increased and thus lowering the value for **A**. Unfortunately by neglecting the higher end of the spectra much more flux penetrated the Pb, so increasing the overall continuum and promoting the K-edges and fluorescence of both the Ta and Sn.

Run 5 was the optimum run and used aspects of all the previous runs to minimise and smooth the continuum. The amounts of copper were kept small as the copper was seen not as a material to stop the background as a whole. It was used to reduce fluorescence from the higher Z materials and to produce fluorescence below the lower threshold of the detector, caused by photons entering the aperture. The material emphasis remained with the Pb but comparable amounts were placed in the Ta and Sn layers.

Run 6 was a requested run [A. Parsons (GSFC), *private communication*] as a test of proposed geometry of the lower shield section, SS00. In all the previous runs the shield section had been extended to meet SS01 but in this case the material only extended as far as the detector extends and so leaves a gap between SS00 and SS01. The mass was made up in the rest of the shielding in the same proportions as **run 5**. This new geometry allowed more background flux through than in **run 5** and

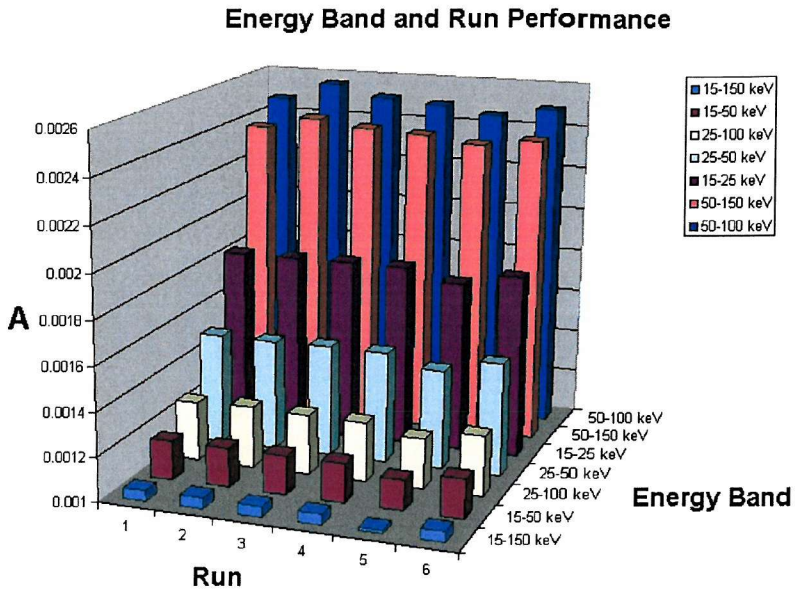

Figure 5.9: **The run and energy band performance.** *This 3D plot shows how each trigger band performed for each run. The best performing bands are over the full range (***15-150 keV***), between* **15-50 keV** *and* **25-100 keV**. *The lowest values of* **A** *signify the weakest strength GRB detectable, i.e. the sensitivity.*

this is demonstrated in the band sensitivity and it is worse than all the other runs.

So to conclude, the shield configuration for **run 5** proved to be the most effective for triggering bursts and will be used in the passive shielding. Figure 5.9 shows the performance of the energy bands for each run. The only energy band that was not consistent with the other was the 100-150 keV band. Within the optimum run, the minimum value for A in the 100-150 keV band was much larger than for the other bands (4-10 times larger). The performance for this energy band was best for **run 2** as expected. However, the overall best performance was achieved.

Now that a graded-Z shield design has been achieved, a sensitivity estimate can be calculated. The sensitivity is obviously directly effected by the levels of background noise, minimised with the most efficient shielding design. The sensitivity estimate can be seen in figure 5.10.

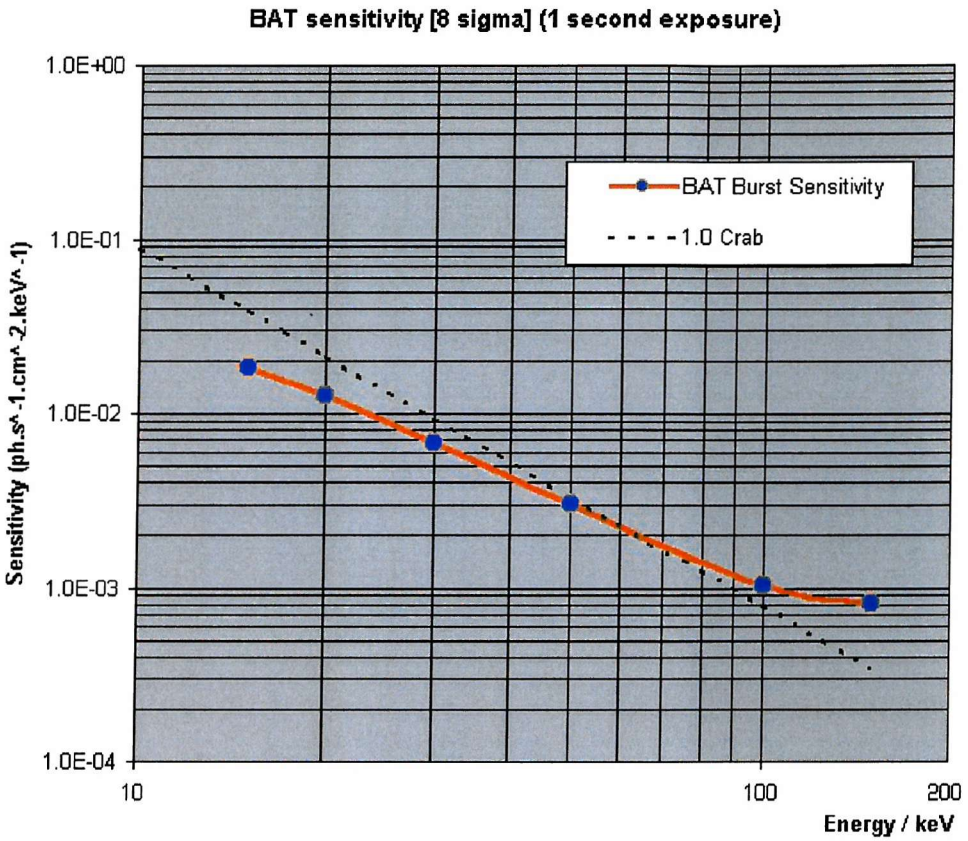

Figure 5.10: **Estimated on-axis burst sensitivity.** *This sensitivity is for a SNR of 8 during a 1 second exposure. Included as a comparison is the Crab spectrum (spectral index: 2.05).*

5.3.3 Further GRB Applications

The initial purpose for constructing a Swift mass model was to aid in the design of the passive shielding. Once a model was constructed other investigations were carried out. Either requested by the BAT team or brought to the attention of the mission scientists from experience on previous missions.

Off-Axis Burst Effects

For the purposes of optimising the shield an on-axis GRB was simulated. The shieldings purpose is to reduce the background as far as possible so that bursts detected through the coded mask aperture could be detected to the best sensitivity. However should a burst go off outside the field of view the count-rate will increase as the flux passes through the shield. This can be considered to be an interferring source of background unless information as to the burst position can be obtained from the flux passing through the shielding. Due to the irregular shape of the mask support struture and the varying thickness of the shielding a disinct pattern could be projected onto the CZT array. This pattern will be specific to a particular burst position and so could be deconvolved to find that position. SwiMM was employed to see if this pattern would be significant and if a burst position could be obtained.

Figure 5.11 shows the flux distribution that an offaxis GRB can produce on the detector plane. For this evaluation the CZT detector array was approximated into 256 blocks (128 pixels were grouped together as one). This flux is purely from the GRB but includes all scattered and penetrative components. A definite pattern can be seen. The positions and sizes of the steps between the shield sections were used to estimate a position. Should an approximate position be determined the spacecraft could automatically slew to the position and the now fully-coded image could be measured more accurately.

This estimation included a fit to the positions of the steps on the detector plane. The bursts were simulated arriving at the detector plane offaxis by greater than 62^o and orthogonal to the edge of the detector array. To determine the azimuthal direction a whole series of bursts would have to be performed to build up a matrix of the patterns incident on the CZT. Figure 5.12 shows the fitting of two simulated bursts to obtain the zenith angle. This rather crude method can place a burst to within a degree. However this is a fit to flux that originates from a burst and a burst only. Should the background levels be high in relation to this penetrating flux then the fltting will not be nearly so accurate. Figure 5.13 shows the flux density of the background added to the flux density of an off-axis burst. The steps due to the varying shield thickness are washed out by the background flux. The same statistical process to fit to a position does not obtain a χ^2 value below 30.

This method would not be feasible to identify bursts outside the field of view. An autonomous process to identify bursts through the shielding would be intensly

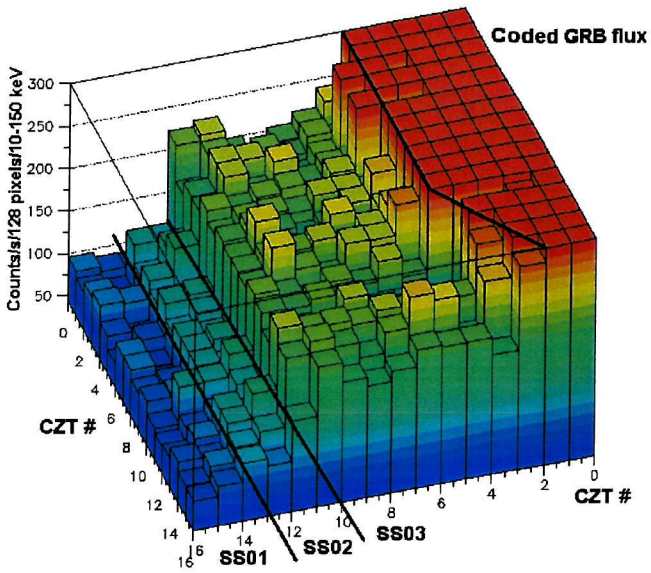

Figure 5.11: **The flux distribution of an offaxis GRB.** *The burst was simulated coming from a direction 55 degrees from the normal. The trapeziodal corner of the aperture can be made out alongside the three count-rate distributions associated with the varying thicknesses of the three shield sections.*

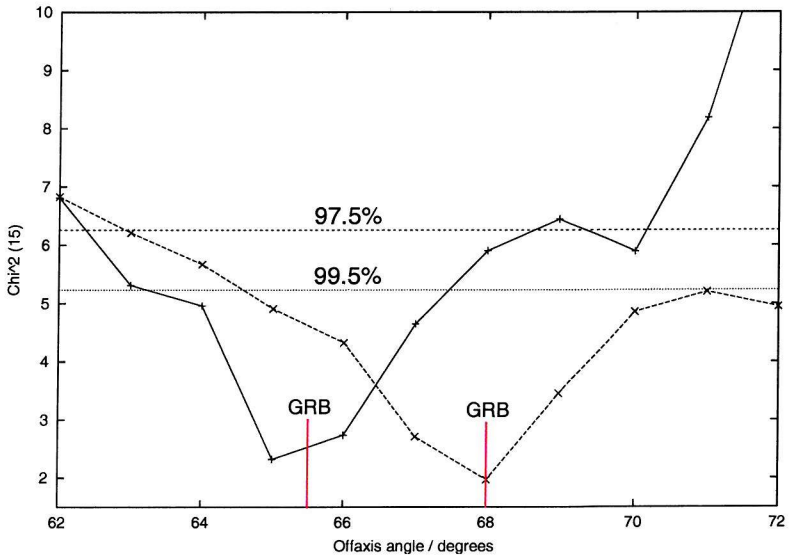

Figure 5.12: **A χ^2 fit to determine the positions of two bursts.** *The confidence levels of 97.5% and 99.5% have been included.*

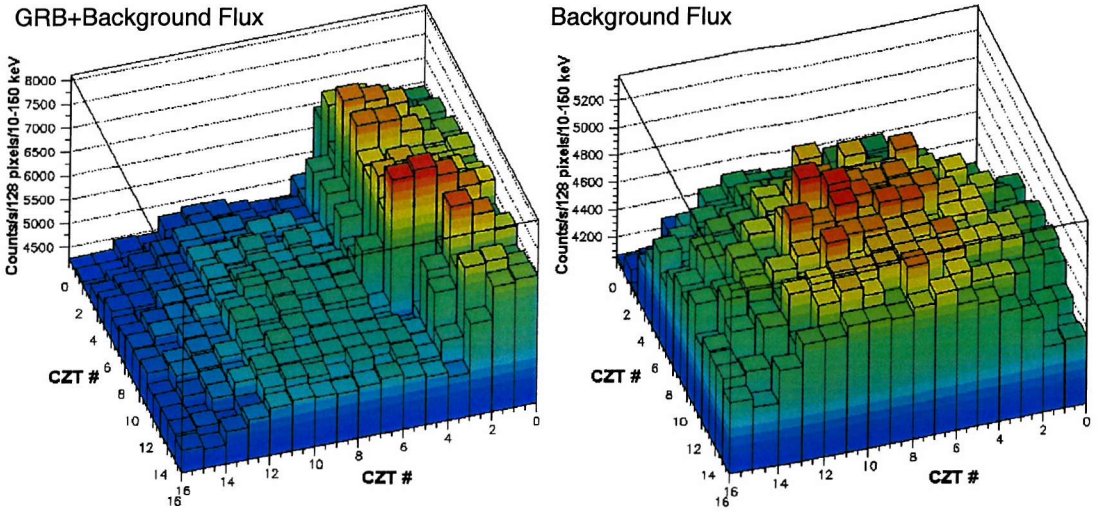

Figure 5.13: **Flux distributions including background.** *The burst is clearly represented through the aperture. However there is no evidence of the burst through the shielding transmission.*

complex and operationally impractical unless a burst was particularily strong. Unfortunately the transmission of the shielding will only aid in the spatial variations accross the CZT and so such bursts will be considered a source of background.

GRB Self-Contamination

Due to the strong flux received from a burst there will inevitably be scattering of the incident burst flux from the material surrounding the detector plane into the CZT detector plane. The scattered flux will contaminate the pure burst spectra, should the coded-mask imaging technique not be used for spectral infomation, as is the case with the BAT. With standard gamma ray-source observations the region of sky has to be observed for a long period of time to get the required significance in the spectrum. In this case the scattered flux is low in comparison to the background. In the case of GRB the fluxes are so strong that a signal-to-noise ratio of 8 can be obtained over very short time scales and so the background is low in comparison. This is where the scattered component can alter the spectrum. The scattered components are accounted for during calibration and the production of a Detector Response Matrix (DRM).

SwiMM was used to estimate the degree that this scattered component would affect GRB spectra. This was done by simply seperating the flux that interacts with material before entering the CZT. The photon history recorded within SwiMM will be applied to the calibrations themselves so that any interaction with the calibration room surroundings could be evaluated and removed from the DRM.

Presented here are two simulations of GRBs. Both bursts are exactly the same

Table 5.5: *The percentage of spoilt flux for GRB observations for the energy band 100-150 keV.*

Offaxis Angle	Azimuthal Angle		
	0^o	90^o	180^o
0^o	3%	3%	3%
20^o	4%	4%	26%
32.8^o (med.)	8%	28%	70%
max.	55% (39^o)	70% (55^o)	94% (38^o)

spectrally and in intensity. The only variation is in the incident angle. One is on axis and the other is 32.8^o off-axis, the median arrival angle for a GRB. 32.8^o is the angle inside of which contains the same solid angle as outside, within the field of view. Figure 5.14 shows the contamination the BAT is likely to experience. The majority of the contamination for an on-axis burst is from fluorescence in the tantulumn and tin within the graded shield. The copper inner layer will minimise this. For the median offaxis burst this fluorescence is stronger and also includes a continuum and components due to lead fluorescence and scattering from outside the BAT.

The degree of contamination is strongest in the higher energy bands but, due to the non-cylindrically-symetrical nature of the BAT will also be highly dependant on the azimuthal angle of the burst. Table 5.5 shows the percentage of flux that is spoilt on entering the detector plane for different azimuthal and zenith angles.

As shown in table 5.5 the percentage flux that interacts with the BAT or spacecraft before contributing to the GRB spectra is highly directional dependant. The calibrations will include reprocessed flux but will not include any scattering off the periferal structure outside the BAT and will unwittingly include any scattering from the calibration equipment. This issue is addressed in chapter 6 in the context of a mission that has finished its operational lifetime, BATSE.

Photofission

A source of contamination for GRB flux that is not immediately obvious is photofission, the process of an X-ray causing the spontaneous emission of a neutron or alpha particle from a nucleus. Photofission commonly occurs in the centre of stars but can be induced in laboratory experiments. Each element has its own resonant energy ranging between 5-25 MeV (FWHM: 2-10 MeV) for all Z [1, 78]. This process is only included in GCALOR for A> 232 and so will be ignored within SwiMM. An estimation for Lead is carried out here to see what kind or neutron flux is expected during a GRB. Lead has a resonant cross-section function centred at 13.8 MeV (FWHM: 2.4 MeV) and peaks at 0.55 Barns which gives a yield of $1.4 \pm 0.2 \, .10^7$ $neutrons.mole^{-1}.Roentgen^{-1}$. This gives the probabilty of a neutron

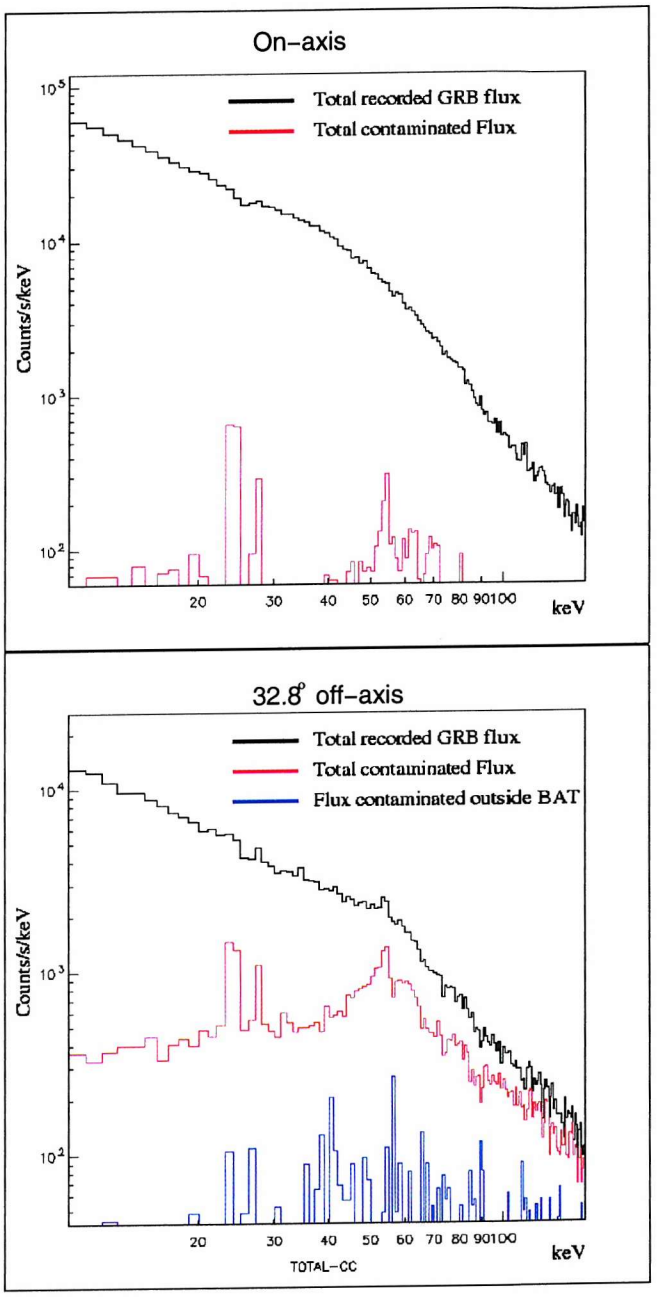

Figure 5.14: **GRB self-contamination.** *The top spectrum contains very little contamination due to the on-axis nature of the burst. The burst spectrum below is 32.8° off-axis, the median angle.*

being emitted through photofission from a Lead nucleus to be 0.017 ± 0.002 per photon (8-24 MeV).

This corresponds to ~ 0.0014 $neutrons.s^{-1}$ for the average background flux and ~ 4.7 $neutrons.s^{-1}$ during a burst, for Lead. The materaials in the detector array (Cadmium, Zinc and Telurium) all have smaller atomic masses and Z values and so less neutrons are expected. This source of self-contamination can therefore be ignored as the background will dominate this effect vastly. However any physical processes that may effect the systematics that are not included in GGOD must be evaluated for an accurate simulation.

False Triggering

The Swift mission will re-point to a GRB position automatically while in low Earth orbit. While in this orbit the spacecraft will encounter electrons and protons trapped in radiation belts. These charged particles are retained by the "magnetic bottle" of the Earths magnetic field. These electrons could easily contribute a large step in the count-rate, providing a possible false trigger. They could provide the count-rate but should the electrons arrive in anything but a plane wave then no image can be obtained, providing the flight software with a means to identify it as a misleading trigger. Unfortunately the possibility, during a radiation belt passage, of the electrons arriving as a plane wave is flnite. Should this happen the possibility of a mask pattern being projected upon the detector array is uncertain as electrons will interact with the Korex mask structure far easier than photons.

These concerns were raised during the mission design stage and were addressed by the mass model. The worst case scenario was considered in order to see if a pattern could be projected. The first thing to calculate was the degree of curvature within the magnetic field. Should this radius of curvature be too big or small then the electrons could not form a suitable plane wave or shadowgram. Figure 5.15 shows how the electron curvature radius is related to energy, with both classical and relativistics treatments.

With the radius of curvature being between 27m and 70m (at 600 km, Incl. 0^o), the possiblity for a plane wave of electrons to form (on the scale of the BAT) is again finite. The flux density at the centre of the SAA was taken and the proportion that could enter the aperture was simulated as an on-axis plane wave incident on SwiMM. If this simulation forms a shadowgram then other criteria for identifying these false triggers needs to be considered. Figure 5.16 shows the pattern that an on-axis GRB produces compared with one that the radiation belt electrons could produce. It can be seen that even though the count-rate is much higher than the background or indeed a GRB, no shadowgram can be produced. This infomation therefore supplies the flight software with a means to ignore any electron induced false triggers.

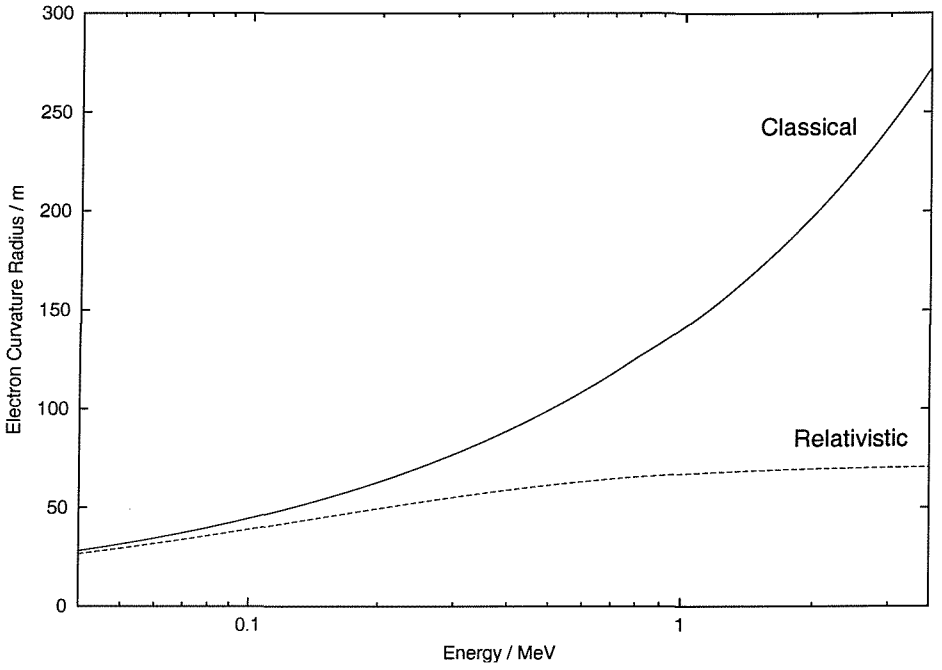

Figure 5.15: **The radius of curvature of the electron trajectories within the Earth's magnetic field against energy.** *Both the classical and relavisitic appraoches are presented here. Over the energy range of the trapped electron flux (0.04-3.75 MeV) the radius of curvature ranges between ~27m and 70m (272m, classical).*

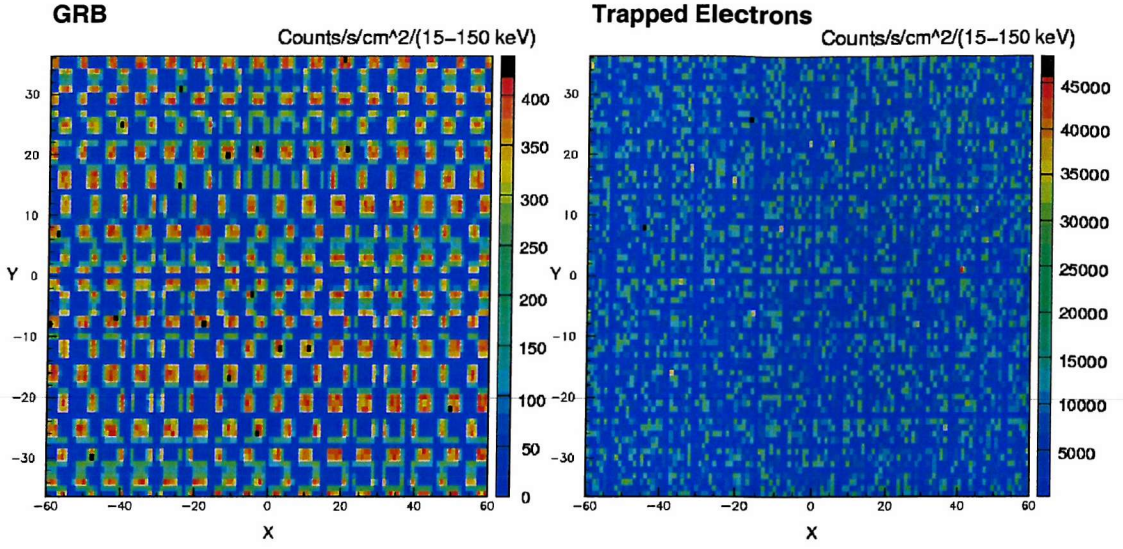

Figure 5.16: **The comparative projected mask patterns for a GRB and trapped electrons.** *The pattern consists of 795 chequered mask tiles projected onto 264 CZT large CZT pixels. The pattern, though irrelevant, can be seen as the GRB illuminates the detector array. However the electrons interact with the mask structure too much for the collimation to project a pattern onto the detector.*

5.4 Summary

The BAT will hope to detect 300-400 bursts per year in its mission lifetime with a third of them being observed by the two narrow field instruments. One major problem in the BATSE observations and the theory of GRBs was that there seemed to be a paucity of weak bursts. With the burst sensitivity of the BAT expected to be 5 times better than that of BATSE then this problem will be investigated thouroughly. The optimising of the shielding will drive the threshold of the weakest detectable bursts down and maximise the number of detectable bursts.

An aspect of observing GRBs is that, unlike other gamma ray sources, their stength is far stronger and do not require long observing times to get the required statistical significance. Generally, the flux reaching the instrument is far stronger than the background and so self-contamination of the source flux is a definite issue that would require addressing in the production of the detector response. With the aid of SwiMM, the calibrations will be performed with this very much in mind. Questions raised about the performance of the BATSE detectors' response, in particular the handling of the scattered flux, adds a needless uncertainly in the current GRB catalogue. Every mission aims to learn from inadequacies made in previous missions and Swift is no exception.

Chapter 6

BATSE Burst Self-Contamination

6.1 Introduction

Arguably the most conclusive of Gamma Ray Burst (GRB) experiments has been the Burst And Transient Source Experiment (BATSE). Indeed, the reason that INTEGRAL does not include a burst monitor is that the Compton Gamma Ray Observatory and in particular BATSE was expected to clear up the issue of what causes GRBs. The most significant and perhaps unexpected discovery was that GRBs were extra-galactic in origin, the implications of which were huge. Instead of solving the puzzle of GRBs, BATSE has prompted all planned gamma ray missions to focus, at least in part, on the science of GRBs. From dedicated missions like Swift to basic burst monitors aboard the Mars Explorer and Ulysses the study of GRBs continue.

The biggest problem theorists encounter is that the light-curves and spectra vary from GRB to GRB. This obviously makes it hard to produce a generic model for GRBs. Fortunately progress has been made in parameterising the spectra [?] by using the data from the BATSE experiment and in particular using the Spectroscopy Detectors (SDs). The SDs are NaI scintillator detectors and are situated below the Large Area Detectors (LADs), also NaI scintillation detectors, on each of the 8 BATSE modules. Figure 6.1 shows a BATSE module and the difference in the normal vectors of the two scintillation detectors.

Band *et al.* (1993) studied the time-averaged gamma ray spectra taken from the SDs aboard each BATSE module and a relationship was obtained with three spectral parameters. This relationship is shown in equations 6.1 and 6.2 and enables GRBs to be charaterised by the parameters α, β and E_0. Unfortunately, these three parameters vary from burst to burst with no obvious common theme. The break in the spectrum, E_0, varies from 100 keV to 1MeV.

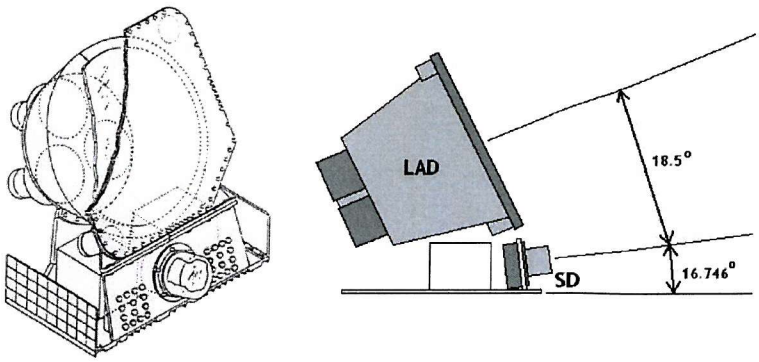

Figure 6.1: **A BATSE module.** *Shown is a scale drawing of a BATSE module alongside a schematic of how the two detectors are orientated. Due to engineering considerations the two detectors in each BATSE module are pointed in two slightly different directions, separated by 18.5°.*

$$N_E(E) = A.\left(\frac{E}{100keV}\right)^{\alpha}.e^{-\frac{E}{E_0}}, \quad (\alpha-\beta)E_o \geq E \tag{6.1}$$

$$N_E(E) = A.\left(\frac{(\alpha-\beta)E_o}{100keV}\right)^{\alpha-\beta}.e^{\beta-\alpha}.\left(\frac{E}{100keV}\right)^{\beta}, \quad (\alpha-\beta)E_o \leq E \tag{6.2}$$

The spectral characterising of GRB has aided theorists in handling the diversity of the spectra. However, a problem has arisen in the burst data analysis that this chapter will address. When the data was recorded by the LADs and SDs the final spectrum was achieved by running the recorded data through the Detector Response Matrix (DRM). The problem was that different spectra were being produced by the LAD and SD (M. Briggs, private communication 2001). A possible explanation for this was the different pointing angles for the two detectors (separated by 18.5°). The more off-axis a burst is to a detector the more source flux that will be contaminated by way of scattered flux and also, trivially, the larger the presented thickness of the detector. The different pointing directions of the two detectors meant that the amount of flux that was reprocessed was different for each detector. Should the DRMs not account for this reprocessed flux correctly then a discrepancy between the spectra obtained from the two instruments would appear. This chapter aims to evaluate whether the difference in pointing is responsible for the spectral discrepancy. Two recorded GRBs were simulated, one as a control whereby both the LAD and SD recorded the same spectrum and one that was recorded as having different spectral parameters for the LAD and SD. The first step was to see if the problem could be reproduced and the second to adjust the levels of reprocessed flux recorded in the simulation to see if the resultant spectra could be altered.

By using a mass modelling approach the path history of each photon is simulated and recorded. By recording a brief path history of each photon the contribution of

Table 6.1: **Trigger Characteristics.**

Trigger	**1625**	**143**	
LAD offaxis angle	27.185^o	32.344^o	
SD offaxis angle	8.965^o	50.274^o	
Duration	23.744 s	9.472 s	
α	-0.993	-0.850 (LAD)	-0.907 (SD)
β	-2.68	-2.42 (LAD)	-2.72 (SD)
E_0	523 keV	747 keV (LAD)	753 keV (SD)
A	0.0466	0.120 (LAD)	0.0118 (SD)
BATSE module	6	5	

the reprocessed flux to the recorded spectra can easily be determined and filtered if necessary. A mass model of the BATSE instruments has been constructed for the purpose of flat fielding the LAD continuous (CONT) data to aid in the production of an all-sky survey using an occulatation technique. The BATSE Mass Model (BAMM) was used for this investigation [128]. The GRB flux simulated will be fired into the model and defined by the spectral parameters (α, β and E_0), the strength (**A**) and the duration.

6.2 The Bursts

Two burst were selected to investigate the contribution of reprocessed flux on the spectral fitting. These were GRB 920525 (trigger no. 1625) and GRB 910503 (trigger no. 143) and will be referred to by the trigger number. The reasons behind selecting these two are that both of these bursts are incident on the LAD with approximately the same off-axis angle but differ greatly in the SD incident angle. The LAD reprocessed flux will therefore be at the same levels for both triggers whereas the SD reprocessed flux will differ significantly. Trigger 143 is the burst that is considerably off-axis for the SD detector and is also one of the strongest bursts ever detected and so good statistics can be achieved in the contaminated flux. By using these two bursts the performance of the LAD in observing both bursts was expected to be the same. The control for each burst will be the performance of the LAD while the comparative performance of the SD will provide the means to evaluate the consequences of the DRM. The two bursts are compared in table 6.1, including the fitted spectral parameters and incident angles (M. Briggs, private communication, 2001).

By simulating the two bursts and passing the results through the same analysis process as standard GRB analysis the difference between the LAD and SD could be reproduced. Should the discrepancy between the LAD and SD be reproduced then criteria can be imposed on the re-processed flux to see which aspect of this flux is

ill accounted for in the SD detector response.

6.3 The Modelling Process

The modelling process was straight forward but required integration into the standard data analysis. The data sets used were the High Energy Resolution (HER) data sets, an extension of the continuous (CONT) data set with different look up tables for the energy band boundaries. This gave 128 bands for the LADs (HER) and 252 bands for the SDs (SHER). For the LAD the usual 2.048 s data packets are read out in lots of 8 giving a minimum timing resolution of 16.384 s. For the SD the packets are grouped into 16 and so has a minimum timing resolution of 32.768 s.

The principle of this approach was that the period of the burst within the HER or SHER data set would be replaced by the count-rate obtained from the mass model. Using the same energy boundaries included in the data files, the section of data was simply replaced. This modified HER data set would then be analysed using the standard Detector Response Matrix (DRM). The fit to the simulated data was then compared to the spectrum fired into the model. Figure 6.2 shows the data flow of this procedure. Filtering the event list will change how the various components contribute to the final spectra.

6.3.1 Data Error Reproduction

When substituting the burst flux in the HER and SHER data sets with the output from the simulated flux the performance of final spectral fitting will depend on the error bars in the data. The simulations will have there own intrinsic Poisson error. The recorded data will also include errors due to the level of the flux over the background noise along with the Poisson counting statistics. The reproduction of the correct errors is vital to reproducing the same fitting procedure.

To simulate the background levels alongside the burst flux would be a folly as the data already exists. The background was evaluated as it is in standard burst evaluations: The average background count-rates before and after the burst were taken and the mean count-rate taken. This background flux was then used to adjust the Poisson errors of the simulation as shown in equation 6.3.

$$\Delta Flux_{simulated} = \sqrt{Flux_{filtered} + \overline{Background}} \tag{6.3}$$

6.3.2 Event Filtering Criteria

The production of the BATSE detector responses involved individual calibration of each of the 8 modules on the ground alongside Monte Carlo techniques to estimate the effects that the CGRO bus and other instruments would have on the BATSE

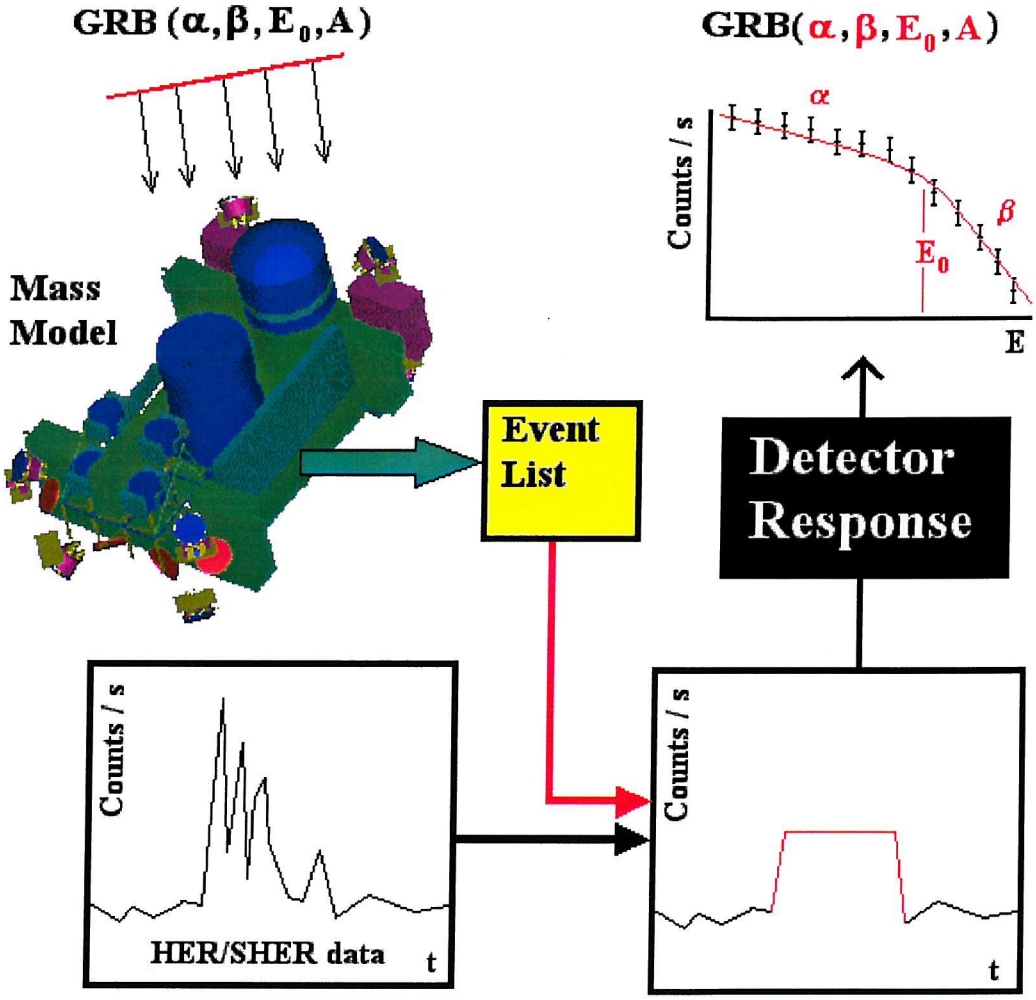

Figure 6.2: **The data-flow for evaluating the BATSE GRB self-contamination.** *The comparison of the parameters of the input and output spectrum is result of this process. The only variable component is the event list. Altering the criteria by which events will contribute to the total flux will change the final time-averaged spectral fit.*

DRM. Once in orbit, in-flight calibrations were carried out to finally configure the DRM. This multi-stage process was the only practical way of calibrating the instrument. The only true empirical calibration was of the individual BATSE modules. The correction applied to this was from Monte Carlo simulations performed prior to the 1991 launch to compensate for the rest of the spacecraft and so could be assumed to be the weakest part of the calibration process due to the inadequacies of computer techniques compared with the modern day. Therefore, assuming the discrepancy can be reproduced, the first filtering criteria to be employed will be to divide the reprocessed flux between photons interacting with just the BATSE module before being detected and those that interact with some part of the rest of the spacecraft before being detected. Should the results show that any discrepancy can be corrected by filtering out flux that interacts with material outside the BATSE module then it can be concluded that the initial Monte Carlo corrections were inadequate and require correction.

Some useful selection considerations need to also be mentioned at this point. Preece *et al.* (1996) [90] showed that for the lower energy bands of the SDs there was evidence for the inclusion of a low energy component to the standard model of GRBs (Eqns. 6.1 and 6.2). Indeed, for trigger 143, the residuals in the 10.2-18.7 keV energy range had a significance of 22.54 σ (defined as $\frac{Counts_{observed}-Counts_{model}}{data\ error}$). For this approach to work a good level of confidence in the model needs to be present. By inspecting the level of re-processed flux in figure 6.3, the re-processed flux peaks above 100 keV and becomes more significant up to higher energies. Below 100 keV the significance is less. A lower limit of 40 keV was placed on all fitting procedures to maintain the area of the spectrum where the re-processed flux will have the most effect while at the same time retaining confidence in the Band *et al.* (1993) model.

This Mass Modelling approach simply records the energy deposits within the detector scintillator crystals and a brief history of each photon. The HER/SHER data will record the same energy deposits but only after they have passed through the Photo-Multiplier Tubes (PMT) and Central Electronics Unit (CEU). Any non-linearities within the PMT and CEU were corrected for by adjustments to the gains within the system. However there will ultimately be consequences of the detector electronics included inside the detector response. Should the effects of the PMTs and electronics be included into the model then the spectra obtained from simulations should fit identically with the spectra fired into the model. As the effects of the electronics are not included then some small effects may come into play and a "perfect" reproduction of the burst data may not give exactly the same parameters as was used to fire in the input spectrum. Trigger 1625 is known to produce the same spectral parameters for the LAD and SD and so how trigger 1625 performs in this process will be used as a measure of how much the electronics and PMTs effect this investigation. Trigger 143 can then be scrutinised as a comparison to trigger 1625. The only characteristic difference between the two triggers is the incident angle at which the burst is observed.

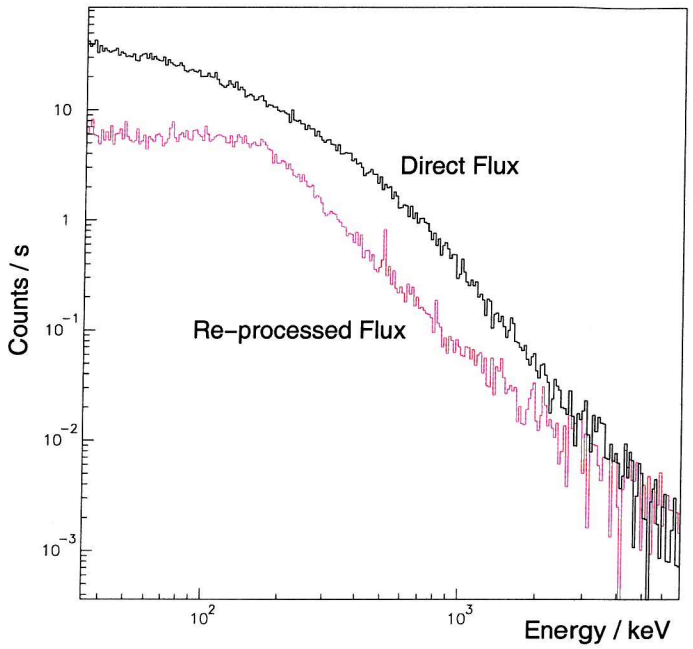

Figure 6.3: **The direct and re-processed flux for Trigger 143.**

6.4 The Results

The method outlined in the previous section was carried out and the burst data was replaced with the time-averaged simulated flux. Figure 6.4 shows this replacement. The process of analysing the burst is independant of the burst profile as each band is time-averaged.

The two parameters that will be most dependent on the shape of the spectrum will be the two spectral indicies, α and β. Admittedly the position of E_0 will be important but will most likely be a consequence of the α and β values. Referring to table 6.1 the E_0 discrepancy between the SD and LAD values is small in comparison. In conjunction with this, the burst strength determining parameter, A, varies little where the spectral fit varies. For these reasons any discrepancy will be presented by a significance contour plot of the two parameters, α and β. A significance contour plot is a 2 dimensional histogram of the reduced χ^2 value for a fit determined by a grid of values of α and β. The centre of the contours will be the best fit to the data and the extent of the contours will be determined by the errors in the data.

6.4.1 Trigger 1625

The first burst investigated was the control burst. The significance contours for the fit to the two simulated detectors are shown in figure 6.5. For each of the two

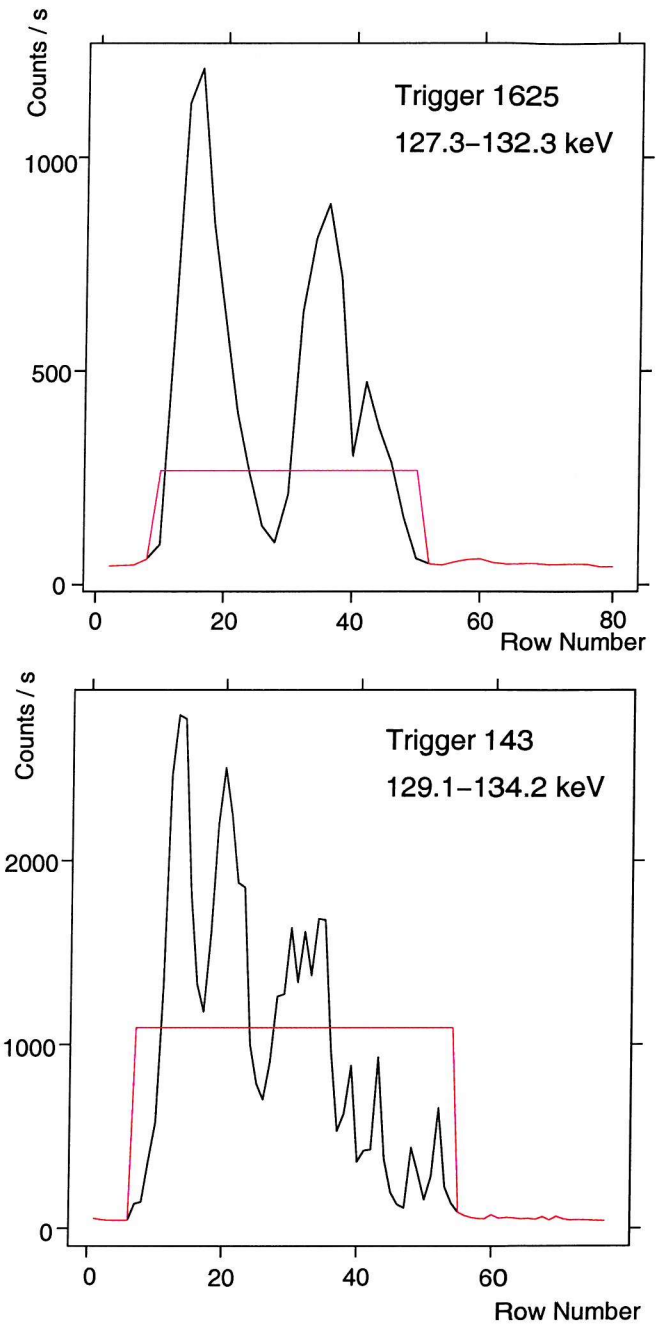

Figure 6.4: **The burst profiles for Triggers 1625 and 143.** *The measured burst profiles in black have been replaced by the time averaged simulated data in red. The red count rate level does not include any background component as so appears slight lower than the average burst flux. The energy band (channel 30) is purely for arbitrary demonstration.*

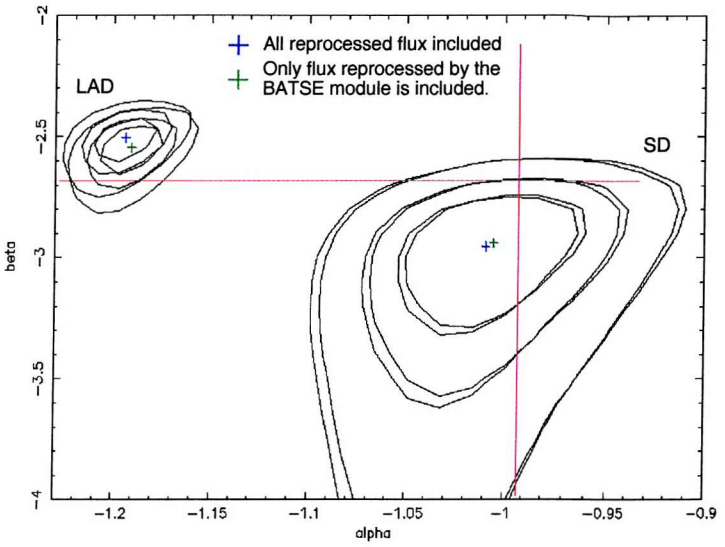

Figure 6.5: **The significance contours of Trigger 1625.** *The contours shown are for confidence levels of 99%, 95% and 68%. The contours with the blue cross at the centre are for the spectral fit to all flux entering the detector. The contours with the green centre cross includes the scattered flux that has interacted with the BATSE module alone, all flux re-processed by the spacecraft was filtered out. The lines red mark the input spectral parameters to the model.*

detectors the simulated data was filtered to show the difference in including flux re-processed outside the BATSE module. By excluding all flux scattered off the spacecraft and other instruments the spectral fits are closer to the input values of α and β. The change is small compared to the size of the contours. Both detectors obtain an estimate of β within the 95% confidence level. However a difference remains when determining the value for α. The true value for α lies well within the 68% confidence level (1 sigma) for the SD but is out by 0.2 for the LAD. The most likely explanation is that this is a consequence of the non-inclusion of the detector electronics in the model. The investigation into the performance for trigger 143 will expect the LAD to perform similarly. The fit of the SD detector is the important factor. The difference between the SD and LAD fits for each trigger is where the contrast exists.

6.4.2 Trigger 143

The significance contours for trigger 143 can be seen in figure 6.6. The difference between this simulated data and the simulations of trigger 1625 is striking. The obvious thing to notice is that the two sets of contours are tighter and much further apart. The fact that the contours are closer together is a result of the much higher count-rate. Firstly the LAD will be considered.

The centre of the LAD contours is away from the true values by approximately the same amounts as in the trigger 1625 analysis. The contours are tighter and so the α and β values are more confidently predicted. Should the count rate simply have been higher for trigger 1625 then the confidence contours would draw in and appear as the do for trigger 143. Again for trigger 143, the sole inclusion of flux that has only been scattered by the BATSE module has moved the centre of the contours closer to the true values. Due to the higher count-rate in this trigger the two LAD fitted values for α and β no longer agree within the confidence contours, an interesting by-product of this study. In conclusion, the LAD has performed for trigger 143 as it did for trigger 1625. The fitted values obtained from the SD can now be compared.

The most obvious difference in figure 6.6 when compared to trigger 1625 is the position of the SD parametrical fit. Again the contours are much tighter but, as is not the case with the LAD fitting, the position of the α and β values is far removed from the true values and the LAD values. The performance of the LAD for trigger 143 is equivalent to the performance of the LAD for trigger 1625, as was expected. However, the SD fitting procedure has clearly included some effect that has caused the position of both the spectral indicies to be different from the input values by far more than for trigger 1625. In conclusion, the problem that this chapter is addressing has been successfully re-produced within a simulation.

Now that the original problem has been reproduced explanations, i.e. the effects of the scattered flux can be tested, as to how the two detectors can obtain such different values. The power of the Mass Modelling approach can be brought to bear. By selecting and weighting the reprocessed flux the position of the fitted parameters may move. By finding what has caused these parameters to move so far from the input values, an indication of how the DRM is inadequate can be concluded. As it stands it seems that the inclusion of the scattered flux from outside the BATSE module worsens the fit. The fact that the contours for the LAD are not coincident with the true values is an area that would require further investigation as it is. This approach has the benefit of knowing the source spectra before deconvolving a spectrum from the detector response, something that is only done during calibrations and even then not to the same extent.

The next step was to separate the re-processed flux from the flux that goes straight into the detector from the burst. After changing the weighting of this reprocessed flux the same analytical procedure was carried out on trigger 143 to see if this alters the position of the significance contours. This is easily done but by altering the levels of the scattered flux the total count rate would change and so the confidence contours would expand or close-in accordingly. For this reason when the weighting of the scattered flux is changed the direct fiux is correspondingly altered so that the total flux is always constant for each energy band.

By changing the levels of the scattered contribution to the burst flux the position

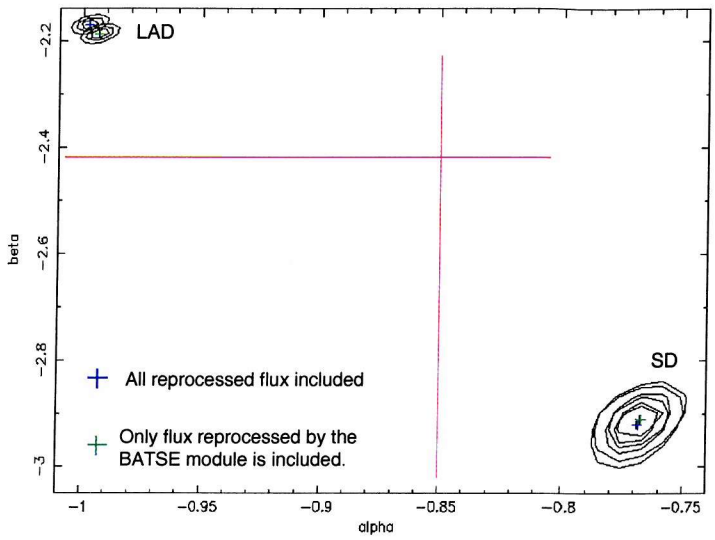

Figure 6.6: **The significance contours of the off-axis Trigger 143.** *The contours shown are for confidence levels of 99%, 95% and 68%. The contours with the blue cross at the centre are for the spectral fit to all flux entering the detector. The contours with the green centre on includes the scattered flux that has interacted with the BATSE module alone, all flux re-processed by the spacecraft was filtered out. The lines mark the input spectral parameters to the model.*

of the contour plots did change. By proportionally increasing the re-processed flux the α parameter moves closer the true value while the β parameter moves away and vice versa when the re-processed flux is proportionally decreased. So any change in the weighting of the re-processed flux would have to be energy dependent. An example of a beneficial energy dependent change to the re-processed components is shown in figure 6.7. The weighting used for the scattered components was a linear weighting with respect to the channel number. For channel 1 the reprocessed weighting was 0.1 with the weighting for channel 252 being 2.0. This linear weighting converts to the energy dependent relationship as seen in figure 6.8.

6.4.3 Conclusions

The primary aim of this investigation was to determine if the scattered component to the recorded data was responsible for any inconsistencies between the LAD and SD detector results. One possible reason for this was inadequate detector responses for the SDs. Two bursts were used as a comparison and it has shown that when a burst is off-axis from the SD, in this case 50.3^o offaxis, the spectral parameters obtained for the LAD and SD were different whereas when the burst was more on-axis the LAD and SD spectral parameters were much more similar. The BATSE Mass Model (BAMM) reproduced this problem and it was concluded that the burst direction, and so the degree of flux reprocessing, was responsible as this was the

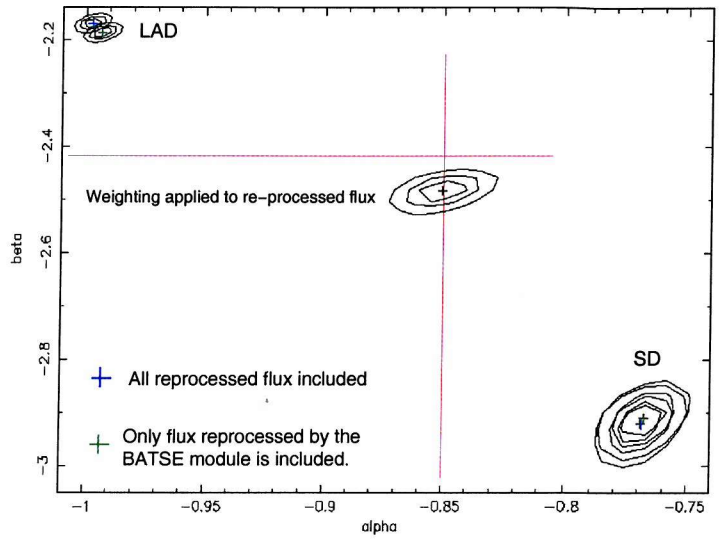

Figure 6.7: **The significance contour plots for Trigger 143 Including a modified SD fit.** *The original significant contours have been left on the plot for comparison. The set of contours most central to the plot are for a scattered flux with a modified weighting. The modification is shown in figure 6.8.*

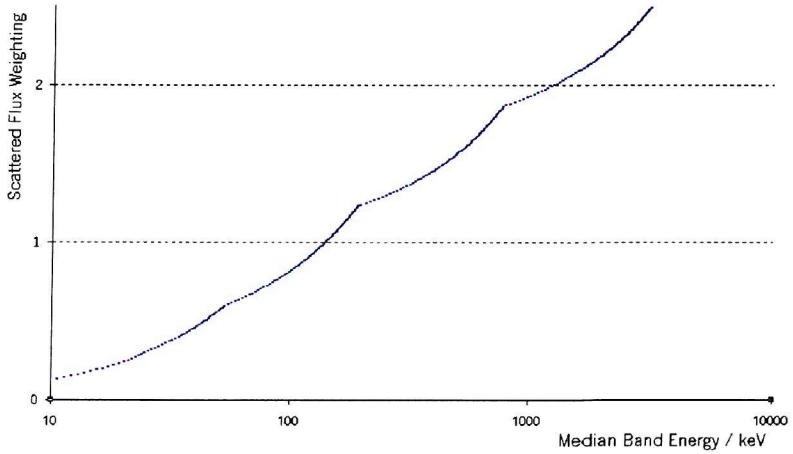

Figure 6.8: **The weighting that when applied to the re-processed flux gives a better fit to the true flux.** *The weighting used here was a linear function of the channel number. Channel 1 had a reprocessed weighting of 0.1 while channel 252 had a weighting of 2.0. This plot is not linear due to the energy band boundaries being non-linear.*

major difference between the two bursts. Both bursts were of different strengths and of different spectral parameters but this would simply lead to the two bursts having different spectra and would not give a difference between the two instruments.

By filtering the event list produced by the model the proportion of flux that is reprocessed before entering the detector can be altered. It was seen that the DRM for the SD was over-estimating the low energy (< 140 keV) reprocessed flux and under-estimating the higher energy reprocessed flux.

Another question this chapter has raised is the accuracy of the LADs with respect to the input spectrum. For the purposes of this investigation the LAD fitted values were assumed to be correct. It is conceivable that the discrepancy between the LAD fitted spectral parameters and the true data is also due to an incorrect estimation of the re-processed flux. For both triggers the spectral fit was out by a similar amount and was off-axis by a similar amount. At this stage no comparison for on-axis bursts has been simulated and so this effect may well be present in burst detection from every direction.

One effect that was seen in every simulation was from the separation of the flux scattered by the spacecraft from the flux scattered by the BATSE module. In each case by excluding the flux scattered from other parts of the spacecraft the fit moved closer to the true values.

Though it has been shown that the DRMs require some adjustment with regards to the re-processed flux entering the SD there is also evidence for looking into the same effect for the LADs. Not only are the levels and energy dependence in question but the source of the scattered flux also. For the next step, bursts would not have to be used directly. Instead a standard DRM would have to be produced using a series of mono-energetic and multi-directional simulations. This would then have to be compared to the current DRM production method.

The implications of inaccuracies in the detector responses is large in that the BATSE burst catalogue is the largest and most comprehensive GRB catalogue available. As it stands the distributions of α and β show no obvious correlations with a theory due to the diverse nature of GRB spectra. Any relationship that could be extracted is certainly not helped by the fact that an off-axis burst is not well reproduced with the current detector responses for the Spectroscopy Detectors.

Chapter 7

The Swift Hard X-ray Survey

7.1 Introduction

During the hard X-ray survey programme the main problem facing the survey scientists will be the removal of the background (J. Tueller, private communication, 2002). Throughout the Swift orbit the spatial and temporal background modulations will both be important to image deconvolution. High frequency spatial variations across the detector plane will add artifacts to a deconvolved image whereas the total background levels will reduce the sensitivity. The removal of these two sources of modulation cannot be separated as any temporal modulation will alter the spatial distribution across the detector array depending on parameters determined by the pointing angle and position above the Earth. Effective coded aperture imaging by way of multi-orbit observations requires that the background variation is correctly accounted for across the detector in both position and time.

Coded-mask imaging is designed to measure background flux alongside the source flux over the detector plane. However, this is only effective for a simple background. Coded-aperture imaging is not as efficient should the background vary across the detector plane over small spatial scales, the same order of magnitude as the mask pattern. The background modulation will interfere with the mask modulation and undesirable artifacts in the deconvolved image will occur. It is also worth noting that any flux originating from an object other than the source being studied will be considered to be "background".

By attempting to account for the background by empirically fitting any recorded data with a polynomial, assumptions are being made about the calibration and the environment of the spacecraft. Concurrently, fitting a high order polynomial to the background across the detector plane in this way includes a fit to and subsequent removal of the source flux. To avoid this, a lower order polynomial can be used but at the expense of accurately predicting the modulation. An empirical fit to data recorded by the instrument can never separate the background from the source flux completely.

In such a wide field instrument, many sources will be visible and so variations across the 32,768 pixels will be highly complex due to the discrete emitting objects alone. It is worth noting that any flux originating from an object other than the source being studied will be considered to be "background". The various sources of background will contribute to the high frequency spatial variations and interfere with the image deconvolution. Empirically fitting these background modulations will give better source images than not accounting for the background modulations at all but information is being lost unnecessarily. For this reason a non-empirical approach is needed to study the background exclusively. This can then be used to maximise the significance of the source-induced high frequency variation, the mask pattern, from any similarly high-frequency background spatial modulation.

This chapter describes a non-empirical approach to removing the background modulation. Unfortunately a drawback of any non-empirical approach is the need for verification. Therefore, before the methods presented in this chapter were applied to Swift, the modelling was also carried out in the context of available data from the BATSE instrument and from proton beam experiments on Cadmium Telluride.

7.2 Modelling the Dynamic Background

7.2.1 Introduction

The dynamic background needs to include all significant background components that an instrument will experience in the context of how that component varies temporally and so spatially. Four components will be calculated here:

- Cosmic Diffuse X-Rays (CDX) modulated by atmospheric absorption and Earth shadowing.
- Fully directional dependent atmospheric albedo gamma radiation
- Cosmic Rays modulated by B-field path discrimination and rigidity anisotropy
- Delayed activation building up asymptotically to an equilibrium

Each of the first three modulate with respect to the pointing angle and where the spacecraft is over the Earth. However each component is effected in different ways by this modulation. Excluding the effects of the South Atlantic Anomaly (SAA), the delayed activation is not traditionally modulated on orbital timescale but builds up over a period of time according to the Cosmic Ray flux. The only significant source of background that is excluded is the SAA. During SAA passages instruments are turned off so as not to risk permanent damage. During SAA passages no data will be recorded that would require analysis, leaving any prediction of prompt SAA flux redundant. The SAA is only included in the context of predicting the radiation

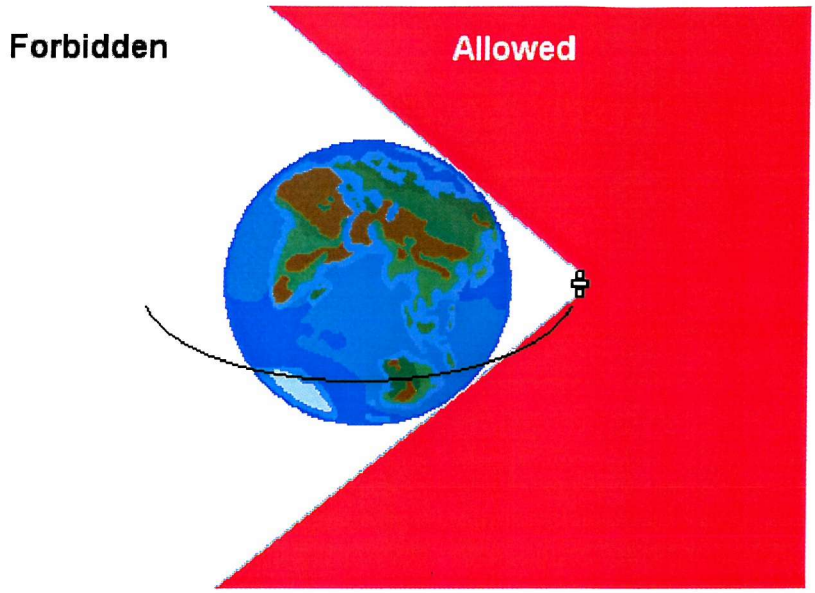

Figure 7.1: **The directional filtering of the CDX background.**

damage timescales and a discussion of the effects of the SAA on the orbital varying background is included when the activation of the instrument is addressed.

The principle behind modelling the dynamic background for the first three components is the same. Firstly the instrument in question is simulated receiving the correct flux density of each of the three components from all directions. The initial momentum vector of each individually simulated photon or proton is stored along side the path history. The event list is then filtered to only include events that originate from realistic directions dependent on the spacecrafts position and pointing direction. By using this method, only three simulations have to be run, one for CDX, Albedo and Cosmic Rays. Once this filtering has been achieved the integrated total Cosmic Ray flux can be used to further simulate the activated isotopes within the instrument geometry.

7.2.2 Cosmic Diffuse X-Rays

The simplest component to model in this way is the Cosmic Diffuse X-ray (CDX) background because away from the Earth the flux can be considered to be isotropic and so only the position of the shadow the Earth casts on the spacecraft needs to be considered. Figure 7.1 is a simple diagram of the principle behind calculating the CDX modulation.

Photons originating from behind the Earth are ignored but photons grazing the atmosphere will suffer attenuation but still reach the spacecraft and should therefore be included. Figure 7.2 shows how the transmission of the atmosphere varies with arrival angle. Also shown is the energy dependence of the relation, suggesting that

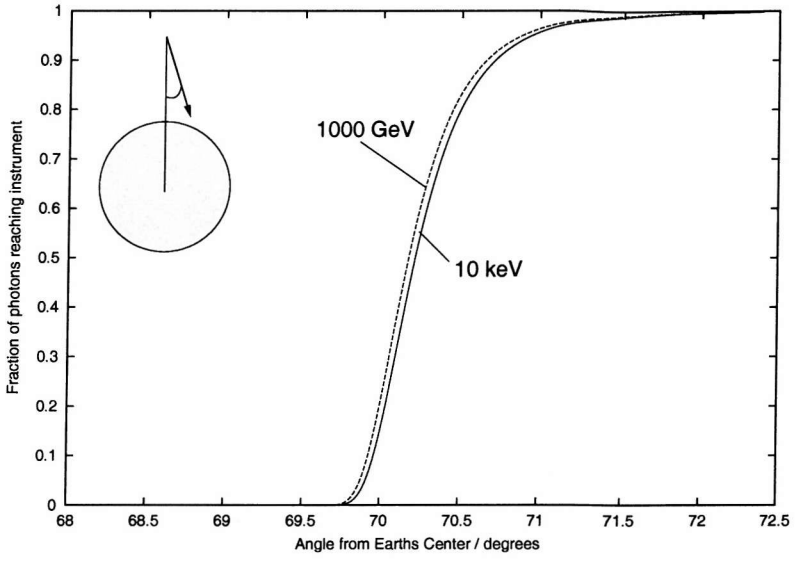

Figure 7.2: **The angular attenuation of the atmosphere.** *Shown here are two lines to demonstrate that the angular dependence is virtually independent of energy.*

the total atmospheric thickness is the overriding consideration and not the initial photon energy. The principle behind this attenuation calculation will be described in more detail when the atmospheric albedo radiation is considered. During the filtering process, an energy independent atmospheric relationship was used. During the simulations of background modulation some assumptions have to be made for the sake of simulation efficiency. The energy dependence of this attenuation is not significant on the angular scale. The difference in the arriving flux between 1000 GeV and 10 keV is within 1% when integrating over the projected solid angle. It is also worth noting that an angular variation in the arrival flux will not necessarily be seen in the final spectra. The Mass Modelling reprocesses all flux and will wash out any of the smaller angular variations like this energy dependence. The attenuation function that was included was not used to select photons that would or would not reach the detector but rather to adjust the weighting of each photon. For an exposure of t seconds the weighting of each photon is $\frac{1}{t}$, this was modified to $\frac{attenuation}{t}$ to account for this effect.

7.2.3 The Atmospheric Albedo Gamma Radiation

The radiation due to Cosmic Rays interacting with the atmosphere is a far more complex problem than the CDX background modulation. As described in chapter 3 a fully non-empirical model for the atmospheric albedo radiation requires an integration over the visible atmosphere including an emissivity function, atmospheric attenuation, particle density functions and accurate modelling of the magnetic field. The aim was to produce a directional distribution of flux as a function of energy and position above the Earth. As this approach contains a high level of complexity a degree of simplification has had to be included. This was either for simulation

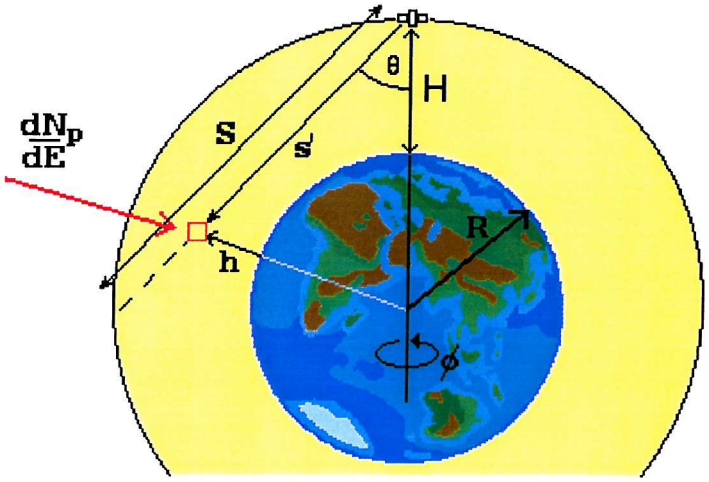

Figure 7.3: **The parameters used in the full atmosphere integration of atmospheric flux.**

efficiency or the simplification of insignificant but complex physical processes. These will be discussed on a case by case basis.

The integration can be broken down by considering the individual terms. Figure 7.3 shows the parameters used by the integration. For the sake of easy interpretation it can be explained as if the system is cylindrically symmetric and so the flux will only be dependent on θ and energy. The inclusion of the azimuthal dependence is simply a question of including some simple trigonometry that would distract from the principles explained here.

The process considers that each element emits gamma rays determined by an emissivity function [25]. Each element will be attenuated according to the amount of absorbing material between the element and the spacecraft. All elements along a line of sight will be integrated, with the limit being the position along the line of sight that is at the same altitude as the spacecraft. The attenuation of the material between the element and the spacecraft is determined by the variation in particle density along this line. For the purpose of this investigation the only method of gamma ray attenuation included was the Compton effect. This assumption is based on figure 2.1 and assumed that the highest Z major element is Oxygen (Z=8). Compton scattering will dominate in a medium of Z=8 between ~0.04-30 MeV. Depending on the energy range that any simulation is to run over, this was thought to be a decent approximation. Further terms for the attenuation could be included should this direction dependence be investigated at much higher or lower energies. The integration along the line-of-sight of the gamma ray flux reaching the spacecraft is described by the equation 7.1.

$$Albedo\,[\theta, E] = \int_0^S F\,[s', \theta, E]\ ds \tag{7.1}$$

This can now be broken down into a function of intensity at the element and the attenuation between the element and the space craft. χ is the atmospheric depth in $g.cm^{-2}$.

$$F\,[s', \theta, E] = I_o\,[E, \chi]\ e^{-\int_0^{s'} \mu[E,\theta,h]\ ds} \tag{7.2}$$

Each term in equation 7.2 can now be broken down further and analysed separately before inclusion. First, the attenuation function can be split into a particle density function, N_z, and the Compton cross section $\sigma\,(E)$. This is shown in equation 7.3. The Compton cross section can be defined by equation 7.4 where $\alpha = \frac{E}{m_e c^2}$ with m_e being the electron mass.

$$\mu\,[E, \theta, h] = \sigma\,(E) \sum_{0 \to max\ Z}^{Z} N_Z\,[\theta, h]\ Z \tag{7.3}$$

$$\sigma\,(\alpha) = \frac{\pi r^2}{\alpha}\left(\left[1 - \frac{2\,(\alpha+1)}{\alpha^2}\right] ln\,(2\alpha+1) + \frac{1}{2} + \frac{4}{\alpha} - \frac{1}{2\,(2\alpha+1)^2}\right) \tag{7.4}$$

The particle density function can be seen in figure 7.4 and a fit was applied to the more prevalent elements. A height dependent convolved function of the particle density/atomic number product is shown in figure 7.5 and in equation 7.5. Though this function does not have the accidence of the data it will suffice for the purposes of the simulations, providing a simple mathematical alternative to including long-winded data files.

$$\sum_Z N_Z Z = 10^{63.27h^{-0.328}} \tag{7.5}$$

Dean (1989) presented the relations, obtained empirically, for the depth dependent emissivity of the Earth's atmosphere. This is quoted in equation 7.6. This leaves a depth dependent function of emissivity measured in $photons.s^{-1}.keV^{-1}.g^{-1}$ with a rigidity correction so that the function can be modified for a specific rigidity. The initial function was obtained from data taken from balloon flights over Palestine, Texas at a rigidity of 4.7. This rigidity correction was described in chapter 2 and is shown in equation 7.7. The rigidity correction is a function of the Cosmic Ray spectrum and cutoff energy, E_{min}, imposed by the magnetic field deflection which is in turn a function of the McIlwain parameter, L. The McIlwain parameter is dependent of the position of the element within the Earth's magnetic field. How they are related will be addressed shortly.

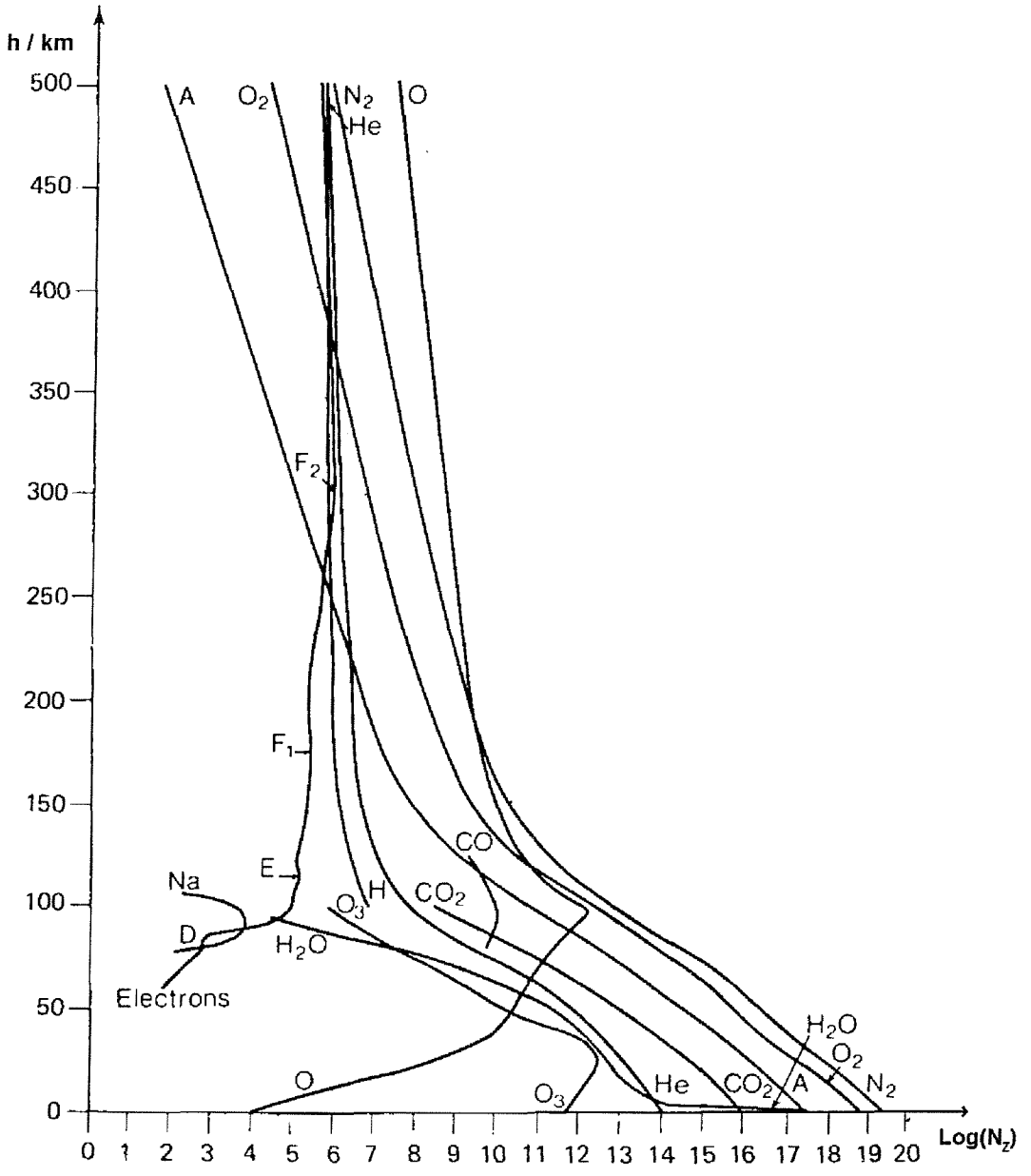

Figure 7.4: **The altitude dependent particle density.** *This plot shows the particle densities of the various elements in the Earth's atmosphere as they vary with altitude. Adapted from "The Handbook of Space and Astronomy" by Zombeck.*

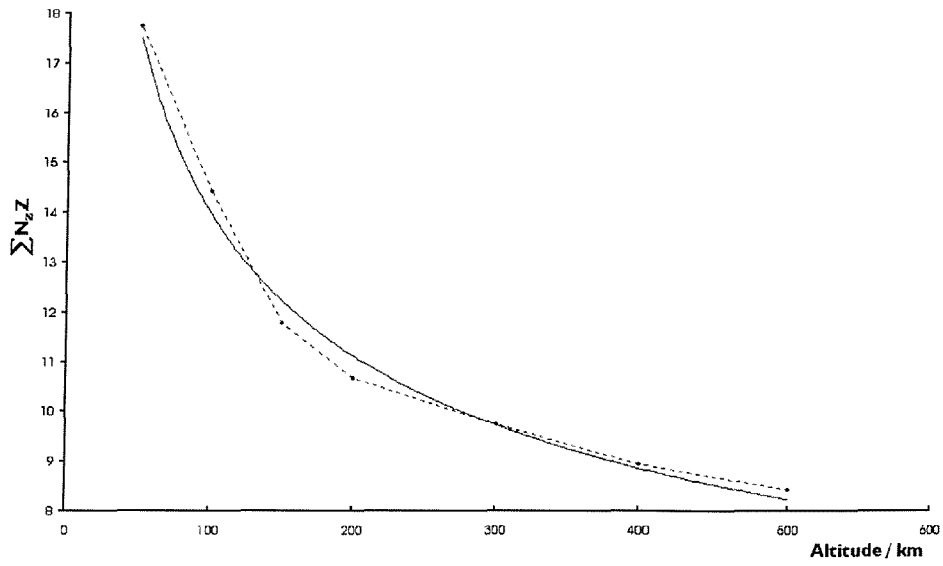

Figure 7.5: **The $\sum N_z Z$ altitude relation.** *The dotted line is effectively the amalgamation of all the element lines in figure 7.4. The solid line is a suitable fit to the data.*

$$I_o\left[E,\chi\right] = 0.75\chi^{0.51}E^{-\left(1.65+0.00256\chi^{\frac{1}{2}}\right)} \times \frac{M_R\left(R_c\right)}{M\left(4.7\right)} \tag{7.6}$$

$$M_R\left(R_c\right) = \int_{10^3\left(-0.938+\left(0.938^2+R_c\right)^{0.5}\right)}^{\infty} \frac{dN\left(E_p\right)}{dE_p} E_p^{0.7}\, dE \tag{7.7}$$

A simple conversion for the sake of consistency in standard units is the conversion of atmospheric depth ($g.cm^{-2}$) and altitude (km). This is included as equation 7.8 and is again a simple mathematical expression fitted to data [134].

$$\chi = 15.74.10^6\ h^{-7.65} \tag{7.8}$$

So, now the flux reaching the spacecraft from any small volume of atmosphere can be calculated using simple trigonometry and with only the following parameters:

- The pointing direction (θ,ϕ)
- The altitude of the spacecraft, H
- The McIlwain parameter at the element, L

Before a full integration can be achieved, a distribution for the McIlwain parameter needs to be sought out. Several approaches to this were considered. The first was to assume to assume the Earth's magnetic field is a simple dipole field,

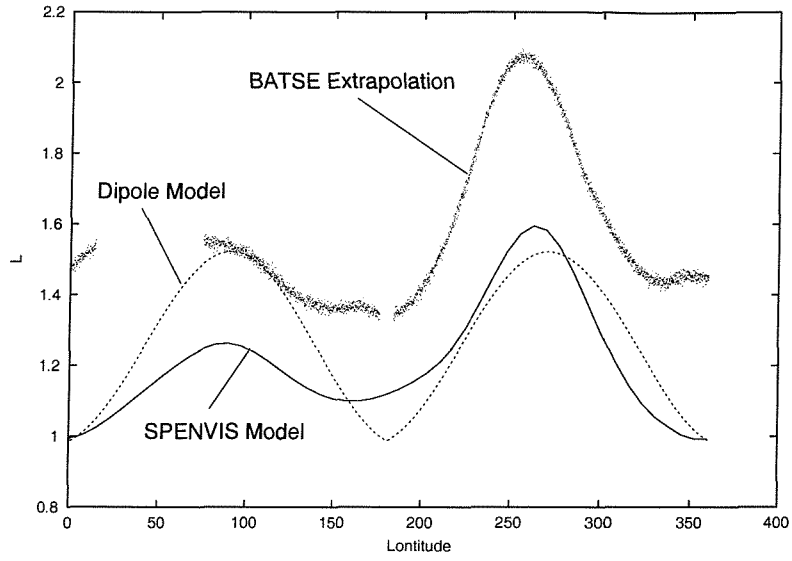

Figure 7.6: **The three models for L.** *Presented here are three approaches for estimating the McIlwain parameter, L, for a single CRGO orbit (500km, 28°). The comparison should be made to the data extrapolated from the BATSE CPD count-rate. This extrapolation will be too high as all counts in the CPD are assumed to be from Cosmic Ray interactions, however the variability should be faithful.*

as a first order approximation. This was compared to BATSE data extrapolations of the L parameter over one orbit. This method employed the Charged Particle Detector (CPD) attached to the surface of each Large Area Detector (LAD). The particle count-rate was extrapolated backwards to determine a value for the McIlwain parameter. This method could not be relied upon to produce the absolute value due to the assumption that all counts received are Cosmic Rays not entirely deflected by the magnetic field. However, the variability in L during the orbit could be implied confidently. An alternative, and entirely non-empirical, approach to obtaining the correct McIlwain parameter distribution was to employ the Space ENVironment Information System (SPENVIS) [107], a series of models describing the space environment sponsored by ESA and based at the Belgium Institute for Space Aeronomy (BIRA-LASB). SPENVIS includes the DGRF/IGRF 45-95 model [5], the GSFC 12/66 model [13], a centred dipole model [4] and the Jensen-Cain model [46]. The combination of these can produce an accurate distribution of the McIlwain parameter. Figure 7.6 shows the variation in L for these three approaches. The BATSE extrapolated data will correctly verify the variability but the offset may not be correct. The simple dipole approximation does not perform well, the main problem being the difference between the two hemispheres. The SPENVIS model reproduces the variability of the BATSE CPD data and is expected to maintain the true values. This model can be obtained from the SPENVIS interface [107] in terms of orbital variations or, more importantly for the albedo flux, in the form of a grid of L values in longtitude, latitude and altitude (an example can be seen in figure 7.7).

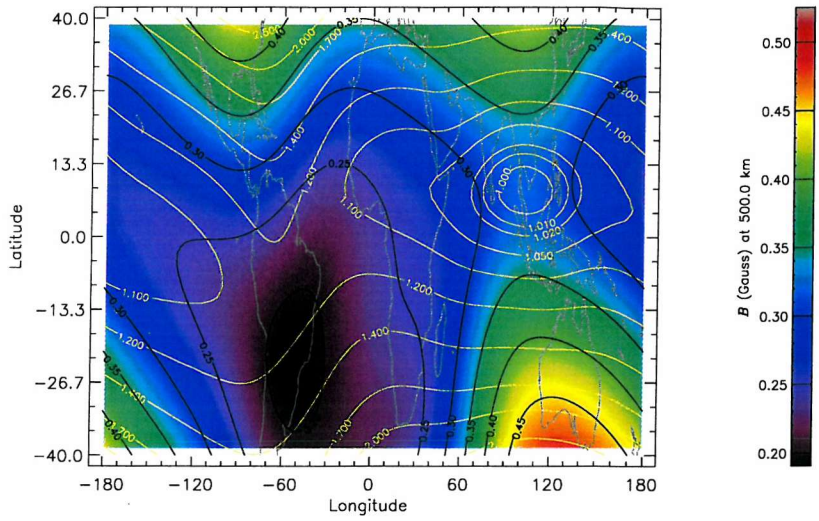

Figure 7.7: **A map of the B-field with contours of L.** *This SPENVIS model interpretation of the Earth's magnetic field shows the variations in B and L at an altitude of 500 km.*

Now a verified model for the magnetic field can be included, the integration can be carried out. The emissivity of any point within the atmosphere can be calculated from the inclusion of the SPENVIS model and the emissivity function (eqn. 7.6). The line of sight integration can then be performed for all angles of θ. The azimuthal averaged variation over θ can be seen in figure 7.8. The inclusion of a full ϕ dependence is shown in figure 7.9.

Now that a fully non-empirical model has been achieved, verification is required by empirical methods. This can be compared to a method used during the SwiMM graded-Z shield optimisation. The component for the atmospheric flux used in chapter 4 was an angle averaged flux quoted by Gehrels (1992) [36]. This albedo integration model was averaged over all angles and compared to the quoted angle-averaged flux in figure 7.10. The two energy spectra are very similar in total integrated flux and spectral index. However there are differences. The spectrum measured by instruments in orbit drops below the theoretical model at higher energies. This difference is due to pair production becoming more likely in the interaction of the photons at these energies (see figure 2.1). This would imply that less photons will be attenuated at higher energies and so the theoretical model will over-estimate the flux. There is also evidence of possible over-estimation at lower energies where the photoelectric effect starts to become significant. As discussed previously the only effect included to attenuate photons in the atmosphere was the Compton effect. So, in the intermediate energy range this effect will dominate and the flux predicted is expected and is seen to be the most accurate. In this comparison the theoretical flux is lower than the measured flux. However, during the measurement of the atmospheric angle-averaged albedo flux, the instruments were also measuring a

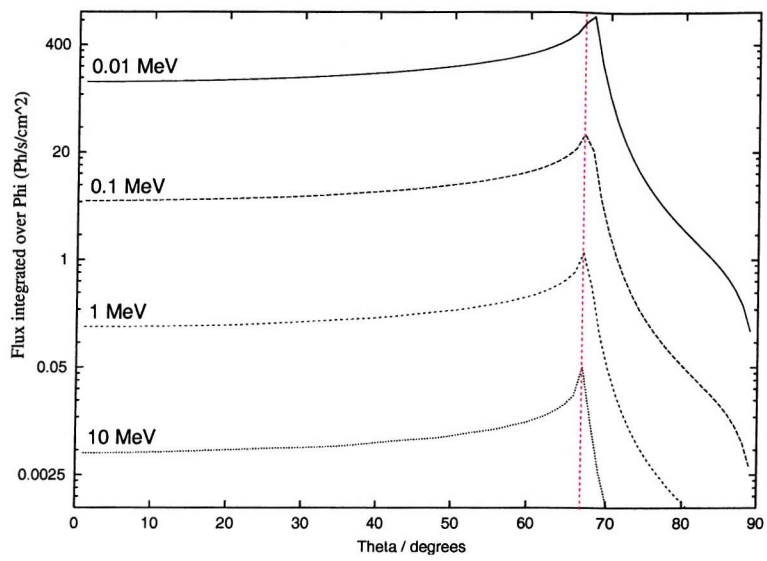

Figure 7.8: **The θ dependent angular variation of the albedo flux.** *This plot shows the angular dependence of the albedo flux integrated over the azimuthal angle, ϕ. Notice the brightening at the Earth's limb, marked with a red-dashed line.*

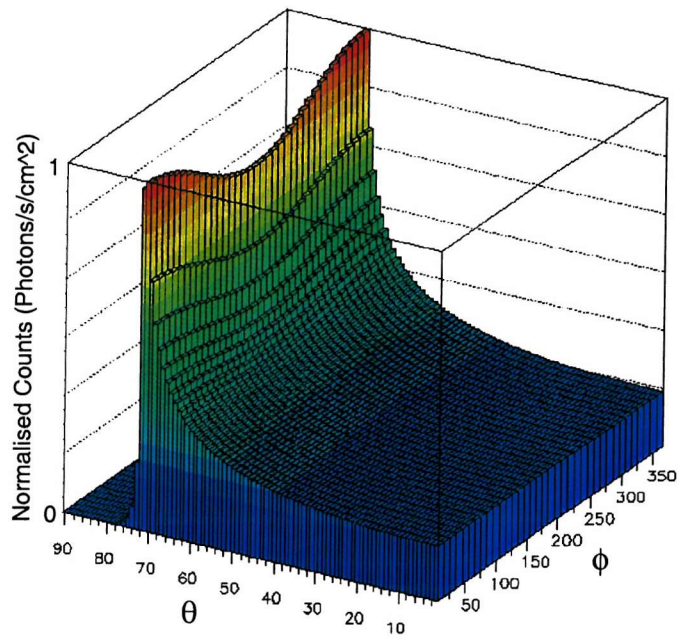

Figure 7.9: **The θ and ϕ dependence of the albedo flux.** *This normalised plot shows the full angular dependence at a latitude of 10°. The limb brightening is the main feature and is strongest when looking toward the north, where L is lowest.*

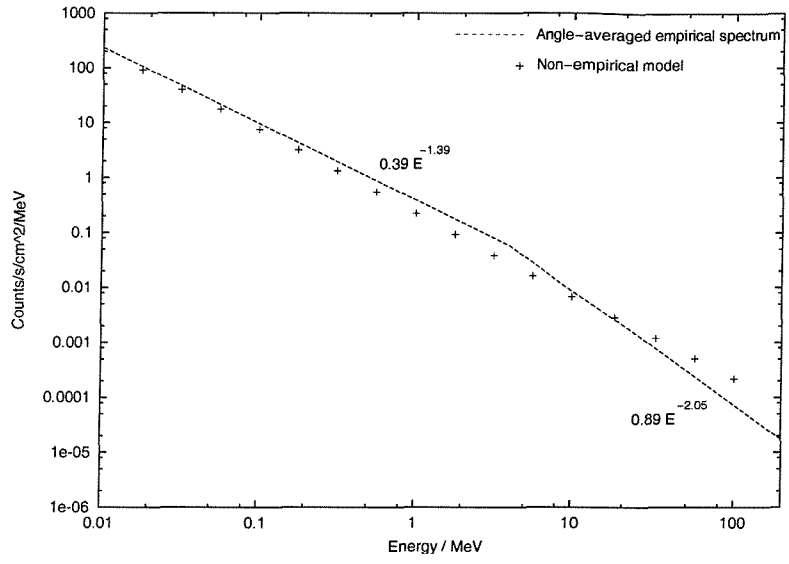

Figure 7.10: **The verification of the atmospheric model.** *Compared here are the measured angle averaged spectrum taken from Gehrels (1992) and the non-empirical atmospheric integration described in this section.*

component from the Cosmic Diffuse X-ray background passing through the Earth's atmosphere. How much this component is hard to estimate without the specific data the measured spectrum was adapted from. Therefore, the theoretical model is expected to predict a lower count-rate as only albedo gamma rays are considered.

As far as which spectrum to ultimately use is concerned (ignoring the angular dependence) there are inaccuracies in both approaches. The benefits of using the non-empirical method is that the origin of all the photons are known and that it stems from a model that has all angular dependencies included. This is vital when considering the modulations in the background and not simply the total count-rate. Unfortunately a correction would now need to be applied to account for the significance of the photoelectric effect and pair-production at lower and higher energies. This correction was not applied in the case of calculating the SwiMM background modulations due to the simulation energy range of 15keV-10MeV. At both 15 keV and 10 MeV the predicted flux is lower than the empirical measurements so if a correction is included based on the angle-averaged measurements the model would loose its current level of independence from recorded data. The model would then include an aspect about which the physical processes were unclear and therefore would be including an unnecessary systematic error. Future versions of the atmospheric model will require the inclusion of the photoelectric effect and pair production but were not included for the purposes of SwiMM partially to maintain the relative simplicity of the model and partially due to the irrelevance of these small effects over the simulations' energy range.

7.2.4 Cosmic Rays

Evaluating the Cosmic Ray modulation involves including aspects that were considered during the CDX and Albedo gamma ray modelling. Cosmic Rays can be stopped from reaching the instrument by two mechanisms. The first is that the Earth will block out a proportion of the Cosmic Rays. Due to the trajectories of the charged particles in the Earth's magnetic field, the Earth will create a shadow (as with the CDX modulation) but be modified by the allowed paths within the B-field. The second mechanism is the deflection of particles by the magnetic field.

B-field Trajectory Discrimination

As was shown in the previous section, the Earth's magnetic field is significantly different from a simple dipole field in terms of the variations in the McIlwain parameter. In this case the magnetic field determines the trajectories of all incident cosmic rays, and applying anything but a simple dipole field would be a far too intensive and intricate a problem for the expected returns. The irregularities in the field will effect the variations in the rigidity considerably but as each particle passes through a significant proportion of the magnetic field these irregularities will be averaged when considering the path deviations during the trajectory. Parallel to this is the fact that each particle will come from a different direction and so pass through a different part of the magnetic field. These two effects will mean that, together, the particles arriving at the instrument will have passed through more than half the Earth's magnetic field and so that the irregularities are unlikely to effect the orbital variation in the Cosmic Ray background.

A dipole field was used to map the trajectories of the charged particles. Each incident angle at the spacecraft has energy limitations as shown by figure 7.11. The diagram shows the case where the particles are traveling perpendicular to the field. A *sine* term was included to account for the full 4π variation. In theory, particles could arrive from any direction were the field weak enough but in practice the field is strong enough to deflect the lower energy Cosmic Rays and so the paths with the most curvature will never occur at the altitudes concerned.

Rigidity

A source of Cosmic Ray flux modulation is the by now familiar problem of rigidity variation. As required by the albedo gamma ray flux a grid of of the McIlwain parameter was obtained from SPENVIS. This grid can now be applied to the Cosmic Ray modulation. The values for the McIlwain parameter can be converted into a directional dependent relationship for the minimum energy cutoff using equations 3.4 and 3.2. Figure 7.12 shows how this cutoff energy varies over an orbit (500 km, 28^o) while figure 7.13 shows how the cutoff energy varies with the arrival direction, a characteristic of charged particles in a magnetic field.

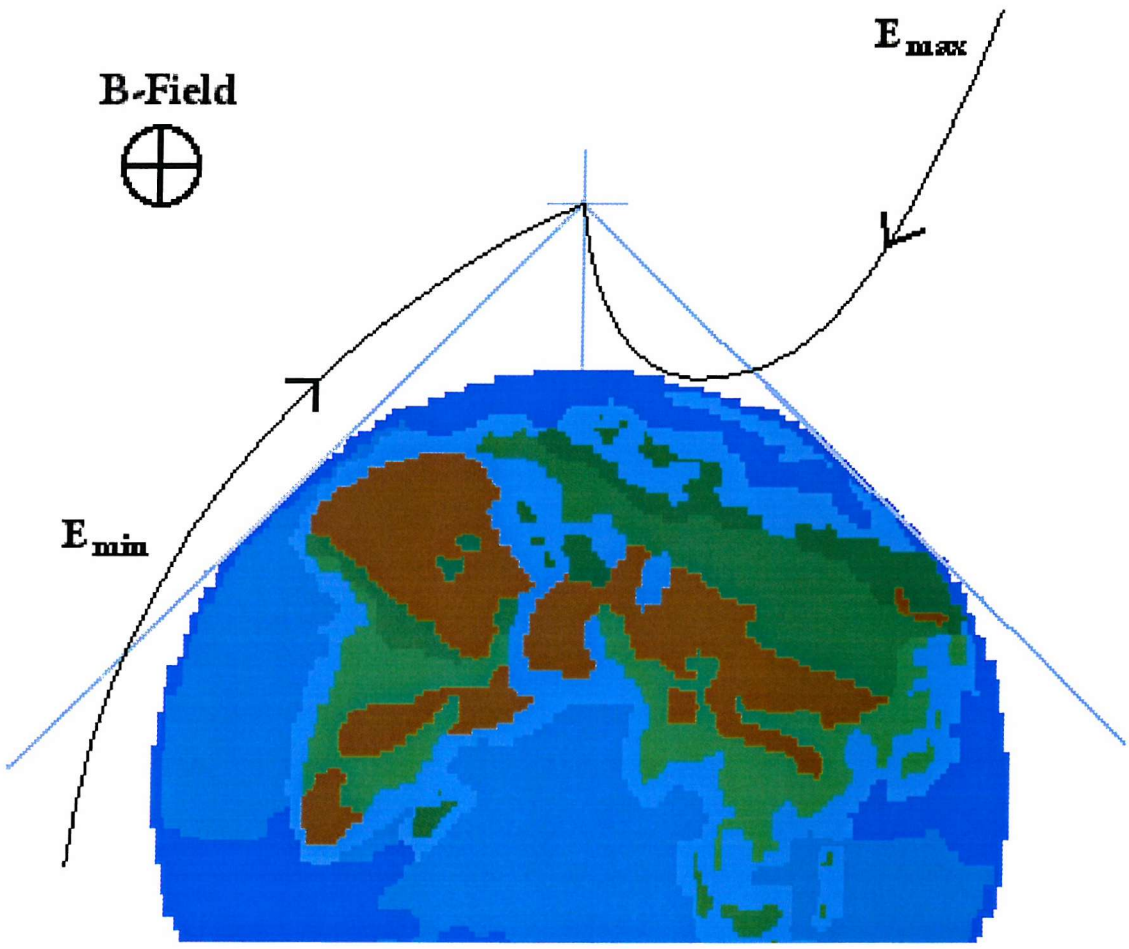

Figure 7.11: **Schematic of B-field path discrimination.** *This diagram shows how the paths of charged particles differ from CDX photons due to the magnetic field. Particles can arrive at the spacecraft from any direction but they are limited by the strength of the magnetic field and so to what energies they can arrive at. The radius of curvature is proportional to* $\sqrt{E}$.

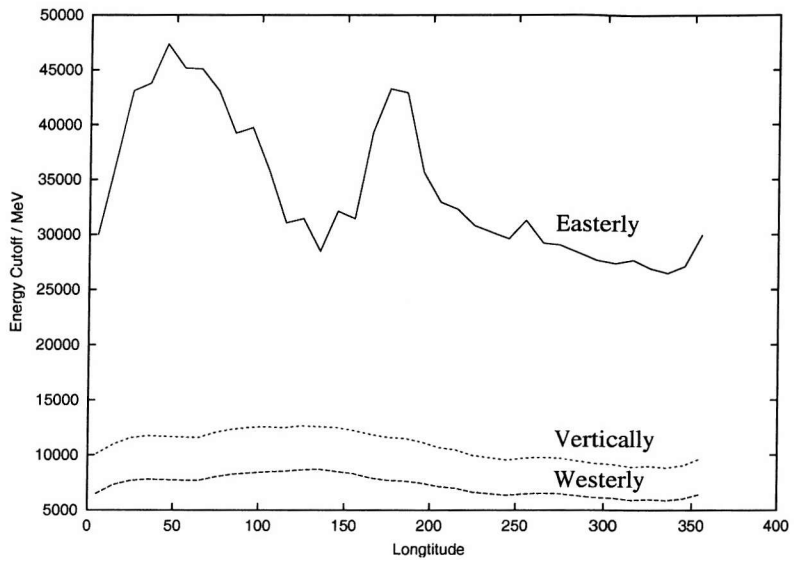

Figure 7.12: **The orbital variation in the cutoff energy of Cosmic Rays.** *This variation is for a standard orbit (500 km, 28°) and shows the vertical, easterly and westerly cutoff energies.*

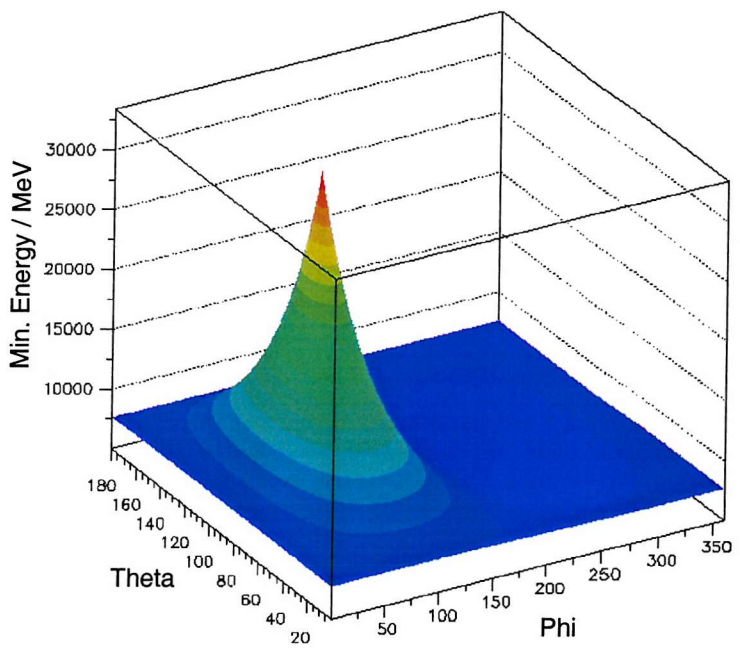

Figure 7.13: **The arrival direction variation in cutoff energy.** *This plot is calculated at a magnetic latitude of* 0° *and where L=1.3.*

7.2.5 Summary

Three models have been assembled to account for modulations in the CDX background, the Earth albedo gamma radiation and the Cosmic Ray flux. Each model was based on non-empirical methods i.e. based on pure physics and the published spectra of each source of the background flux. These were applied to Swift to determine the temporal and spatial modulations. However, confidence in the models cannot be obtained by comparing the simulation results to data recorded by the BAT instrument. So, verification was obtained by considering the BATSE data (CDX, albedo, Cosmic Rays) alongside CdTe bean experiments (activation).

7.3 Model Verification

7.3.1 Introduction

Outlined in the previous sections are various methods to predict the modulations in the background based on non-empirical methods. Though all the physics is correct and any assumptions justified, the success of such an approach is determined by its consistency with the data. All prompt aspects to the background that the BAT will experience on-board Swift were experienced by BATSE due to their similar orbits. Should the variability in the background measured by BATSE be reproduced by the models developed for SwiMM then the results for the simulations of BAT can be relied upon. Each BATSE module utilised a NaI scintillation method of gamma ray detection and so was not a suitable comparison for the activation study. A more comparative verification for the activation was carried out by modelling an experiment whereby a proton beam was incident on a passive block of CdTe.

7.3.2 BATSE Variability

Data from the BATSE experiment were compared to the modelled background modulations. The above criteria were used to filter runs of the BATSE Mass Model (BAMM) [128]. By applying the developed techniques to known data any inaccuracies can be determined and corrected for. The data from the BATSE DISCLA data set was selected at random and the models applied to the LAD data for several orbits. The data presented here was from TJD 9600. Figure 7.14 shows the filtering that was done. What is shown is the directional dependent count-rate contributions. The top three plots show the contributions to the filtering process of the three components. It is worth noting the difference between the CDX and Cosmic Ray components. By not including the path discrimination within the magnetic field a lot more Cosmic Rays would be excluded and so over estimate the background due to this component. The reason why the direction from which the background flux originates is over 4π is that all 8 LADs are included in the plot giving full sky coverage.

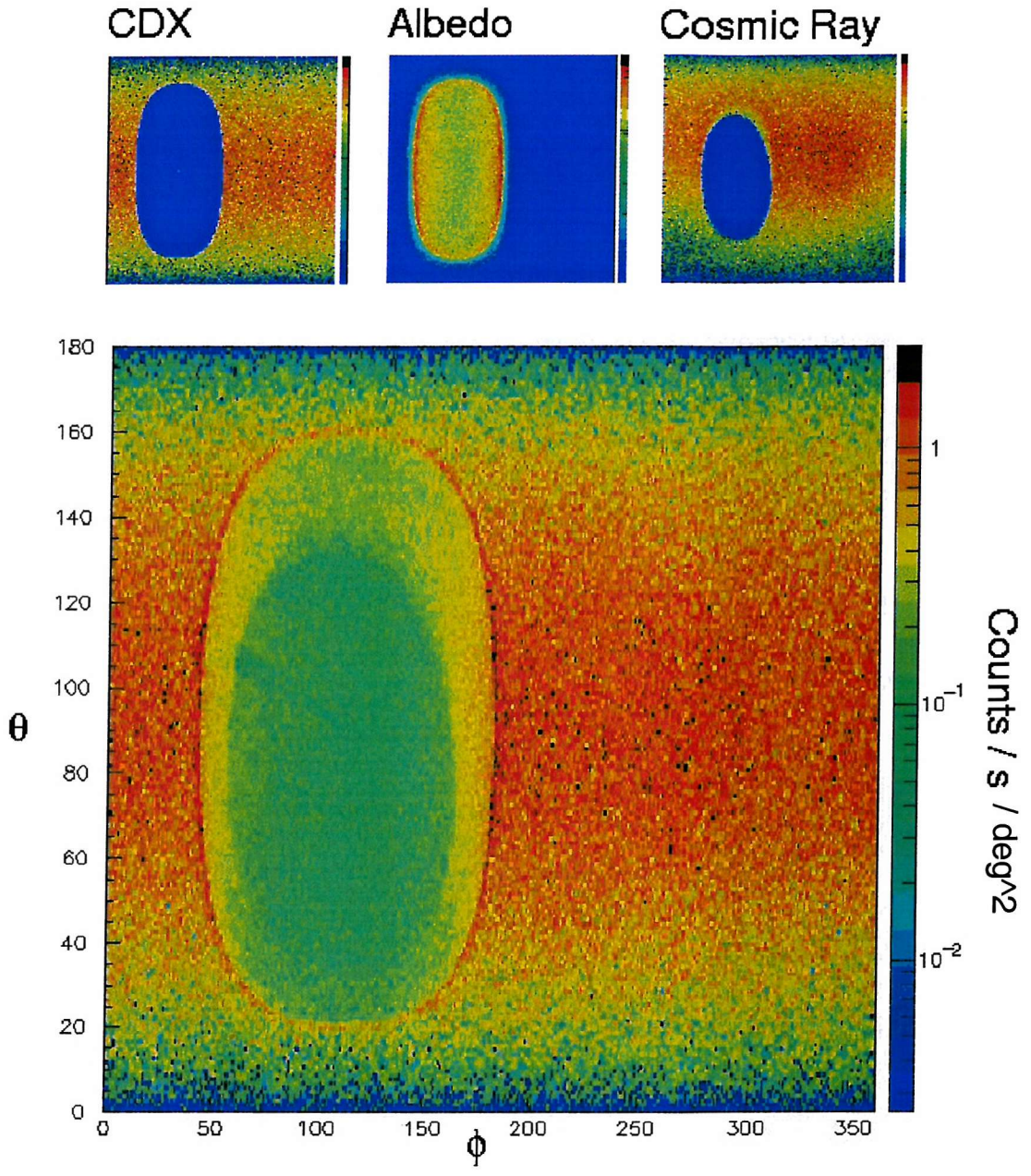

Figure 7.14: **Mass model filtering.** *The arrival direction of every photon included in the unfiltered simulation was recorded. This plot shows the arrival directional dependence of the events that remain after the filtering process. The three components are shown above the total directional dependent count-rate contributions.*

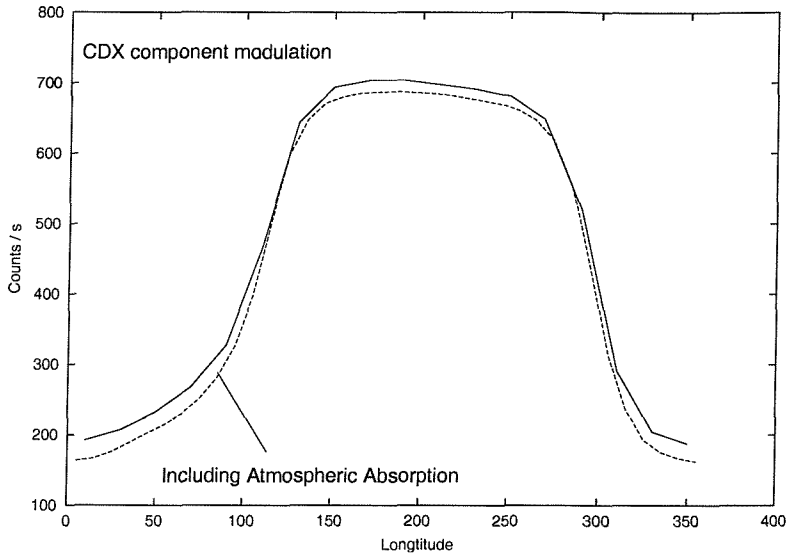

Figure 7.15: **The effects of the atmospheric absorption on the CDX component in the 32.9-42.0 keV energy band.**

Input Spectra

An aspect that could present the biggest problem was initially discovered in the simplest of the three variable components, the Cosmic Diffuse X-ray background. The variability of this source of background is well understood. Efforts were put in to include the subtle effect of absorption at the Earths limb by the atmosphere. This has a noticeable and understandable effect on the CDX count-rate, as seen in figure 7.15. However, a factor that by far outweighs this effect is the choice of CDX input spectrum.

Figure 7.16 shows the results from the filtering of two simulations. Both models were identical apart from the spectrum of the input photons. Table 7.1 contains the spectra used in the two simulations. The difference in count-rate for all LADs is large. The count-rate can differ by as much as 20% for the lower bands, far outstripping any difference in count-rate from the inclusion of a physical process like absorption by the atmosphere. This was a major problem in the background modelling, brought about by the only empirical aspect to the procedure. The two spectra used in this test were commonly used and accepted values for the fit to the CDX background. In chapter 2 the many origins of the CDX background were discussed, with no one source dominating over the entire energy range. The energy range of interest is 0.01-40 MeV, which would cover most instruments that require this modelling. By simple inspection of various published data a simple power law fit is inadequate. Figures 7.17 [99] and 7.18 [?] show the structure within the CDX background for higher and lower energy ranges respectively. The two fits applied to the data collated for each figure were simulated and give the difference seen in figure 7.16. Both fits are valid as a first order approximation but, as the BATSE

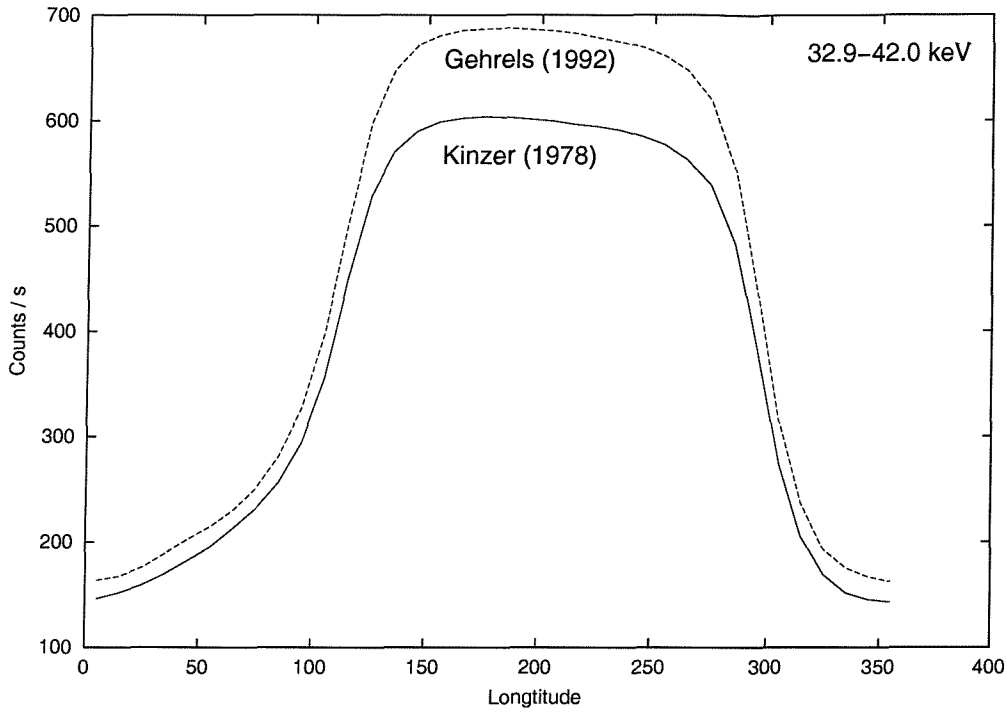

Figure 7.16: **The difference in the CDX background component for two different published input spectra.** *This plot shows just the CDX background component for the energy band 32.9-42.0 keV.*

Table 7.1: *The two input CDX spectra used in figure 7.16*

Source of Spectra	Spectrum $[ph.s^{-1}.cm^{-2}.sr^{-1}.keV^{-1}]$
Gehrels (1992)	161.505 $E^{-2.38}$ [E: 20-100 keV]
	111.734 $E^{-2.3}$ [E:>100keV]
Kinzer (1978)	67 $E^{-2.17}$ [E: >20 keV]

modelling shows, the background modulation is very sensitive to any small change. This sensitivity to small changes in the input spectrum could be used to extrapolate the true spectrum of the CDX background from fitting the modelled CDX modulations to the 10 years of BATSE data. This would provide a method to determine the input spectrum to be used in all background simulations and indeed for more astronomical purposes.

Though there are more complex approaches to fitting the CDX background [38], an adjusted combination of the two fits were used to represent the softening above 100 keV. The input spectrum that reproduced the best results for the BATSE data is shown in equation 7.9, measured in $ph.s^{-1}.cm^{-2}.sr^{-1}.keV^{-1}$.

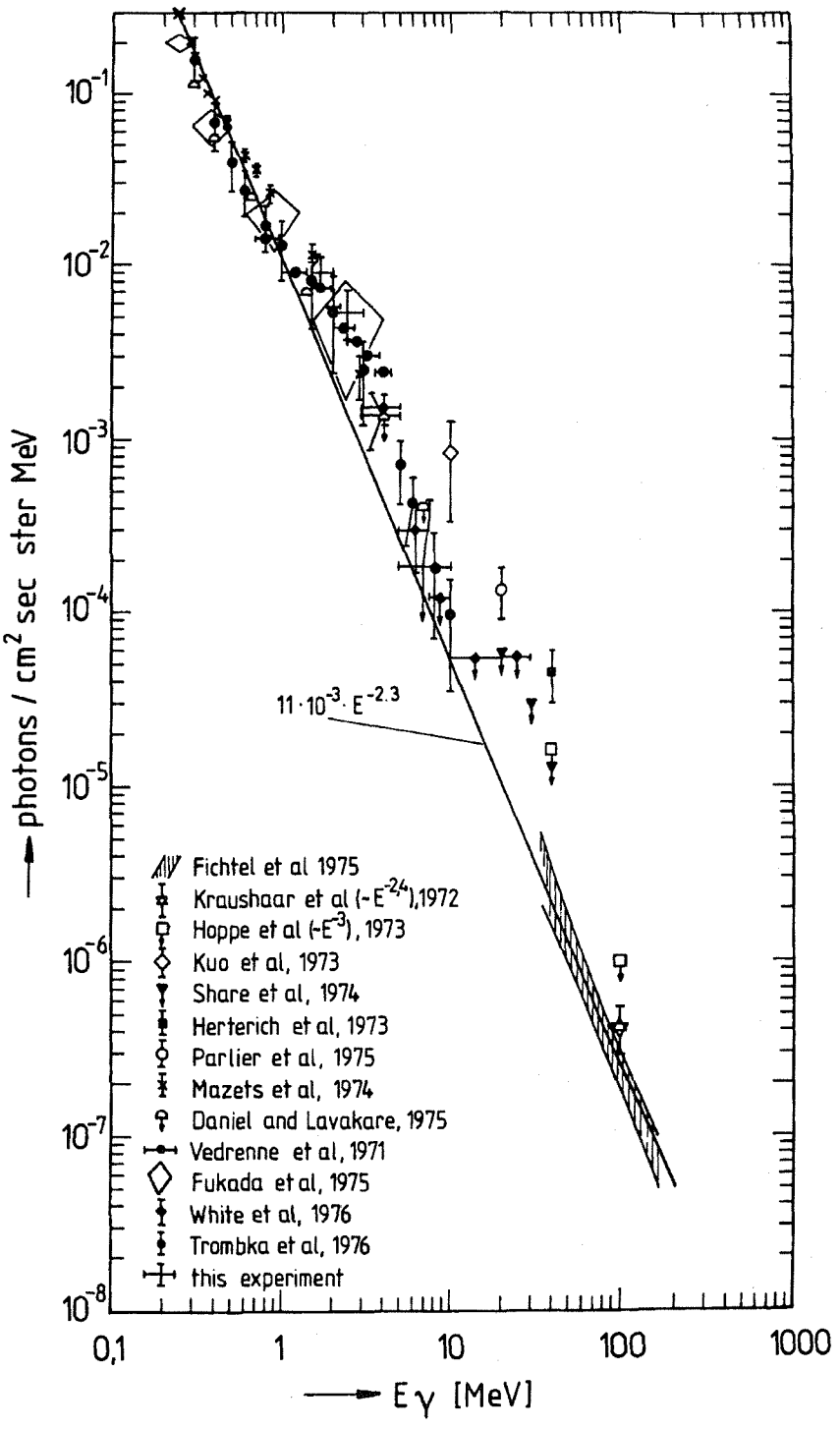

Figure 7.17: **The CDX spectrum [Schonfelder *et al.* (1977)].** *This spectrum for the CDX background contains data from many sources and has a spectral fit of index -2.3 included. Though a power law can describe a basic trend there is clearly much more structure present. This fit is the one quoted in Gehrels (1992).*

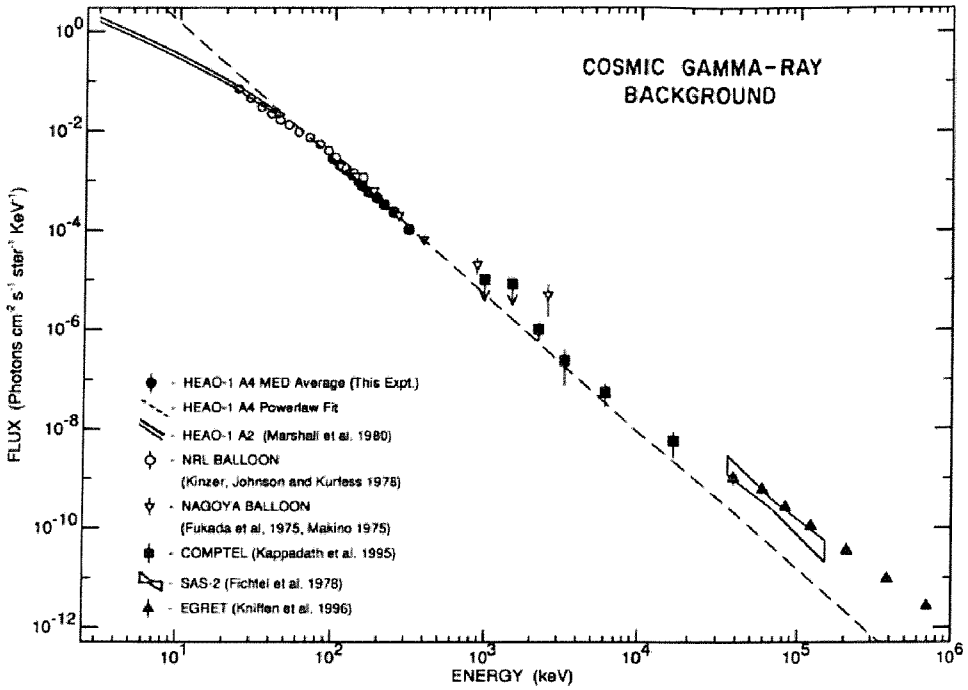

Figure 7.18: **The CDX spectrum [Kinzer *et al.* (1997)].** *This spectrum also contains data from several sources and includes the fit quoted from Kinzer (1997), index -2.17. The spectra clearly softens at higher and lower energies.*

$$\begin{aligned}
\frac{dI(E)}{dE} &= 6.67E^{-1.4} \quad (10-20keV) \\
\frac{dI(E)}{dE} &= 67.0E^{-2.17} \quad (20-100keV) \\
\frac{dI(E)}{dE} &= 121.9E^{-2.3} \quad (>100keV)
\end{aligned} \tag{7.9}$$

Here the inadequacies of the input CDX background spectrum have been outlined. This arose due to the obvious dominance of this effect in the low energy bands. At higher energies no single component dominates and so any errors in the input spectrum for Cosmic Rays and the convolved spectral errors in the non-empirical atmospheric albedo approach is not so immediately obvious, if there are any. Before the modulation can be calculated with total confidence, all three components' input spectra would have to undergo an extrapolation from the data. This would provide a further means to verifying the input spectral parameters. The drawback to extrapolating a background component spectrum is that included in the data are counts from the galactic plane, strong sources within the field of view, activation of the instrument and scattered flux from all these sources. To account for all these components, models for every component would have to be included

and an iterative method carried out. This was not carried out because the aims of the background evaluation for the BAT was to provide an initial estimation for the background modulation that will be refined further during calibration, beam experiments, initial in-flight data and more detailed models. By including data analysis from another experiment at this stage would be including possible external systematic errors. The results presented below provide a good indication that the modulations are being represented correctly though the absolute values cannot be as certain due to the other components involved.

Results

The mass model runs were filtered according to the non-empirical criteria. These results were compared to data from the LADs on-board the CGRO for a series of orbits during TJD 4600. This day was selected as the orbits were far from SAA passages and contained no significant burst triggers. The data is shown in conjunction with the total background count-rates obtained from the modelling in figures 7.19 (low energy) and 7.20 (high energy). The data is matched well but not without discrepancies. Though the absolute count-rate includes many sources and several components not included in the modelling it appears as though the CDX component is overetimated in relation to the other two components which appear to be underestimated. This is clearest in the lowest energy band. The area where the total modelled count-rate pulls away from the data is where the albedo flux becomes significant. By increasing the albedo flux accordingly the data would be matched perfectly though any increase would have to be justified non-empirically. This trade off between the CDX and albedo flux is also seen in the first plot in figure 7.20, during the latter part of the orbit.

Though some discrepancies do exist in this verification, the model has performed well. The temptation to remove any irregularities should be resisted unless a physical reason can be found to justify such a move. As discussed in the previous section a lot can hinge on the initial input spectrum fired into the model. The effect of an input spectrum that is incorrect can be large and so any inconsistencies can be addressed in those terms, initially at least.

7.3.3 CdTe Beam Experiments

The fourth major component to an instruments gamma ray background is the activation that occurs as the spacecraft is bombarded with Cosmic Rays and trapped charged particles. The GGOD suite of software models this component which should also be verified. Part of the SwiMM evaluation is to determine how the detectors will perform during irradiation in space. This could be modelled or estimations obtained from beam experiments. Experiments were conducted by the Institute for Space and Astronautical Sciences (ISAS) by which a passive CdTe block is irradiated and then left so that all activated isotopes decay emitting an induced gamma ray spectrum. These spectra were obtained by a HPGe solid state detector after various decay

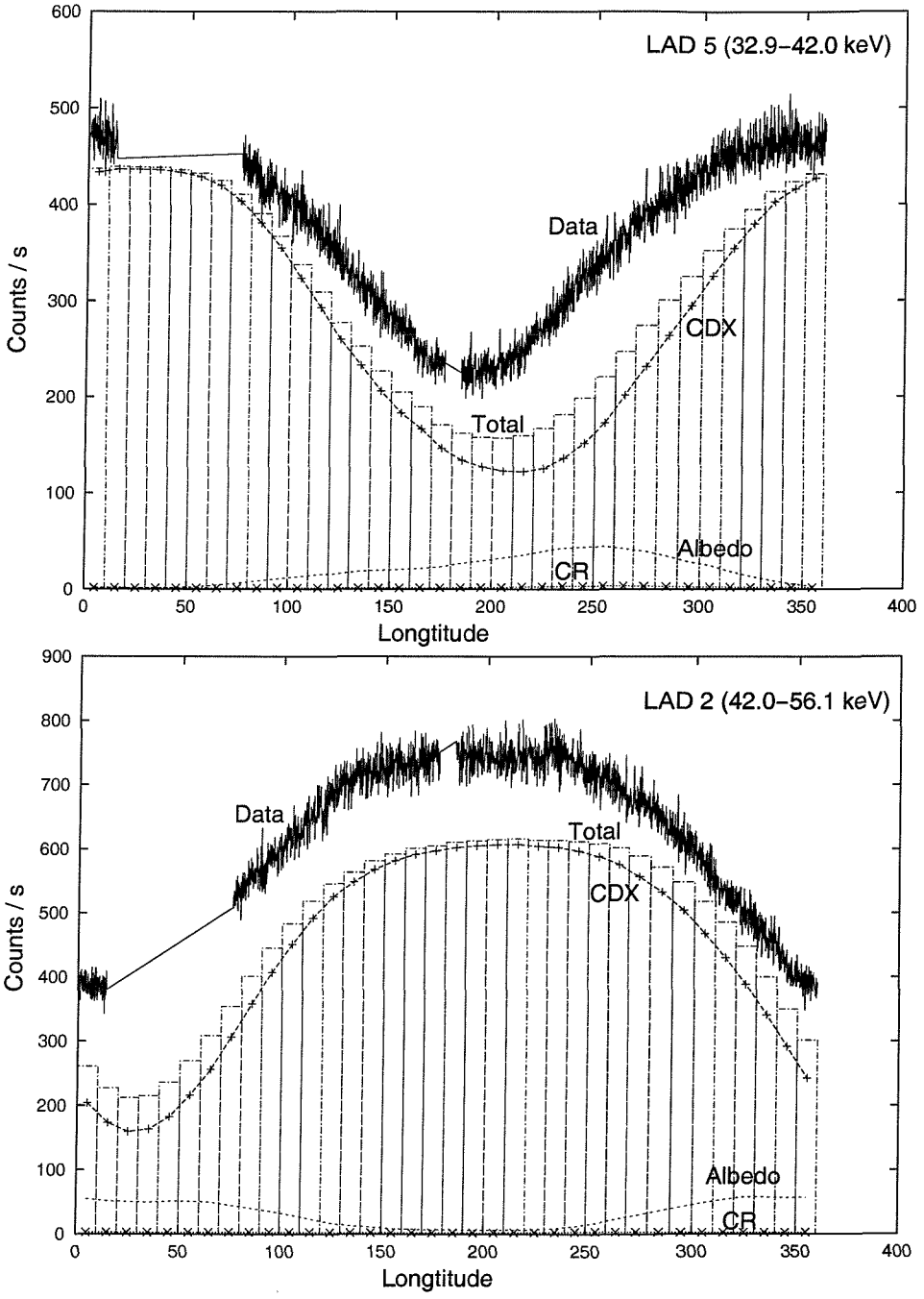

Figure 7.19: **Background modulations for low energy bands.** *Shown here are the model results compared to the DISCLA data set for an orbit during TJD 4600. The CDX background component dominates as expected.*

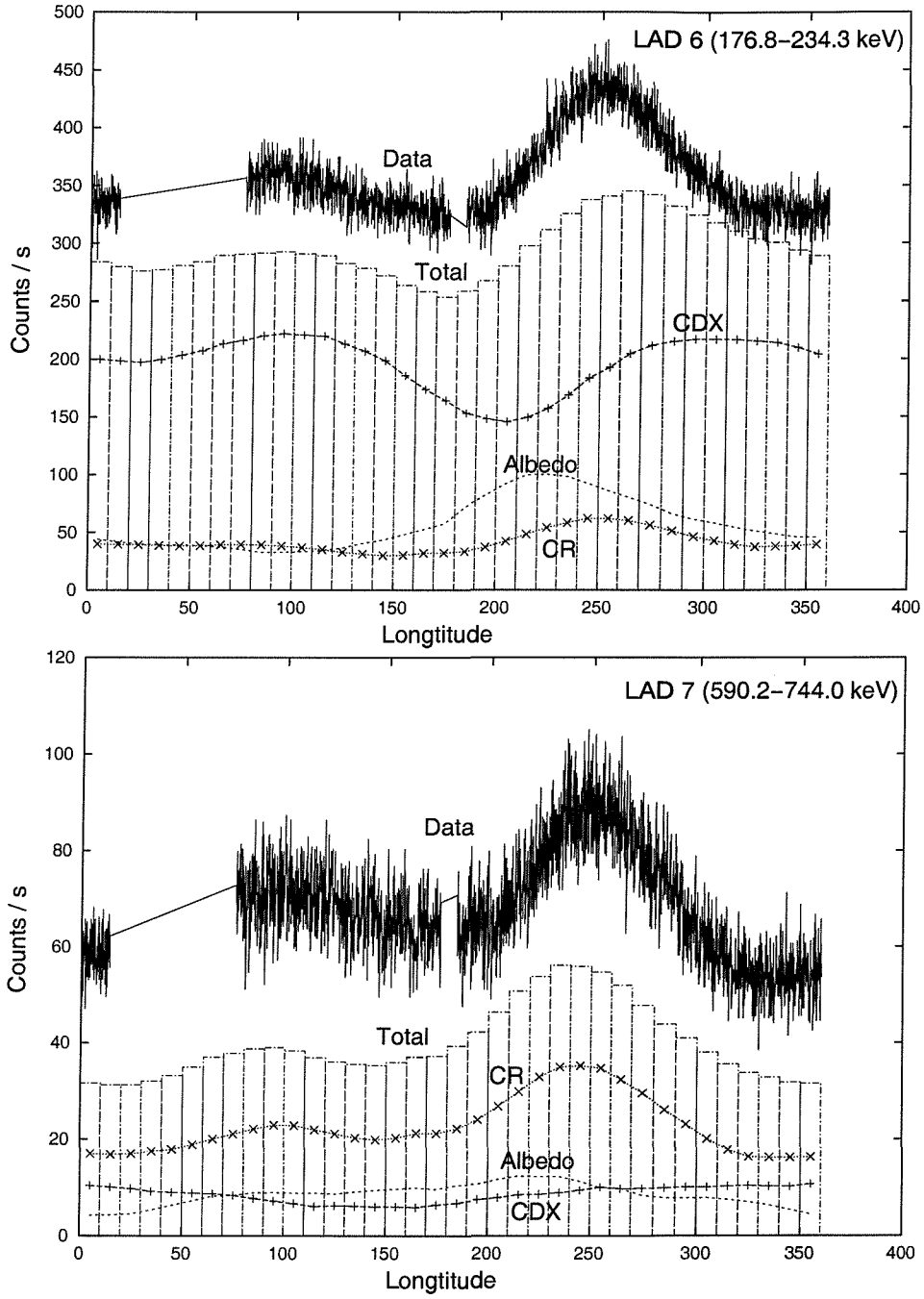

Figure 7.20: **Background modulations for high energy bands.** *Shown here are the model results compared to the DISCLA data set for an orbit during TJD 4600. The CDX background is significant but the two other modelled components contribute.*

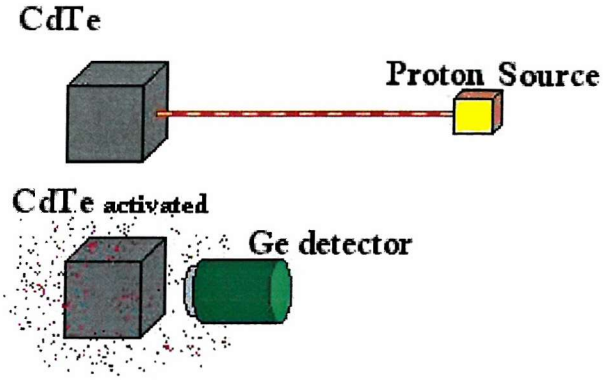

Figure 7.21: **The modelled interpretation of the experimental procedure.** *The CdTe block is not used as a detector, the only gamma ray detection happens at the Ge detector. Sources of background that will occur but will not be observed by the Ge detector in the experiment or simulation are α and β decays.*

times. The spectra measured by the solid state detector will be self detected by the pixel when it is incorporated into the BAT and launched into space. This will give the BAT team an indication as to how much self-irradiation will occur and what lines will be observed. CdTe was chosen due to its atomic similarity to CZT and is inexpensive in relation to CZT. The CdTe was irradiated with a mono-energetic (155 MeV) proton beam for 82 minutes (Y. Kobayashi (2001), private communication). Figure 7.21 shows a brief schematic.

Figure 7.22 shows the spectra obtained from the beam experiment and from the mass model simulations. A table of all the line energies can be seen in appendix B. The correlation is good between the two spectra. Out of the 134 lines detected between 25 keV and 1 MeV, 64% were accurately predicted, 13% showed up in the data but not in the model, 13% could be attributed to material surrounding the experimental apparatus (Pb), 9% were predicted by the model but were not seen in the data and 7% remain unidentified. The majority of the discrepancies occurred in the higher energy range and could be attributed to poor statistics. Removing the lines that resulted from Pb being present within the apparatus and so would not be predicted, gives a value of 74% of lines correctly predicted. The reason that the remaining lines were unaccounted for is due to a combination of poor statistics, multiple scattering of events, unknowns in the apparatus (e.g. CdTe isotope abundances) and isotope decays left out of the DECAY look-up tables. All lines, no matter how weak were included, giving an uncertainly in a lines existence and so uncertainly in their prediction or detection. Certainly some lines are missing in the model at this stage, the inclusion of these should be performed during calibration.

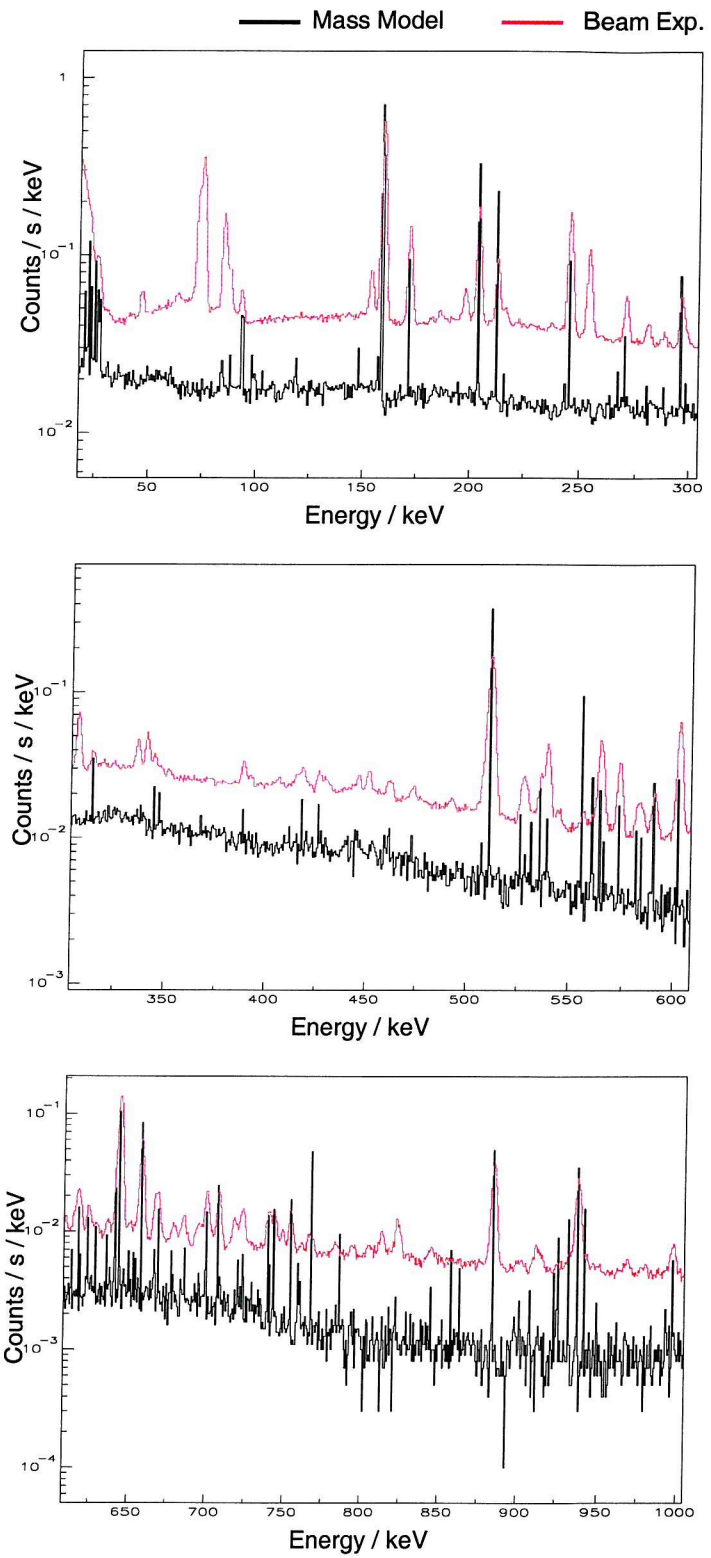

Figure 7.22: **The comparative spectra from the beam experiment and the mass model.**

7.3.4 Verification Summary

Two aspects to the modelling of the BAT background have been verified by the modelling independent experiments with the same criteria that was applied to SwiMM. The temporal modulation modelling method of the background was well reproduced by the BATSE data. Certain inconsistencies remained and will remain until further verification studies can be performed to identify the causes of any inconsistencies with the data, most probably after the launch of Swift. The activation showed a 74% accuracy in the prediction of lines in a CdTe activation experiment. This 74% efficiency could be a result of various factors, one of which was the modelling procedure, and so was considered a lower limit to the accuracy. Both of these provide confidence that any prediction in the BAT background maintains a high level of accuracy.

An area that remains unverified is the important spatial variation across the detector plane. This variation is hard to verify in that every instrument will produce characteristically different data. The LAD modules aboard the CGRO retained no spatial information and so could not be used. The importance of this form of variation is paramount in coded aperture instruments. Therefore, after the launch of INTEGRAL, the possibility exists for an accurate assessment of this form of background. However, this form of modulation can be assumed to be partially verified as it is an extrapolation of the filtering technique that reproduced the variations in the BATSE data.

7.4 SwiMM Results

Now the various aspects of the background modelling have been verified, the same approaches can be applied to the BAT. As long as factors such as the possible underestimation of the Albedo component or the 74% accuracy of the delayed component lines are known about in advance the results from SwiMM can be presented in the environment of confident extrapolation with any possible imperfections already predicted.

7.4.1 Background Modulation

The predictions of background modulations within the BAT aboard Swift is vital in the design of the software and data analysis for the hard X-ray survey. Here the orbital modulations in the total count-rate alongside the resultant spatial modulations across the detector plane are presented. The orbital total count-rate modulations will be discussed first with the spatial background distribution, resulting from the various pointings throughout an orbit, discussed second. The orbital modulation filtering for SwiMM will include a single pointing and as a result the spacecraft will be pointing towards the Earth during a part of the orbit. Obviously during its operational lifetime the BAT will not expect to receive a terrestrial trigger and so will be continually pointing away from the Earth. During one orbit the spacecraft is expected to slew several times to maintain the maximum likelihood of a trigger.

Table 7.2: **The modelled orbit characteristics.**

Altitude	600 km
Inclination	20^o
Orbit Init. Long.	35.32^o
RA	$128^o56'5.28"$
Dec.	$-45^o13'45.48"$

This mono-pointing orbit was selected so that the full range of variations would be shown. Once a schedule of initial pointings is determined or the initial data sets start arriving an estimate of the modulations that the BAT is likely to experience can be produced. It is possible that a matrix of all pointings from all positions above the Earth could be produced. This approach could prove to be the most efficient instead of producing simulations for each orbit. However, it would be nonsensical to produce such a matrix until some initial data starts coming in, by which the model can be verified and adjusted according to the suspected imperfections or to any newly discovered short fallings. The orbit characteristics are shown in table 7.2.

Figure 7.23 shows each of the three background components variability over one orbit. The modulation due to the Earth passing in and out of the field of view is the most obvious effect on the background modulation, though not as prevalent in the Cosmic Ray modulation. The CDX energy dependency is an effect of the input CDX spectrum. In the case of the Albedo flux the relation with energy is more complex due to the convolution of the various physical processes involved in the filtering. Also, a point worth noticing, especially in the albedo flux, are the sharper changes in the count-rate as the Earth's atmosphere passes in and out of the field of view at lower energies. This can be attributed to the limited transparency of the shielding at these energies. At higher energies the shielding is more transparent and so the change is smoother. The low count-rates in the Cosmic Ray filtering result in producing a more irregular line. The peak in the count-rate is due the lowest rigidity during the orbit, especially obvious since this occurs when the BAT is pointing directly towards the Earth. The shielding is next to irrelevant when considering background counts due to Cosmic Ray interaction.

The total count-rates can be seen in figures 7.24 and 7.25. These total count-rate predictions provide a good estimate as to the contributions that each component makes total background, and so give a good indication of the signal-to-noise ratio over one orbit. Bands 1 and 2 are clearly dominated by the CDX component with only the shape of the modulation being effected by the other components as the BAT begins to point toward the Earth. The Albedo component starts to have an effect on the modulations in bands 3 and 4. The shape of the high energy band was still dominated by the CDX component but above 100 keV the Albedo component cannot be ignored. This is due to the energy dependence of the background components

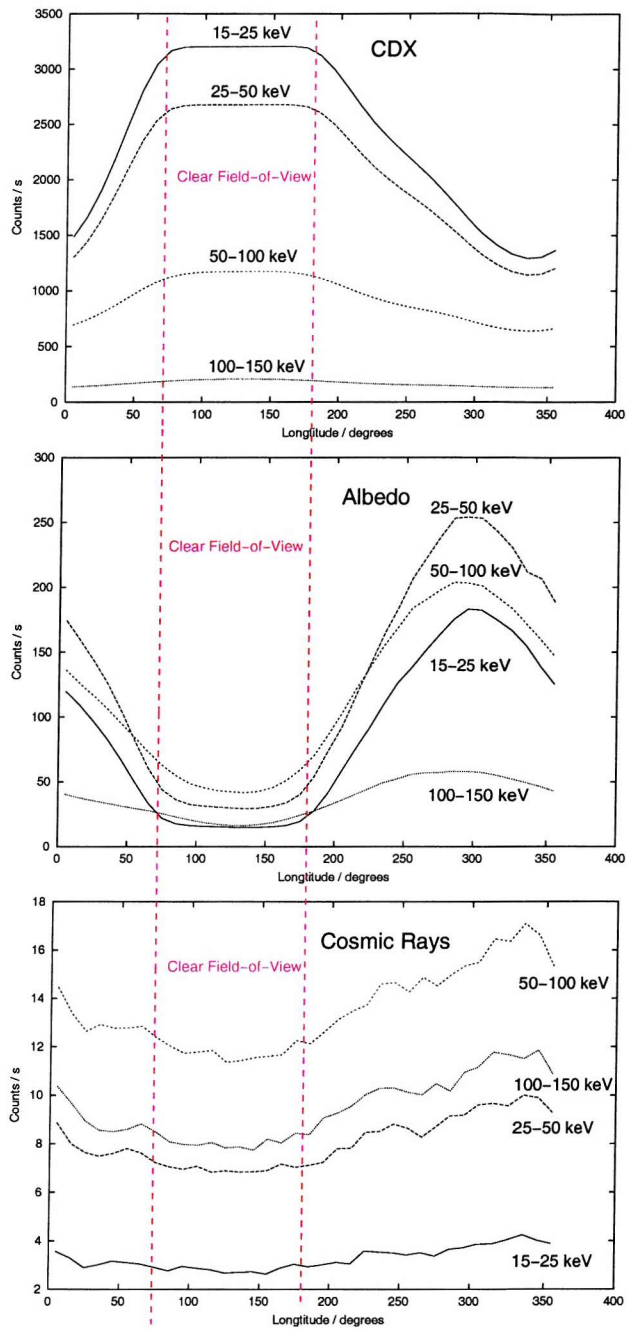

Figure 7.23: **The variability in the background components.** *Each component is split into 4 energy bands. The section of the orbit where the Earth is not in the field of view is marked by a red-dashed line.*

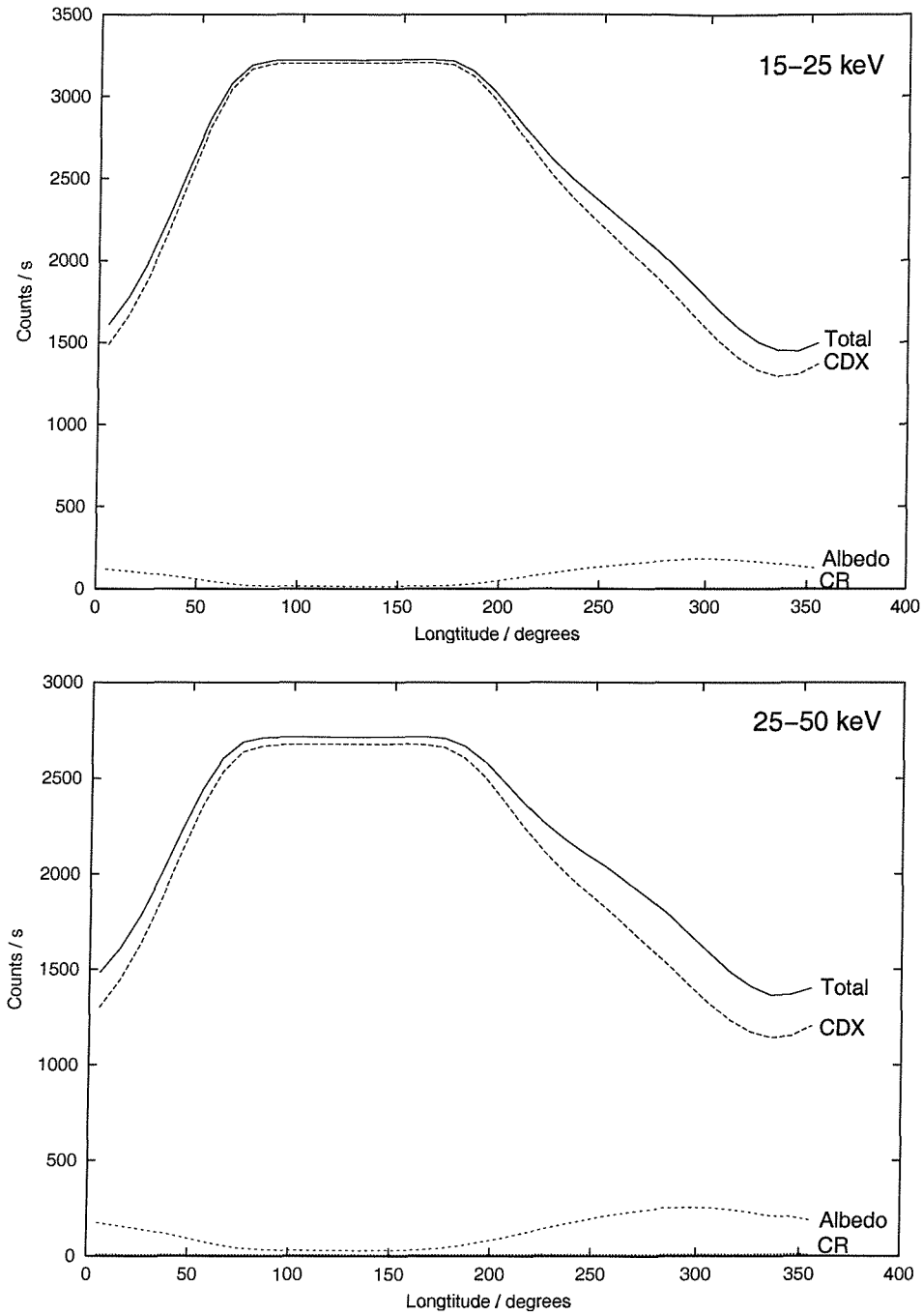

Figure 7.24: **The variability in the background for bands 15-25 keV and 25-50 keV.** *The total is included alongside the three modulating components: Cosmic Diffuse X-rays (CDX), Atmospheric Albedo Radiation (Albedo) and Cosmic Rays (CR).*

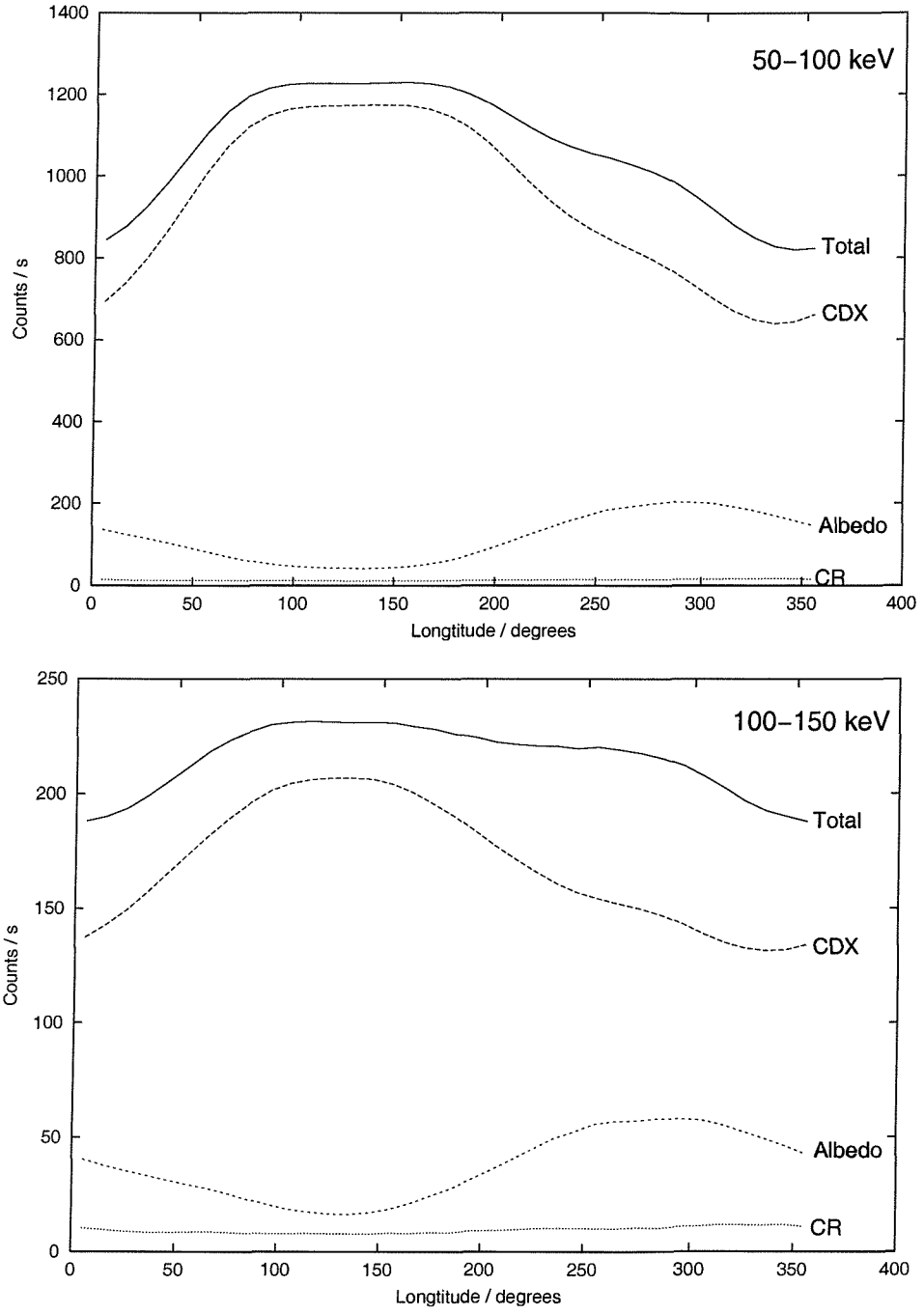

Figure 7.25: **The variability in the background for bands 50-100 keV and 100-150 keV.** *The total is included alongside the three modulating components: Cosmic Diffuse X-rays (CDX), Atmospheric Albedo Radiation (Albedo) and Cosmic Rays (CR).*

and also due to the transparency of the shielding, effectively increasing the field of view leaving the detector exposed to more atmospheric radiation than it would, should the shielding be perfect.

Spatial Variations

During the survey mode of the BAT, the background induced spatial variations across the plane will interfere with the autocorrelation function of the pattern, possibly giving the impression of areas being partially coded and giving false images. At the very least it will reduce sensitivity and give an extra variation in sensitivity over the field of view. The noise in all pixels can contribute to the noise in a single image due to the extent of the shadowgram. Removing all spatial variations not due to the mask pattern (or as much as possible) will enable the entire CZT detector plane to perform with equal maximum sensitivity, with the autocorrelation function giving as close to the theoretical delta function as possible.

Figure 7.26 shows the spatial distribution of the background at longtitude 315^o. Three main factors are affecting the spatial background modulation. The first is the large CDX contribution through the aperture and the second is due to the smaller atmospheric albedo contribution. At the pointing angle simulated here the field of view is split diagonally by the atmosphere and outer space with a degree of overlap. The count-rates for the CDX and Albedo components are clustered, as a result, to opposite corners. This distribution will change during orbit and be determined by the position of the Earth's horizon with respect to the field of view. The third effect is a result of flux penetrating the shielding, giving an increase in the count-rate in the edge pixels of the CZT and can be seen in figure 7.27. This effect is seen only in the CDX component in this case as a significant fraction of the field of view is taken up by the Earths atmosphere. This effect is most demonstrative when considering the Albedo component as it is rarely in the field of view. This atmospheric flux penetrates the shielding and the count-rate at the edges was seen to be twice the central count-rate. This third effect may be insignificant in the total count-rate modulation but it is highly localised and so modulates the *spatial* distribution to a level that will interfere with image deconvolution.

Another source of spatial systematic variation across the detector plane will be structural shadows projected onto the detector array by strong off-axis sources. This is unavoidable but easily accounted for. These shadows will be cast mainly by the UVOT or XRT as they have the highest density of material above the detector plane. Figure 7.28 shows the effects that such structural shadows can have.

Off-Axis Strong Sources The various diffuse components have been discussed but contributions to the background come in the form of any source of gamma radiation that is not the source being studied. For this reason The Crab Pulsar was simulated as a source of gamma rays. The BAT utilises coded mask imaging so a strong-off axis source will contribute to the noise in any source within the field of

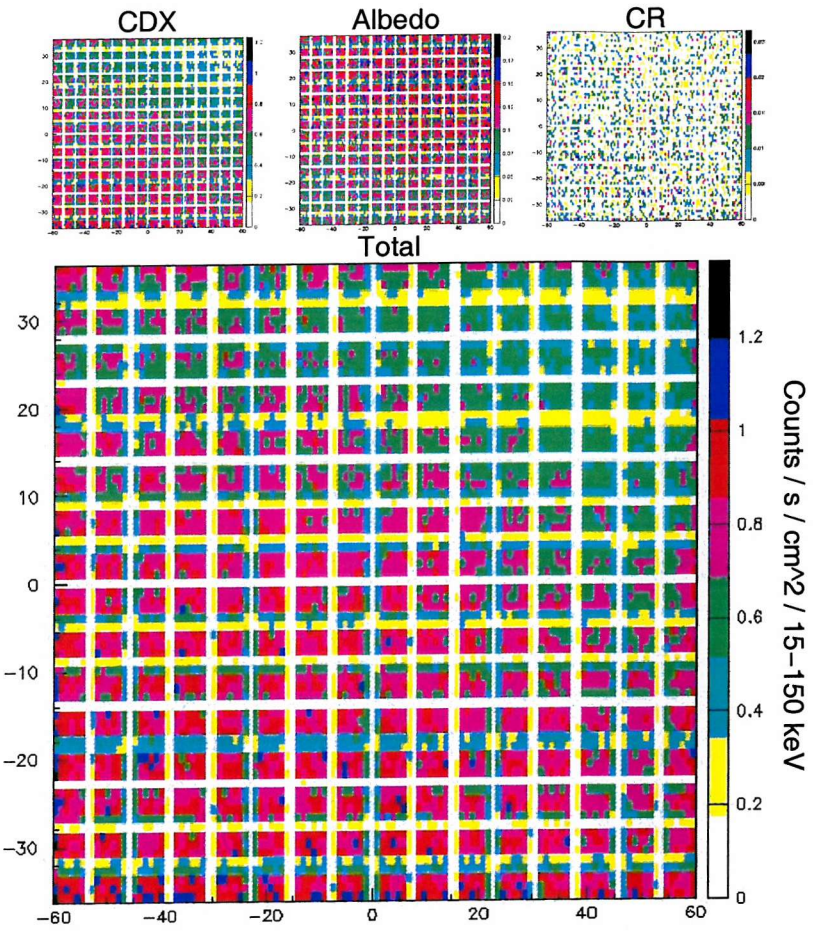

Figure 7.26: **The spatial distribution of the background across the detector plane.** *The colour scale of each individual component is normalised.*

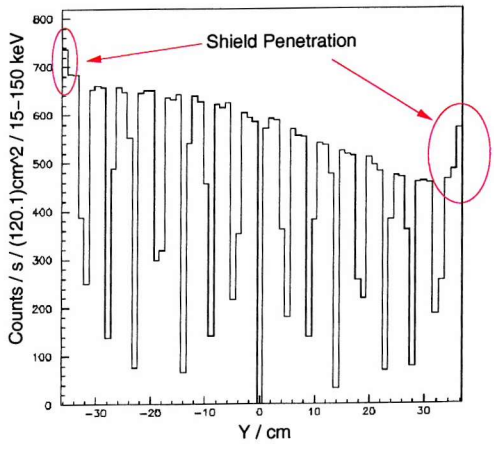

Figure 7.27: **The penetration of the shielding at the very edges of the detector plane.** *This plot is a projection of the count density across the detector plane in one dimension,* **y**.

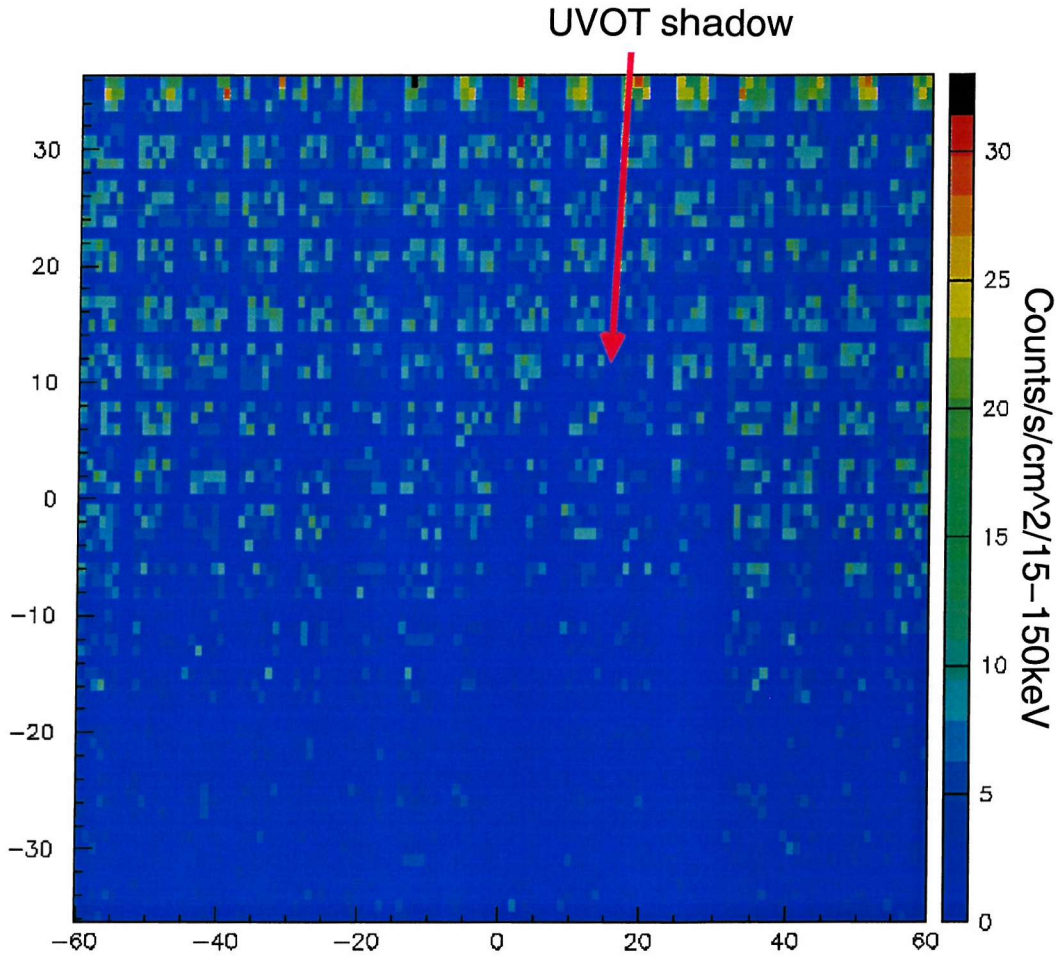

Figure 7.28: **The shadowing effect of the UVOT.** *The cylindrical shape of the UVOT baffle can be seen projected upon the CZT array during a 0.5 second exposure off-axis GRB simulation. The very edge of the mask pattern can be made out at the top of the plot.*

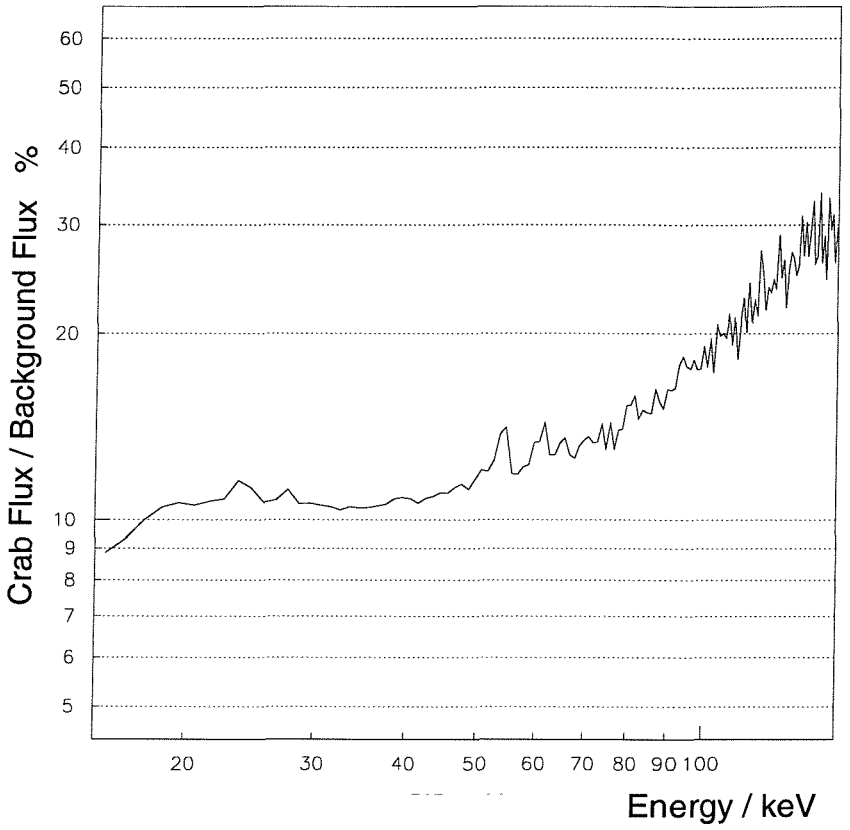

Figure 7.29: **The percentage contribution of a strong off-axis source to the background.**

view, reducing the sensitivity. An off-axis source such as The Crab would require removal to extract the maximum sensitivity of the system. The Crab spectrum is shown in equation **??**.

$$\frac{dN}{dE_\gamma} = 24.0\ E^{-2.3} \quad \left[ph.s.cm^{-2}.keV^{-1}\right] \tag{7.10}$$

The Crab was simulated at 32.8^o off-axis. 32.8^o is the angle inside of which contains the same solid angle as outside, within the field of view and so is the median angle at which an off-axis source will be. The spectrum recorded was compared to the total predicted background flux and the energy dependent ratio is shown in figure 7.10. This interfering source has an energy dependent contribution that ranges from 9-30% of the background flux. Though The Crab is the strongest discrete source the contribution of the clusters of sources around the galactic centre will also provide a significant level of background.

Transient and bursting sources (excluding GRBs) will also provide an occasional very strong source of background. Though some transient events can be predicted in advance and some specific sources, though unpredictable, are known to flare strongly. These sources can be accounted posthumously in the survey data extraction. However, it may be that if the flaring source is in the field of view that section of data will have to be discarded.

7.4.2 Activation

The three components considered so far have all been prompt components modulated by the position of the Earth, its atmosphere and magnetosphere with respect to the spacecraft. The fourth component is the activated component that results from prolonged exposure to Cosmic Ray protons. Using the GGOD suite a prediction of the isotope production rates during Cosmic Ray exposure was calculated for each volume within the model. These isotope production rates were converted into isotope decay rates given a specific time of activation. A second Monte Carlo was run to simulate the isotope decay products from each volume within the model of the BAT. Contributions from material outside the BAT volume were not considered at this stage as the significance of any activation is dependent on a $\mathbf{r}^2$ relationship with the distance from the detector plane. The contributions of all volumes within the BAT were combined to give the spectrum adding to the background flux by way of radioactive decay. Figure 7.30 shows a sample activated spectrum after 1 year of Cosmic Ray irradiation. Each of the 28 lines are numbered and a table of them is presented in table 7.3.

3 lines in table 7.3 remain unidentified. These lines were predicted by the model but no comparative line was found when using reference material **??**. The 59.5 keV and 118.5 keV lines were due to a prompt interaction such as fluorescence on the evidence that one is double the other due to simultaneous energy deposits. The 137.5 keV line would not be due to a single fluorescence due to its relatively high energy, it is most likely that it was again a combination of two or more prompt events. The origin of each line is known as each contributing volume was simulated separately. Figure 7.31 shows which origins of this activated background are most significant at which energies. In order, the 5 strongest sources of isotopic decay were the CZT detector plane, the detector electronics, the coded mask, the graded-Z shielding and then the support structure below the DAP.

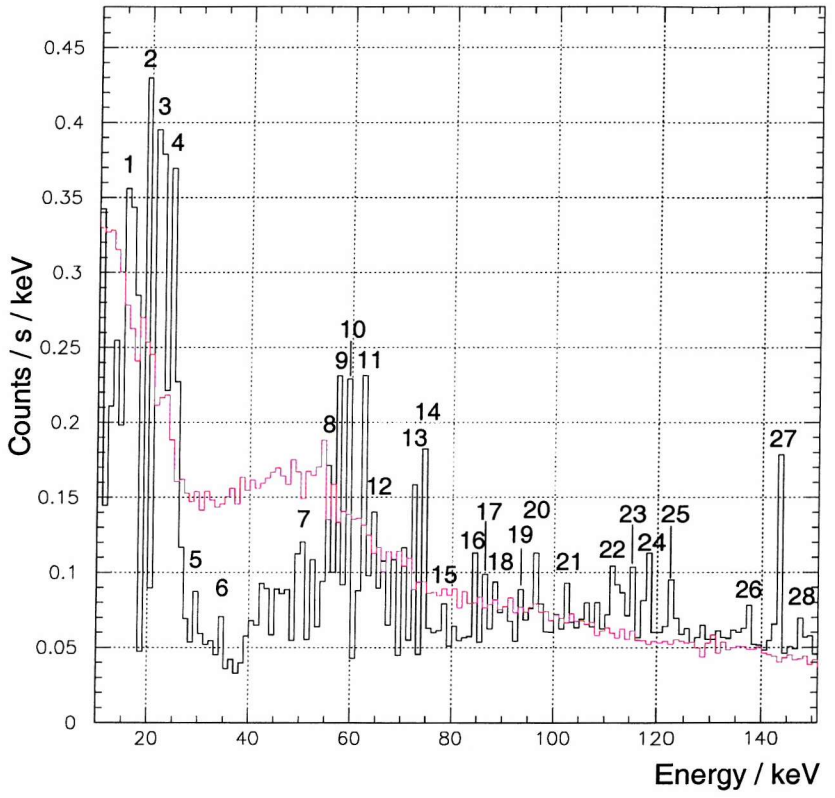

Figure 7.30: **The activated spectrum after 1 year in orbit.** *The numbered lines are listed in table 7.3. The black line is the spectrum incident on the BAT whereas the red line includes the charge-trapping characteristic.*

Table 7.3: **The modelled activation lines after an irradiation period of 1 year.**

Line Number	Energy [keV]	Parent	Half-life	Origin
1	16.40	Zn^{72}	46.5 h	CZT
2	19.39	Lu^{171}	8.24 d	Ta shielding
3	23.28	Sn^{126}	10^5 y	Sn shielding
	23.87	Sb^{119}	38.2 h	CZT (Te)
4	23.93	Hf^{172}	1.87 y	Ta shielding
	24.46	Pd^{101}	8.47 h	CZT (Cd)
5	30.60	Tl^{201}	72.9 h	Pb shielding/mask
	30.63	Mg^{28}	20.9 h	DAP (Al)
6	35.49	I^{125}	59.4 d	CZT (Te)
7	49.72	Te^{132}	3.20 d	CZT
8	54.97	Xe^{125}	16.9 h	CZT (Te)
9	57.53	Ta	n/a	*Shield Fluorescence*
10	57.61	Te^{127}	109 d	CZT
11	$\sim$ 59.5	?	?	CZT
12	64.28	Sn^{126}	10^5 y	Sn shielding / CZT
	64.95	Ta	n/a	*Shield Fluorescence*
	65.22	Ta	n/a	*Shield Fluorescence*
	65.55	Te^{121}	16.78 d	CZT
13	72.00	W^{187}	23.72 h	Ta shielding
	72.81	Pb	n/a	*Shield Fluorescence*
14	74.78	Pd^{100}	3.63 d	CZT (Cd)
	74.97	Pb	n/a	*Shield Fluorescence*
	75.88	Lu^{171}	8.24 d	Ta shielding
15	78.63	Lu^{173}	1.47 y	Ta shielding
	79.62	Xe^{133}	5.24 d	CZT (Te)
16	84.02	Pd^{100}	3.63 d	CZT (Cd)
	84.45	Pb	n/a	*Shield Fluorescence*
17	84.94	Sn^{126}	10^5 y	Sn shielding / CZT
	84.94	Pb	n/a	*Shield Fluorescence*
	87.57	Sn^{126}	10^5 y	Sn shielding / CZT
18	88.04	Cd^{109}	463 d	CZT
	88.32	Ta^{176}	8.09 h	Ta shielding
19	93.12	Cd^{107}	6.5 h	CZT
	93.31	Cu^{67}	61.83 h	Cu shielding / CZT
	93.33	Ta^{180}	8.15 h	Ta shielding
20	96.73	Ag^{111}	7.45 d	CZT (Cd)
21	103.1	Zn^{72}	46.5 h	CZT

Continued ...

Line Number	Energy [keV]	Parent	Half-life	Origin
22	111.2	Ta^{184}	8.7 h	Ta shielding
	111.8	Te^{132}	3.20 d	CZT
23	115.2	Pb^{212}	10.64 h	Pb shielding
	116.3	Te^{132}	3.20 d	CZT
24	$\sim$ 118.5	?	?	*CZT Fluorescence*
25	122.0	Hf^{171}	12.1 h	Ta shielding
	122.1	Co^{57}	271.8 d	Cu shielding / CZT
26	$\sim$ 137.5	?	?	*Various*
27	145.0	Zn^{72}	46.5 h	CZT
	145.3	Xe^{127}	36.4 d	CZT (Te)
28	147.6	Pb^{200}	21.5 h	Pb shielding/mask

Now that a spectrum of the activated flux has been predicted, the process can be re-run for irradiation periods from a week to 5 years. This will give an indication as to how this component to the background will evolve over the mission lifetime. At 1 year the level of this background component is very small in comparison to the total background. Due to most of the activated flux being from the CZT itself and the electronics below the detector the spatial variation is expected to be negligible. Figure 7.32 shows the evolution of the activated flux over the mission lifetime. The gradual increase is as expected as isotopes with longer and longer half-lives become more significant while the low half-life isotope decays continue to be re-populated.

By considering the standard form of Cosmic Ray flux, the activated component is insignificant in comparison to the total background. However there is another source of charged particles to activate the spacecraft and instrument, the regions of trapped charged particles. In particular the SAA is expected to be a large source of activation. During each passage the instrument will be turned off so that the large proton flux does not damage the sensitive electronics. The prompt background due to these protons will not be an issue as the BAT will be inactive during and shortly after an SAA passage. Unfortunately this large dose will create an activation that will vary on orbital timescales. Figure 7.33 shows the count-rate of a BATSE LAD during an SAA passage. The gaps in the data are where the instrument has been turned off. When the instrument is turned on again the count-rate is far stronger due to the decay of activated isotopes. This increased count-rate soon decays exponentially before the next passage but the combination of several passages activates the spacecraft so much that a slower varying decay is combined with the more immediate decay. This regular re-activation gives the activated component a much more complex structure than the gradual asymptotic increase seen in figure 7.32. The main problem with including a component due to the SAA is that there is a large range as to what proton flux the instrument will experience during an SAA

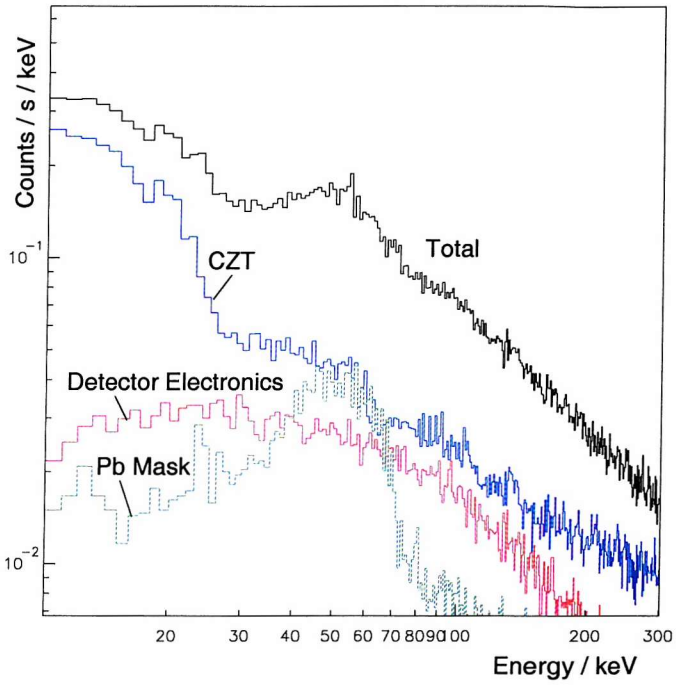

Figure 7.31: **The significant origins to the delayed activated background.** *This spectrum includes the charge trapping characteristic of CZT and shows the prediction of the activated component to the background after 1 year in orbit.*

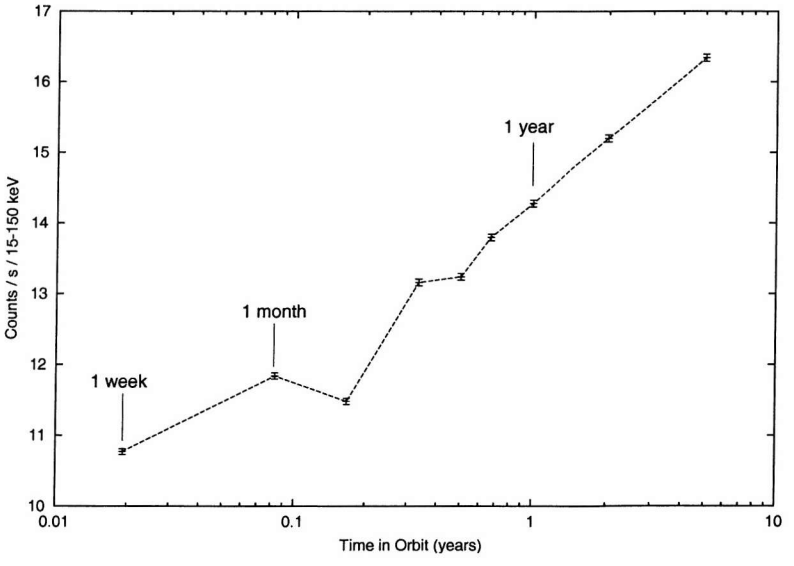

Figure 7.32: **The predicted activation count-rate over the mission lifetime.** *The activated flux was integrated over the whole detector plane but does not include any activation as a result of passages through areas of trapped charged particles.*

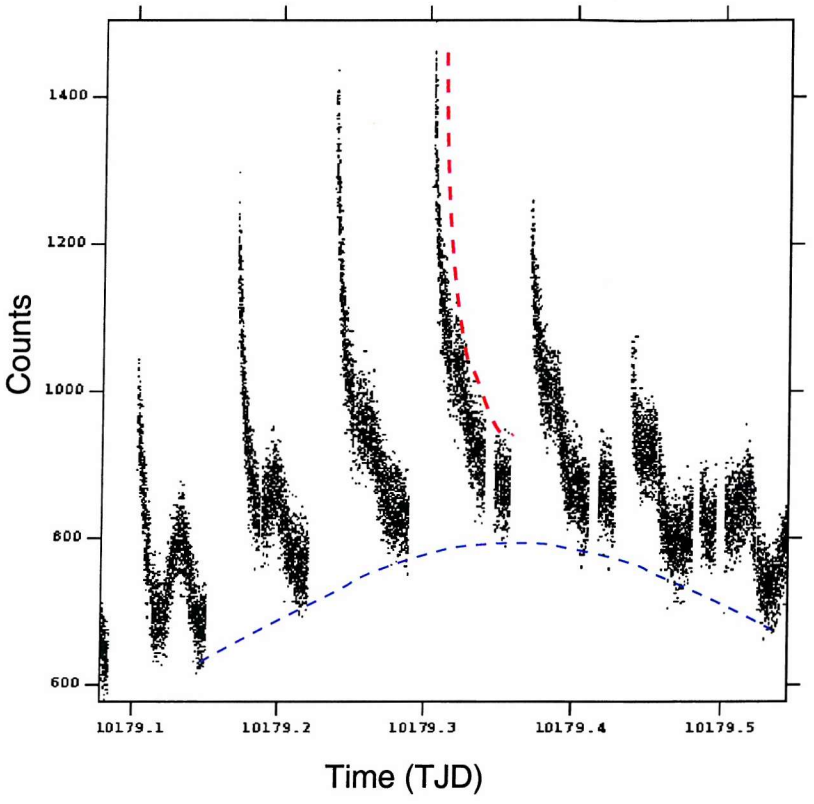

Figure 7.33: **Count-rate variations during a series of SAA passages.** *The gaps in the data are due to the instrument being turned off during the highest particle fluxes to prevent instrument damage. The red and blue lines represent two activation/decay relationships that a series of SAA passages can be broken down into.*

passage. This uncertainly in the prompt flux will carry over to an uncertainly in the activated component. Future evaluation of this activation should be carried out by breaking down the problem into three parts. The first would be to evaluate the decay of the instrument after a single passage as it leaves the SAA. The second would consider the total activation as sequential orbits pass through the region and the radioactive decay that results between subsequent encounters with the SAA. Finally the activation due to the combination of all SAA passages needs to be evaluated so as to modify figure 7.32. The first two parts to evaluating a contribution due to the SAA can clearly be seen in figure 7.33, marked in red and blue respectively.

7.4.3 CZT Lifetime

One problem with using solid state detectors during astronomical missions is that they are susceptible to radiation damage. This radiation damage occurs more readily as very little material is actually used to interact with the gamma ray photons com-

pared to scintillation or ionisation chamber methods. This radiation damage acts to compound a problem that already exists within the CZT, the variable charge trapping characteristics. The characteristics of each pixel can vary greatly, an unfortunate side effect of the crystal growing procedure. Each pixel can therefore be characterised by two combinations of two parameters, μ (the mobility) and τ (the lifetime) for the electrons and electron-holes. The two $\mu\tau$ products give the average distance the electron or electron-hole travels before recombination and parameterises the response of the CZT pixel. An increase in $\mu\tau_e$ would move the peak to a higher energy and an increase in $\mu\tau_h$ would give the peak a longer low energy tail, according to equation 5.1. During calibration the $\mu\tau$ products for each pixel can be measured and included in the response matrix for the whole detector. Combining this with the coded mask methodology the pixel to pixel variations can be minimised. Unfortunately the susceptibility of the CZT to radiation damage means that the individual $\mu\tau$ products measured on the ground will vary after a spell in orbit, creating ever increasing systematic errors in the detector response.

This effect has been quantified through beam experiments [105]. The radiation dose that a CZT pixel can cope with before any significant radiation degradation occurs is 10^{10} $protons.cm^{-2}$ (at 1.3 MeV). Though the value for 200 MeV is thought to be 10^9 $protons.cm^{-2}$, the full energy dependence of this quantity is unknown. Until further investigations have been performed, the absolute value of 10^{10} $protons.cm^{-2}$ will be used across the spectrum. This was assumed to be a reasonable approximation as the prompt proton spectrum (i.e. all counts not including radioactive decay) has >50% of its flux in the 1-3 MeV band due to the position of the Landau thin-absorber function.

By integrating the number of interactions due to protons over one orbit, a duration after which radiation damage will occur can be extrapolated. The standard filtering technique described in the previous sections gives an average flux of 27 $protons.s^{-1}.cm^{-2}$ suggesting a lifetime for the CZT of >11 years, over double the expected lifetime of the spacecraft. However, the area that the standard filtering technique does not take into account are the passages of the spacecraft through the trapped radiation belts. SPENVIS [107] calculates that Swift will be encountering some kind of trapped radiation flux (defined as L<1.1) for >70% of its time in orbit. The average spectrum over a days worth of orbits ($\sim$16 orbits), including SAA passages, was modelled. The results of the extra trapped particle flux gave an extra 29 $protons.s^{-1}.cm^{-2}$ on top of the standard filtered flux. This gives a limit of 5.6 years before any significant degradation. For a mission that is expected to last no more than 5 years, this is a favourable estimate. However, several assumptions have been made about the energy dependence and any kind of gradual degradation under 10^{10} protons has been ignored. With the procurement of more experimental data, this estimate can be refined.

7.5 Summary

The Swift hard X-ray survey will use the redundant time between burst triggers to achieve a survey of the 15-150 keV energy band to an unprecedented sensitivity. The pre-launch plan is to integrate every 5 minutes and combine the data to produce a preliminary survey after 6 months in orbit. The removal of the systematic and dynamic background will be vital to this survey. This chapter has described how the various components to the spatial and temporal varying background can be removed using verified and entirely non-empirical methods. The initial survey is expected to be produced using mostly empirical methods. So, the approach presented here will be performed in parallel to the first 6 month survey but without the same time constraints so as to reach as close to the theoretical sensitivity as possible.

Currently, this non-empirical method lacks in two specific areas, the effects of SAA passages and the "input spectra" contributions to the prompt components. These two areas may well require verification from initial BAT data and the necessary physics-based corrections applied. Previous modelling within gamma ray missions have been either temporal (BATSE) or spatial (INTEGRAL) and have involved some kind of empirical fitting. This approach is unique in that the spatial and temporal components are modelled simultaneously and without any empirical component beyond the measurement of the space environment.

The continual development and application of this approach will improve the sensitivity of the Swift survey and will pave the way for maximising the sensitivity of future gamma ray missions.

Bibliography

[1] Baldwin, G. C. and G. S. Klaiber
X-ray Yield Curves for gamma-n Reactions
Physical Review, 73:1156–1164, 1948.

[2] Ballantyne, D. R. and E. Ramirez-Ruiz
Iron K alpha Emission from X-Ray Reflection: Predictions for Gamma-Ray Burst Models
The Astrophysical Journal, 559:L83–L86, 2001.

[3] Band, D., J. Matteson, L. Ford, B. Schaefer, D. Palmer, B. Teegarden, T. Cline, M. Briggs, W. Paciesas, G. Pendleton, G. Fishman, C. Kouveliotou, C. Meegan, R. Wilson, R. and P. Lestrade.
BATSE observations of gamma-ray burst spectra. I - Spectral diversity
Astrophysical Journal, 413:281–292, 1993.

[4] Bartels, J.
The eccentric dipole approximating the Earth's magnetic field
J. Geophysical Research, 41:225–250, 1936.

[5] Barton, C. E.
International Geomagnetic Reference Field: The Seventh Generation
J. Geomag. Geoelectr., 49:123–148, 1997.

[6] Bertsch, D. L., T. Dame, C. E. Fichtel, S. D. Hunter, P. Sreekumar, J. G. Stacy and P. Thaddeus
Diffuse Gamma-Ray Emission in the Galactic Plane from Cosmic-Ray, Matter, and Photon Interactions
Astrophysical Journal, 416:587, 1993.

[7] Biermann, P. L., T. K. Gaisser and T. Stanev.
Origin of galactic cosmic rays
Physical Review D (Particles and Fields), 51(7):3450–3454, 1995.

[8] Bignami, G. F., G. Boella, J. J. Burger, B. G. Taylor, P. Keirle, J. A. Paul, H. A. Mayer-Hasselwander, E. Pfeffermann, L. Scarsi and B. N. Swanenburg
The COS-B experiment for gamma-ray astronomy
Space Science Instrumentation, 1:245–268, 1975.

[9] Bildsten, L., D. Chakrabarty, J. Chiu, M. H. Finger, D. T. Koh, R. W. Nelson, T. A. Prince, B. C. Rubin, D. M. Scott, M. Stollberg, B. A. Vaughan, C. A. Wilson, R. B. Wilson
Observations of Accreting Pulsars
The Astrophysical Journal Supplement, 113:367, 1997.

[10] Boella, G., R. C. Butler, G. C. Perola, L. Piro, L. Scarsi and J. A. M. Bleeker
BeppoSAX, the wide band mission for X-ray astronomy
Astronomy and Astrophysics Supplement series, 122:299–307, 1997.

[11] Briggs, M. S., W. S. Paciesas, G. N. Pendleton, N. Geoffrey, C. A. Meegan, G. J. Fishman, J. Gerald, J. M. Horack, M. N. Brock, N. Martin N., C. Kouveliotou, D. H. Hartmann and J. Hakkila.
BATSE Observations of the Large-Scale Isotropy of Gamma-Ray Bursts
Astrophysical Journal, 459:40, 1996.

[12] Burrows, D. N., J. E. Hill, J. A. Nousek, A. A. Wells, A. D. Short, R. Willingale, O. Citterio, G. Chincarini and G. Tagliaferri
Swift X-Ray Telescope
SPIE, 4140:64-75, 2000.

[13] Cain, J. C., S. J. Hendricks, R. A. Langel, and W. V. Hudson
A Proposed Model for the International Geomagnetic Reference Field
J. Geomag. Geoelectr., 19:335, 1967.

[14] Cameron, R. A., J. D. Kurfess, W. N. Johnson, R. L. Kinzer, R. A. Kroeger, M. D. Leising, R. J. Murphy, G. H. Share, M. S. Strickman and J. E. Grove
Operation and performance of the OSSE instrument
The Compton Observatory Science Workshop, 3–14, 1992.

[15] Campbell, W.
Introduction to geomagnetic fields.
Cambridge University Press, 1997.

[16] Cash, W.
Generation of Confidence Intervals for Model Parameters in X-ray Astronomy
Astronomy and Astrophysics, 52:307, 1976.

[17] Castander, F. J. and D. Q. Lamb.
A Photometric Investigation of the GRB 970228 Afterglow and the Associated Nebulosity
Astrophysical Journal, 523:593, 1999.

[18] Chapman, S. and J. Bartels.
Geomagnetism (2 volumes).
Oxford University Press, 1940.

[19] Cline, T. L., U. D. Desai, R. W. Klebesadel and I. B. Strong.
Energy Spectra of Cosmic Gamma-Ray Bursts
Astrophysical Journal, 185:L1, 1973.

[20] Colafrancesco, S.
Clusters of Galaxies and the Diffuse Gamma-ray Background.
Astroparticle Physics, 9:227–246, 1998.

[21] Costa, E. *et al.*
Discovery of an X-ray afterglow associated with the gamma-ray burst of 28 February 1997
Nature, 387:783–785, 1997.

[22] Cowley, A. P.
Evidence for Black Holes in Stellar Binary Systems
Annual Reviews of Astronomy and Astrophysics, 287:30, 1992.

[23] Dar, A. and A. De Rujula.
Is the Diffuse Gamma Background Radiation Generated by Galactic Cosmic Rays?.
The Monthly Notices of the Royal Astronomical Society, 323:391–401, 2001.

[24] de Jager, O. C.
Evidence for particle acceleration in a magnetized white dwarf from radio and gamma-ray observations
Astrophysical Journal Supplement, 90(2):775–782, 1994.

[25] Dean, A. J., F. Lei, K. Byard, A. Goldwurm, C. J. Hall and J. S. S. Harding.
The Gamma-ray Emissivity of the Earths Atmosphere
Astronomy and Astrophysics, 219:358–361, 1989.

[26] Dean, A. J., F. Lei, R. Gurriaran, A. J. Bird and J. J. Lockley
The Space Radiation Environment and Background Noise in Astronomical Gamma Ray Telescopes
Journal of British Interplanetary Science, 53:97–103, 2000.

[27] Dyer, C. S., A. J. Sims, P. R. Truscott, J. Farren, C. Underwood.
Radiation environment measurements on shuttle missions using the CREAM experiment
IEEE Transactions on Nuclear Science, 39(6):1809–1816, 1992.

[28] Eikenberry, S. S., K. Matthews, E. H. Morgan, R. A. Remillard and R. W. Nelson
Evidence for a Disk-Jet Interaction in the Microquasar GRS 1915+105
Astrophysical Journal Letters, 494:L61, 1998.

[29] Fichtel, C. E., G. A. Simpson and D. T. Thompson
Diffuse Gamma Radiation.
The Astrophysical Journal, 222:833–849, 1977.

[30] Fichtner, H.
Anomalous Cosmic Rays: Messengers from the Outer Heliosphere
Space Science Reviews, 95(3/4):639–754, 2001.

[31] Firestone, R. B., V. S. Shirley, C. M. Baglin, S. Y. F. Chu and Jean Zipkin
Table of Isotopes, Volumes I and II, (Wiley), 1996.

[32] Fishman, G., J. and C. A. Meegan.
Gamma-Ray Bursts
Annual Review of Astronomy and Astrophysics, 33:415–458, 1995.

[33] Frail, D. A., S. R. Kulkarni, R. Sari, S. G. Djorgovski, J. S. Bloom, T. J. Galama, D. E. Reichart, E. Berger, F. A. Harrison, P. A. Price, S. A. Yost, A. Diercks, A., R. W. Goodrich and F. Chaffee
Beaming in Gamma-Ray Bursts: Evidence for a Standard Energy Reservoir
Astrophysical Journal, 562:L55–L58, 2001.

[34] Fusco-Femiano, R., D. dal Fiume, L. Feretti, G. Giovannini, P. Grandi, G. Matt, S. Molendi and A, Santangelo
Hard X-Ray Radiation in the Coma Cluster Spectrum
The Astrophysical Journal, 513:L21–L24, 1999.

[35] Fusco-Femiano, R., D. Dal Fiume, M. Orlandini, G. Brunetti, L. Feretti and G. Giovannini
Hard X-Ray Emission from the Galaxy Cluster A3667
The Astrophysical Journal, 552:L97–L100, 2001.

[36] Gehrels, N.
Instrument Background in Gamma-ray Spectrometers flown in Low Earth Orbit.
Nuclear Instruments and Methods in Physics Research, A313:513–528, 1992.

[37] Gledhill, J. A.
Aeronomic effects of the South Atlantic anomaly
Reviews of Geophysics and Space Physics, 14:173–187, 1976.

[38] Gruber, D. E., J. L. Matteson and L. E. Peterson
The Spectrum of Diffuse Cosmic HArd X-rays Measured with HEAO 1
Astrophysical Journal, 520:124–129, 1999.

[39] Harmon, B. A., G. J. Fishman, C. A. Wilson, W. Paciesas, S. N. Zhang, M. H. Finger, T. Koshut, M. L. McCollough, C. R. Robinson and B. C. Rubin
The Burst and Transient Source Experiment Earth Occultation Technique
The Astrophysical Journal Supplement Series, 138:149–183, 2002.

[40] Hasinger, G.
The Extragalactic X-ray and Gamma ray Background.
Astronimy and Astrophysics, 120:607–614, 1996.

[41] Hess, V. F.
Physik Zeitschrift, 13:1084, 1912.

[42] in 't Zand, J. J. M., J. Heise and R. Jager
The optimum open fraction of coded apertures. With an application to the wide field X-ray cameras of SAX
Astronomy and Astrophysics, 288:665–674, 1994.

[43] Impey, C.
Quasars, Blazars and The Gamma-ray Sky.
The Astronomical Journal, 112(6):2667–2683, 1996.

[44] Iwabuchi, K.
Contribution of Supernova Gamma-Rays to the Gamma-Ray Background Emission.
Publications of the Astronomical Society of Japan, 53(4):669–673, 2001.

[45] Jager, R., W. A. Mels, A. C. Brinkman, M. Y. Galama, H. Goulooze, J. Heise, P. Lowes, J. M. Muller, A. Naber, A. Rook, R. Schuurhof, J. J. Schuurmans, J. J. and G. Wiersma
The Wide Field Cameras onboard the BeppoSAX X-ray Astronomy Satellite
Astronomy and Astrophysics Supplement series, 125:557–572, 1997.

[46] Jensen, D. C. and J. C. Cain
An Interim Geomagnetic Field
J. Geophysical Research, 67:3568, 1962.

[47] Kanbach, G., C. Reppin and V. Schonfelder.
Support for CRAND theory from measurements of Earth albedo neutrons between 70 and 250 MeV
Journal of Geophysical Research, 79:5159–5165, 1974.

[48] Kaplan, D. L., S. R. Kulkarni, M. H. van Kerkwijk, R. E. Rothschild, R. L. Lingenfelter, D. Marsden, R. Danner and T. Murakami
Hubble Space Telescope Observations of SGR 0526-66: New Constraints on Accretion and Magnetar Models
The Astrophysical Journal, 556:399–407, 2001.

[49] Kappadath, S. C., J. Ryan, K. Bennett, H. Bloemen, D. Forrest, W. Hermsen, R. M. Kippen, M. McConnell, V. Schoenfelder, R. van Dijk, M. Varendorff, G. Weidenspointner and C. Winkler.
The preliminary cosmic diffuse gamma-ray spectrum from 800keV to 30MeV measured with COMPTEL.
Astronomy and Astrophysics, 120:619–622, 1996.

[50] Kinzer, R. L., W. N. Johnson and J. D. Kurfess.
A balloon observation of the diffuse cosmic X-radiation above 20 keV.
The Astrophysical Journal, 222:370–378, 1978.

[51] Kinzer, R. L., G. V. Jung, D. E. Gruber, J. L. Matteson and L. E. Peterson.
Diffuse Cosmic Gamma Radiation Measured by HEAO 1.
The Astrophysical Journal, 475:361, 1997.

[52] Kinzer, R. L., P. A. Milne, J. D. Kurfess, M. S. Strickman, W. N. Johnson and W. R. Purcell
Positron Annihilation Radiation from the Inner Galaxy
Astrophysical Journal, 559:282–295, 2001.

[53] Klebesadel, R. W., I. B. Strong and R. A. Olson.
Observations of Gamma-Ray Bursts of Cosmic Origin
Astrophysical Journal, 182:L85, 1973.

[54] Klecker, B.
Energetic Particle Environment in Near-Earth Orbit
Advances in Space Research, 17(2):37–45, 1996.

[55] Klein, K. and G. Trottet.
The Origin of Solar Energetic Particle Events: Coronal Acceleration versus Shock Wave Acceleration
Space Science Reviews, 95(1/2):215–225, 2001.

[56] Kndlseder, J., D. Dixon, K, Bennett, H. Bloemen, R. Diehl, W. Hermsen, U. Oberlack, J. Ryan, V. Schnfelder and P. von Ballmoos
Image reconstruction of COMPTEL 1.8 MeV (26) AL line data
Astronomy and Astrophysics, 345:813–825, 1999.

[57] Kouveliotou, C., C. A. Meegan, G. J. Fishman, N. P. Bhat, M. S. Briggs, T. M. Koshut, W. S. Paciesas and G. N. Pendleton.
Identification of two classes of gamma-ray bursts
Astrophysical Journal, 413:L101–L104, 1993.

[58] Langel, R.A.
Main Field
Geomagnetism, 1:249–512, 1987.

[59] Lemaitre, G. and M. S. Vallarta.
On the Allowed Cone of Cosmic Radiation.
Physical Review, 50:493–504, 1936.

[60] Levine, A. M., F. L. Lang, W. H. G. Lewin, F. A. Primini, C. A. Dobson, J. P. Doty, J. A. Hoffman and S. K. Howe, A. Scheepmaker, W. A. Wheaton, J. L. Matteson, W. A. Baity, D. E. Gruber, F. K. Knight, P. L. Nolan, R. M. Pelling, R. E. Rothschild and L. E. Peterson
The HEAO 1 A-4 catalog of high-energy X-ray sources
Astrophysical Journal Supplement Series, 54:581–617, 1984.

[61] Loeb, A. and E. Waxman.
Cosmic γ-ray Background from Structural Formation in the Intergalactic Medium.
Nature, 405:156–158, 2000.

[62] Longair, M. S.
High Energy Astrophysics (Cambridge University Press), 1990.

[63] Mahoney, W., J. C. Ling and A. C. Jacobson.
HEAO 3 measurements of the atmospheric positron annihilation line.
Journal of Geophysical Research, 86(A13):11098–11104, 1981.

[64] Mao, S.
Gravitational lensing, time delay, and gamma-ray bursts
Astrophysical Journal, 389:L41–L44, 1992.

[65] Mao, S. and B. Paczynski.
On the Galactic disk and halo models of gamma-ray bursts
Astrophysical Journal, 389:L13–L16, 1992.

[66] Mason, G. M.
The composition of Galactic cosmic rays and solar energetic particles
Reviews of Geophysics, 25:685–696, 1987.

[67] Mason, K. O., M. S. Cropper, T. E. Kennedy, J. Nousek, P. Roming and M. McLelland
The Ultra-Violet and Optical Telescope (UVOT) on Swift
American Astronomical Society, HEAD meeting 32, 34:11, 2000.

[68] McConnell, M., J. Ryan, R. Diehl, V. Schonfelder, A. Strong, H. Bloemen, W. Hermsen, K. Bennett, R. van Dijk and S. Fletcher
A Possible Point Source of 2.2 MeV Gamma-Rays
American Astronomical Society, 29:1370, 1997.

[69] McConnell, M. L., J. M. Ryan, W. Collmar, V. Schnfelder, H. Steinle, A. W. Strong, H. Bloemen, W. Hermsen, L. Kuiper, K. Bennett, B. F. Phlips and J. C. Ling
A High-Sensitivity Measurement of the MeV Gamma-Ray Spectrum of Cygnus X-1
The Astrophysical Journal, 543:928–937, 2000.

[70] Merrill, R., M. W. McElhinny and P. L. McFadden
The magnetic field of the Earth, Paleomagnetism, the core, and the deep mantle.
Academic Press, San Diego., 1996.

[71] Meszaros, P., M. J. Rees and R. A. M. J. Wijers.
Viewing Angle and Envioronmental Effects in GRB: Sources of Afterglow Diversity
Astrophysical Journal, 499:301, 1998.

[72] Metzger, M. R., S. G. Djorgovski, S. R. Kulkarni, C. C. Steidel, K. L. Adelberger, D. A. Frail, E. Costa and F. Frontera.
Spectral Contraints on the redshift of the optical counterpart to the Gamma-Ray Burst of 8th May 1997
Nature, 387:878–880, 1997.

[73] Morris, D. J., H. Aarts, K. Bennett, M. Busetta, R. Byrd, W. Collmar, A. Connors, R. Diehl, G. Eymann and C. Foster.
Neutron induced background in the COMPTEL detector on the Gamma Ray Observatory
The Compton Observatory Science Workshop, pp102–108, 1992.

[74] Morris, D. J., H. Aarts, K. Bennett, J. A. Lockwood, M. McConnell, J. M. Ryan, V. Schoenfelder, H. Steinle and X. Peng.
Neutron measurements in near-Earth orbit with COMPTEL
Journal of Geophysical Research , 100(A7):12243–12249, 1995.

[75] Moskalenko, I. V. and A. W. Strong.
Anisotropic Inverse Compton Scattering in the Galaxy.
The Astrophysical Journal, 528:357–367, 2000.

[76] Mukherjee, S., E. D. Feigelson, G. T. Babu, F. Murtagh, C. Fraley and A. Raferty
Three types of Gamma-Ray Bursts
Astrophysical Journal, 508:314–327, 1998.

[77] Mucke, A. and M. Pohl.
The Contribution of Unresolved Radio-loud AGN to the Extragalactic Diffuse Gamma-ray Background.
The Monthly Notices of the Royal Astronomical Society, 312(1):177–193, 2000.

[78] Nathans, R. and J. Halpern
Systematics of Photoneutron Reactions
Physical Review, 93:437–442, 1954.

[79] Owens, A.
Nuclear Instruments and Methods, A238:473, 1985.

[80] Paczynski, B.
On the Galactic Origin of Gamma-Ray Bursts
Acta Astronomica, 41:157–166, 1991.

[81] Paczynski, B.
Cosmological gamma-ray bursts.
Acta Astronomica, 41:257–267, 1991.

[82] Paczynski, B.
Are Gamma-Ray Bursts in Star-Forming Regions?
Astrophysical Journal Letters, 494:L45, 1998.

[83] Parsons, A., S. Barthelmy, L. Barbier, E. Fenimore, N. Gehrels, D. Palmer and J. Tueller
The Swift Burst Alert Telescope (BAT)
American Astronomical Society, HEAD meeting 31, 26:12, 1999.

[84] Philippot, J. C.
IEEE, NS-17(3):446, 1970.

[85] Pian, E., P. Soffitta, A. Alessi, L. Amati, E. Costa, F. Frontera, A. Fruchter, N. Masetti, E. Palazzi, A. Panaitescu and P. Kumar.
BeppoSAX confirmation of beamed afterglow emission from GRB 990510
Astronomy and Astrophysics, 372:456–462, 2001.

[86] Pinto, O., Jr., W. D. Gonzalez, I. R. C. Pinto, A. L. C. Gonzalez, O. Jr. Mendes.
The South Atlantic Magnetic Anomaly - Three decades of research
Journal of Atmospheric and Terrestrial Physics, 54:1129–1134, 1992.

[87] Piro, L., E. Costa, M. Feroci, G. Stratta, F. Frontera, L. Amati, D. dal Fiume, L. A. Antonelli, J. Heise, J. in 't Zand, A. Owens, A. N. Parmar and G. Cusumano, M. Vietri and G. C. Perola
Iron line signatures in X-ray afterglows of GRB by BeppoSAX
Astronomy and Astrophysics Supplement, 138:431–432, 2000.

[88] Porciani, C. and P. Madau.
On the Association of gamma-Ray Bursts with Massive Stars: Implications for Number Counts and Lensing Statistics
Astrophysical Journal, 548:522–531, 2000.

[89] Poulsen, J. M., P. Sarra, A. J. Bird, E. M. Quadrini, P. Ubertini, M. Frutti, R. Ronchi, A. Colferai and S. di Cosimo
IBIS calibration unit on INTEGRAL satellite
Proceedings of the 4th INTEGRAL workshop, 615–618, 2001.

[90] Preece, R. D., M. S. Briggs, G. N. Pendleton, W. S. Paciesas, J. L. Matteson, D. L. Band, R. T. Skelton and C. A. Meegan
BATSE Obervations of the Gamma-Ray Burst Spectra. III. Low Energy Behaviour of Time-Averaged Spectra
Astrophysical Journal, 473:310–321, 1996.

[91] Preszler, A. M., S. Moon and R. S. White.
Atmospheric Neutrons
Journal of Geophysical Research, 81:4715–4722, 1976.

[92] Purcell, W. R., L.-X. Cheng, D. D. Dixon, R. L. Kinzer, J. D. Kurfess, M. Leventhal, M. A. Saunders, J. G. Skibo, D. M. Smith and J. Tueller
OSSE Mapping of Galactic 511 keV Positron Annihilation Line Emission
Astrophysical Journal, 491:725, 1997.

[93] Ramaty, R. and R. E. Lingenfelter
Gamma-ray line astronomy
Nature, 278:127–132, 1979.

[94] Ramaty, R., M. Leventhal, K. W. Chan and R. E. Lingenfelter
On the origin of variable 511 keV line emission from the Galactic center region
Astrophysical Journal, 392:L63–L66, 1992.

[95] Reames, D. V., J. P. Meyer and T. T. von Rosenvinge.
Energetic-particle abundances in impulsive solar flare events
Astrophysical Journal Supplement Series, 90(2):649–667, 1994.

[96] Ruiz-Lapuente, P., M. Casse and E. Vangioni-Flam.
The Cosmic Gamma-ray Background in the MeV Range.
The Astrophysical Journal, 549:483–494, 2001.

[97] Sanderson, T. R., R. G. Marsden, A. M. Heras, K. -P. Wenzel, J. D. Anglin, A. Balogh and R. Forsyth.
Ulysses Particle Observations of the March 1991 Solar Flare Events
Geophysical Research Letters, 19(12):1263–1266, 1992.

[98] Sato, G., T. Takahashi, M. Sugiho, M. Kouda, Shin Watanabe, Y. Okada, T. Mitani and K. Nakazawa
Characterization of CdTe/CdZnTe detectors
IEEE Nuclear Science Symposium Conference Record, 4:2299–2303, 2001.

[99] Schoenfelder, V., U. Graser and J. Daugherty.
Diffuse cosmic and atmospheric MeV gamma radiation from balloon.
Astrophysical Journal, 217:306–319, 1977.

[100] Schonfelder, V., F. Graml and F. P. Penningsfield.
The vertical component of 1-20 MeV gamma rays at balloon altitudes.
Astrophysical Journal, 240:350–362, 1980.

[101] Schoenfelder, V., H. Aarts, K. Bennett, H. de Boer, J. Clear, W. Collmar, A. Connors, A. Deerenberg, R. Diehl, A. von Dordrecht, J. den Herder, W. Hermsen, M. Kippen, L. Kuiper, G. Lichti, J. Lockwood, J. Macri, M. McConnell, D. Morris, R. Much, J. Ryan, G. Simpson, M. Snelling, G. Stacy, H. Steinle, A. Strong, B. N. Swanenburg, B. Taylor, C. de Vries and C. Winkler
Instrument description and performance of the Imaging Gamma-Ray Telescope COMPTEL aboard the Compton Gamma-Ray Observatory
Astrophysical Journal Supplement Series, 86:657–692, 1993.

[102] Schonfelder, V.
Gamma-ray Properties of Active Galactic Nucleii
Astrophysical Journal Supplement, 92:593–598, 1994.

[103] Seckel, D., T. Stanev and T. K. Gaisser.
Cosmic ray albedo gamma rays from the quiet sun
The Compton Observatory Science Workshop, pp542–549, 1992.

[104] Setti, G. and L. Woltjer.
The Gamma-ray Background.
The Astrophysical Journal Supplement Series, 92:629–631, 1994.

[105] Slavis, K. R., P. F. Dowkontt, F. Duttweiler, J. W. Epstein, P. L. Hink, G. L. Huszar, E. Kalemci, P. Leblanc, J. L. Matteson, M. R. Pelling, R. E. Rothschild, E. A. Stephan, T. O. Tumer and G. J. Visser
Performance of a prototype CdZnTe detector module for hard x-ray astrophysics
SPIE, 4140:249–356, 2000.

[106] Smart, D. F. and M. A. Shea.
Geomagnetic cutoffs: A Review for Space Dosimetry Applications.
Advances in Space Research, 14(10):787–796, 1994.

[107] SPace Environment Infomation System
http://www.spenvis.oma.be/

[108] Sreekumar, P., D. L. Bertsch, B. L. Dingus, J. A. Esposito, C. E. Fichtel, R. C. Hartman, S. D. Hunter, G. Kanbach, D. A. Kniffen, Y. C. Lin, H. A. Mayer-Hasselwander, P. F. Michelson, C. von Montigny, A. Muecke, R. Mukherjee, P. L. Nolan, M. Pohl, O. Reimer, E. Schneid, J. G. Stacy, F. W. Stecker, D. L. Thompson and T. D. Willis.
EGRET Observations of the Extragalactic Gamma-Ray Emission
The Astrophysical Journal, 494:523, 1998.

[109] Sreekumar, P.
Extragalactic Gamma-Ray Emission: CGRO Results.
The 5th Compton Symposium, pp459–466, 1999.

[110] Stecker, F. W. and M. H. Salamon.
The Gamma-Ray Background from Blazars: A New Look.
The Astrophysical Journal, 464:600, 1996.

[111] Stening, R. J., A. D. Richmond and R. G. Roble.
Lunar tides in the Thermosphere-Ionosphere-Electrodynamics General Circulation Model
Journal of Geophysical Research, 104(A1):1–14, 1999.

[112] Steinle, H., K. Bennett, H. Bloemen, W. Collmar, R. Diehl, W. Hermsen, G. G. Lichti, D. Morris, V. Schonfelder, A. W. Strong and O. R. Williams
COMPTEL observations of Centaurus A at MeV energies in the years 1991 to 1995
Astronomy and Astrophysics, 330:97–107, 1998.

[113] Stormer, C.
The Polar Aurora.
Clarendon Press, Oxford, 1955.

[114] Strong, A. W., K. Bennett, H. Bloemen, R. Diehl, W. Hermsen, W. Purcell, V. Schoenfelder, J. G. Stacy, C. Winkler and G. Youssefi
Diffuse galactic hard X-ray and low-energy gamma-ray continuum.
Astronomy and Astrophysics, 120:381–387, 1996.

[115] Takahashi, T. and S. Watanabe
Recent progress in CdTe and CdZnTe Detectors.
IEEE Transactions on Nuclear Science, 48(4):950–959, 2001.

[116] Toms, M. E. and W. E. Stephens
Photoneutrons from Lead
Physical Review, 108:77–81, 1957.

[117] Tranquille, C. and E. J. Daly.
The radiation environment for earth-orbiting astronomical satellites
British Interplanetary Society, Journal, 43:51–56, 1990.

[118] Valinia, A., F. E. Marshall and R. L. Kinzer.
Measurement of the Galactic X-Ray/Gamma-Ray Background Radiation: Contribution of Discrete Sources.
Astrophysical Journal, 534(1):277–282, 2000.

[119] Van Allen, J. A.
Radiation Belts around the Earth.
San Francisco: Freeman, 1958.

[120] van Paradijs, J., P. J. Groot, T. Galama, C. Kouveliotou, R. G. Strom, J. Telting, R. G. M. Rutten, G. J. Fishman, C. A. Meegan, M. Pettini, N. Tanvir, J. Bloom, H. Pedersen, H. U. Nordgaard-Nielsen, M. Linden-Vornle, J. Melnick, G. van der Steene, M. Bremer, R. Naber, J. Heise, J. in 't Zand, E. Costa, M. Feroci, L. Piro, F. Frontera, G. Zavattini, L. Nicastro, E. Palazzi, K. Bennet, L. Hanlon and A. Parmar.
Transient optical emission from the error box of the gamma-ray burst of 28 February 1997
Nature, 386:686–688, 1997.

[121] Watanabe, K., D. H. Hartman, M. D. Leising and L. S. The.
The Diffuse Gamma-ray Background from Supernovae.
The Astrophysical Journal, 516:285–296, 1999.

[122] Watanabe, K., M. D. Leising, G. H. Share and R. L. Kinzer.
The MeV Cosmic Gamma-ray Background Measured with SMM.
The 5th Compton Symposium, pp471–474, 1999.

[123] Webber, W. R. and J. A. Lezniak.
The comparative spectra of cosmic-ray protons and helium nuclei
Astrophysics and Space Science, 30:361–380, 1974.

[124] Weidenspointner, G., K. Bennett, R. van Dijk, S. C. Kappadath, J. Lockwood, D. Morris, V. Schnfelder and M. Varendorff.
The local neutron flux at low earth-orbiting altitudes
Advances in Space Research, 21(12):1781–1784, 1998.

[125] Weidenspointner, G., M. Varendorff, R. Diehl, G. G. Lichti, V. Schonfelder, S. C. Kappadath, J. Ryan, H. Bloemen, W. Hermsen and W. Bennett.
The Cosmic Diffuse Gamma-Ray Background measured with COMPTEL.
The 5th Compton Symposium, pp467–470, 1999.

[126] Weidenspointner, G., M. Varendorff, U. Oberlack, D. Morris, S. Plschke, R. Diehl, S. C. Kappadath, M. McConnell, J. Ryan, V. Schnfelder and H. Steinle.
The COMPTEL instrumental line background
Astronomy and Astrophysics, 368:347–368, 2001.

[127] Weisskopf, M. C., E. H. Silver, H. Kestenbaum, K. S. Long and R. Novick
A precision measurement of the X-ray polarization of the Crab Nebula without pulsar contamination
Astrophysical Journal, 220:L117–L121, 1998.

[128] Westmore, M. J.

PhD. Thesis, 2002.

[129] Wijers, R. A. M. J., M. J. Rees and P. Meszaros.
Shocked by GRB 970228: the afterglow of a cosmological fireball
MNRAS, 288:L51–L56, 1997.

[130] Wilson, R. R.
Monte Carlo study of shower production
Physical Review, 86:261–269, 1952.

[131] Wilson, R. B., B. A. Harmon, M. H. Finger, G. J. Fishman, C. A. Meegan and W. S. Paciesas
Long-term source monitoring with BATSE
The Compton Observatory Science Workshop, 35–46, 1992.

[132] Zdziarski, A.
The Average X-ray/Gamma-ray Spectra of Seyfert Galaxies from GINGA and OSSE and the Origin of the Cosmic X-ray Background.
The Astrophysical Journal, 483:L63–L66, 1994.

[133] Zdziarski, A.
Contributions of AGNs and SNe Ia to the cosmic X-ray and Gamma-ray Backgrounds.
The Monthly Notices of the Royal Astronimical Society, 281:9, 1996.

[134] Zombeck, M. V.
The Relative Abundances of the Chemical Elements in the Cosmic Rays and in the Solar System Normalised to 100 at Carbon.
The Handbook of Space Astronomy and Astrophysics, p219–230, 1990.

Appendix A

Graded-Z Shield Optimisation Spectra

Here are the important spectra taken during the SwiMM graded-Z shield optimisation. Two spectra will be presented for each simulation. The first will be the total background including all the components convolved with the charge trapping function. The second will be spectra of the component flux passing through each shield section unhindered. This will be compared to the aperture background flux.

Run	Configuration Summary
1	SS ratios and thicknesses are equal
2	Pb shield only
3	SS weighted with the theoretical material ratio
4	SS weighted and material skewed to Ta and Sn
5	Optimum run
6	Optimum run - alternative SS00 geometry

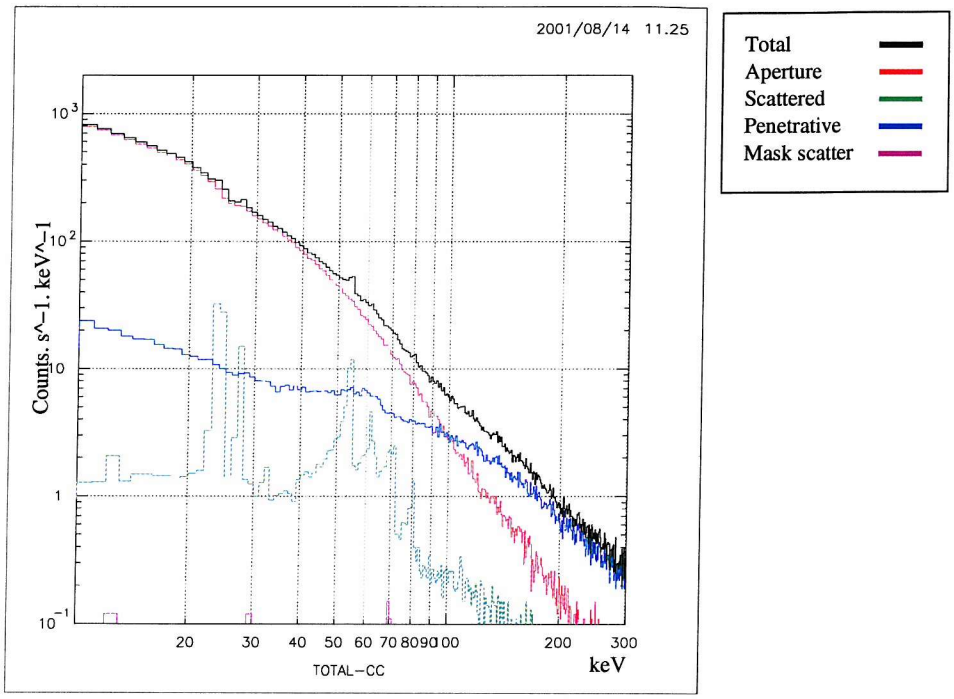

Figure A.1: **RUN 1: Total Background**

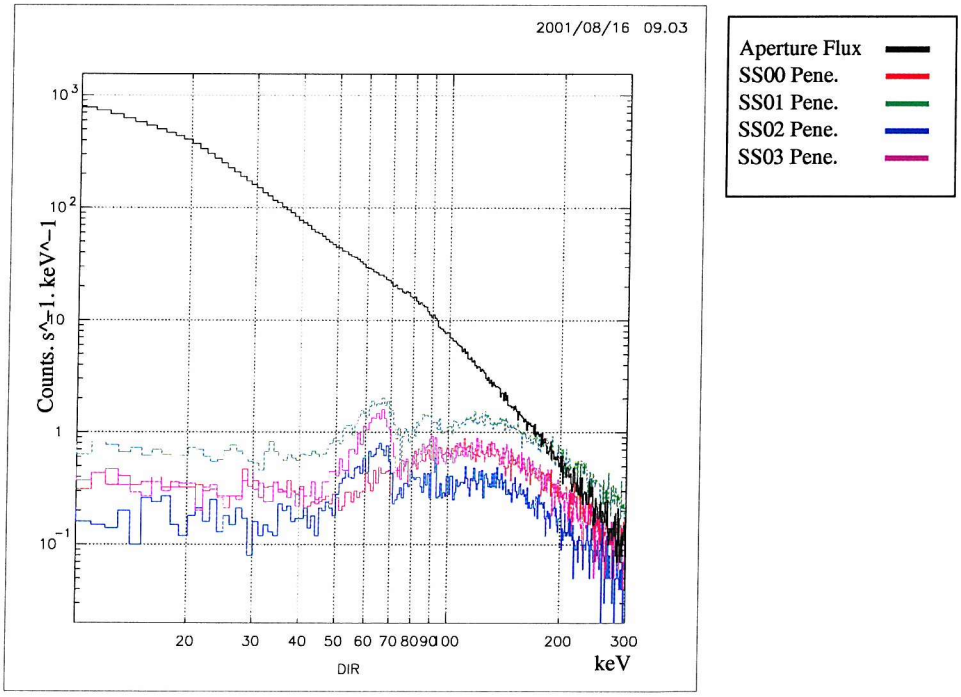

Figure A.2: **RUN 1: Penetrative Flux**

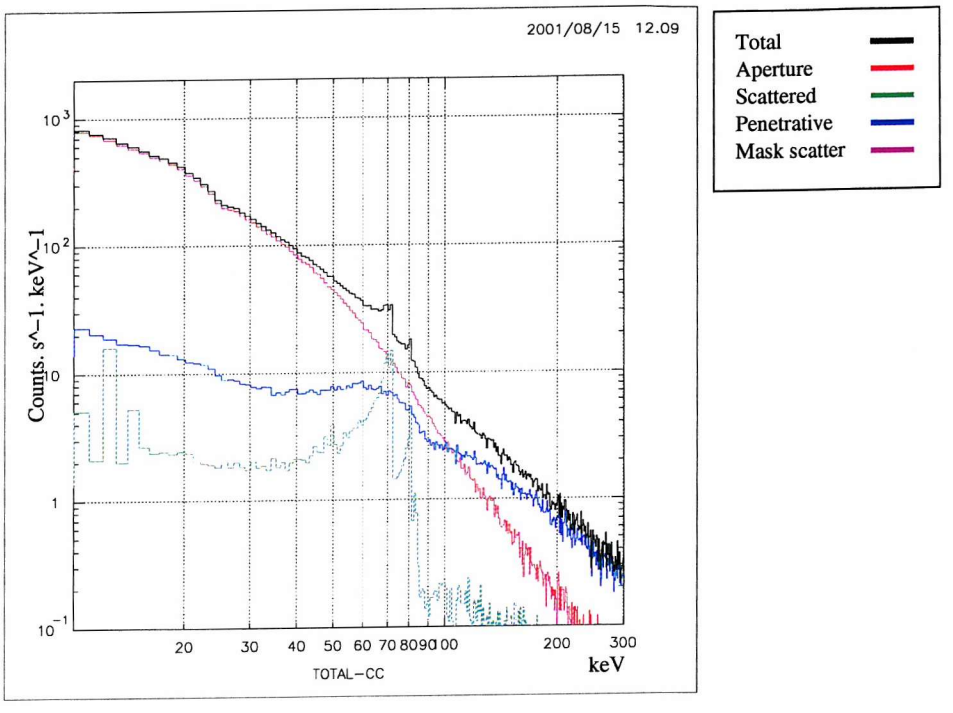

Figure A.3: **RUN 2: Total Background**

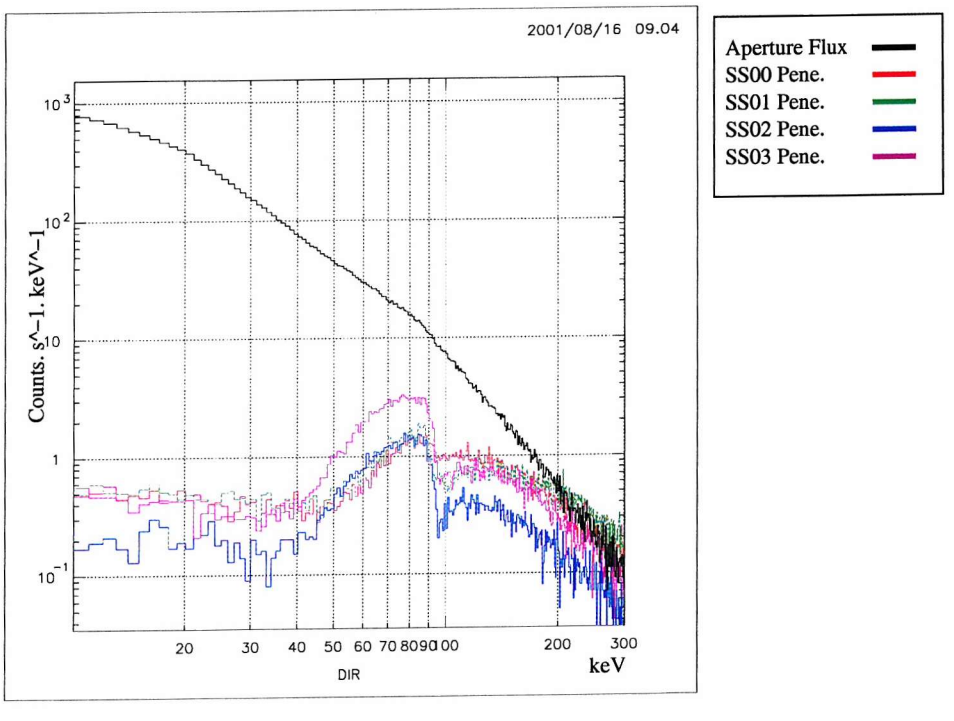

Figure A.4: **RUN 2: Penetrative Flux**

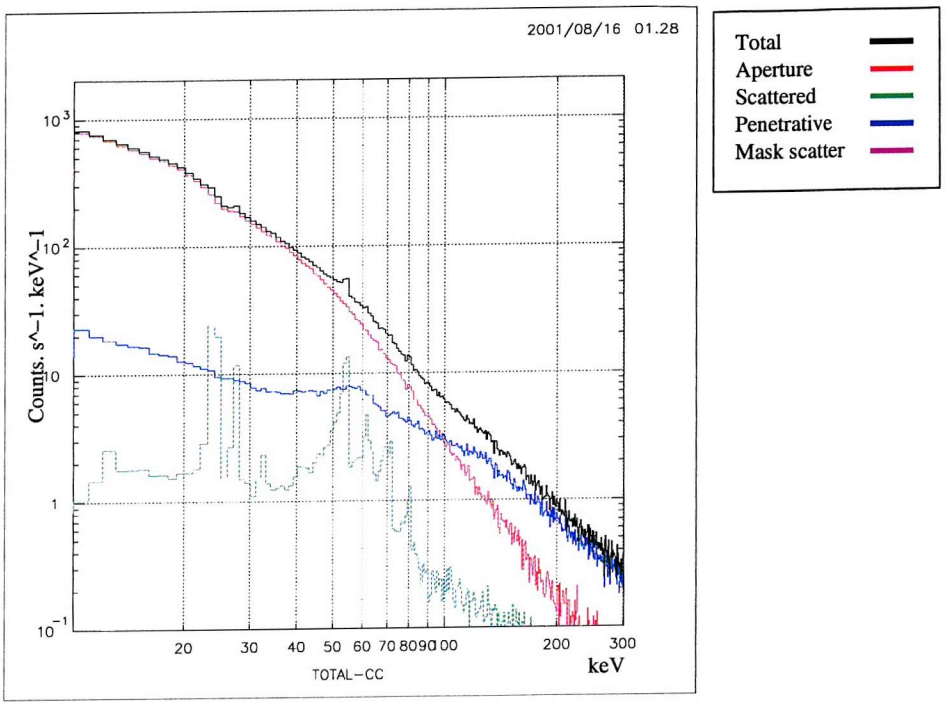

Figure A.5: **RUN 3: Total Background**

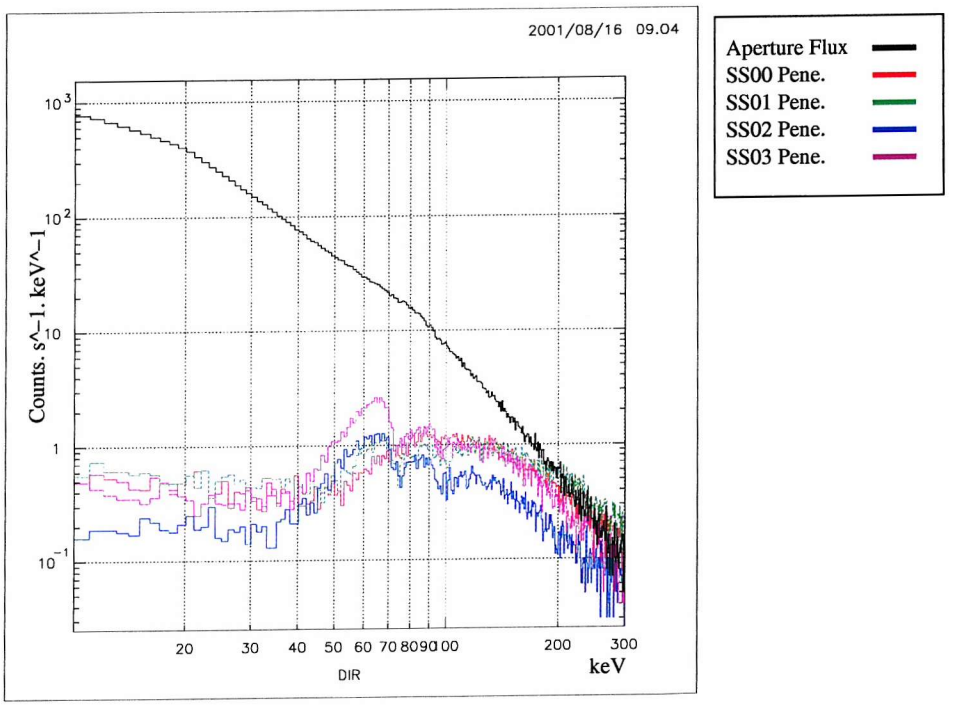

Figure A.6: **RUN 3: Penetrative Flux**

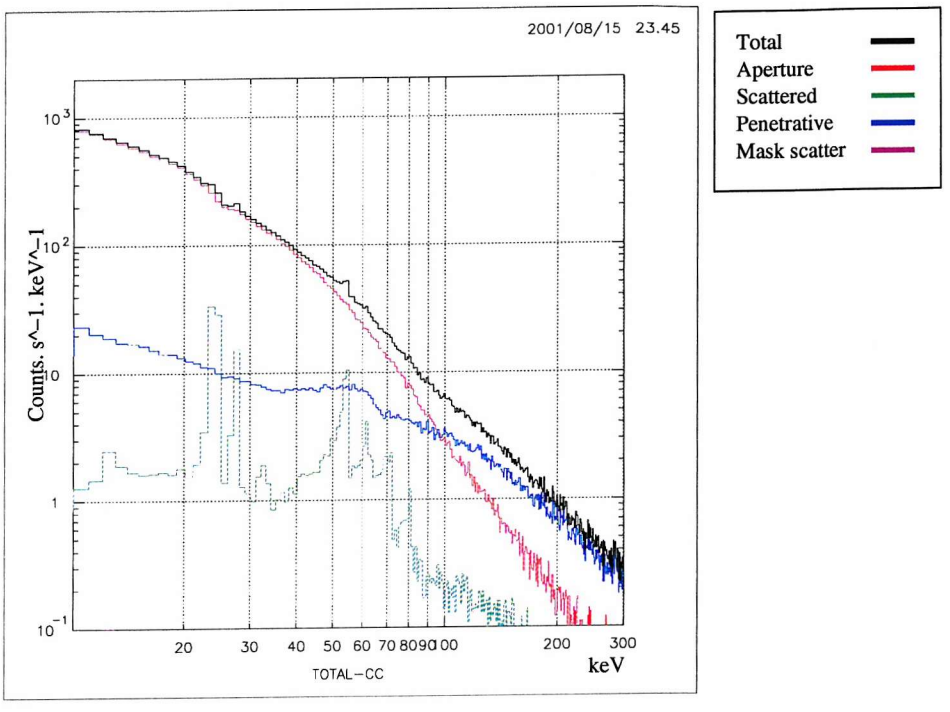

Figure A.7: **RUN 4: Total Background**

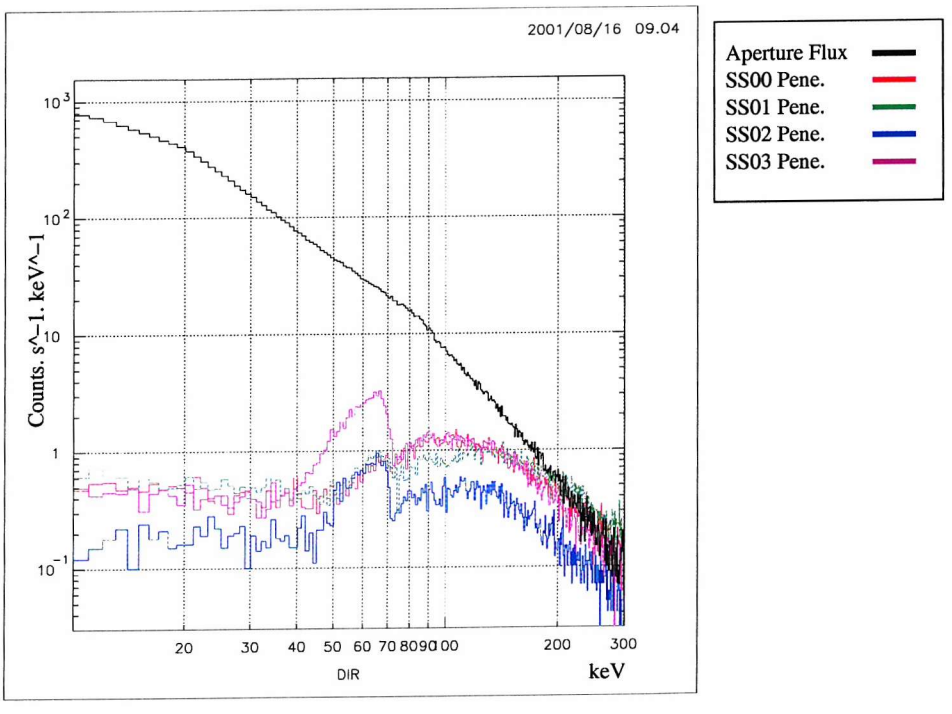

Figure A.8: **RUN 4: Penetrative Flux**

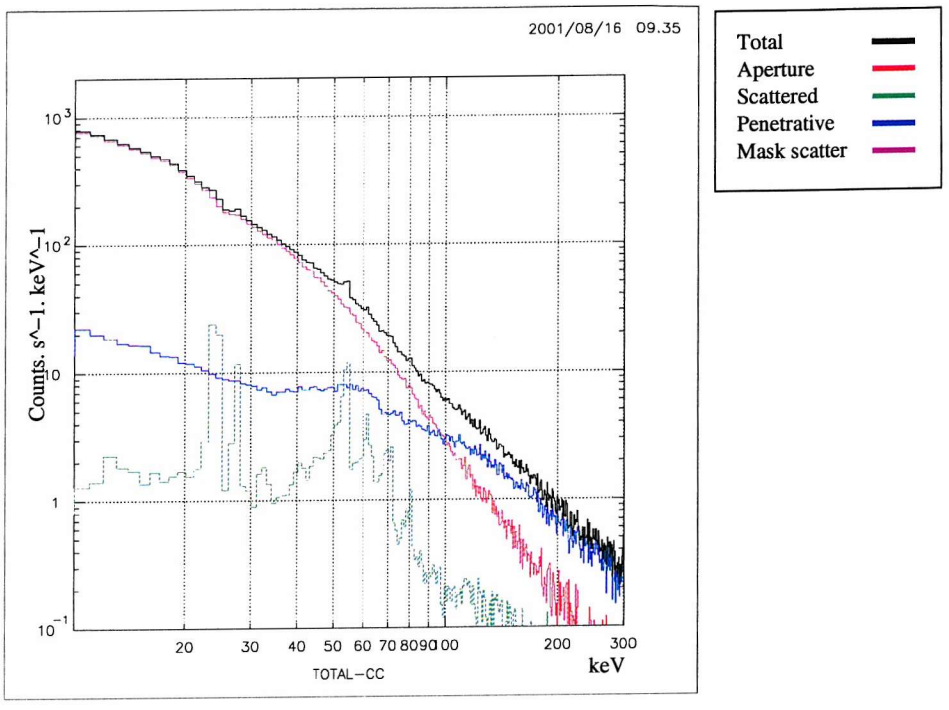

Figure A.9: **RUN 5: Total Background**

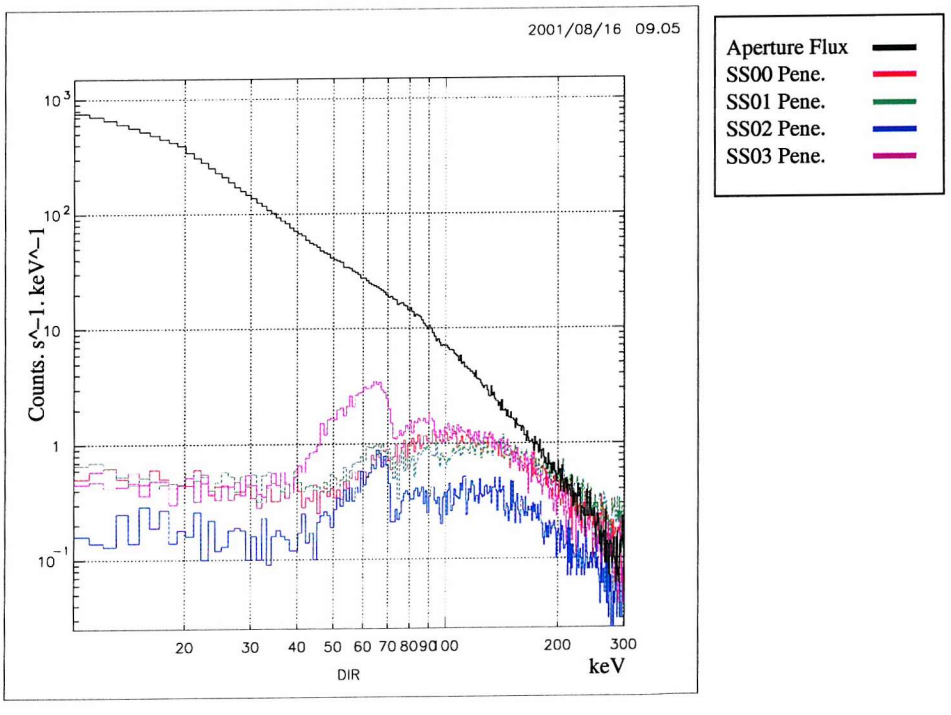

Figure A.10: **RUN 5: Penetrative Flux**

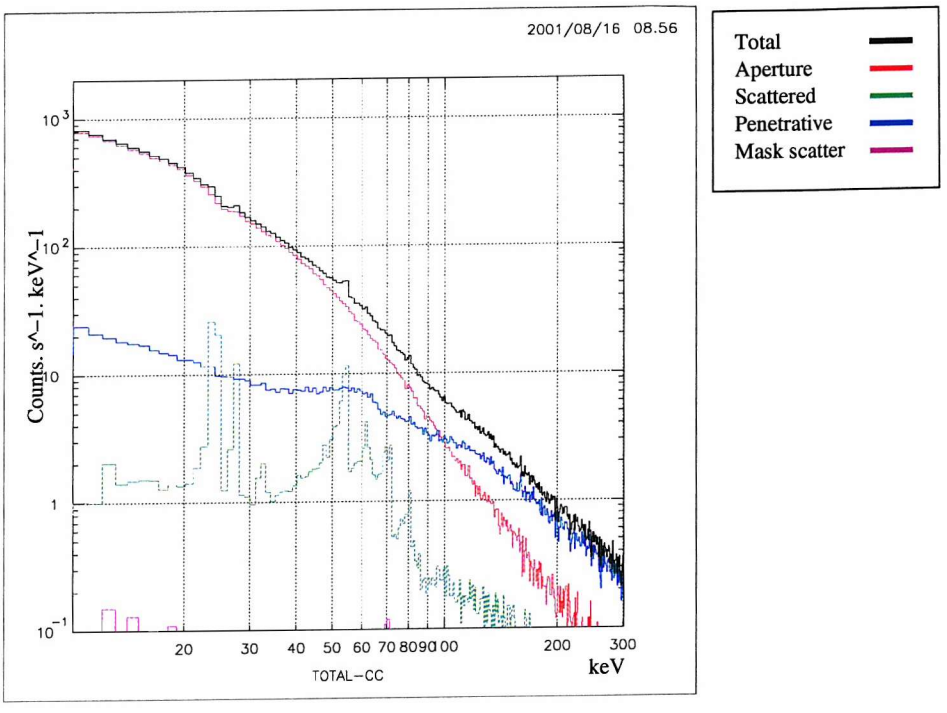

Figure A.11: **RUN 6: Total Background**

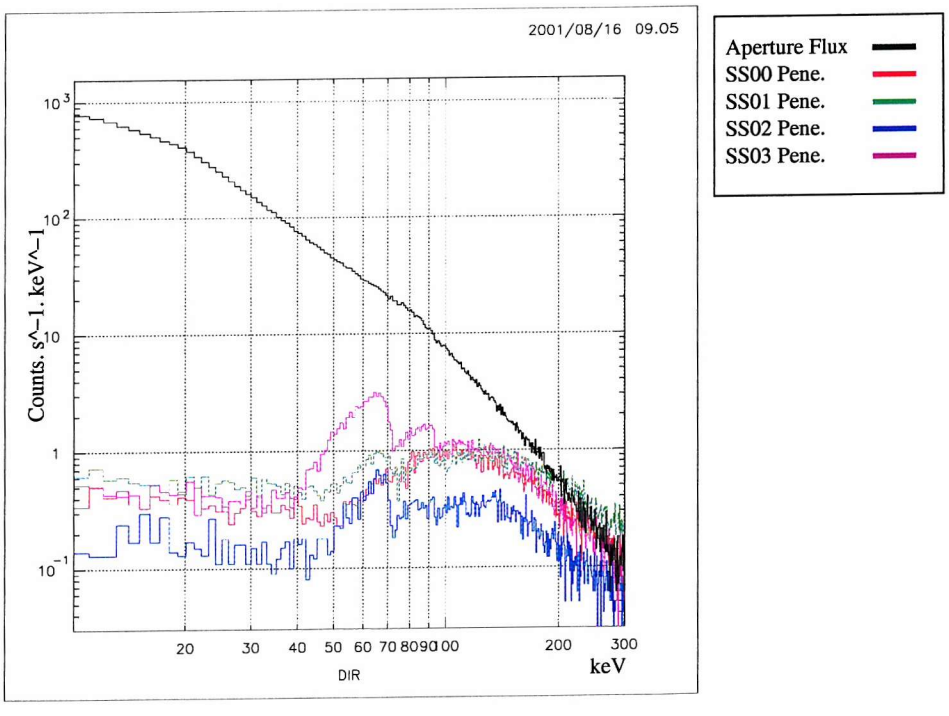

Figure A.12: **RUN 6: Penetrative Flux**

Appendix B

CdTe Beam Experiment and Mass Model Verification Table

Line Energies from figure 7.22.

Energy [keV]	Emission Parent	Half-life	Origin	Exp.	MM
< 30	Cd/Te *fluor.*	n/a	Cd/Te	⋆	⋆
46.5	Pb^{210}	22.3 y	Pb Shielding	⋆	
61.5	Hg^{195}	9.9 h	Pb Shielding	⋆	
72-74	Pb *fluor.*	n/a	Pb Shielding	⋆	
84-87	Pb *fluor.*	n/a	Pb Shielding	⋆	
88.0	Cd^{109}	462.6 d	Cd	⋆	⋆
89.9	Sb^{120}	5.8 d	Cd	⋆	
93.1	Cd^{105}	6.5 h	Cd	⋆	⋆
96.7	Ag^{111}	7.5 d	Cd		⋆
116.3	Te^{132}	3.2 d	Te		⋆
148.6	Xe^{122}	20.1 h	Te		⋆
150.8	In^{111}	2.8 d	Cd	⋆	
153.6	Te^{119}	4.7 d	Te	⋆	⋆
157.2	Hg^{192}	4.9 h	Pb Shielding	⋆	
159.0	I^{123}	13.27 h	Te	⋆	⋆
171.3	In^{111}	2.8 d	Cd	⋆	⋆
172.1	Xe^{127}	36.4 d	Te	⋆	
180.1	Hg^{195}	9.9 h	Pb Shielding	⋆	
186.1	Au^{193}	17.7 h	Pb Shielding	⋆	
186.4	Hg^{192}	4.9 h	Pb Shielding	⋆	
202.9	Te^{127}	9.35 h	Te	⋆	⋆
202.9	Xe^{127}	36.4 d	Te	⋆	⋆
203.5	In^{109}	4.2 h	Cd	⋆	⋆
211.8	unknown	unknown	unknown	⋆	⋆
215.1	Te^{127}	9.35 h	Te	⋆	⋆
243.4	Xe^{125}	16.9 h	Te	⋆	⋆
254.4	Ag^{111}	7.5 d	Cd	⋆	⋆
254.4	In^{111}	2.8 d	Cd	⋆	⋆
252.4	Sb^{127}	3.9 d	Te	⋆	
253.7	Sb^{118}	5.0 h	Te	⋆	
269.7	Pd^{101}	8.5 h	Cd	⋆	⋆
270.5	Te^{119}	4.7 d	Te	⋆	⋆
280.4	Ag^{105}	41.2 d	Cd	⋆	⋆
280.5	Sn^{110}	4.1 h	Cd/Te	⋆	⋆
289.0	unknown	unknown	unknown	⋆	⋆
296.0	Au^{192}	4.9 h	Pb Shielding	⋆	
296.3	Pd^{101}	8.5 h	Cd	⋆	⋆
306.5	Hg^{192}	4.9 h	Pb Shielding	⋆	
314.1	Sb^{128}	9.0 h	Te	⋆	⋆
316.3	Ag^{113}	5.4 h	Cd	⋆	⋆
324.8	Cd^{107}	6.5 h	Cd	⋆	
336.2	Cd^{115}	53.5 h	Cd	⋆	
342.1	Ag^{111}	7.5 d	Cd	⋆	
344.5	Ag^{105}	41.3 d	Cd	⋆	⋆

Cont...

Energy [keV]	Emission Parent	Half-life	Origin	Exp.	MM
346.0	unknown	unknown	unknown	⋆	⋆
387.9	Hg^{195}	4.6 h	Pb Shielding	⋆	
391.3	Pd^{111}	5.5 h	Cd	⋆	
407.6	Hg^{193}	11.8 h	Pb Shielding	⋆	
418.0	Te^{127}	9.4 h	Te	⋆	⋆
418.1	I^{130}	12.4 h	Te	⋆	⋆
426.3	In^{109}	4.2 h	Cd	⋆	⋆
427.1	Ir^{187}	10.5 h	Pb Shielding	⋆	
443.4	Ag^{105}	4.1 d	Cd	⋆	⋆
443.8	Ru^{103}	39.3 d	Cd	⋆	⋆
451.0	Ag^{106}	8.3 d	Cd	⋆	
460.6	Ru^{97}	2.9 d	Cd	⋆	⋆
469.4	Ru^{105}	4.4 h	Cd	⋆	
470.5	Te^{121}	16.8 d	Te	⋆	⋆
492.3	Cd^{115}	53.4 h	Cd	⋆	
507.6	Te^{121}	16.8 d	Te	⋆	⋆
511.0	e^+e^-	n/a	n/a	⋆	⋆
511.8	Ag^{106}	8.3 d	Cd	⋆	⋆
526.6	Sb^{128}	9.0 h	Te	⋆	⋆
527.9	Cd^{115}	53.5 h	Cd	⋆	⋆
529.0	I^{123}	13.27 h	Te	⋆	⋆
536.1	I^{130}	12.4 h	Te	⋆	⋆
538.5	I^{123}	13.3 h	Te	⋆	⋆
539.6	Rh^{100}	20.8 h	Cd	⋆	⋆
544.7	Sb^{129}	4.4 h	Te	⋆	
556.7	Te^{129}	33.6 d	Te		⋆
557.0	Ru^{103}	39.3 d	Cd	⋆	⋆
558.5	In^{114}	49.5 d	Cd		⋆
564.1	Sb^{122}	2.7 d	Te	⋆	⋆
573.1	Te^{121}	16.7 d	Te	⋆	⋆
573.3	Hg^{193}	11.8 h	Pb Shielding	⋆	
575.0	Pd^{111}	5.5 h	Cd	⋆	
582.1	Tc^{95}	61.0 d	Cd	⋆	⋆
582.1	Nb^{95}	86.6 h	Cd	⋆	⋆
584.0	unknown	unknown	unknown	⋆	⋆
585.1	Hg^{195}	9.9 h	Pb Shielding	⋆	
590.4	Pd^{101}	8.5 h	Cd	⋆	⋆
593.3	Te^{127}	109.0 d	Te		⋆
602.7	Sb^{124}	60.2 d	Te	⋆	⋆
610.3	Ru^{103}	39.3 d	Cd	⋆	
617.8	Rh^{99}	4.7 h	Cd	⋆	⋆
623.7	In^{109}	4.2 h	Cd	⋆	⋆
628.1	Rh^{102}	207 d	Cd	⋆	⋆

Cont...

Energy [keV]	Emission Parent	Half-life	Origin	Exp.	MM
632.8	Pd^{111}	5.5 h	Cd	⋆	⋆
638.0	Sn^{113}	115.0 d	Cd/Te	⋆	⋆
644.0	Te^{119}	16.0 h	Te	⋆	⋆
644.6	Ag^{105}	41.3 d	Cd	⋆	⋆
645.9	Sb^{124}	60.2 d	Te	⋆	
650.9	Te^{127}	109.0 d	Te	⋆	⋆
657.8	In^{110}	4.9 h	Cd	⋆	⋆
657.8	Ag^{110}	248.8 d	Cd	⋆	⋆
658.9	Te^{109}	109.0 d	Te	⋆	⋆
666.3	I^{126}	13.1 d	Te	⋆	⋆
668.5	I^{130}	12.4 h	Te	⋆	⋆
675.9	Tl^{198}	5.3 h	Pb Shielding	⋆	
676.4	Ru^{105}	4.4 h	Cd	⋆	⋆
685.7	Sb^{127}	3.9 d	Te	⋆	⋆
695.9	Te^{129}	33.6 d	Te	⋆	⋆
699.9	Te^{119}	16.0 h	Te	⋆	⋆
707.4	In^{110}	4.9 h	Cd	⋆	⋆
717.2	Ag^{106}	8.3 d	Cd	⋆	⋆
722.8	I^{124}	4.8 d	Te	⋆	⋆
739.5	I^{130}	12.4 d	Te	⋆	⋆
743.2	Sb^{128}	9.0 h	Te	⋆	⋆
753.8	Sb^{128}	9.0 h	Te	⋆	⋆
766.8	Rh^{102}	2.9 y	Cd	⋆	⋆
779.8	Hg^{195}	9.9 h	Pb Shielding	⋆	
783.7	Sb^{127}	3.9 d	Te		⋆
796.5	Cd^{107}	6.5 h	Cd	⋆	⋆
812.8	Sb^{129}	4.4 h	Te	⋆	
817.0	Te^{129}	33.6 d	Te	⋆	⋆
822.5	Sn^{125}	9.64 d	Cd/Te	⋆	⋆
822.6	Rh^{100}	20.8 h	Cd	⋆	⋆
844.0	unknown	unknown	unknown	⋆	⋆
852.2	Te^{131}	30 h	Te	⋆	⋆
856.0	unknown	unknown	unknown		⋆
862.0	unknown	unknown	unknown		⋆
884.7	Ag^{110}	249.8 d	Cd	⋆	⋆
884.7	In^{110}	4.9 h	Cd	⋆	⋆
909.8	Te^{121}	154.0 d	Te	⋆	⋆
913.0	Ir^{187}	10.5 h	Pb Shielding	⋆	
914.6	Sb^{129}	4.4 h	Te	⋆	⋆
922.0 ⋆	unknown	unknown	unknown		⋆
926.0 ⋆	unknown	unknown	unknown		⋆
933.8	Cd^{115}	44.6 d	Cd		⋆

Cont...

Energy [keV]	Emission Parent	Half-life	Origin	Exp.	MM
937.5	Ag^{110}	249.8 d	Cd	⋆	⋆
937.5	In^{110}	4.9 h	Cd	⋆	⋆
922.0	unknown	unknown	unknown		⋆
926.0	unknown	unknown	unknown		⋆
998.3	Te^{121}	154 d	Te	⋆	⋆